

Abstract

Title of Dissertation: HIGH-RESOLUTION IMAGING OF
DENSE GAS STRUCTURE AND
KINEMATICS IN NEARBY MOLECULAR
CLOUDS WITH THE CARMA
LARGE AREA STAR FORMATION SURVEY

Shaye Storm, Doctor of Philosophy, 2015

Dissertation directed by: Professor Lee Mundy
Department of Astronomy

This thesis utilizes new observations of dense gas in molecular clouds to develop an empirical framework for how clouds form structures which evolve into young cores and stars. Previous observations show the general turbulent and hierarchical nature of clouds. However, current understanding of the star formation pathway is limited by existing data that do not combine angular resolution needed to resolve individual cores with area coverage required to capture entire star-forming regions and with tracers that can resolve gas motions.

The original contributions of this thesis to astrophysical research are the creation and analysis of the largest-area high-angular-resolution maps of dense gas in molecular clouds to-date, and the development of a non-binary dendrogram algorithm to quantify the hierarchical nature and three-dimensional morphology of cloud structure.

I first describe the CARMA Large Area Star Formation Survey, which provides spectrally imaged N_2H^+ , HCO^+ , and HCN ($J = 1 \rightarrow 0$) emission across diverse regions of the Perseus and Serpens Molecular Clouds. I then present a detailed analysis of the Barnard 1 and L1451 regions in Perseus. A non-binary dendrogram

analysis of Barnard 1 N_2H^+ emission and all L1451 emission shows that the most hierarchically complex gas corresponds with sub-regions actively forming young stars. I estimate the typical depth of molecular emission in each region using the spatial and kinematic properties of dendrogram-identified structures. Barnard 1 appears to be a sheet-like region at the largest scales with filamentary substructure, while the L1451 region is composed of more spatially distinct ellipsoidal structures.

I then do a uniform comparison of the hierarchical structure and young stellar content of all five regions. The more evolved regions with the most young stellar objects (YSOs) and strongest emission have formed the most hierarchical levels. However, all regions show similar mean branching properties at each level, suggesting that dense gas fragmentation proceeds in a hierarchically similar way from earlier to later stages of star formation. Compared to the more evolved YSOs, the youngest YSOs are preferentially forming within leaves and at high-level locations in dendrogram hierarchies, indicating that dense gas in molecular clouds must reach a state of hierarchical complexity before young stars form efficiently.

**HIGH-RESOLUTION IMAGING OF
DENSE GAS STRUCTURE AND
KINEMATICS IN NEARBY MOLECULAR
CLOUDS WITH THE CARMA
LARGE AREA STAR FORMATION SURVEY**

by

Shaye Storm

Dissertation submitted to the Faculty of the Graduate School of the
University of Maryland at College Park in partial fulfillment
of the requirements for the degree of
Doctor of Philosophy
2015

Advisory Committee:

Professor Lee Mundy, chair

Professor Eve Ostriker

Professor Alberto Bolatto

Dr. Mark Wolfire

Professor Richard Walker, Dean's representative

© Copyright by
Shaye Storm
2015

Preface

This thesis contains a combination of research that has already been published and new results to be published in the future. Chapter 2, entitled “CARMA Large Area Star Formation Survey: Project Overview with Analysis of Dense Gas Structure and Kinematics in Barnard 1,” has been published in the *Astrophysical Journal* (Storm, S., Mundy, L. G., Fernández-Lopez, M., et al., 2014, *ApJ*, 794, 165). Chapter 1, entitled “Introduction,” includes parts of the introduction from the published work presented in Chapter 2. Chapter 3, entitled “CARMA Large Area Star Formation Survey: The Young L1451 Region within Perseus,” is in preparation to be submitted to the *Astrophysical Journal* (Storm, S., Mundy, L. G., Lee, I. J., et al., 2015, *ApJ*, in preparation). The cross region comparison in Chapter 4 builds from the previous chapters and from published results of Serpens Main (Lee, K. I., Fernández-López, M., Storm, S., et al., 2014, *ApJ*, 797, 76) and results in preparation for Serpens South (Fernández-López et al. 2015) and NGC 1333 (Mundy et al. 2015).

The thesis observations and research are based on a CARMA Key Project that was proposed in December 2011. I was a co-investigator on the proposal for the CARMA Large Area Star Formation Survey, with Professor Lee Mundy as the Principal Investigator. The project was based on pilot observations of the Perseus NGC 1333 region, and was approved in February 2012 to observe two additional regions within Perseus and two regions in Serpens. I led the observations and data

calibration for the Key Project for its entire duration, from April 2012 to August 2013. After the observations were complete, I led the effort to determine the best mapping techniques. Once the science-ready data cubes for each region were created, I led the science analysis of the two youngest Perseus regions: Barnard 1 and L1451. Other team members led the science of NGC 1333 and the Serpens regions, while I contributed to those works. I was the principal developer of the dendrogram analysis of all regions that went into each published and upcoming paper mentioned above. Katherine Lee and Aaron Meisner led the construction of *Herschel*-based column density and temperature maps presented in Chapters 3 and 4.

To my family.

Acknowledgements

Graduate school has been the best time of my life. I have many people to acknowledge and thank. I must thank Lee Mundy for his guidance as an astronomer, scientist, and negotiator. I always enjoyed our meetings and discussions, and felt comfortable asking questions and expressing ideas. I also owe Lee thanks for supporting many trips to observatories and conferences around the country and world. I want to give a big thank you to Peter Teuben—this thesis is built on hundreds of hours of CARMA observations, and it is Peter who played a critical role in processing all that data. I also want to thank Peter for the countless times he helped me troubleshoot MIRIAD and other computing problems, for taking great photos, and for being a great person to bounce ideas off of. Thank you as well to Marc Pound, who was another vital person for figuring out subtle MIRIAD tasks and computer needs, and for keeping the atmosphere of the LMA friendly. I want to thank Eve Ostriker for her guidance in my research. Eve was an invaluable resource for connecting the observations in this thesis to theories of star formation. From the time I took her

Radiative Processes class, to the end of my grad school career, she was always willing and able to help me understand the processes in molecular clouds.

Grad school started off with coursework, and I want to thank the great professors I had: Eve Ostriker, Andy Harris, Derek Richardson, Alberto Bolatto, Sylvain Veilleux, Patrick Harrington, Cole Miller, and Stacy McGaugh. I learned a lot in those classes, and I still refer to Eve and Alberto's ISM notes for my research.

I had a great group of classmates to share those classes and the rest of grad school with. Thanks to Che-Yu for being my star formation theorist companion, to Alex for his soccer coaching, and to DJ for fun nights in DC. Thanks to Rodrigo for being a great officemate, and for hosting us in Chile around his wonderful wedding. Thanks to Katie for the best (eventually not so-)Secret Santa gift ever. The academically-older grad students made my early years at Maryland memorable; thanks to Bevin, Lisa, Stacey, and Hao for making those early years more fun, and for giving me guidance. And a big thank you to the postdocs and academically-younger grad students that made my last years more enjoyable; thanks to David, Amy, Laura, and Maxime.

The Maryland Astronomy Department has an awesome professional staff. Adrienne Newman and Susan Lehr made my numerous travel expense forms relatively pain-free and were always willing to help with a smile. Erik McKenzie and Mary Ann Phillips were always there to take care of any administrative need, big or small. I also want to thank Stuart Vogel, who has been a great department chair for my entire tenure.

I greatly enjoyed my brief teaching assistant tenure under Grace Deming during my first year. Thanks to Grace for skillfully guiding my first teaching experience and for all the tasty muffins on test days. Thank you to Tracy Huard for guiding my research with Lee during my second year as I was first being introduced to the world of star formation. Thank you to Mark Wolfire, who has been attentive to any computer or ISM questions I have had.

As this thesis is built on CARMA data, I must thank the great CARMA and OVRO staff. I spent thirteen weeks at CARMA as an observer, and enjoyed every one of those trips. Thank you to: Nikolaus Volgenau, Cecil Patrick, Mary Daniel, Terry Sepsey, Erik Leitch, James Lamb, Dave Woody, and any other person I may have interacted with during my time there. I also need to thank Owens Valley and Cedar Flat, themselves, for providing immense beauty and clean air.

I had a skilled team supporting my thesis research, and I thank all members of the CLASSy collaboration that helped me with data analysis, science discussions, and paper writing. A special thank you goes out to Katherine and Manuel for sharing the expansive CLASSy workload.

I developed many great friendships at Maryland. I am grateful to Kári and Thora for letting me crash at their apartment so much during our first year, and then for letting me move in with them shortly after. And for adventurously touring me around Iceland (twice!), and for all the years of friendship that we shared across Maryland and Virginia. Thanks to Mary and James for making my first two years more homey, for helping me get my driver's license, and then for the fun visits in California.

My astronomy studies began back in college. I want to thank Susan Benecchi who led the rooftop observing seminar that got me thinking astronomy was something worth pursuing in more serious depth. I also want to thank Jim Elliot for giving me my first astronomy research experience, during which I spent many nights at Wallace Observatory and learned my first astronomy-related computer skills. After deciding to major in the Planetary Science track of Course 12, I was lucky to do research related to asteroids under Rick Binzel. Rick was a great advisor and helped propel me to two summer research experiences that cemented my desire to attend graduate school for astronomy. I want to thank all the people associated with the Kitt Peak and IfA-Hawaii REUs, particularly my mentors, Nalin and Bobby.

I am thankful that my great friendships from college have stayed strong through graduate school. I am grateful to Boris for all of his support at MIT, for introducing me to what I now consider quality music, for taking a competitive liking to handball, and for being great at keeping in touch across long distances. I'd like to thank Sam for being a great little brother—we complement each other well.

Thanks to Barnet for being the cool uncle that every person would love to have, and (along with Barbara) for hosting fun weekends for me and my friends.

I want to thank my great mom, dad, and brother for all their support during grad school and the years leading up to this thesis. Thanks for the countless boxes of goodies, for keeping track of my busy travel schedule, for the visits to DC, for the meetups out west around observing runs, and for the immense amounts of unconditional love.

And most of all, thank you, Megan. You are the best thing that has ever happened to me and I am incredibly excited for all of the experiences we will share throughout our lives.

Contents

List of Tables	xiii
List of Figures	xiv
1 Introduction	1
1.1 Historical View of Molecular Cloud Observations	1
1.2 Properties of Molecular Clouds	4
1.3 Molecular Cloud Surveys	6
1.3.1 CARMA Large Area Star Formation Survey	8
1.4 The Perseus and Serpens Molecular Clouds	9
1.5 N_2H^+ , HCO^+ , and HCN As Dense Gas Tracers	12
1.5.1 Chemical Pathways	13
1.5.2 Molecular Excitation	15
1.5.3 Applications to this Thesis	21
1.6 Technical Overview of CARMA	23
1.7 Thesis Outline	25
2 Project Overview with Analysis of Barnard 1	26
2.1 Introduction	27
2.2 Observations	29
2.2.1 CARMA Interferometric Observations	29
2.2.2 CARMA Single-Dish Observations	34
2.2.3 Joint Deconvolution of Interferometric and Single-Dish Cubes	35
2.2.4 Continuum Mapping	36
2.3 Continuum Results	37
2.4 Morphology of Dense Molecular Gas	40
2.4.1 Main Core Zone	42
2.4.2 Ridge Zone	45
2.4.3 SW Clumps Zone	48
2.5 Kinematics of Dense Molecular Gas	49
2.6 Dendrogram Analysis of N_2H^+	58

2.6.1	The Non-binary Dendrogram	59
2.6.2	Dendrogram Tree Statistics	62
2.6.3	Dendrogram Spatial Properties	66
2.6.4	Dendrogram Kinematic Properties	69
2.7	Size-Linewidth and Cloud Structure	75
2.7.1	Total Linewidth of Dendrogram Structures	76
2.7.2	Resolved Linewidths of Dendrogram Structures	78
2.7.3	Inferring Cloud Depth from Resolved Size-Linewidth Relations	80
2.8	Summary of Barnard 1 Results	88
3	The Young L1451 Region	91
3.1	Introduction	92
3.2	Observations	95
3.3	Continuum Results	98
3.4	Morphology of Dense Molecular Gas	99
3.4.1	Integrated Intensity Emission	99
3.4.2	Channel Emission	101
3.5	Kinematics of Dense Molecular Gas	111
3.6	Dendrogram Analysis of Molecular Emission	114
3.6.1	The Non-binary Dendrograms	114
3.6.2	Dendrogram Spatial and Kinematics Properties	117
3.6.3	Tree Statistics	121
3.7	Dust in L1451	132
3.7.1	L1451 Column Density and Temperature	132
3.7.2	Dendrogram Analysis of Dust	135
3.8	Understanding Star Formation in L1451	138
3.8.1	Connecting molecular structures to physical cloud structures .	138
3.8.2	Energy balance of structures	141
3.8.3	Closer Look at L1451-mm and L1451-west	149
3.8.4	Depth of L1451 Structures: A Non-Filamentary Region	154
3.9	Summary of L1451 Results	160
4	Comparing All CLASSy Regions	165
4.1	Introduction	166
4.2	Integrated Intensity Maps Across Regions	169
4.3	YSO Statistics Across Regions	172
4.4	N ₂ H ⁺ Dendrograms Across Regions	173
4.5	Statistical Comparison of Hierarchies	176
4.6	Linking Stellar Content to Hierarchies	181
4.7	Summary	192

5	Key Findings, Summary, and Future Work	196
5.1	Key Findings of Thesis	196
5.2	Summary of Thesis	199
5.2.1	CLASSy Observations	199
5.2.2	The Barnard 1 and L1451 Regions	200
5.2.3	A Closer Look At L1451	205
5.2.4	Comparing All CLASSy Regions	206
5.3	Looking Forward	207
A	Differences Between Clump-finding and Dendrograms	209
B	A New Non-binary Dendrogram Procedure	214
C	How to Compare Non-Binary Dendrograms of Different Regions	219
C.1	Noise Dependence of Dendrogram Structure and Statistics	220
C.2	Comparing Regions at Different Distances	227
C.3	Summary	229
D	<i>Herschel</i>-identified YSOs	230
	Bibliography	230

List of Tables

2.1	Observation Summary	30
2.2	Correlator Setup Summary	33
2.3	Observed Properties of Continuum Detections	38
2.4	Outflow Identification	46
2.5	N ₂ H ⁺ Dendrogram Leaf and Branch Properties	73
2.5	N ₂ H ⁺ Dendrogram Leaf and Branch Properties	74
3.1	Observation Summary	96
3.2	Correlator Setup Summary	97
3.3	Observed Properties of Continuum Detections	99
3.4	HCO ⁺ Dendrogram Leaf and Branch Properties	125
3.4	HCO ⁺ Dendrogram Leaf and Branch Properties	126
3.4	HCO ⁺ Dendrogram Leaf and Branch Properties	127
3.5	HCN Dendrogram Leaf and Branch Properties	128
3.6	N ₂ H ⁺ Dendrogram Leaf and Branch Properties	129
3.7	Tree Statistics	130
3.8	Dust Structure Properties	137
3.9	Virial Parameters	145
4.1	YSO Statistics in CLASSy Regions	174
4.2	Tree Statistics	179
4.3	YSOs Found Within Leaves	183
4.4	Leaves With YSOs	183
D.1	Non-c2d YSOs Identified with <i>Herschel</i>	231

List of Figures

1.1	Optical view of a molecular cloud	2
1.2	Nearby molecular clouds on galactic coordinates	3
1.3	Overview of CLASSy regions in Perseus	9
1.4	Overview of CLASSy regions in Serpens	10
1.5	Excitation Temperature vs. Critical Density	17
1.6	Line Temperature as Function of Column Density and Density	19
1.7	View of CARMA antennas	24
2.1	Barnard 1 mosaic	31
2.2	Continuum detections in Barnard 1	37
2.3	Integrated intensity maps of Barnard 1	41
2.4	Example spectra for all molecules from Barnard 1	42
2.5	Integrated intensity maps from the Barnard 1 main core zone	44
2.6	HCO ⁺ and HCN outflows in Barnard 1	47
2.7	Integrated intensity maps from the Barnard 1 ridge zone	49
2.8	Narrow filament discovery in Barnard 1	50
2.9	Integrated intensity maps from the Barnard 1 SW clumps zone	51
2.10	Maps of centroid velocity and velocity dispersion in Barnard 1	56
2.11	Centroid velocities from Barnard 1 main core and ridge zones	57
2.12	Small-scale kinematics within Barnard 1	57
2.13	Non-binary dendrogram for Barnard 1	61
2.14	Barnard 1 dendrogram leaves overplotted on integrated intensity	62
2.15	Dendrogram structures across channels	63
2.16	Fitting for dendrogram spatial properties	68
2.17	Fitting for dendrogram kinematic properties	70
2.18	Histograms of Barnard 1 dendrogram structure properties	75
2.19	Size-linewidth relations using total linewidth	78
2.20	Size-linewidth relations using discrete linewidths	79
2.21	Cartoon connecting size-linewidth with cloud depth	85
2.22	Size-linewidth relations from numerical simulations	87
3.1	L1451 mosaic	97

3.2	L1451 continuum detection	99
3.3	Integrated intensity maps of L1451	101
3.4	HCO ⁺ channel maps of L1451	107
3.5	HCN channel maps of L1451	108
3.6	N ₂ H ⁺ channel maps of L1451	109
3.7	Spectra from Feature A within L1451	110
3.8	Spectra from Feature B within L1451	110
3.9	Maps of centroid velocity and velocity dispersion in L1451	114
3.10	HCO ⁺ non-binary dendrogram from L1451	118
3.11	HCN non-binary dendrogram from L1451	119
3.12	N ₂ H ⁺ non-binary dendrogram from L1451	119
3.13	Histograms of L1451 HCO ⁺ dendrogram properties	131
3.14	Histograms of L1451 HCN dendrogram properties	131
3.15	Histograms of L1451 N ₂ H ⁺ dendrogram properties	132
3.16	Column density map of L1451	133
3.17	Dust temperature map of L1451	134
3.18	Extinction map of L1451 with dust dendrogram structures	136
3.19	L1451 dendrogram branches on column density	139
3.20	L1451 dendrogram leaves on column density	139
3.21	CDF of column density with and without molecular emission	141
3.22	L1451-mm vs. L1451-west	150
3.23	Size-linewidth relations for all L1451 tracers	155
4.1	Cartoon hierarchy of cloud	167
4.2	All N ₂ H ⁺ integrated intensity maps	169
4.3	Column Density maps for B1 and L1451	171
4.4	Column Density versus Integrated Intensity	171
4.5	Serpens Main non-binary dendrogram	176
4.6	Serpens South non-binary dendrogram	177
4.7	NGC 1333 non-binary dendrogram	177
4.8	Barnard 1 non-binary dendrogram	178
4.9	L1451 non-binary dendrogram	178
4.10	Serpens Main dendrogram structures and YSOs	188
4.11	Serpens South dendrogram structures and YSOs	189
4.12	NGC 1333 dendrogram structures and YSOs	190
4.13	Barnard 1 dendrogram structures and YSOs	191
4.14	Separation of YSOs and dendrogram leaves	192
4.15	Dendrogram level of YSOs	193
A.1	Comparing Cloudprops and dendrogram algorithms	210
A.2	One-dimensional dendrogram example	212

B.1	Cartoon explaining new non-binary dendrogram algorithm	216
C.1	Dendrogram structure maps for different noise and parameters	223
C.2	Dendrograms for different noise and parameters	224
C.3	Dendrogram structure maps for different noise and uniform parameters	225
C.4	Dendrograms for different noise and uniform parameters	226

Chapter 1

Introduction

Galaxies are gravitationally bound collections of stars, gas, dust, and dark matter. How stars form within galaxies is a fundamental question of astronomy and human understanding. The life and death cycle of stars drives the chemical evolution of the universe and the evolution of galaxies; the population statistics of stars affects how many habitable exoplanets exist, and our Sun provides energy to support life on our planet. This thesis is focused on the structure and kinematics of molecular clouds, which are the birthplace of stars within galaxies. The goal is to achieve a more complete understanding of how the gas and dust of galaxies turns into stars.

1.1 Historical View of Molecular Cloud Observations

Modern-day astronomers are interested in molecular clouds because we know they are collections of molecular gas and dust where stars form; there is a strong correlation between star formation and molecular gas, as opposed to atomic gas (e.g., Bigiel et al. 2008; Leroy et al. 2008). However, less than a century ago, molecular

clouds were only known as “holes in the heavens” due to the way they obscured optical starlight and produced dark patches in an otherwise bright night sky. Barnard (1913) was the first to propose that these dark patches were “not vacancies, but rather some kind of obscuring body lying in the Milky Way, or between us and it, which cuts out the light from the stars.” Figure 1.1 shows an optical image of a molecular cloud, where dark patches are easily visible. The first detection of interstellar molecules from these patches came around 1940 from optical stellar absorption features (e.g., Swings & Rosenfeld 1937; McKellar 1940; Adams 1941). The first radio telescope detection of molecular emission came in 1963 with the centimeter-wavelength observation of the OH radical (Weinreb et al. 1963). Detections later pushed into the millimeter wavelength regime with improved instrumentation, and the CO line was first detected by Wilson et al. (1970). From the late-1970s onward, mapping molecules in Milky Way and extragalactic molecular clouds from (sub)millimeter to centimeter wavelengths became common (e.g., Morris & Rickard 1982; Genzel & Stutzki 1989).



Figure 1.1: The Perseus Molecular Cloud, showing examples of optically dark patches, bright O and B stars, and background stars that have been reddened by dust. Photo Credit: David Pearson.

There have been numerous observations of molecular clouds over the past decades that have greatly improved our understanding of star formation (see reviews by Shu et al. 1987; Kennicutt & Evans 2012). In addition to the observation of molecules, there have been campaigns to observe the thermal continuum emission from cold cloud dust, as well as the infrared emission from young stellar objects (YSOs) forming in clouds (some of these campaigns are discussed in Section 1.3). The most well-studied Milky Way molecular clouds are nearby. Specifically, they are in Gould’s Belt, which Benjamin Gould described as a ring of bright stars (Gould 1874). The belt is a flattened, elliptical disk several hundred parsecs in radius that contains numerous bright O- and B-type stars and stellar nurseries (Perrot & Grenier 2003). Figure 1.2 shows the belt in galactic coordinates, along with the location of several molecular clouds. The proximity of the belt’s molecular clouds to the Sun makes them popular targets for observations that desire high spatial resolution. For example, Taurus (Torres et al. 2012), Perseus (Hirota et al. 2011), Serpens (Dzib et al. 2010), and Orion (Kim et al. 2008) are ~ 133 , 235, 415, and 418 pc from the Sun, respectively. At these distances, $5''$ angular resolution can resolve down to spatial scales ~ 700 – 2500 AU, meaning it is possible to study individual protostellar cores and cloud structures that will form stars.

1.2 Properties of Molecular Clouds

Most of the Milky Way interstellar medium (ISM) is atomic due to the dissociation of molecules by far ultraviolet (FUV) photons (Krumholz et al. 2008). To form a molecular cloud, gas in the ISM must be accumulated to high enough column densities (i.e., from gravity and turbulence) to shield the gas from the FUV photons—a minimum visual extinction (A_V) of ~ 0.5 – 1.0 is required (van Dishoeck & Blake

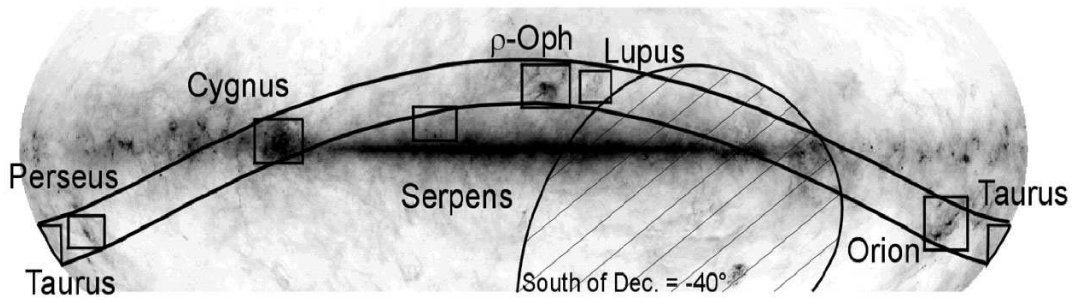


Figure 1.2: An IRAS 100 μm map of the galactic plane showing locations of nearby molecular clouds, including the Perseus and Serpens clouds studied in this thesis. The solid lines mark the location of the Gould Belt across galactic coordinates. Image from the JCMT Gould Belt Legacy Survey team: <http://www.eaobservatory.org/jcmt/science/legacy-survey/gbs/>.

1998). Once this shielding occurs, HI can form H_2 and C^+ can turn into CO, leading to clouds that are readily observable in molecular CO emission (Dobbs et al. 2014). Roman-Duval et al. (2010) did a survey of the ^{12}CO and ^{13}CO in Milky Way clouds, and found cloud masses between 10^2 – $10^7 M_\odot$, a median H_2 number density of 230 cm^{-3} , a median surface density of $144 M_\odot \text{ pc}^{-2}$, and a median global velocity dispersion $\sim 1.3 \text{ km s}^{-1}$. For a molecule rich galaxy, like the Milky Way, most of the molecular mass is found in giant molecular clouds (GMCs) that have masses above $10^4 M_\odot$ (Williams et al. 2000). The nearby clouds of the Gould Belt are smaller and less massive than those GMCs, but their proximity to the Sun makes them superior locations to study the small-scale details of star formation.

The environment of a molecular cloud is magnetized and turbulent. The ratio of magnetic energy to gravitational potential energy in clouds is not large enough to prevent gravitational collapse; Crutcher (2012) showed that molecular clouds and cores, where $N_H \geq 10^{21} \text{ cm}^{-2}$, are magnetically supercritical (cloud mass greater than magnetic critical mass). Turbulence has more clear influence on molecular cloud structure. Observations of molecular linewidths show that all molecular clouds are turbulent, with typical non-thermal velocities ~ 1 – 4 km s^{-1} on scales ~ 1 – 10 pc

(Solomon et al. 1987; Heyer & Brunt 2004). These velocities correspond to supersonic motions with Mach numbers of 3–20 in the cold, molecular component of the ISM, where typical temperatures range from 10–20 K (Ferrière 2001) and the corresponding isothermal sound speed is $\sim 0.2\text{--}0.3 \text{ km s}^{-1}$. Supersonic flows are capable of causing strong density perturbations in clouds, since the gas is highly compressible (Dickman 1985; Scalo 1987; Mac Low & Klessen 2004). Numerical simulations show that these density perturbations can take the shape of observed cloud structure, and then fragment and collapse under self-gravity to form dense cores (e.g., Gong & Ostriker 2011; Federrath & Klessen 2012; Chen & Ostriker 2014).

Turbulence and self-gravity work together to create a large dynamic range of spatial and density cloud structure that stretches from the lowest-extinction edge of a cloud to the highest-extinction clumps within the cloud where stars will actively form. Observations of ^{12}CO and ^{13}CO reveal that the large-scale cloud is filled with relatively low-density ($n \leq 10^{2-3} \text{ cm}^{-3}$), supersonically turbulent gas at all spatial scales, and can extend for several tens of parsecs (e.g., Kutner et al. 1977; Lada & Reid 1978; Ridge et al. 2006). Overdensities formed within the low-density gas create zones of active star formation at parsec scales with $n \geq 10^{3-5} \text{ cm}^{-3}$, such as the NGC 1333 region within the Perseus cloud complex that was mapped in N_2H^+ by Walsh et al. (2007). These parsec-scale overdense regions evolve and fragment to even higher densities ($n \geq 10^{5-7} \text{ cm}^{-3}$) as they form pre-stellar and proto-stellar cores on scales of $\sim 0.01\text{--}0.1 \text{ pc}$ (see di Francesco et al. 2007; Ward-Thompson et al. 2007, and references therein).

The progression of molecular cloud structure across spatial scales and densities can be represented as a hierarchy, where the smaller, denser regions are substructures of the larger, less-dense regions. Houlahan & Scalo (1992) developed a structure tree representation of molecular clouds to quantify this nested, hierarchical nature,

and that method led to the usage of dendrogram algorithms in the past few years to analyze hierarchical cloud structure (Rosolowsky et al. 2008b; Goodman et al. 2009). The progression to higher densities also comes with a decreasing volume filling factor—most of the mass in a cloud is at low densities, so material above 10^5 cm^{-3} , which is at the hierarchical peak of the cloud density structure, represents a small percentage of the cloud’s total mass and volume (Mac Low & Klessen 2004).

The formation of overdensities within clouds and their subsequent evolution to even higher densities, and ultimately to stars, is the focus of active research. It is known that supersonic turbulent flows, magnetic fields, and self-gravity are all involved, but the interplay between them across a broad range of size scales, and across different environments, is not fully understood theoretically or observationally.

1.3 Molecular Cloud Surveys

There have been numerous surveys of nearby molecular clouds in the past decades. The young stellar content of Gould’s Belt clouds was assessed by *Spitzer* Legacy Surveys including the c2d survey (e.g., Evans et al. 2009) and the Gould’s Belt survey (e.g., Gutermuth et al. 2008). Complementary observations of gas and dust are needed to link those protostars to their environment to understand how they formed. It is also important to observe regions with pre-stellar cores and condensations to map the state of clouds before star formation has begun.

A fundamental limitation of existing gas and dust observations is the lack of high-resolution data tracking the structure and kinematics across complete, parsec-scale star forming regions. To resolve 10,000-AU envelopes of dense gas and dust that surround protostars or protostellar multiples, we require at least 3000-AU spatial resolution to have a few beams across those envelopes. If we want to then understand

the environment from which those cores are forming, we need to be sensitive to scales of one to a few parsecs to track the relationship between the gas and stars as clusters of stars form.

The thermal continuum emission from molecular cloud dust has been most recently observed throughout large areas of many clouds from 70–500 μm with the *Herschel* Gould Belt Survey (André et al. 2010) and at 450 and 850 μm with the JCMT Gould Belt Survey (Sadavoy et al. 2013). Those observations are limited from achieving the goals stated above because the ground-based observations are not sensitive to structure more than ~ 0.17 pc at the distance of Perseus due to spatial filtering (Sadavoy et al. 2013), while the *Herschel* observations are limited to ~ 8500 AU spatial resolution at the distance to Perseus for column density and temperature maps.

The gas structure and kinematics of clouds, commonly traced by CO isotopologues, has been observed by several campaigns, including the FCRAO observations from the COMPLETE team of Perseus and Ophiucus (Ridge et al. 2006), JCMT observations of Perseus (Hatchell et al. 2005), and JCMT Gould Belt Legacy Survey observations (e.g., Buckle et al. 2012). The main observational limitation of these observations is that the excitation properties of CO make it a better tracer of the lower-density regions of the clouds than of the higher-density regions where stars are actively forming, and that the ^{12}C and ^{13}C species are often optically thick in cold regions preventing a view of the full column of material. Chemically, CO tends to deplete due to freeze-out onto grains in regions with density above a few $\times 10^4 \text{ cm}^{-3}$ (Bacmann et al. 2002) and gas temperature less than 20 K (Collings et al. 2003), which is another reason it is not a good tracer of the coldest, densest cores where stars will form. Observations of molecular species and transitions that are excited at these higher physical densities and column densities are needed to peer through

the lower density gas, and to highlight the structure and kinematics of the material directly feeding into the star formation.

In summary, existing surveys have shown the complex dust and gas structure of molecular clouds, but they have not adequately captured the wide range of spatial scales of the high physical density regime where stars form. To do this, new surveys with higher resolution and larger spatial coverage of the high-density regime are needed. These new surveys can improve our understanding of the internal physical state of molecular clouds, with long term goals of understanding what drives and controls the rate of star formation, why the stellar initial mass function has its shape, and whether that shape depends on environment. In the near term, such surveys that follow the structure and kinematics of cloud overdensities over a wide range of spatial scales can provide a clearer picture of how material fragments along the pathway to star formation.

1.3.1 CARMA Large Area Star Formation Survey

We started filling the need for new surveys with a Key Project on the Combined Array for Research in Millimeter-wave Astronomy (CARMA). We carried out a large area, high angular resolution survey of dense gas in nearby molecular clouds. The CARMA Large Area Star Formation Survey (CLASSy) spent 700 hours imaging five large areas of star formation in the N_2H^+ , HCO^+ , and HCN ($J = 1 \rightarrow 0$) molecular lines. We chose these molecules because they are all tracers of dense gas and sample a range of chemical/physical environments within a cloud (see Section 1.5). They are all also observable in a single CARMA correlator setting.

CLASSy observed the Perseus Molecular Cloud Complex towards NGC 1333, Barnard 1, and L1451 (see Figure 1.3), and the Serpens Molecular Cloud towards Serpens Main and Serpens South (see Figure 1.4), to capture a range of star-forming

environments and evolutionary stages. We mapped each region with ~ 1600 and ~ 3000 AU spatial resolution at the distances of Perseus and Serpens (235 and 415 pc), respectively, to meet the requirement of resolving individual star-forming cores ($\sim 10,000$ AU). We also covered large enough areas to capture the environment in which the cores formed—up to linear scales of 1 to 2 pc across each region. These survey data were combined with many ancillary datasets—*Spitzer* catalogs of young stellar objects (YSOs), *Herschel* images of heating sources, *Herschel* and JCMT maps of dust and continuum sources, to name a few—to provide a total picture of star-forming objects and the structure and kinematics of the dense gas which is fueling their formation.

We review each CLASSy cloud in Section 1.4, discuss details of each molecule in Section 1.5, and present the technical details of observations, calibration, and mapping as part of Chapter 2.

1.4 The Perseus and Serpens Molecular Clouds

The Perseus and Serpens Molecular Clouds were chosen as targets for CLASSy because they are nearby, and because of the large amounts of existing ancillary data from other telescopes to combine with new CARMA observations of dense gas. Here we review basic properties of each cloud.

Perseus is located 235 pc from the Sun (Hirota et al. 2011), and is the closest cloud that is forming large numbers of low to intermediate-mass stars (Bally et al. 2008). The total mass of the cloud is estimated to be $\sim 4.8 \times 10^3 M_{\odot}$ based on extinction maps from 2MASS and *Spitzer* data (Enoch et al. 2006; Ridge et al. 2006; Evans et al. 2009). It appears elongated across $\sim 7^{\circ}$ (29 pc) of the sky in roughly the east-west direction, with an estimated total area of ~ 70 pc² based on the $A_V=3$ mag

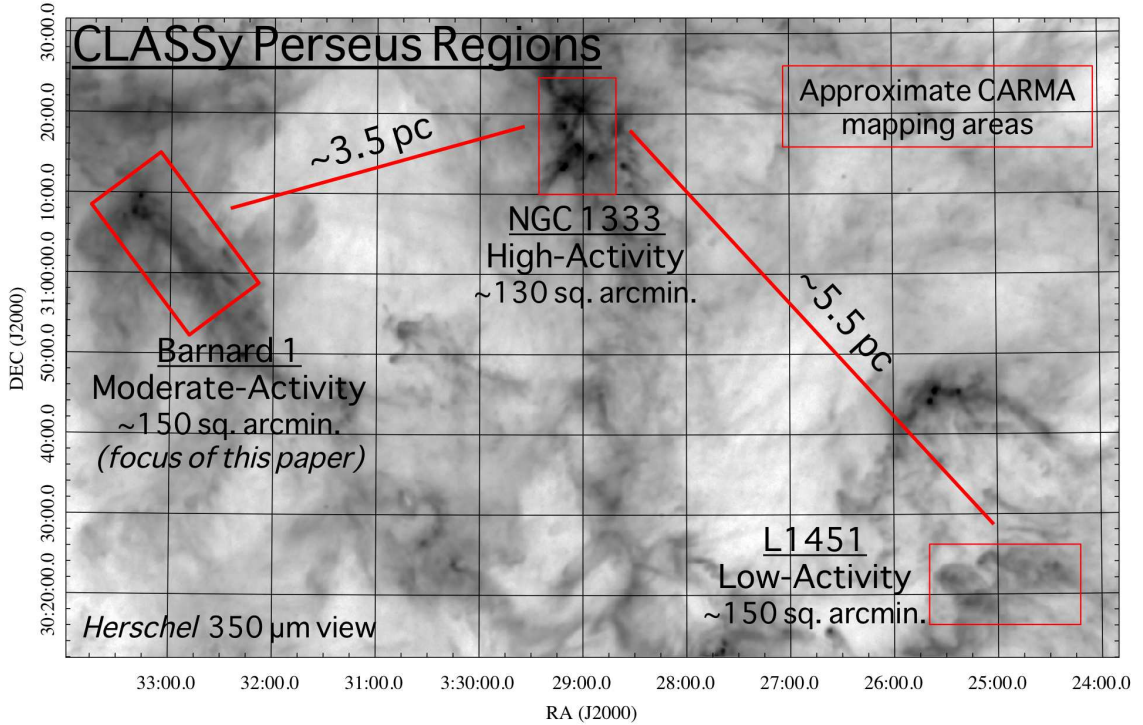


Figure 1.3: Overview of the CLASSy regions in the western portion of the Perseus Molecular Cloud, as seen by *Herschel* 350 μm (André et al. 2010) where the darker shades of grey represent stronger dust emission relative to the lighter shades of grey. The approximate areas mapped by CARMA are represented with rectangles; the actual areas are not single rectangular fields for Barnard 1 and L1451. Projected distances between regions are given, assuming a distance of 235 pc.

contour from 2MASS extinction (Ridge et al. 2006). The star formation within the cloud is not distributed uniformly across this entire area. The main sites of clustered star formation can be separated into an eastern and western half. The most prominent region in the eastern half is the IC 348 star-forming cluster (not pictured in Figure 1.3), which contains nearly half of the Perseus YSOs identified by the *Spitzer* c2d project (Jørgensen et al. 2008). The cluster is considered to be the oldest region of ongoing star formation in Perseus at 2–4 Myr old (Bally et al. 2008).

The western half of Perseus contains younger, more active clusters of star formation. The most prominent region in this half is the NGC 1333 star-forming

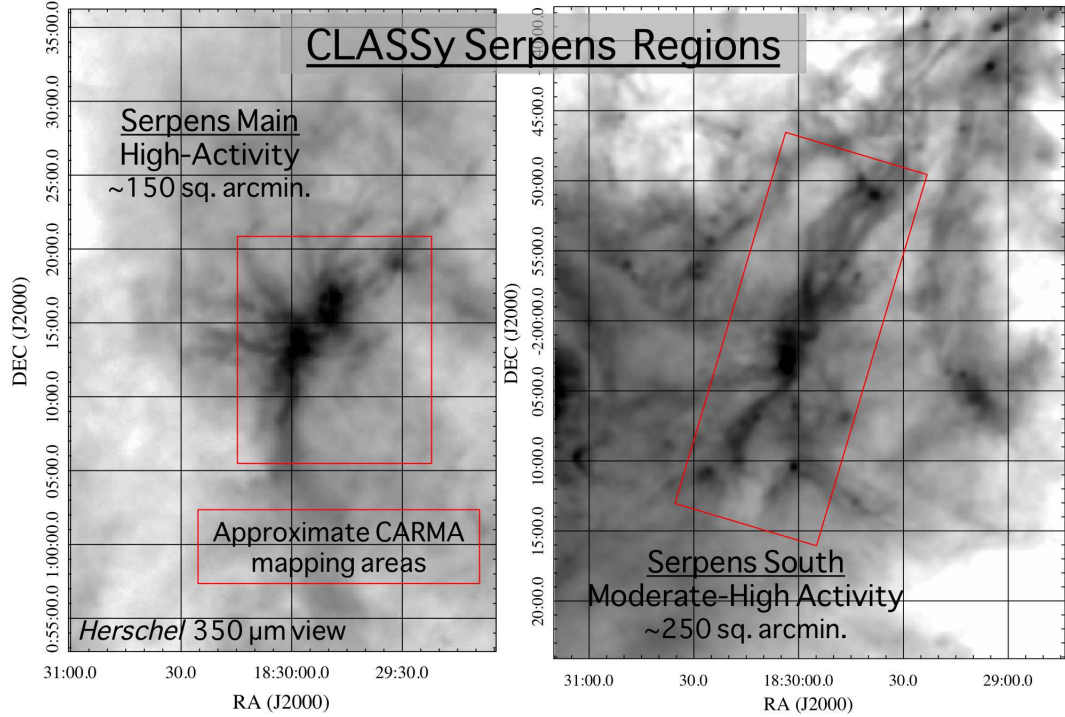


Figure 1.4: Overview of CLASSy regions in the Serpens Molecular Cloud, as seen by *Herschel* 350 μm (André et al. 2010). The approximate areas mapped by CARMA are represented with rectangles; the actual areas are not single rectangular fields for either region. The Serpens Main data is presented in Lee et al. (2014), while an analysis of the Serpens South N_2H^+ filaments is in Fernández-López et al. (2014).

cluster, which has about 115 associated YSOs (Jørgensen et al. 2008) and dozens of protostellar outflows and shocks (Arce et al. 2010). NGC 1333 is estimated to be younger than IC 348, at an age of about 1–2 Myr (Wilking et al. 2004; Bally et al. 2008). There are several smaller regions of star formation within a few parsecs of NGC 1333, including Barnard 1, L1448, L1455, and L1451, which are thought to be of a similar age as, or slightly younger than, NGC 1333, based on their star formation statistics. CLASSy focused on three evolutionarily distinct regions of star formation in the western half of Perseus that are in close proximity: NGC 1333, Barnard 1, and L1451. Figure 1.3 shows a view of the cool dust in this region, and we discuss specifics of each region in later chapters. Chapters 2 and 3 focus on Barnard 1 and

L1451, respectively, while Chapter 4 compares the dense gas structure and young stellar content of all three regions.

The Serpens Molecular Cloud is located 415 pc from the Sun (Dzib et al. 2010). This measurement was done using the very long baseline array (VLBA), and is from a source in the Serpens Main core. Therefore, the distance measurement might not apply to Serpens South, which is located about 24 pc to the South in the Aquila Rift system. However, since no VLBA measurements have been made for sources in Serpens South, and since both regions have gas with similar radial velocities (Gutermuth et al. 2008), we assume both CLASSy Serpens regions are at 415 pc.

The total mass of the cloud that contains Serpens Main is estimated to be $\sim 2016 M_{\odot}$, with a total area of $\sim 18 \text{ pc}^2$ (Evans et al. 2009). It has two primary clustered regions with young star formation—one being the aforementioned, well-studied Serpens Main, and the other being a recently discovered region known as the Serpens G3YG6 cluster (Djupvik et al. 2006). Serpens Main is the region with highest extinction and largest concentration of YSOs in the cloud (Harvey et al. 2007), and most of its mass is concentrated into two central clusters (Eiroa et al. 2008). It is estimated to have an age of $\sim 2 \text{ Myr}$ (Erickson et al. 2015). Serpens South was discovered as part of the *Spitzer* Gould Belt Legacy Survey in the Serpens-Aquila Rift (Gutermuth et al. 2008). The region has a bright “hub” of dense gas with a high fraction of younger YSOs, suggesting a recent burst of star formation (Gutermuth et al. 2008). Several filaments radiate from the hub, which have made this region a popular target for studying the role of filaments in star formation (Kirk et al. 2013; Fernández-López et al. 2014; Nakamura et al. 2014). We note that we will refer to Serpens Main and Serpens South as both being in the Serpens Molecular Cloud, even though major surveys, such as *Spitzer* c2d, did not include Serpens South in their area coverage.

The CLASSy work on Serpens Main and Serpens South has been led by Katherine Lee (Lee et al. 2014) and Manuel Fernández López (Fernández-López et al. 2014), respectively. These regions are not the focus of the work in this thesis, but are occasionally touched on in comparison to Perseus regions in Chapters 2 and 3, and are used in Chapter 4 as part of a cross-comparison between all CLASSy regions.

1.5 N_2H^+ , HCO^+ , and HCN As Dense Gas Tracers

CLASSy utilizes the N_2H^+ , HCO^+ , and HCN ($J = 1 \rightarrow 0$) transitions as probes of gas distribution and kinematics. In this section, we review important aspects of their molecular excitation and emission, which are needed to interpret CLASSy data. In general, the strength of emission seen from a molecule depends on gas density, molecular column density, gas temperature, and kinematics, whose values depend on the physical properties and chemistry of the cloud.

1.5.1 Chemical Pathways

Starting with chemistry, a molecule must be present in the gas phase if there is any chance to observe it. Therefore, it is useful to look at the formation and destruction paths for our three molecules. The most common chemical pathway for the formation of N_2H^+ in dense clouds is: $\text{H}_3^+ + \text{N}_2 \rightarrow \text{N}_2\text{H}^+ + \text{H}_2$ (Prasad & Huntress 1980). The H_3^+ parent is an abundant ion in dense molecular gas, and is formed through a two-step process: cosmic ray (cr) ionization of H_2 to form H_2^+ , followed by $\text{H}_2^+ + \text{H}_2 \rightarrow \text{H}_3^+ + \text{H}$ (McCall et al. 1999). The N_2 parent is commonly created from $\text{N} + \text{NH} \rightarrow \text{N}_2 + \text{H}$. A second frequent path to form N_2H^+ occurs from cosmic ray ionization of He to form He^+ , followed by $\text{He}^+ + \text{N}_2 \rightarrow \text{N}_2^+ + \text{He}$, and then

$\text{N}_2^+ + \text{H}_2 \rightarrow \text{N}_2\text{H}^+ + \text{H}$ (Prasad & Huntress 1980).

The most common destruction mechanism of N_2H^+ involves reaction with CO, which is often the second most abundant molecule in molecular clouds (after H_2): $\text{N}_2\text{H}^+ + \text{CO} \rightarrow \text{HCO}^+ + \text{N}_2$ (Prasad & Huntress 1980). Since CO is strongly depleted from freeze-out onto grains when densities are above a few $\times 10^4 \text{ cm}^{-3}$ (Bacmann et al. 2002) and when temperatures get below $\sim 20 \text{ K}$ (Collings et al. 2003), the primary destruction pathway is very depletion-sensitive. In chemical models and observations, N_2H^+ is typically one of the last observable species to be depleted (Bergin & Langer 1997; Caselli et al. 2002). Hence, N_2H^+ is preferentially a good tracer of cold material at relatively high density.

The primary production pathway for HCO^+ in dense parts of clouds is $\text{H}_3^+ + \text{CO} \rightarrow \text{HCO}^+ + \text{H}_2$ (Prasad & Huntress 1980). At lower column densities associated with surfaces of photodissociation regions (PDRs), HCO^+ is produced from $\text{CO}^+ + \text{H}_2 \rightarrow \text{HCO}^+ + \text{H}$ (Young Owl et al. 2000). This shows that HCO^+ is preferentially found in regions with higher CO abundance and higher ionization fraction. HCO^+ is destroyed by dissociative recombination as $\text{HCO}^+ + \text{e}^- \rightarrow \text{CO} + \text{H}$ (Prasad & Huntress 1980), and by charge exchange with neutral Mg and Fe in denser regions (Young Owl et al. 2000). Thus, HCO^+ can be abundant in both lower density gas with moderate ionization, and in dense, cool gas. The depletion of CO in the coldest gas will limit the abundance of HCO^+ in those regions.

HCN is produced in PDRs and densely clumped regions through reactions including $\text{H}_2\text{CN}^+ + \text{e}^- \rightarrow \text{HCN} + \text{H}$ and $\text{CH}_2 + \text{N} \rightarrow \text{HCN} + \text{H}$ (Young Owl et al. 2000; Boger & Sternberg 2005). The main method of HCN destruction in molecular clouds is cosmic-ray-induced photodissociation (crp) as $\text{HCN} + \text{crp} \rightarrow \text{CN} + \text{H}$ (Boger & Sternberg 2005), while removal through reaction with C^+ and HCO^+ is also common (Young Owl et al. 2000). PDR models of Young Owl et al. (2000)

predict that HCN has a similar abundance to HCO^+ , but observations of the Orion bar in the same paper show that HCN is often more confined to clumps while HCO^+ is more diffuse. Young Owl et al. (2000) argue that differences in the molecular excitation of these two molecules, combined with varying cloud density, is a likely cause for the observed spatial differences in the molecular emission.

The discussion above highlights the differences in chemical pathways and abundances of the three CLASSy molecules: N_2H^+ will be the most abundant of the three in high density, cold regions where CO has been depleted, while HCN and HCO^+ are predicted to have similar abundances throughout the cloud, but emit in distinct spatial locations likely due to differences in excitation (Young Owl et al. 2000). Even with their differences, all three molecules are considered “dense gas tracers” and are more similar to one another in their emission than any of them is to CO, which is excited at lower densities. To quantitatively understand at what cloud densities the $J = 1 \rightarrow 0$ rotational transition of each molecule emits most efficiently, we need to review some basic properties of molecular emission.

1.5.2 Molecular Excitation

The rotational energy levels of linear rotors like N_2H^+ , HCO^+ , and HCN are quantized according to their angular momentum, J . Their rotational levels are excited at a temperature on the order of a few to tens of Kelvins. Vibrational modes and electronic transitions of molecules have energy levels requiring upwards of a few 100–1000 K for excitation. Since cloud temperatures in the absence of strong internal heating sources are 10–30 K, there is only enough energy to excite the rotational modes.

To get a $J = 1 \rightarrow 0$ photon, a molecule must make a radiative transition from the $J=1$ to $J=0$ level. If we treat the molecule in the two-level approximation,

statistical equilibrium dictates that the total number of collisional and radiative transitions from the lower-to-upper state is equal to the number of transitions from an upper-to-lower state¹. Therefore, the excitation of the $J = 1 \rightarrow 0$ transition can be determined by the balance of the rate of downward de-excitations with the rate of upward excitations. The downward rate is controlled by collisional de-excitation (this has a dependence on the collisional cross-section and density of colliders), induced photo emission (this has a dependence on the radiation field), and spontaneous emission (this value is determined for each molecule and transition based on the dipole moment of the molecule and the frequency of the transition). The upward rate is controlled by collisional excitation from the $J=0$ to $J=1$ level (this has a dependence on the cloud kinetic temperature, collisional cross-section, and density of colliders), and by photo absorption from the $J=0$ to $J=1$ level (this has a dependence on the radiation field).

To summarize these terms in an equation, the rate balance for the two level system is given as

$$n_U[A_{UL} + \gamma_{UL}n_{H_2} + B_{UL}J_\nu] = n_L[B_{LU}J_\nu + \gamma_{LU}n_{H_2}]. \quad (1.1)$$

On the left hand side of the equation, n_U is the population number density of the upper level, A_{UL} is the Einstein coefficient for spontaneous emission from an upper-to-lower level transition, γ_{UL} is the collisional rate of de-excitation from the upper-to-lower level, n_{H_2} is the number density of H_2 , which is the primary collider species in molecular clouds, B_{UL} is the Einstein coefficient for induced emission from an upper-to-lower level transition, and J_ν is the angle-averaged intensity of the radiation field at frequency, ν_{UL} . On the right hand side of the equation, n_L is

¹A two-level system that only considers these levels is an approximation that is useful for describing the statistical equilibrium and excitation of a line, even though molecules have multiple rotational levels that can be excited in cloud environments.

the population number density of the lower level, B_{LU} is the Einstein coefficient for photo absorption from a lower-to-upper level transition, and γ_{LU} is the collisional rate of excitation from the lower-to-upper level.

To quantify the excitation properties of a molecular transition, Equation 1.1 can be solved for n_U/n_L and written in terms of n_{H_2} , A_{UL} , γ_{UL} , the kinetic (thermal) temperature of the gas, T_k , the radiation temperature of the background radiation field, T_r , and the excitation temperature, T_{ex} (see Spitzer 1998, Chapter 4 for discussion). The formal definition of the excitation temperature, T_{ex} , is

$$\frac{n_U}{n_L} = \frac{g_U}{g_L} e^{\frac{-h\nu}{kT_{ex}}} \quad (1.2)$$

where g_U and g_L are the statistical weights of the upper and lower states of the molecule, and the exponential represents the Boltzmann distribution between the given energy states. The excitation temperature is the temperature that we would expect to measure for a system of particles that has a given n_U/n_L ratio.

Since the full n-level equation for the ratio n_U/n_L in terms of these values is complex, for simplicity, the equation of the two-level system in the optically thin limit can be written as

$$e^{\frac{-h\nu}{kT_{ex}}} = \frac{\frac{e^{\frac{-h\nu}{kT_r}}}{1 - e^{\frac{-h\nu}{kT_r}}} + \frac{n_{H_2}\gamma_{UL}}{A_{UL}} e^{\frac{-h\nu}{kT_k}}}{\frac{1}{1 - e^{\frac{-h\nu}{kT_r}}} + \frac{n_{H_2}\gamma_{UL}}{A_{UL}}}, \quad (1.3)$$

with Figure 1.5 showing how T_{ex} behaves as a function of $n_{H_2}\gamma_{UL}/A_{UL}$.

From Figure 1.5 and Equation 1.3, it is clear that when collisional excitation and de-excitation dominates in high density gas, T_{ex} approaches T_k ; when radiative processes dominate in low density gas, T_{ex} instead approaches T_r , which is the cosmic background radiation field in the absence of a significant local radiation field. In the latter case, the cloud will be in complete thermodynamic equilibrium with the CMB radiation field meaning that no line will be observed. In Figure 1.5, T_{ex} begins to rise

significantly above the background radiation field near $n_{H_2}\gamma_{UL}/A_{UL} = 1$; the n_{H_2} that produces a value of unity for this expression is defined as the critical density of the given transition.

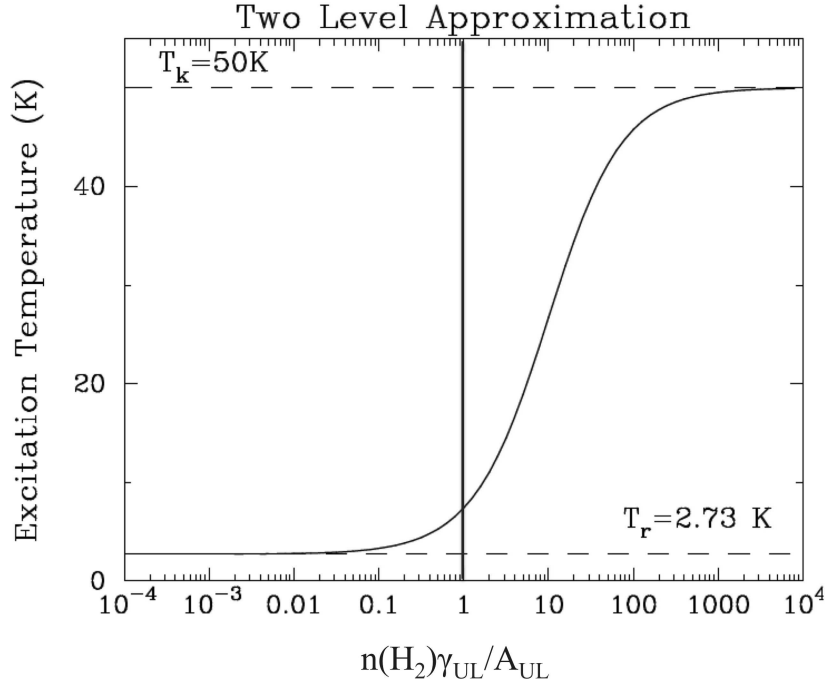


Figure 1.5: Excitation temperature as a function of critical density for the low opacity limit.

The curve in Figure 1.5 is an approximation at the optically thin limit with no radiative trapping, which is not always the case for transitions in dense clouds where column densities can be high and lines can be optically thick. The effective critical density would be lower when high column density and photon trapping is taken into account. Because of this, it is not formulaic to solve for the density at which a given molecule will start efficiently emitting, and radiative transfer code is needed to model molecular emission in a variety of non-thermalized conditions to find the density and column density that will produce emission for a given molecule in molecular cloud environments.

To demonstrate how molecular emission depends on volume density and column

density in a cloud environment, we used the Large Velocity Gradient (LVG; Sobolev 1957; Rybicki & Hummer 1978) radiative transfer code in MIRIAD (Multichannel Image Reconstruction, Image Analysis and Display; Sault et al. 1995). We made grids of line emission from a 10 K cloud as a function of H_2 density (cm^{-3}) and molecular column density (cm^{-2}) for HCN and HCO^+ ($J = 1 \rightarrow 0$), and present the results in Figure 1.6. The dark areas of the grids are where the excitation temperature of the transition is close to the cosmic background radiation temperature, meaning that only very weak, or undetectable, emission is produced.

For a fixed, low column density, if the H_2 densities are increased, then weak emission begins to appear as purple intensity in the bottom-right of the grids—these are the densities needed to collisionally excite the transitions above the cosmic background radiation field, and correspond to the critical density in Figure 1.5 (solid vertical line) where T_{ex} begins to rise. For a fixed, low density, if the molecular column densities are increased, then weak emission begins to appear as purple intensity in the top-left of the grids—these are the column densities needed to excite the transition through radiative trapping of photons. In the center to upper-right of the grid, it is clear that increasing density and column density (within these plotted limits) both lead to stronger line emission.

There are two important things to note from Figure 1.6. First, it is clear that an observed line temperature can be produced by a combination of different density and column density. This visualizes the cross-correlation of the two quantities at low optical depths ($T_B \sim T_{ex}\tau \propto T_{ex}N_x$ for $\tau \ll 1$), and shows that molecular emission in clouds is really a tracer of both density *and* column density, even though it is often said that a specific molecule “X” traces gas above some density (also see Evans 1999; Shirley 2015). Second, a given $J = 1 \rightarrow 0$ line temperature occurs at higher densities and column densities for HCN than HCO^+ . This shows that HCN traces

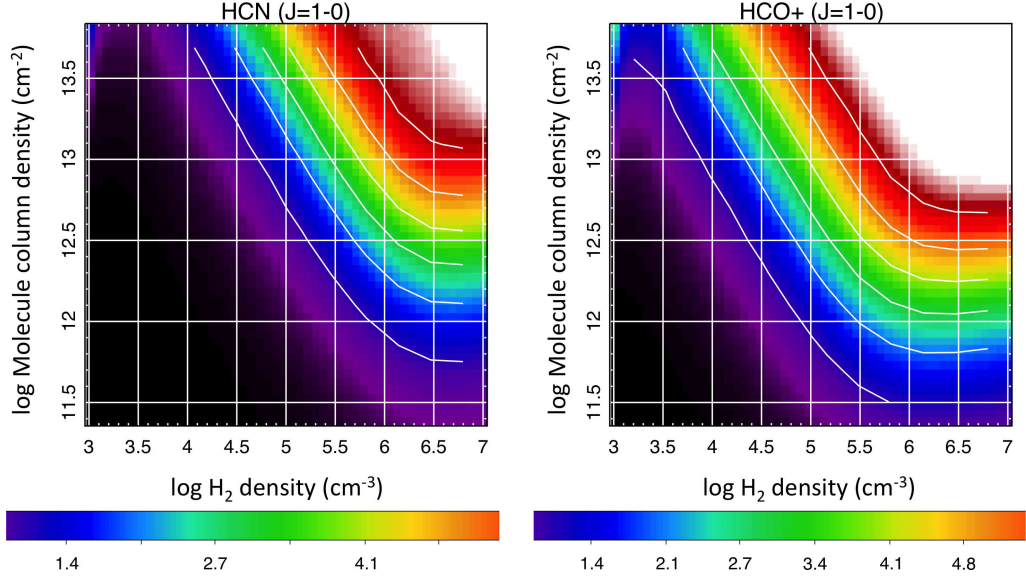


Figure 1.6: Grids of HCN and HCO⁺ brightness temperatures (K) as a function of H₂ density (cm⁻³) and molecular column density (cm⁻²), for a fixed kinetic temperature of 10 K. The grids were calculated using the LVG radiative transfer models in MIRIAD. The solid white contours represent 1–6 K emission line temperatures, in 1 K increments. The contour at the purple/dark blue transition corresponds to 1 K. The white region of the grid represents temperatures that exceed ~ 6.5 K.

higher dense gas column densities than HCO⁺ by about an order of magnitude, and is why HCN is often referred to as a “higher density gas tracer” than HCO⁺. We do not show a grid for N₂H⁺, but it traces slightly higher dense gas column densities than HCN.

We have focused on emission so far, but self-absorption is also commonly seen towards molecular clouds. Self-absorption is observed as a dip in the emission profile of a line, and will be present if emitted photons pass through a significant column of lower-density or lower temperature material where the species is abundant and overpopulated in the lower energy level of the transition before reaching the observer. This condition is often met in molecular clouds for HCO⁺ and HCN: a cloud naturally has lower-density, larger-scale regions surrounding higher-density, smaller-scale regions, and from the discussion in Section 1.5.1, we know that HCO⁺

and HCN can be created in both high- and low-density layers of a molecular cloud (Young Owl et al. 2000). For $J = 1 \rightarrow 0$ photons that are emitted from deep inside the cloud by HCN and HCO^+ molecules, if there is a significant column of lower-density material with HCO^+ and HCN in the $J=0$ state between the cloud and the observer, then those $J = 1 \rightarrow 0$ photons will be readily absorbed in the outer layer. This will produce a self-absorption dip at the velocity of the lower density gas. The key point is that low density gas, $n \sim 10^2 - 10^4 \text{ cm}^{-3}$, can have significant opacity in the $J = 1 \rightarrow 0$ transition yet have very low excitation temperature. This gas absorbs photons but has nearly no emission. If a transition exhibits significant self-absorption across a cloud, then it can become challenging to understand cloud properties. This is one of the reasons most of this thesis focuses on N_2H^+ emission, which suffers from the least amount of self-absorption.

1.5.3 Applications to this Thesis

In this thesis, we analyze the N_2H^+ , HCO^+ , and HCN $J = 1 \rightarrow 0$ intensity (Jy beam $^{-1}$ units, analogous to line temperature in K units) and integrated intensity (Jy beam $^{-1}$ km s $^{-1}$ units, analogous to K km s $^{-1}$ units) emission structure of the CLASSy clouds, as opposed to their true density and column density structure. With only a single transition for each molecule, we are restricted in what physical properties of the cloud we can measure. To estimate physical densities using our CLASSy data, a second transition, for example, $J = 3 \rightarrow 2$, would need to be observed at the same high angular resolution. The strength of the two lines could be used to estimate molecular column density and density.

In theory, the N_2H^+ $J = 1 \rightarrow 0$ transition has hyperfine structure which should allow for the measurement of opacity (if $1 \lesssim \tau \lesssim 10$ in the strongest hyperfine lines), and hence allow an estimate of the N_2H^+ column density from the $J = 1 \rightarrow 0$

line alone. In practice, the signal-to-noise of individual spectra is not high enough to derive reliable opacity and excitation estimates across large areas of our maps, and the observed hyperfine ratios are often not consistent with the expected ratios for local thermodynamic equilibrium (LTE) for a single excitation temperature (e.g., Caselli et al. 1995; Matthews et al. 2006; Daniel et al. 2007); this makes any column density derivation uncertain. Rather than relying on a single molecular transition to estimate column densities, it is more reliable to derive column densities using continuum observations at multiple wavelengths, such as those for L1451 in Chapter 3 using *Herschel* observations from 160–500 μm . However, those observations are limited in angular resolution compared to our CLASSy data (36'' for *Herschel* at 500 μm versus 7'' for CLASSy), so they are not ideal for much of the analysis we set out to do.

Even without knowing precise column density or density values within each CLASSy beam, we know from the discussion above that the molecular emission is tracing high physical and column density material. Star formation requires high physical and column densities—high column density, low volume density regions will not form stars. Therefore, even though line intensity and integrated intensity do not directly scale to column density or density, we know they are tracing cloud regions that are viable locations for star formation. In the analysis that follows in later chapters, particularly in Chapter 4, we will assume that high (low) intensity and integrated intensity implies high (low) column density of dense gas.

We can assign ballpark numbers to our discussion of gas emission as a combined tracer of density and column density using a radiative transfer code such as RADEX (van der Tak et al. 2007). It is possible to excite HCO^+ ($J = 1 \rightarrow 0$) emission to above 1 K brightness temperature near densities $\sim 10^4 \text{ cm}^{-3}$ with molecular column density of $\sim 10^{13} \text{ cm}^{-2}$ and gas kinetic temperature at $\sim 10 \text{ K}$. For simi-

lar column density and kinetic temperature, HCN ($J = 1 \rightarrow 0$) is excited to 1 K brightness temperature near densities $\sim 10^5 \text{ cm}^{-3}$. N_2H^+ ($J = 1 \rightarrow 0$) is typically an order of magnitude less abundant in molecular clouds relative to HCO^+ or HCN (Blake et al. 1987; Friesen et al. 2010; Sanhueza et al. 2012); for molecular column density $\sim \text{few} \times 10^{12} \text{ cm}^{-2}$ and gas kinetic temperature $\sim 10 \text{ K}$, N_2H^+ ($J = 1 \rightarrow 0$) is excited above 1 K brightness temperature near densities of $\sim 10^5 \text{ cm}^{-3}$. In general, if column densities or gas kinetic temperatures are higher than the values used here, the physical density needed to excite observable lines decreases.

The earlier discussion of chemistry stated that HCO^+ and HCN are abundant in even lower-density, outer regions of clouds. However, those regions do not have the physical conditions needed to excite the ground state transitions, and mainly play a role in self-absorption. We also note that these transitions are emitting from even higher density regions than the ballpark numbers listed, but that the fraction of total molecular cloud mass decreases with increasing density (Mac Low & Klessen 2004). This means that even if there is gas with densities greater than 10^6 cm^{-3} , it will be emitting HCO^+ ($J = 1 \rightarrow 0$) photons that are a small fraction of the total number of HCO^+ ($J = 1 \rightarrow 0$) photons emitted by the cloud. In this sense, a tracer is most sensitive to the lowest density where it begins to efficiently emit. A caveat to this argument is that if the observing beam is small enough to isolate the densest regions, or if an interferometer is used to resolve out all the lower-density emission, then lower-density photons will not dominate the emission.

1.6 Technical Overview of CARMA

This thesis primarily uses data from the Combined Array for Research in Millimeter Astronomy (CARMA). This section provides a brief technical introduction to the CARMA facility, with a focus on the systems used for observations in the upcoming chapters. More details specific to CLASSy observations can be found in Chapter 2.

CARMA is a heterogeneous, 23-element interferometer, located in the eastern Sierras of California at an elevation of 7217 feet. It has six 10.4-m dishes, nine 6.1-m dishes, and eight 3.5-m dishes, with a total collecting area of 850 meters squared. The interferometer can operate as a single 23-element array, or as an independent 15-element array with the larger dishes and an independent 8-element array with the smaller dishes. The antennas are typically arranged in one of five configurations, ranging from the most compact, providing baselines between 4.0 and 66 m, to the largest with baselines between 0.2 and 2 km. The most compact and most extended arrays provide angular resolution near $11''$ and $0.3''$ respectively at 100 GHz.



Figure 1.7: View of CARMA antennas. Credit: Jens Kauffmann.

CARMA can observe at wavelengths of 1 mm, 3 mm, or 1 cm. All of the CARMA observations in this thesis were done at the 3 mm wavelength using the 23-element array. All of the 6.1-m and 10.4-m antennas are outfitted with 3 mm single-polarization, double sideband receivers. The incoming radio frequency signal is mixed with a local oscillator frequency to produce an intermediate frequency.

The sidebands are then separated in the correlator by phase-switching the local oscillators. The 3.5-m antennas can also observe at 3 mm, though they have single-sideband receivers, which means that 23-element observations only produce usable data in the upper sideband. All antennas have 1 cm receivers that can be tuned to 27–36 GHz. The 6.1-m and 10.4-m antennas have 1 mm dual circular polarization, double sideband receivers that can be tuned to 215–265 GHz.

The CLASSy observations used the CARMA spectral line correlator, which is a double sideband correlator with 4 GHz of bandwidth per sideband in standard operation. In 23-element mode, only the upper sideband is used, and four of the standard eight tunable bands can be configured with bandwidths ranging from 2 to 500 MHz. The channel resolution of those bands depends on the bit level chosen in the correlator, which can be set to balance sensitivity and spectral resolution. As an example, for 3-bit observing in 23-element mode, there are 47 channels across the 500 MHz band with 10.4 MHz channel width, and 159 channels across the 8 MHz band with 0.05 MHz channel width.

1.7 Thesis Outline

This thesis is structured as follows. Chapter 2 presents an overview of the CLASSy project with a focus on the Barnard 1 region within Perseus. It discusses CLASSy observations and data calibration, spectral line fitting, dendrogram analysis, and a method to determine the depth of clouds from size-linewidth relations. Chapter 3 presents the analysis of the L1451 region of CLASSy, with a focus on the state of star formation in such a young region. Chapter 4 presents a comparison of all five CLASSy regions, with a dendrogram analysis of their N_2H^+ integrated intensity maps, and a comparison between dendrogram structures and young stellar content.

A summary and look toward future work is in Chapter 5.

Chapter 2

Project Overview with Analysis of Dense Gas Structure and Kinematics in the Barnard 1 Region of Perseus

Abstract

We present details of the CARMA Large Area Star Formation Survey (CLASSy), while focusing on observations of Barnard 1. CLASSy is a CARMA Key Project that spectrally imaged N_2H^+ , HCO^+ , and HCN ($J = 1 \rightarrow 0$ transitions) across over 800 square arcminutes of the Perseus and Serpens Molecular Clouds. The observations have angular resolution near $7''$ and spectral resolution near 0.16 km s^{-1} . We imaged ~ 150 square arcminutes of Barnard 1, focusing on the main core, and the B1 Ridge and clumps to its southwest. N_2H^+ shows the strongest emission, with morphology similar to cool dust in the region, while HCO^+ and HCN trace

several molecular outflows from a collection of protostars in the main core. We identify a range of kinematic complexity, with N_2H^+ velocity dispersions ranging from $\sim 0.05\text{--}0.50 \text{ km s}^{-1}$ across the field. Simultaneous continuum mapping at 3 mm reveals six compact object detections, three of which are new detections. A new, non-binary dendrogram algorithm is used to analyze dense gas structures in the N_2H^+ position-position-velocity (PPV) cube. The projected sizes of dendrogram-identified structures range from about 0.01–0.34 pc. Size-linewidth relations using those structures show that non-thermal line-of-sight velocity dispersion varies weakly with projected size, while rms variation in the centroid velocity rises steeply with projected size. Comparing these relations, we propose that all dense gas structures in Barnard 1 have comparable depths into the sky, around 0.1–0.2 pc; this suggests that over-dense, parsec-scale regions within molecular clouds are better described as flattened structures rather than spherical collections of gas. Science-ready PPV cubes for Barnard 1 molecular emission are available for download.

2.1 Introduction

This chapter presents the initial results for the Barnard 1 region. Barnard 1 is located 3.5 pc to the east of NGC 1333 in the western half of the Perseus Molecular Cloud (see Figure 1.3 in Chapter 1). We assume a distance of 235 pc based on VLBI parallax measurements towards nearby sources in Perseus (SVS-13 in NGC 1333 (Hirota et al. 2008) and L1448-C in L1448 (Hirota et al. 2011)). In the context of the CLASSy campaign, we classify Barnard 1 as a moderate-activity star forming region, compared to the highly active NGC 1333 region that is dominated by a complex array of protostellar outflows, and the low-activity L1451 complex that has only one candidate protostar (Pineda et al. 2011).

Previous surveys of the young stellar content and dust in Barnard 1 reveal a northeast-southwest oriented filament exhibiting a wide range of star formation (see Figure 2.1)—progressing from a tight collection of pre- and proto-stellar cores in the northeast “main core” that includes the well-studied B1-b and B1-c cores (Hirano et al. 1999; Matthews et al. 2006; Hiramatsu et al. 2010), to a long filament of starless gas and dust known as the B1 Ridge (Enoch et al. 2006), followed by a collection of gas and dust clumps in the southwest that includes one protostellar core and several Class II YSOs. In total, the *Spitzer* c2d team identified thirteen young stellar objects (YSOs) in our field (Jørgensen et al. 2006; Rebull et al. 2007; Evans et al. 2009). Twelve dust clumps were identified by Hatchell et al. (2005) using SCUBA 850 μm data, while Kirk et al. (2006) identified five; the difference was attributed to different CLUMPFIND (Williams et al. 1994) thresholds. Jørgensen et al. (2007) associated an embedded YSO with five of the SCUBA dust clumps, while the rest of the dust clumps appeared starless.

This diversity of star formation activity along a single filament makes Barnard 1 a compelling region to spectrally image at high angular resolution. CLASSy adds to the large collection of work already done on Barnard 1, and provides the first large area (150 square arcminute), high angular resolution ($7''$; 0.008 pc at 235 pc) spectral view of the dense gas ($n \gtrsim 10^{4-6} \text{ cm}^{-3}$) across the entire field. This will allow us to quantify the structure and kinematics of the gas that is actively participating in the current generation of star formation in greater detail than ever before.

The primary goals of this chapter are to present: (1) the details of our CLASSy observations and data calibration, (2) an overview of the dense gas morphology and kinematics in Barnard 1, and (3) a dendrogram analysis of the N_2H^+ emission. In Section 2.2, we describe the CARMA observations, data calibration, and imaging. The continuum detections are summarized in Section 2.3. Section 2.4 provides a

large-scale view of the dense gas structure using integrated intensity maps. In Section 2.5, we discuss techniques for spectral line fitting and present centroid velocity and velocity dispersion maps. In Section 2.6, we create a dendrogram representation of the N_2H^+ gas and calculate properties of identified dendrogram structures. In Section 2.7, we use the spatial and kinematic properties of dendrogram-identified structures to construct size-linewidth relations; these relations are then used to probe the physical and turbulent nature of Barnard 1. Section 2.8 has a summary of the initial results. Appendix A compares clump-finding and dendrogram methods for identifying objects in this region, and Appendix B details our new dendrogram algorithm that can produce non-binary hierarchies.

2.2 Observations

CARMA is an ideal facility for producing molecular line maps that are sensitive to a wide range of spatial scales. The newly commissioned CARMA23 mode uses the cross-correlations from all twenty-three antennas, which increases CARMA’s imaging capability from the standard CARMA15 mode. Using CARMA23 in concert with CARMA’s single-dish capability and fast mosaicing can produce large maps that are sensitive to line-emission at all spatial scales. We detail the observations, data calibration, and map making in the sections below.

2.2.1 CARMA Interferometric Observations

We mosaiced an approximately $8' \times 20'$ area of Barnard 1 using CARMA. The total observing time (150 hours) was split evenly between DZ and EZ configurations, which have projected baselines from about 1–40 k λ and 1–30 k λ , respectively. DZ configuration observations occurred in the Spring and Fall of 2012, and EZ configura-

Table 2.1. Observation Summary

Array	Dates	Total Hours	Flux Cal.	Gain Cal.	Mean Flux (Jy)
DZ	April - May 2012	50	Uranus	3C84/3C111	18.3/3.8
	October 2012	25	Uranus	3C84/3C111	17.5/2.9
EZ	July - September 2012	75	Uranus	3C84/3C111	18.9/3.6

tion observations occurred in the Summer of 2012. Table 2.1 provides a summary of the observations and calibrators. The “Z” in the DZ and EZ configurations refers to use of the 23-element observing mode (CARMA23), which utilizes cross-correlations from all 23 antennas: six 10.4-meter antennas, nine 6.1-meter antennas, and eight 3.5-m antennas. (Standard CARMA15 observing only includes the 10.4-meter and 6.1-meter antennas.)

CARMA23 provides more baselines compared with the CARMA15 mode—this enhances imaging capabilities by filling in more of the uv -plane. It also offers shorter baselines, which are important for two reasons: (1) more extended emission, if present, is recovered, and (2) the increased uv -coverage improves the link between the zero spacing information from single-dish and the interferometer visibilities when doing joint deconvolution.

Our CARMA23 mosaic of Barnard 1 is made up of three adjoining rectangular regions, each at a position angle of 40° east of north; it contains 743 individual pointings in a hexagonal grid with $31''$ spacing. See Figure 2.1 for a depiction of the pointing centers overlaid on a *Herschel* $250\ \mu\text{m}$ image (André et al. 2010). The reference position of the map, which is the center of the northern rectangle, is at $\alpha=03^{\text{h}}33^{\text{m}}20^{\text{s}}$, $\delta=31^\circ08'45''$ (J2000); it encompasses the Barnard 1 main core with the B1-b and B1-c continuum cores. The other two rectangles extending toward the southwest were chosen to follow the *Herschel* dust emission.

During each pass through the map, we integrated for 15 seconds on each mosaic

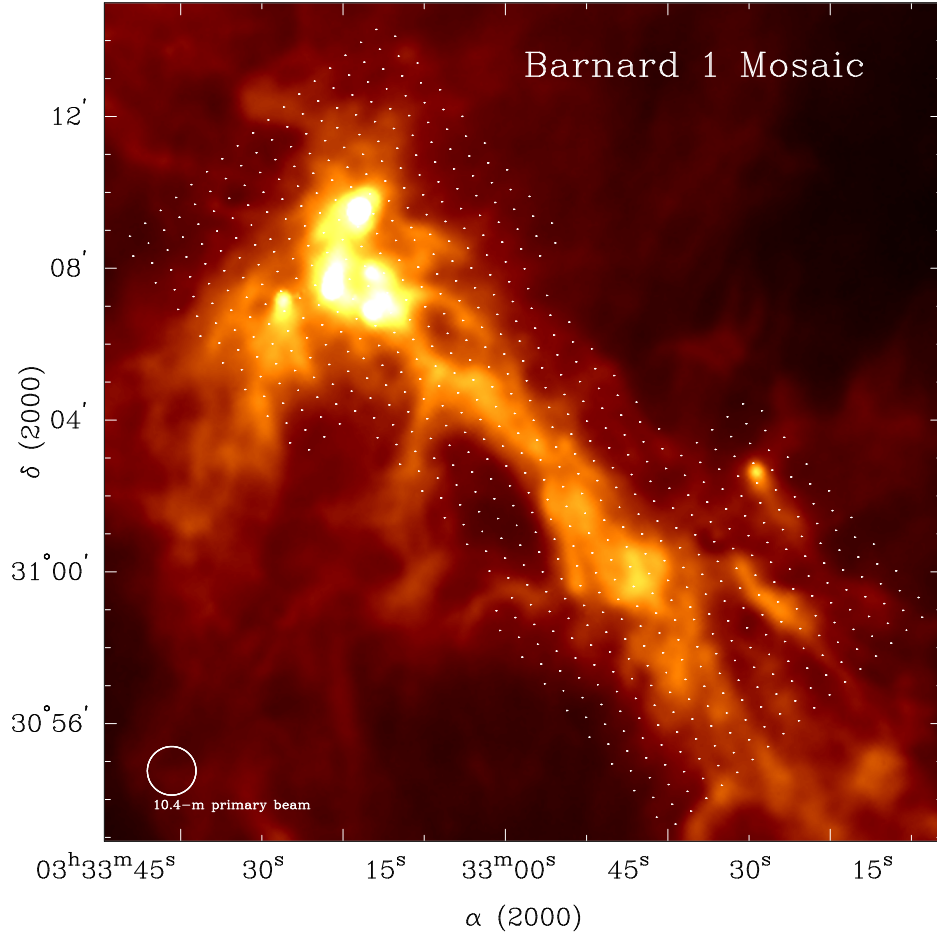


Figure 2.1: Mosaic pointing centers overlaid on a *Herschel* 250 μm image of Barnard 1 (white is brighter emission, red is fainter emission). We sampled the field at 31'' spacing; the smallest CARMA primary beam, from the 10.4-m antennas, is about 77'' near 90 GHz. We planned the observations to cover the brightest dust emission in the Barnard 1 main core, and then cover the filamentary emission that extends to the southwest. Additional pointings around the edge aid in joint deconvolution by limiting strong emission at the edges of the single-dish maps.

position before moving to the next mosaic position. We used a newly commissioned “continuous integration” technique that improves on-source efficiency (on-source integration time compared to wall clock time) of large CARMA mosaics from about 35% to 48%. The improvement comes from continuously taking data, even while antennas slew to a new mosaic position; the data for a given antenna is automatically blanked while it is slewing. This technique removes the built-in software delay

associated with a slew to a new target or mosaic position. The gain in on-source efficiency is critically important for large mosaic observations, with many moves and short integration times between moves. This method should not be confused with on-the-fly mosaicing, where the antennas are continuously moving while taking data.

In CARMA23 mode, the correlator has four spectral bands in the upper side band. The lower side band is not present on the 3.5-m telescopes; it is present but not used on the 10.4 and 6.1-m telescopes. We tuned to the $J = 1 \rightarrow 0$ transitions of N_2H^+ , HCO^+ , and HCN , and used a 500 MHz wide band for calibration and continuum detections. Table 2.2 has an overview of the correlator setup. The molecular lines were each placed in 8 MHz bands, which have 159 channels that are 0.049 MHz wide in 3-bit mode; this corresponds to $\sim 0.16 \text{ km s}^{-1}$ velocity resolution near 90 GHz. All hyperfine components of N_2H^+ and HCN fit within the 8 MHz bands. However, there is high-velocity HCO^+ and HCN emission from outflows that lies outside our bandwidth.

Two team members independently inspected, flagged, and calibrated each observing track during the 150 hour campaign using MIRIAD (Multichannel Image Reconstruction, Image Analysis and Display; Sault et al. 1995). The flags for each track were then copied to our MIS (MIRIAD Interferometric and Single-Dish; Teuben et al. 2013) pipeline that has the capability to calibrate all of the tracks with minimal user input and create combined visibility datasets and maps of all the observed sources. Standard interferometric calibration steps (e.g., passband, gain, flux calibration) were performed in the MIS pipeline calibration code. We observed a nearby quasar every 16 minutes for gain calibration; 3C84 was the main gain calibrator, and 3C111 was used when 3C84 rose above 80° elevation. 3C84 doubled as a passband calibrator. We observed Uranus for absolute flux calibration during

Table 2.2. Correlator Setup Summary

Line	Rest Freq. (GHz)	No. Chan.	Chan. Width (MHz)	Vel. Coverage (km s ⁻¹)	Vel. Resolution (km s ⁻¹)	Chan. RMS (Jy beam ⁻¹)	Synth. Beam ^a
N ₂ H ⁺	93.173704	159	0.049	24.82	0.157	0.14	7.6'' × 6.5''
Continuum	92.7947	47	10.4	1547	33.6	0.0013	8.0'' × 6.2''
HCO ⁺	89.188518	159	0.049	25.92	0.164	0.12	7.8'' × 6.8''
HCN	88.631847	159	0.049	26.10	0.165	0.12	7.9'' × 6.8''

Note. — ^aIn principle, the synthesized beam is slightly different for each pointing. Miriad calculates a synthesized beam for the full mosaic based on all of the pointings.

each track and used the `bootflux` task to determine the absolute flux of the gain calibrators. The flux of 3C84 varied between 16.0 and 19.4 Jy over the course of the campaign, while 3C111 varied between 2.8 and 4.5 Jy. The uncertainty in absolute flux calibration in the 24 combined datasets is about 10%; hereafter, we only report statistical uncertainties in quoting errors in measured values.

2.2.2 CARMA Single-Dish Observations

Simultaneously with the interferometric observations, we obtained CARMA total power observations to recover the line emission resolved out by the interferometer (i.e., CARMA in standard interferometric observing mode). CARMA’s single-dish mode utilizes the autocorrelation capability of the correlator and intersperses observations of an emission-free region between on-source integrations. A total power spectrum can then be constructed from knowledge of the system temperature (T_{sys}), the emission region (the ON position), and the emission-free region (the OFF position).

The OFF position for Barnard 1 was in a gap of ^{12}CO and ^{13}CO emission 28’ west and 1.5’ south of the Barnard 1 mosaic reference position. A hole in lower density CO gas ensured that there was no significant dense gas in that region. We integrated on the OFF position for 30 seconds every 3.5 minutes if the atmospheric opacity was stable on the 3.5 minute timescale; otherwise, we observed purely in interferometric mode. Fourteen of 24 tracks with passing weather grades were observed in single-dish mode. We flagged the autocorrelation data separately from the cross-correlation data to account for cases where the opacity deteriorated in a track that was started in single-dish mode.

We calibrated the autocorrelation data from each antenna in MIRIAD with two steps: (1) `sinbad` calculated $T_{\text{sys}} * (\text{ON} - \text{OFF}) / (\text{OFF})$, and (2) `sinpoly` removed

first-order polynomial baselines from the `sinbad` spectra. We averaged OFF scans on both sides of an ON scan in the `sinbad` calculation to reduce noise introduced from OFF scans.

We converted the calibrated single-dish spectra from each of the six 10.4-m antennas to six single-dish data cubes using the `varmaps` routine. We only used the 10.4-m antennas because they have the highest angular resolution and, hence, best overlap with the 3.5-m baselines in the uv -plane. The 10.4-m antennas have a halfpower beamwidth of 77.3'' (N_2H^+), 80.7'' (HCO^+), and 81.2'' (HCN). The routine gridded each data cube onto $10'' \times 10''$ cells, and used a 50'' smoothing beam to calculate the emission in each cell according to the emission at each mosaic pointing. The size of the smoothing beam was determined empirically; a smaller beam increased the final noise in the maps, while a larger beam smoothed out structure seen in other single-dish maps of this region. The final halfpower beamwidth of the calibrated single-dish cubes is the quadrature sum of the original halfpower beamwidth and the smoothing beam: 92.1'' (N_2H^+), 94.9'' (HCO^+), and 95.4'' (HCN).

We scaled the data cubes from all six antennas to a single reference antenna to account for systematic differences of $\sim 10\%$ arising from physical differences in each antenna and from differences in bandpass shape of each antenna response. We calculated the mean of the six data cubes using `imstack` to improve the signal-to-noise ratio and limit antenna-based artifacts. The antenna temperature rms values in the final cubes are 0.025, 0.027, and 0.026 K for N_2H^+ , HCO^+ , and HCN, respectively.

2.2.3 Joint Deconvolution of Interferometric and Single-Dish Cubes

The final data product for each observed molecular line transition is a spectral line cube produced from a joint deconvolution of the interferometric and single-dish data. The joint deconvolution was done in MIRIAD as summarized below.

We created the interferometric dirty cube and dirty beam from the calibrated visibility dataset using `invert` with system temperature and antenna gain weighting, and Briggs' robustness parameter (Briggs et al. 1999) of -0.5 . We de-selected baselines connecting 10.4 m and 3.5 m dishes due to the illumination of the first negative sidelobe of the 10.4-m beam by the 3.5-m beam. The dirty cube was then cleaned with `mossdi`, a Steer CLEAN algorithm, and the clean components were carried over to the joint deconvolution to aid in the convergence to a solution. The single-dish cube was regridded to the interferometric cube axes, and converted to Jy beam^{-1} units with a $65 \text{ Jy beam}^{-1} \text{ K}^{-1}$ scaling factor¹.

The joint deconvolution was done with a maximum entropy algorithm in MIRIAD, `mosmem`, that used the interferometric dirty cube, single-dish cube, interferometric dirty beam, single-dish beam, and interferometric clean components to solve for the maximum entropy model components. The final cubes are the dirty cube, minus the maximum entropy model components convolved by the dirty beam, plus the maximum entropy model components convolved by the synthesized beam. The noise levels and synthesized beams for the final data cubes are given in Table 2.2.

¹http://www.mmarray.org/memos/carma_memo52.pdf

2.2.4 Continuum Mapping

A 3 mm continuum map was created from the interferometric data in the 500 MHz window. We created and cleaned the dirty map in MIRIAD using `invert` and `mosstdi`, and restored with a synthesized beam of $8.0'' \times 6.2''$. The rms in the calibrated continuum map is ~ 1.3 mJy beam $^{-1}$.

The autocorrelation data from the 500 MHz band was not used in continuum mapping because single-dish continuum observations require fast chopping between on-position and off-position to cancel out variable sky emission; this observing technique is not available at CARMA.

2.3 Continuum Results

We detected four compact continuum sources above the $5\text{-}\sigma$ level; all are associated with young protostars in the main core. Figure 2.2 shows 3 mm continuum images toward the previously known Class 0 source, B1-c (Matthews et al. 2006), and the Class 0 double source, B1-b (Hirano et al. 1999), along with a new $5.8\text{-}\sigma$ detection toward a Class I source, SSTc2d J033327.3+310710 (also at the position of the lower-resolution Per-emb 30 dust source in Enoch et al. 2009).

The structure around B1-c and B1-b is clearly resolved; Per-emb 30 appears to be nearly unresolved. We used MIRIAD's `imfit` to determine the position, peak brightness, total flux density, size, and position angle of each source with an elliptical Gaussian approximation (see Table 2.3). The measured position errors are 0.2–0.7''. The positions of B1-c and B1-b agree with other interferometric observations of these sources (Matthews et al. 2006; Chen et al. 2013; Huang & Hirano 2013).

With linear sizes of 1000–2000 AU, the 3 mm emission is arising from compact cores associated with forming stars. In the optically thin limit, under the assumption

Table 2.3. Observed Properties of Continuum Detections

Source Name (1)	Position (h:m:s, d':") (2)	Pk. Bright. (mJy beam ⁻¹) (3)	Total S _ν (mJy) (4)	Ang. Size (") (5)	P.A. (°) (6)	Decon. Size (") (7)	Decon. P.A. (°) (8)	Lin. Size (AU) (9)	Mass (M _⊙) (10)
B1-c	03:33:17.91, +31:09:32.8	23.0 ± 1.8	52.6 ± 4.2	10.7 × 10.7	-33	8.7 × 7.1	-1	2040 × 1670	1.04 ± 0.08
B1-b South	03:33:21.37, +31:07:26.4	29.1 ± 2.3	42.1 ± 3.3	9.8 × 7.4	-79	5.9 × 3.6	-65	1390 × 850	0.84 ± 0.07
B1-b North	03:33:21.23, +31:07:43.7	27.5 ± 2.2	43.0 ± 3.3	10.1 × 7.7	89	6.2 × 4.5	87	1460 × 1060	0.85 ± 0.07
Per-emb 30	03:33:27.35, +31:07:10.0	6.9 ± 0.8	8.9 ± 1.0	9.7 × 6.6	79	5.5 × 1.7	69	1290 × 400	0.18 ± 0.02
W1	03:33:14.8, +31:07:13	4.1 ± 1.3	^a 0.08 ± 0.03
W2	03:33:16.7, +31:06:53	4.4 ± 1.3	^a 0.09 ± 0.03

Note. — (3) Peak brightness, (4) Total flux density, (5) Major and minor axes (FWHM), (6) Position angle (east of north), (7) Deconvolved major and minor axes (FWHM), (8) Deconvolved position angle, (9) Linear size computed from deconvolved size assuming a distance of 235 pc, (10) Mass calculated using assumptions in the text (^alower-limit mass for weak detections that uses the peak brightness instead of the total flux density).

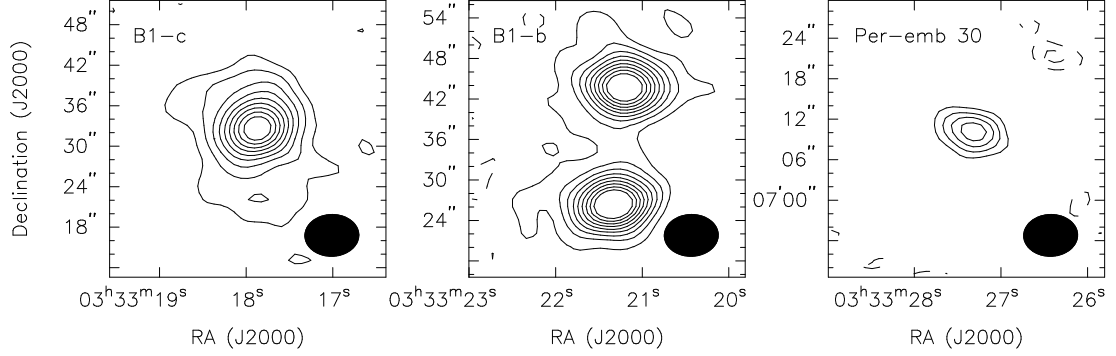


Figure 2.2: The four continuum detections above $5\text{-}\sigma$ in our field. The synthesized beam is $8.0'' \times 6.2''$, and the $1\text{-}\sigma$ sensitivity is $\sim 1.3 \text{ mJy beam}^{-1}$. B1-c and B1-b were previously found to have compact continuum emission associated with young stars. The contour levels in those maps are $(\pm)2, 4, 6, 8, 10, 12, 14, 16, 18$ times $1\text{-}\sigma$. The compact emission within Per-emb 30 is a new detection that peaks at $5.8\text{-}\sigma$. Contour levels in that map are $(\pm)2, 3, 4, 5$ times $1\text{-}\sigma$. The negative contours are represented by dashed lines.

of a single temperature, core mass is related to the total flux density as

$$M = \frac{F_\nu D^2}{\kappa_\nu B_\nu(T_d)}, \quad (2.1)$$

where M , F_ν , D , κ_ν , and $B_\nu(T_d)$, are respectively the total mass, total observed flux density, distance, mass opacity including dust and gas (assuming a gas-to-dust ratio of 100), and blackbody intensity at dust temperature, T_d . We assume $T_d = 20 \text{ K}$. To estimate κ_ν , we assumed a power law opacity curve, $\kappa_\nu = \kappa_o(\nu/\nu_o)^\beta$, where $\nu_o = 1000 \text{ GHz}$ and $\kappa_o = 0.1 \text{ cm}^2 \text{ g}^{-1}$ (Beckwith et al. 1990). For a β of 1.5, κ_ν is $0.0028 \text{ cm}^2 \text{ g}^{-1}$ at 92.79 GHz . The core masses under these assumptions are listed in Table 2.3; statistical errors are reported using the uncertainty in the total flux density. The B1-c mass estimate is about three times lower than the mass reported in Matthews et al. (2006), primarily due to differences in the observed total flux density near 3.3 mm . The B1-b mass estimates are several times larger than results from Huang & Hirano (2013), who observed the sources at 1 mm with higher angular resolution; the disparity increases when adopting their assumed β and T_d values. Since they derived deconvolved sizes of $\sim 300\text{--}500 \text{ AU}$, it is most likely that their

mass estimates are not including extended emission in the protostellar envelope.

In addition to these relatively strong detections, we detected two continuum peaks greater than $3\text{-}\sigma$ (labeled W1-2 in Table 2.3) that are coincident with a source in at least one *Spitzer* or *Herschel* band. The positions, peak brightnesses, and lower-limit masses for these sources are listed in Table 2.3. We determined position using `imfit` with an elliptical Gaussian approximation. Peak brightness was defined as the maximum pixel value within the $3\text{-}\sigma$ contour of the source, with error equal to the $1\text{-}\sigma$ sensitivity of the continuum map. The lower-limit mass was calculated from the peak brightness. W1 is coincident with SSTc2d J033314.3+310710 (Per-emb 6), and W2 is coincident with SSTc2d J033316.4+310652 (Per-emb 10). Deeper, follow-up observations are needed to confirm these detections and calculate physical properties of the sources.

2.4 Morphology of Dense Molecular Gas

Figure 2.3 shows our N_2H^+ , HCN, and HCO^+ ($J = 1 \rightarrow 0$) integrated intensity maps, along with a *Herschel* 250 μm view of Barnard 1 for a qualitative gas-dust comparison. The angular resolution of the dust map is $18.1''$ in comparison to our $\sim 7''$ resolution. To facilitate the discussion later in this section, we identify three zones of emission: the main core zone, the ridge zone, and the SW clumps zone. Figure 2.4 shows example spectra from each zone at the locations marked by crosses in Figure 2.3, and the next three sections discuss the three zones in detail.

The N_2H^+ map was integrated over all seven hyperfine components over velocity ranges from 14.044 to 10.745 km s^{-1} , 8.860 to 4.775 km s^{-1} , and -0.951 to -2.766 km s^{-1} . The HCN map was integrated over all three hyperfine components, excluding channels with outflows, from 12.117 to 10.961 km s^{-1} , 7.326 to

6.005 km s⁻¹, and 0.057 to -1.264 km s⁻¹. The HCO⁺ map was integrated from 7.161 to 5.849 km s⁻¹, again excluding outflow channels. We integrated N₂H⁺ over a wider range of velocities compared to the other molecules to include a narrow, redshifted filament, which can be seen along the southeastern edge of the thicker N₂H⁺ filament in the ridge zone. This redshifted filament, discussed later in this section, is also detected in HCN and HCO⁺, but overlaps in velocity space with HCN and HCO⁺ outflow channels that were excluded from these integrated intensity maps. The rms of the N₂H⁺, HCN, and HCO⁺ integrated intensity maps in Figure 2.3 are 0.17, 0.10, and 0.06 Jy beam⁻¹ km s⁻¹, respectively.

The peak brightness temperature for a single channel (including channels with outflows) in the entire field occurs towards the B1-c continuum core; it is 9.5 K, 9.7 K, and 7.1 K in our synthesized beam for N₂H⁺ (2.85 Jy beam⁻¹ to K conversion factor), HCN (2.91 Jy beam⁻¹ to K conversion factor), and HCO⁺ (2.91 Jy beam⁻¹ to K conversion factor), respectively.

2.4.1 Main Core Zone

The main core zone, shown in Figure 2.5, is the area of strongest dust emission seen by *Herschel*; it contains the largest cluster of young protostellar objects, and is the only region where we have detected compact continuum sources (see Section 2.3) and outflows (see Figure 2.6). The N₂H⁺ emission in this zone follows the overall structure of the dust, although our improved angular resolution reveals more detail than ever before. The HCN and HCO⁺ emission not associated with outflows is much weaker compared to N₂H⁺, and it does not follow the morphological structure of the N₂H⁺ or the dust. Figure 2.5 shows the locations of *Spitzer* YSO candidates (Jørgensen et al. 2006), Bolocam 1 mm clumps (Enoch et al. 2006), and SCUBA 850 μm clumps (Hatchell et al. 2005).

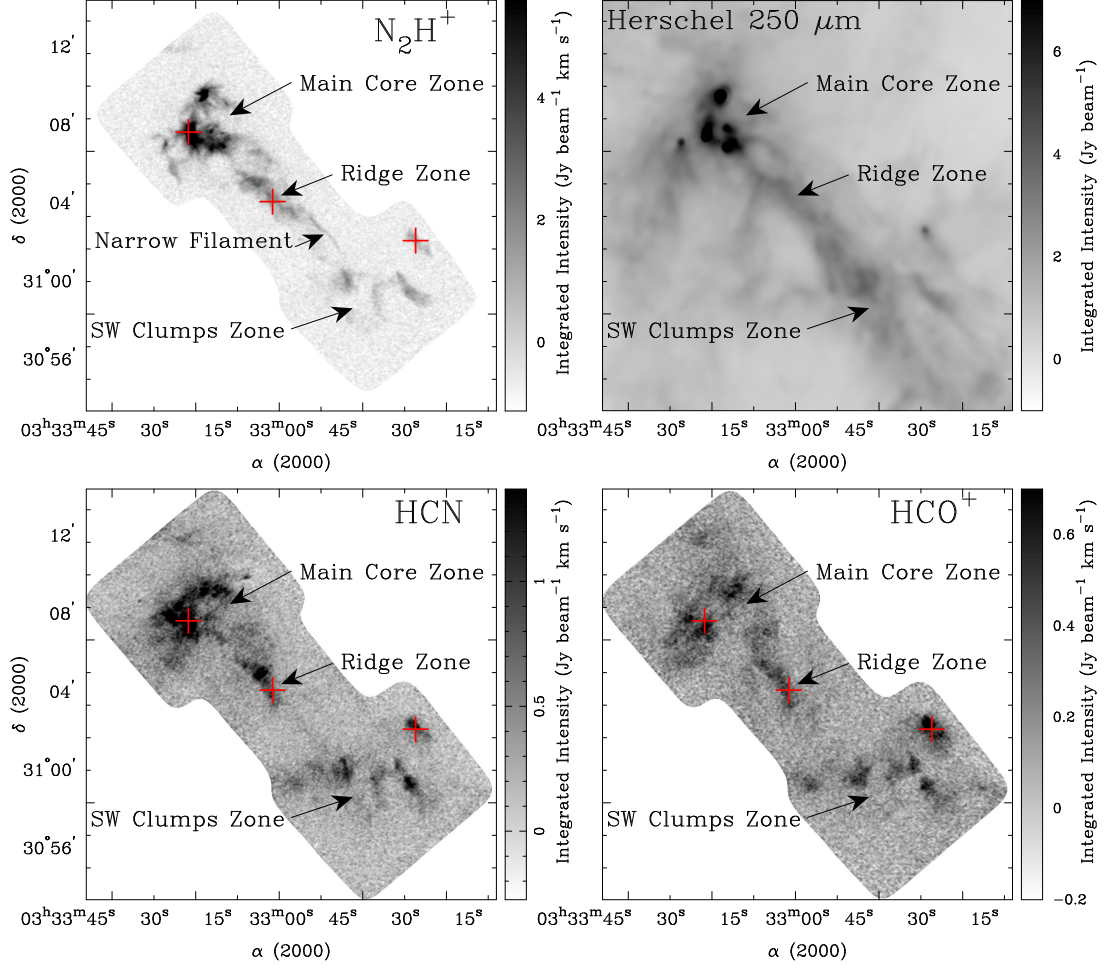


Figure 2.3: Integrated intensity maps of N_2H^+ , HCN, and HCO^+ ($J = 1 \rightarrow 0$) emission towards Barnard 1, with a *Herschel* 250 μm map. Channels containing outflow emission are excluded from these maps, which is why the narrow filament (see Section 2.4.2) appears only in N_2H^+ . The rms values of the N_2H^+ , HCN, and HCO^+ maps are 0.17, 0.10, and 0.06 $\text{Jy beam}^{-1} \text{ km s}^{-1}$, respectively. We break the region into three zones based on qualitative features in the dense gas maps. Crosses in the maps represent the locations of spectra shown in Figure 2.4. FITS cubes of the PPV data used to make this figure are available in the online journal version of this chapter.

The spectra from this zone are the most complex in the Barnard 1 field—Figure 2.4 shows a sample N_2H^+ spectrum from near the B1-b core that exhibits broad lines, while the HCN and HCO^+ spectra from the same location show evidence of red-wing outflow emission overlapping with B1-b. The N_2H^+ emission towards B1-b shows two resolved peaks. There are emission peaks in HCN and HCO^+ to

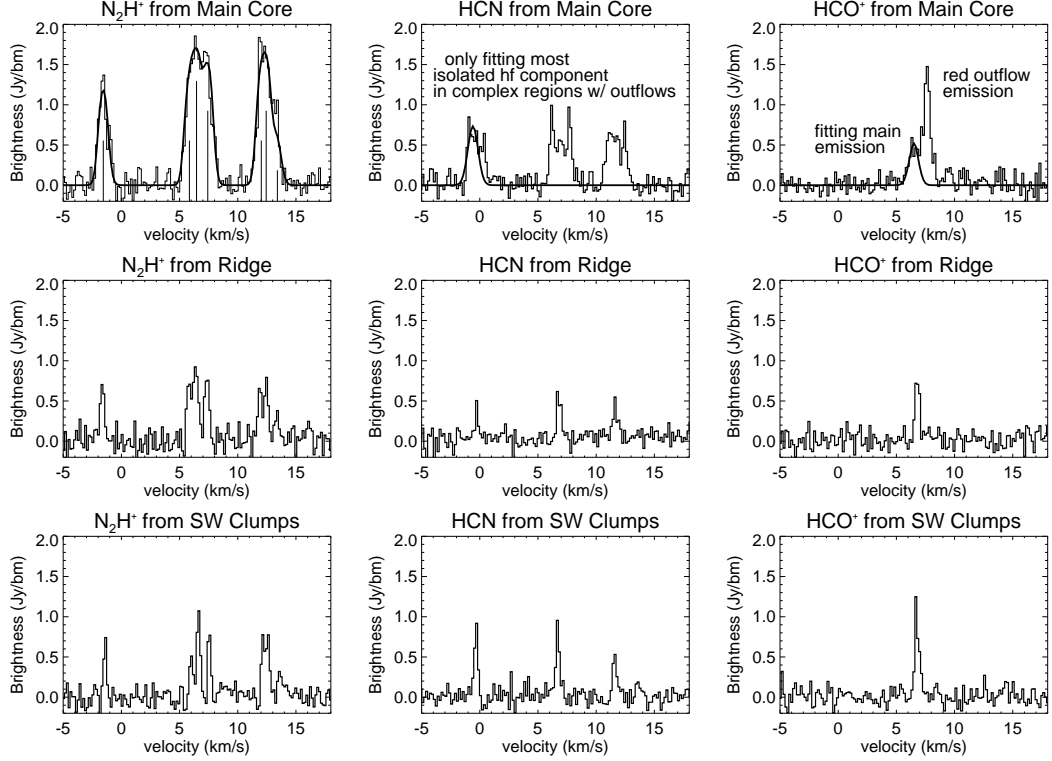


Figure 2.4: Example spectra for all three molecules from each zone. The spectra are averaged over one synthesized beam, and the positions are: $\alpha = 03^{\text{h}}33^{\text{m}}21.633^{\text{s}}$, $\delta = 31^{\circ}07'38.06''$ for the Main Core Zone, $\alpha = 03^{\text{h}}33^{\text{m}}01.482^{\text{s}}$, $\delta = 31^{\circ}04'05.09''$ for the Ridge Zone, and $\alpha = 03^{\text{h}}32^{\text{m}}27.312^{\text{s}}$, $\delta = 31^{\circ}02'05.36''$ for the SW Clumps Zone. We fit the spectra and present maps of centroid velocity and velocity dispersion in Section 2.5. The fits to the main core zone spectra are shown with solid black lines. The N_2H^+ has seven resolvable hyperfine components in narrow-line regions, and HCN has three resolvable hyperfine components. The hyperfine structure of N_2H^+ is shown with vertical bars set within the main core zone spectrum—the relative brightnesses are representative of the hyperfine structure, but the absolute values were picked for ease of visualization. As described in Section 2.5, we exclude outflow emission from HCN and HCO^+ when doing these fits.

wards B1-b South, but not B1-b North (see Figure 2.5). This agrees with findings from Huang & Hirano (2013) and supports the idea that carbon-bearing species are depleted around B1-b North, suggesting it is the younger source of the two.

The N_2H^+ gas emission is very strong at the location of B1-c, while HCO^+ is only detected in outflows; this agrees with observations from Matthews et al. (2006).

HCN gas does exist at the location of B1-c, but is not a strong peak relative to the rest of the main core, like we see with N_2H^+ . HCN is also detected in outflow emission.

There are seven *Spitzer* Class 0/I YSOs in this zone. Two are known to be associated with the B1-c and Per-emb 30 compact continuum cores, which are sites of strong N_2H^+ emission. There are four nearby the larger scale B1-a, B1-b, and B1-d dust clumps, which are also areas of strong N_2H^+ emission. The seventh YSO, which lies west of the strongest dense gas in this zone, only has weak dust and gas emission associated with it. Several of these YSOs are driving outflows, which are discussed later in this section, and identified in Figure 2.6 and Table 2.4.

There are five Bolocam 1.1 mm cores and six SCUBA 850 μm cores in this region. All of these lower resolution dust cores are near N_2H^+ emission peaks, but not necessarily near HCN or HCO^+ peaks. There are several peaks of HCN and HCO^+ that are not associated with strong dust emission.

Figure 2.6 shows HCO^+ and HCN dense gas outflows, which are only detected in this zone. In the HCO^+ map, SSTc2d J033317.9+31092 (B1-c) is clearly driving a bipolar outflow. We detect another bipolar HCO^+ outflow, likely associated with the IRAS 03301+3057 YSO based on a similar detection in CO by Hirano et al. (1997). There is a red outflow just to the west of SSTc2d J033314.4+310711, another to the north SSTc2d J033320.3+310721, and a third to the southeast of SSTc2d J033327.3+310710.

In the HCN map, we again see the bipolar outflow from SSTc2d J033317.9+31092 (B1-c), although the HCN additionally traces an extension of the red part of the outflow to the west, and an associated knot of emission to the east. The western extension flares out into two separate, high-velocity outflows that extend beyond the edge of our spectral window. The eastern knot is likely a bright bow shock

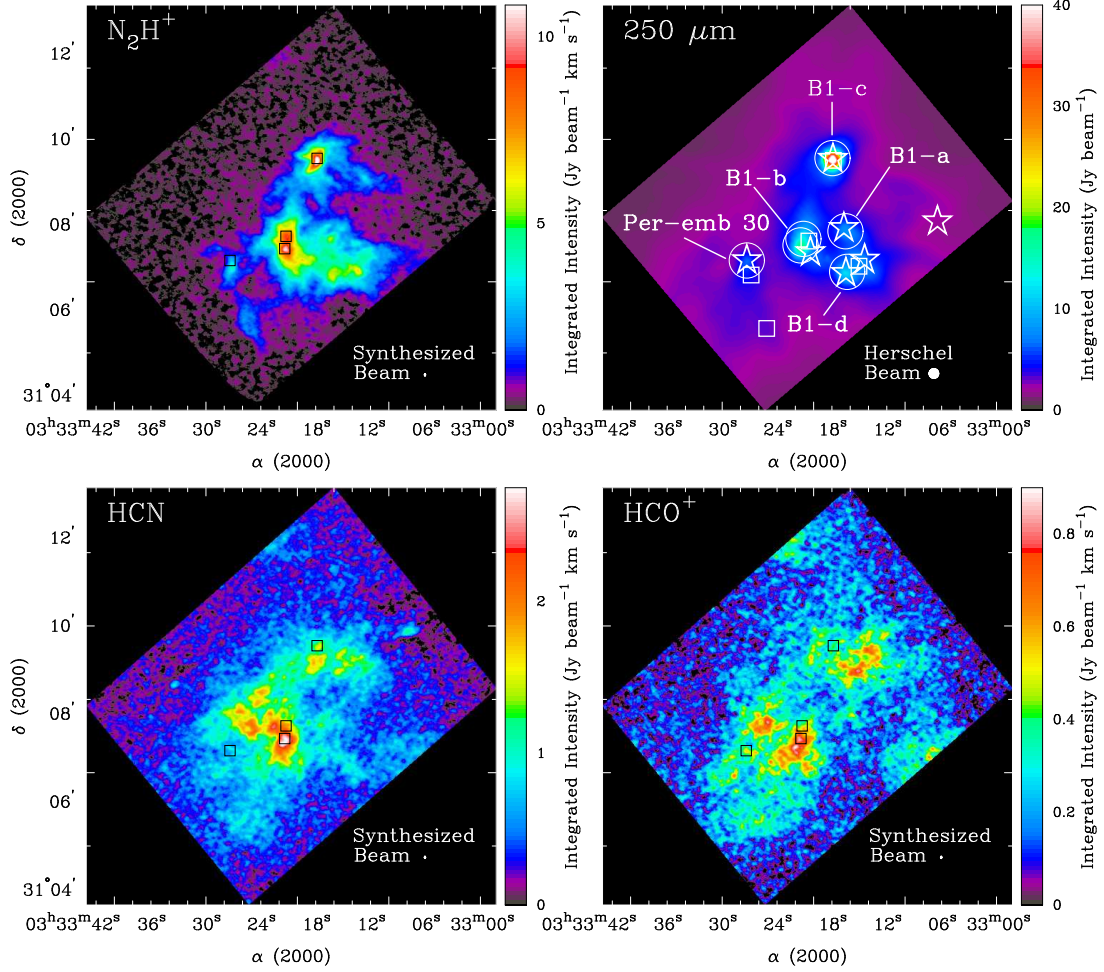


Figure 2.5: Integrated intensity maps of N_2H^+ , HCN , and HCO^+ ($J = 1 \rightarrow 0$) emission toward the main core zone, along with *Herschel* $250 \mu\text{m}$. Channels containing outflow emission are excluded from the integrated intensity maps. The angular resolution of each map is marked with a beam in the lower right corner—the CARMA synthesized beam is $\sim 7''$. The *Herschel* map shows the location of *Spitzer* YSOs (stars), Bolocam 1.1 mm cores (squares), and SCUBA $850 \mu\text{m}$ cores (circles); all YSOs in this region are Class 0/I. Major dust clumps mentioned in the text are labeled in the *Herschel* map. The black boxes in the integrated intensity maps show the locations of the compact continuum sources that were discussed in Section 2.3. The rms of the N_2H^+ , HCN , and HCO^+ integrated intensity maps are 0.17, 0.10, and 0.06 $\text{Jy beam}^{-1} \text{ km s}^{-1}$, respectively.

from the edge of the outflow interacting with cloud material. We confirmed the association of these extended features with the main outflow using *Spitzer* images that trace the shocked gas. The outflows from IRAS 03301+3057 and SSTc2d

J033320.3+310721 are also detected in HCN, while those from J033314.4+310711 and J033327.3+310710 are not.

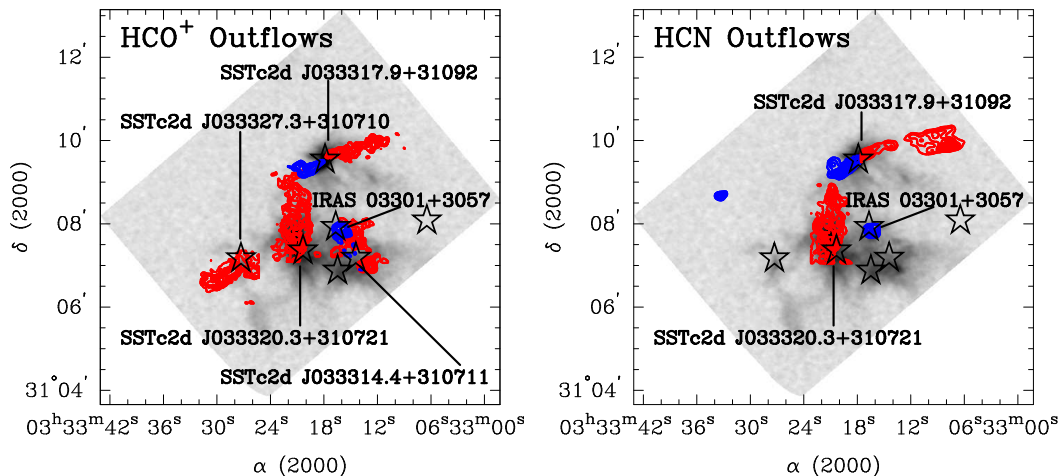


Figure 2.6: HCO^+ and HCN outflows overlaid on N_2H^+ integrated intensity emission. Each outflow was integrated over its own range of velocities to minimize noise introduced from emission-free channels. We are plotting contours of 0.3, 0.4, 0.5, 0.6, 0.7, 0.8, 0.9 times the peak integrated intensity of the outflow, except for the HCN bipolar outflow from SSTc2d J033317.9+31092 where we extend down to 0.1 and 0.2 times the peak. See Table 2.4 for the velocity ranges and peak integrated intensity of each outflow—the outflows are identified in the table by the nearest infrared source plotted in this figure. *Spitzer* YSO positions are indicated with black stars; all YSOs are Class 0/I in this region.

2.4.2 Ridge Zone

The ridge zone, shown in Figure 2.7, lies southwest of the main core. The most striking feature is the backbone of the B1 Ridge that appears as a structure (“Ridge” in the figure) that measures approximately $260''$ long by $80''$ wide in the N_2H^+ map. This corresponds to about 0.30 pc long by 0.09 pc wide at a distance of 235 pc. This structure has several Bolocam and SCUBA cores running along its spine, which are strongly clustered in the northeast half where gas emission from all molecules is the strongest. A single Class 0/I YSO sits at the northeast edge of the structure—none of the dust cores along the structure have associated protostars, and they

Table 2.4. Outflow Identification

Source Identifier ^a	Color (Red or Blue)	Integrated Velocity Range (km s ⁻¹)	Peak Integrated Intensity (Jy beam ⁻¹ km s ⁻¹)
HCO ⁺			
SSTc2d J033317.9+310932 (B1-c, Per-emb 29)	Red	9.62–7.98	1.0
SSTc2d J033317.9+310932 (B1-c, Per-emb 29)	Blue	5.36–3.72	1.9
IRAS 03301+3057 (B1-a, Per-emb 40)	Red	7.66–7.49	0.5
IRAS 03301+3057 (B1-a, Per-emb 40)	Blue	5.36–1.26	2.4
SSTc2d J033327.3+310710 (Per-emb 30)	Red	7.82–7.32	0.8
SSTc2d J033320.3+310721 (Per-emb 41)	Red	9.95–7.33	1.8
SSTc2d J033314.4+310711 (Per-emb 6)	Red	13.73–7.82	4.4
HCN			
SSTc2d J033317.9+310932 (B1-c, Per-emb 29)	Red	18.89–11.78, 10.13–7.66	12.0
SSTc2d J033317.9+310932 (B1-c, Per-emb 29)	Blue	10.63–7.66, 5.67–1.54, (–)1.26–(–)3.08	10.1
SSTc2d J033317.9+310932 (B1-c, Per-emb 29)	Blue ^b	(–)1.26–(–)5.72	3.3
IRAS 03301+3057 (B1-a, Per-emb 40)	Blue	10.30–9.64, 5.34–4.19	2.1
SSTc2d J033320.3+310721 (Per-emb 41)	Red	12.61–12.28, 8.48–7.33, 0.72–0.22	1.5

Note. — (a) Outflows identified by the location of the nearest infrared source. Supplemental Per-emb source identifiers are from Enoch et al. (2009).
(b) This emission corresponds to the blue knot seen in the HCN map of Figure 2.6, east of the main part of the SSTc2d J033317.9+310932 outflow.

are considered pre-stellar. There is a single Bolocam core at the southwestern end of the structure, where the *Herschel* map peaks in an area with little molecular emission; multi-wavelength *Herschel* images show that this region is brighter at shorter wavelengths compared to the northeastern section of the structure. This means it could be a region of slightly higher temperature, which would explain a lower abundance of dense molecular gas. Figure 2.4 shows sample spectra from along this structure.

A second molecular feature in this zone is a newly discovered filament that runs parallel to the main ridge (“Narrow Fil” in Figure 2.7). This filament is extremely narrow and is offset from the rest of the gas in velocity space by about 1.5 km s^{-1} . Figure 2.8 shows molecular line contours overlaid on a *Herschel* $250 \mu\text{m}$ map. The filament is about $20''$ wide and $2.5'$ long, with a small kink half-way along its length. At a distance of 235 pc, this corresponds to 0.022 pc wide by 0.17 pc long. The peak integrated intensity of the filament is $1.2 \text{ Jy beam}^{-1} \text{ km s}^{-1}$, $1.4 \text{ Jy beam}^{-1} \text{ km s}^{-1}$, and $0.9 \text{ Jy beam}^{-1} \text{ km s}^{-1}$, for N_2H^+ , HCN , and HCO^+ , respectively. It is not possible to identify the filament in *Herschel* maps because it is extremely narrow and lies along the same line of sight as the western edge of the B1 Ridge. We briefly discuss the kinematics and possible formation mechanisms of the filament in Section 2.5.

The third molecular feature is gas in the northern part of the zone that provides a tenuous link between the main ridge structure and the main core zone. A Class 0/I YSO is located off the southwestern edge of this feature, but there are no dust condensations directly associated with it.

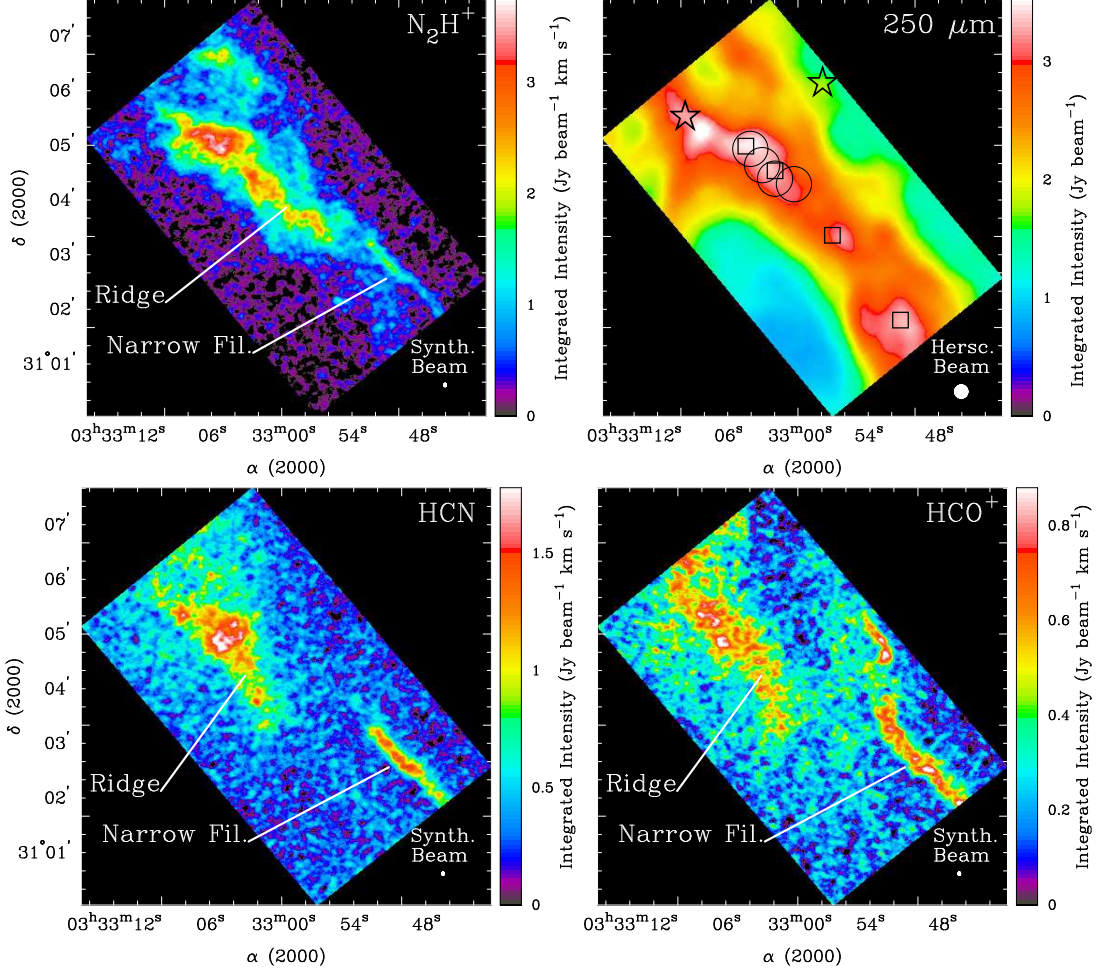


Figure 2.7: Integrated intensity maps as in Figure 2.5, but for the ridge zone. Since the ridge zone does not have outflows, we included extra channels that were excluded from Figure 2.5 to capture the narrow filament that is redshifted by $\sim 1.5 \text{ km s}^{-1}$ from the rest of the Barnard 1 gas. The rms values of these N_2H^+ , HCN, and HCO^+ integrated intensity maps are 0.17, 0.12, and 0.08 $\text{Jy beam}^{-1} \text{ km s}^{-1}$, respectively.

2.4.3 SW Clumps Zone

The SW clumps zone lies southwest of the B1 Ridge, and is shown in Figure 2.9. There are five distinct clumps of N_2H^+ emission, with a sixth clump only detected in HCN and HCO^+ . There are three Class II YSOs in this zone that do not correlate with any gas or dust peaks, which is expected for more evolved protostars. There is one Class 0/I YSO in this zone that lies at the northeast tip of the western-

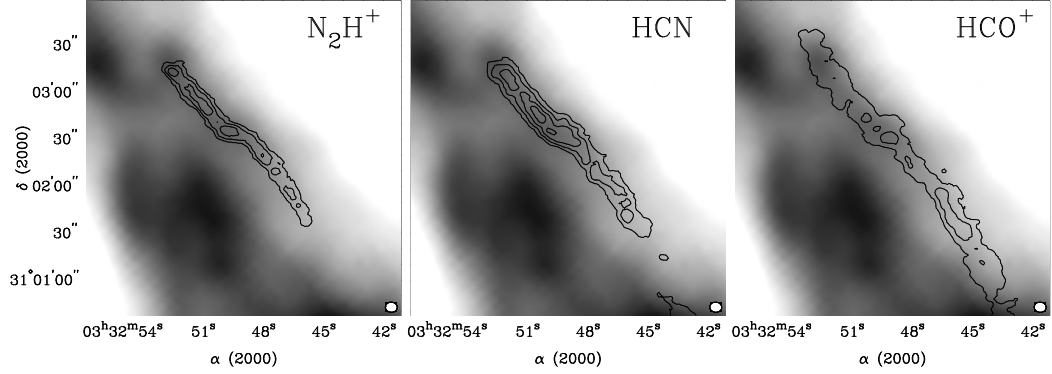


Figure 2.8: We discovered a narrow filament that is offset by 1.5 km s^{-1} from the rest of the gas in Barnard 1. The three figures show the filament detected in N_2H^+ , HCN, and HCO^+ , overlaid on the *Herschel* $250 \mu\text{m}$ dust image. The contours represent integrated intensity emission at 0.3, 0.5, 0.7, and 0.9 times the peak integrated intensity of the HCN filament, which is $1.36 \text{ Jy beam}^{-1} \text{ km s}^{-1}$.

most clump. The strongest integrated HCO^+ emission across the entire Barnard 1 field is located in this clump—Figure 2.4 shows sample spectra from it. The gas morphology of this zone is very different from the main core and ridge zones. Those zones have dense gas peaks embedded within lower-intensity, larger-scale dense gas structures, while the dense gas peaks in this zone are not joined at weaker emission levels.

2.5 Kinematics of Dense Molecular Gas

We modeled the spectra in our position-position-velocity (PPV) cubes to derive the centroid velocity and velocity dispersion for the emission from each molecule along every line of sight.

The $\text{N}_2\text{H}^+(J = 1 \rightarrow 0)$ line is made up of seven resolvable hyperfine components. We model all components simultaneously and assume they are Gaussians with the same dispersion and excitation conditions. The line opacity as a function of velocity,

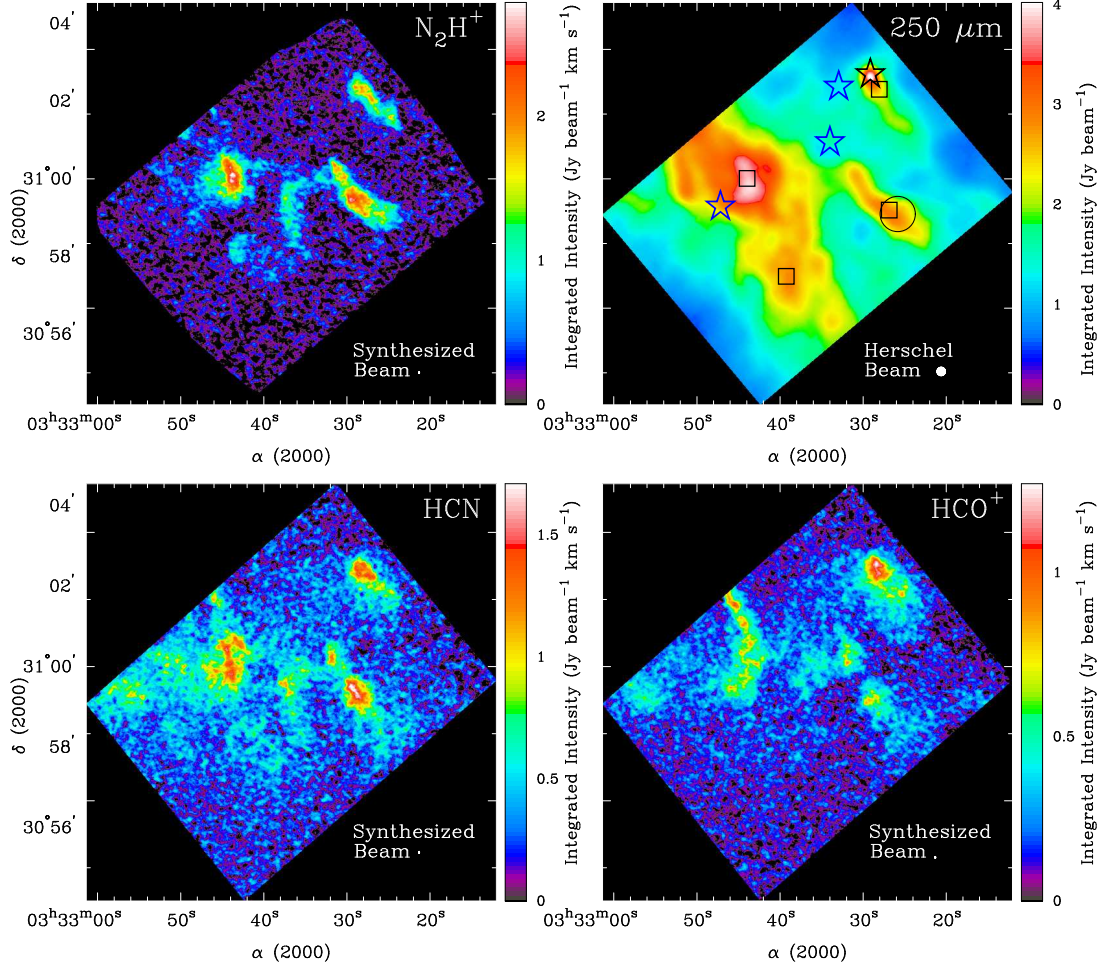


Figure 2.9: Same as Figure 2.5, but for the SW clumps zone. The most western YSO in this zone is a Class 0/I source, while the others are Class II sources (colored blue). Like Figure 2.7, since this zone does not have outflows, we included extra channels to capture the southwestern edge of the narrow filament (best seen in the HCO^+ map) that is redshifted by $\sim 1.5 \text{ km s}^{-1}$ from the rest of the Barnard 1 gas. The rms values of these N_2H^+ , HCN, and HCO^+ integrated intensity maps are 0.17, 0.12, and $0.08 \text{ Jy beam}^{-1} \text{ km s}^{-1}$, respectively.

$\tau(v)$, is modeled as:

$$\tau(v) = \tau \sum_{i=0}^7 C_i e^{-(v-V_{\text{lsr}}-v_i)^2/2\sigma^2}, \quad (2.2)$$

where τ is the total opacity of the emission, C_i is the weighted strength of the i^{th} hyperfine component such that the sum of component strength is unity, V_{lsr} is the centroid velocity of the observed emission, v_i is the rest velocity of the i^{th} hyperfine component, and σ is the velocity dispersion of each hyperfine component.

We assigned C_i and v_i according to the CDMS catalog listings on the Splatalogue webpage² – v_i was calculated from the listed ν_i using the rest frequency of our observations and the radio Doppler formula. A full observed spectrum is then modeled as

$$F(v) = \frac{2k\nu^2\Omega(v)}{c^2} \times T_{\text{ex}}(1 - e^{-\tau(v)}), \quad (2.3)$$

where k is Boltzmann’s constant, Ω is the synthesized beam area, v is the velocity of the observations, and T_{ex} is the excitation temperature.

The four free parameters for the fit are: V_{lsr} , σ , τ , and T_{ex} . We focus on the two kinematic parameters in the following sections. We do not address τ and T_{ex} because they are semi-degenerate, and breaking the degeneracy comes from an accurate understanding of the optical depth, which is beyond the scope of this initial analysis.

In the line fitting procedure, a model spectrum is first created from Equations 2.2 and 2.3 with ten times the velocity resolution of our observed data. We then bin this high-velocity-resolution model spectrum according to our observations’ velocity resolution, and compare that channelized model spectrum to an observed line. The fitting is done in IDL with the MPFIT package (Markwardt 2009), which performs non-linear least-squares minimization of the model fit to an observed spectrum—the outputs are the best-fit values and errors of the four free parameters. Figure 2.10 (top) shows the best-fit centroid velocity (V_{lsr}) and velocity dispersion (σ) maps for N_2H^+ . The pixels that have data values in these maps represent spectra that pass two robustness criteria: peak signal-to-noise greater than five, and integrated intensity greater than four times the rms of the N_2H^+ integrated intensity map.

The vast majority of the field only contains one resolved velocity component along each line-of-sight, and can be adequately fit with the procedure described

²<http://splatalogue.net>

above. However, we manually inspected the field and identified four locations with strong evidence for having two resolved velocity components. Three of those locations are marked with white rectangles in Figure 2.10, and are excluded from the analysis later in the chapter. The fourth location is the northeastern part of the narrow filament in the ridge zone; we manually inspected this region and removed the small number of pixels with confused spectra from the N_2H^+ maps.

The HCN and HCO^+ emission was fit in a similar way; the HCN line is made up of three resolvable hyperfine components, and HCO^+ has no hyperfine structure. Complications arose from outflows in the main core zone. For lines of sight complicated by outflows, we masked channels with outflow emission before fitting the spectral line representing the non-outflow gas. This was only done if the outflow emission was clearly defined in velocity space—we did not fit lines where outflow emission blended with emission nearest to the centroid velocity of the cloud. For HCN lines complicated by outflows, we only fit the highest frequency hyperfine component as it is more isolated in frequency/velocity space from the other two hyperfine components.

The middle and bottom rows of Figure 2.10 show the best-fit centroid velocity and velocity dispersion maps for HCN and HCO^+ , respectively. The integrated intensity criterion is the same as above. However, the peak signal-to-noise criterion is eight for HCN, and ten for HCO^+ , to account for increased uncertainty in fit values with decreasing number of hyperfine components. It is clear from the sparseness of the maps that there are far fewer HCN and HCO^+ regions strong enough to get reliable kinematic measurements compared to N_2H^+ . The HCO^+ and HCN data also show evidence for two velocity components in the same regions as N_2H^+ .

Analyzing all the details of these kinematic maps is beyond the scope of this analysis. However, some features to point out are as follows:

1. The most kinematic complexity exists in the main core zone—it has velocity gradients up to $\sim 10 \text{ km s}^{-1} \text{ pc}^{-1}$ (see Figure 2.11, left), and velocity dispersions ranging from 0.05 km s^{-1} all the way up to 0.5 km s^{-1} . In comparison, the gas structures in the ridge and SW clump zones show smaller variations in centroid velocity and velocity dispersion, and the velocity dispersions are consistently narrower than those found in the main core zone.

2. The narrow filament in the ridge zone, which can be seen in the all three kinematic maps, is redshifted by 1.5 km s^{-1} relative to the rest of the Barnard 1 emission. The mean velocity dispersion along the filament is 0.12 km s^{-1} , 0.16 km s^{-1} , and 0.20 km s^{-1} , for N_2H^+ , HCN, and HCO^+ , respectively. At an assumed kinetic temperature of 11 K based on Green Bank Telescope (GBT) data (Rosolowsky et al. 2008a), N_2H^+ and HCN are detecting subsonic gas motions and HCO^+ is approaching the sonic speed. The 1.5 km s^{-1} radial velocity of the filament gas relative to the bulk Barnard 1 gas suggests that it did not simply fragment from the main reservoir of gas in the region. It is possible that a nearby flow of material piled onto the larger filament and flowed around its western edge; this would cause a column density increase along that edge, thereby strengthening the molecular emission and causing redshift. One problem with this scenario is that we might expect more turbulent linewidths for gas involved in a colliding flow. However, this type of flow event could have happened long enough ago that gravity had time to collect the gas into the filament we now see. Another possibility is that we are viewing a sheet-like structure edge on.

3. The largest structure in the ridge zone has a velocity gradient perpendicular to its major axis (see Figure 2.11, right), which is a feature common in nu-

merical simulations of filament formation from planar converging, turbulent flows (Chen & Ostriker 2014). This type of velocity gradient is seen in several CLASSy filaments across our five regions; Serpens South examples are highlighted in Fernández-López et al. (2014), and we are preparing a paper linking these observations with the numerical simulations (Mundy et al., in preparation).

4. Upon close inspection, several regions of the cloud have well-organized N_2H^+ centroid velocity fields—for example, the dense gas around B1-c shows clear signatures of envelope rotation that was previously reported in Matthews et al. (2006). We show other examples of orderly velocity fields in Figure 2.12, coming from dense gas peaks that are spatially separated from other structures at low emission levels. One of the examples is the dense gas surrounding the newly detected compact continuum core within Per-emb 30, while the other two have no detected protostars at their center. This highlights the ability of CLASSy data to probe the small-scale velocity structure around cores in addition to the large-scale velocity structure across the entire region.
5. The best-fit values of the centroid velocity and velocity dispersion toward the B1-c core are consistent with the results published by Matthews et al. (2006). We detect the same evidence of a rotating N_2H^+ envelope in the centroid velocity map, and detect the same increased velocity dispersion along the HCO^+ and HCN outflow axis. Also, the N_2H^+ centroid velocities and velocity dispersions across the field match well with GBT NH_3 observations toward select dust cores (Rosolowsky et al. 2008a).

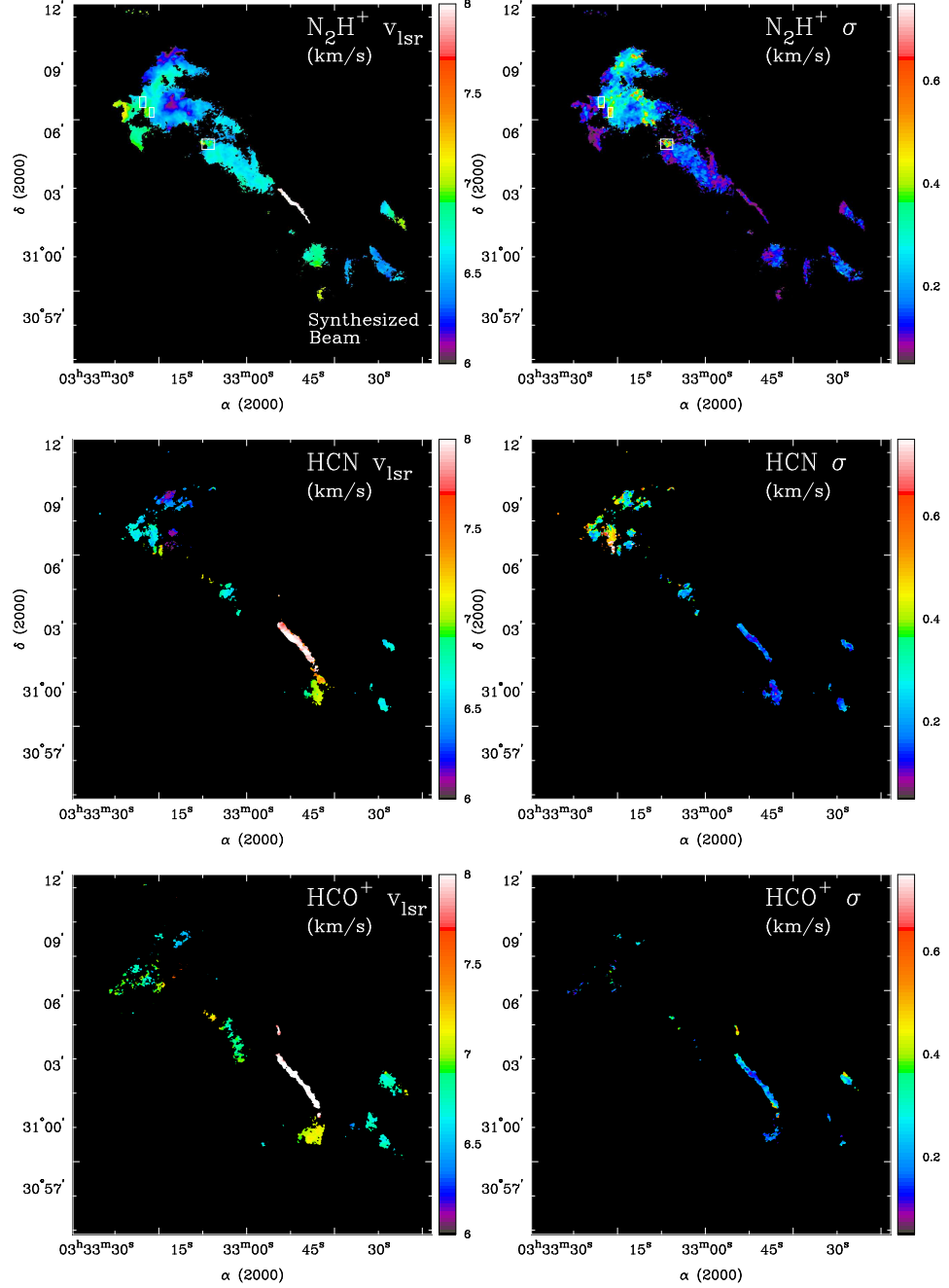


Figure 2.10: *Left:* Centroid velocity maps of N_2H^+ , HCN, and HCO^+ ($J = 1 \rightarrow 0$) emission, from top to bottom. *Right:* velocity dispersion maps of N_2H^+ , HCN, and HCO^+ ($J = 1 \rightarrow 0$) emission, from top to bottom. We masked these maps at different levels (see Section 2.5 text) to visualize only statistically robust kinematic results. The color scales are the same across molecules. The $\sim 7''$ synthesized beam is plotted as a very small white circle in the lower right corner of the N_2H^+ centroid velocity map. The small, white rectangles in the N_2H^+ maps identify regions that likely contain two velocity components along the-of-sight and are excluded from analysis later in the chapter.

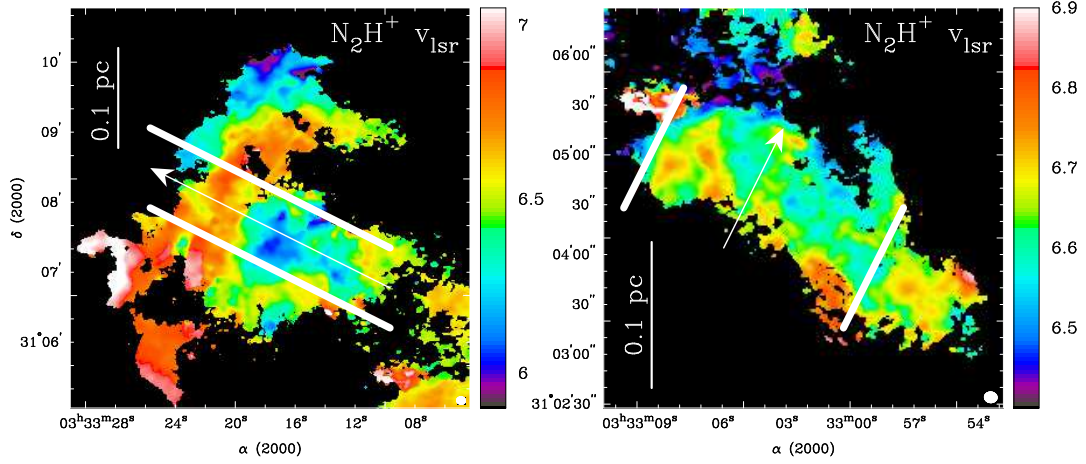


Figure 2.11: *Left*: Zoom-in of the main core zone centroid velocities presented in Figure 2.10, showing the complex velocity structure seen across this large area. The two solid lines enclose a region where we calculated the velocity gradient along the direction indicated by the arrow; we found a peak velocity gradient $\sim 10 \text{ km s}^{-1} \text{ pc}^{-1}$ along this direction. *Right*: Zoom-in of the ridge zone centroid velocities. Between the solid white bars, we measured an average velocity difference $\sim 0.3 \text{ km s}^{-1}$ perpendicular to the major axis of the filament. The synthesized beam is shown in the bottom right corner of each image.

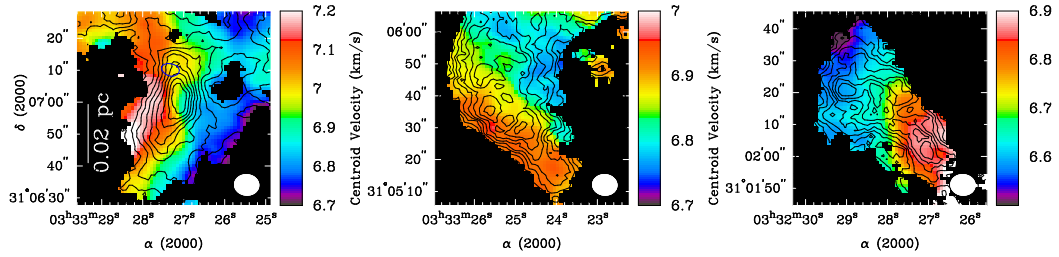


Figure 2.12: Zoom-in on three small-scale regions with orderly centroid velocity fields, highlighting CLASSy’s ability to resolve small-scale kinematic features, in addition to the large-scale structures seen in Figures 2.10 and 2.11. The color intensity is centroid velocity, and the contours are integrated intensity (contour levels in intervals of 10% of the image peak intensity). The left image shows the dense gas around the compact continuum core toward Per-emb 30 (the continuum core is identified with a single contour, colored blue). The center image is of gas south of Per-emb 30 in the main core zone, and the right image is of gas in the SW clumps zone. The synthesized beam is shown in the lower-right corner of each image, and a 0.02 pc scale bar is shown in the left image.

2.6 Dendrogram Analysis of N_2H^+

The previous two sections highlighted the dense gas morphology and kinematics across Barnard 1. Here we quantitatively analyze the N_2H^+ position-position-velocity cube to create a census of dense gas structures. We chose N_2H^+ over HCN and HCO^+ because it is our best tracer of the dense gas that is actively participating in star formation—it closely mimics the dust emission and is less affected by absorption from lower density foreground gas than HCN and HCO^+ .

Several methods exist for identifying structures in an image or cube, and the most appropriate method depends on the data and science goals. In Appendix A, we compare a widely used clump-finding algorithm to the dendrogram method, and conclude that a dendrogram analysis is more suitable for identifying resolved, dense gas structures in nearby molecular clouds. A dendrogram tracks emission structure as a function of isocontour level intensity, and represents the structure as a tree hierarchy made up of leaves and branches (Houllahan & Scalo 1992; Rosolowsky et al. 2008b; Goodman et al. 2009). Leaves are smaller-scale, brighter objects at the top of the emission hierarchy that do not break-up into further substructure, while branches are the larger-scale, fainter objects lower in the hierarchy that do break-up into substructure. The major benefit of a dendrogram analysis over a clump-finding analysis rests in this ability to represent all of the spatial scales in a dataset, as opposed to forcing all emission into distinct clumps associated with a local peak. See Appendix A and Goodman et al. (2009) for more discussion.

In Appendix B, we describe our modifications to the standard dendrogram algorithm that enable non-binary hierarchies, and we argue that non-binary dendrograms provide a more statistically meaningful way to represent hierarchical emission in the presence of noise. The important modifications include: 1) restricting branch-

ing to discrete steps, typically to integer values of the $1\text{-}\sigma$ sensitivity of the data when only analyzing a single map or data cube, instead of allowing branching at infinitely small intensity steps, and 2) using an algorithm that can cluster more than two objects into a single group instead of being restricted to clustering two objects at a time. These changes create an observable emission hierarchy within the noise limits of the data, and allow the quantification of the hierarchical complexity of a dendrogram using tree statistics. The rest of this section focuses on our non-binary dendrogram analysis of the N_2H^+ gas in Barnard 1.

2.6.1 The Non-binary Dendrogram

We used our new non-binary dendrogram code to identify gas structures traced by the isolated hyperfine component of N_2H^+ . We chose to use the isolated hyperfine component of N_2H^+ since it is sufficiently separated from other components in velocity space to prevent contaminating our object identification along the velocity axis. Before running the data through the dendrogram code, we binned the cube by two velocity channels to improve the signal-to-noise. No velocity information was lost since there are no lines of sight that contain two or more independent structures within 1.0 km s^{-1} of each other. We found that binning by two channels provides the most improvement to signal-to-noise without biasing the maps towards wide-line regions. The $1\text{-}\sigma$ sensitivity of the binned data cube is $0.094 \text{ Jy beam}^{-1}$.

Our non-binary dendrogram code takes the same input parameters as the standard IDL implementation discussed in Rosolowsky et al. (2008b). We ran it with the following critical inputs and parameters: (1) a masked cube containing all pixels greater than or equal to $4\text{-}\sigma$ intensity, along with adjacent pixels of at least $2.5\text{-}\sigma$ intensity, (2) a set of local maxima greater than or equal to all their neighbors in $10''$ by $10''$ by three channel (0.94 km s^{-1}) spatial-velocity pixels, (3) a requirement that

a local maximum must peak $2\text{-}\sigma$ above the intensity where it first merges with another local maximum for it to be considered a leaf (referred to as the “`minheight`” parameter in later sections), and (4) a requirement of at least three synthesized beams of spatial-velocity pixels for a leaf to be considered real (referred to as the “`minpixel`” parameter in later sections). The `minheight` and `minpixel` parameters act to prevent noise features from being identified as true dendrogram leaves. An additional input is used in the non-binary algorithm: branching steps restricted to integer values of the $1\text{-}\sigma$ sensitivity of the data (referred to as the “`stepsize`” parameter in later sections). The `stepsize` parameter sets the minimum branching step allowed in a non-binary dendrogram.

The non-binary dendrogram shown in Figure 2.13 contains 41 leaves and 13 branches. The vertical axis of the dendrogram represents the intensity range of the pixels belonging to a leaf or branch. The horizontal axis does not normally carry physical meaning, but in this case we arranged the leaves and branches according to zone. Figure 2.14 shows two-dimensional representations of all leaves overlaid on the N_2H^+ integrated intensity map; these representations were created by integrating over the velocity axis of the leaves and contouring the maximal RA-DEC extent of the integrated emission. The leaves that peak at least $6\text{-}\sigma$ in intensity above their first branch are colored green (leaves 10, 25, and 39). Leaf 25 is the strongest, with a peak intensity of $1.91 \text{ Jy beam}^{-1}$ (in the binned data cube), and represents the gas around B1-b. Leaf 39 is the next strongest at $1.77 \text{ Jy beam}^{-1}$, and represents gas around B1-c. Leaf 10 peaks at $1.04 \text{ Jy beam}^{-1}$, and represents gas around the newly detected compact continuum source within Per-emb 30. As a reminder that the identification of leaves and branches was done in three dimensions, Figure 2.15 shows five N_2H^+ velocity channels near the B1-b cores with the isocontours of leaves 24, 25, and 40, and branch 41, identified with distinct colors.

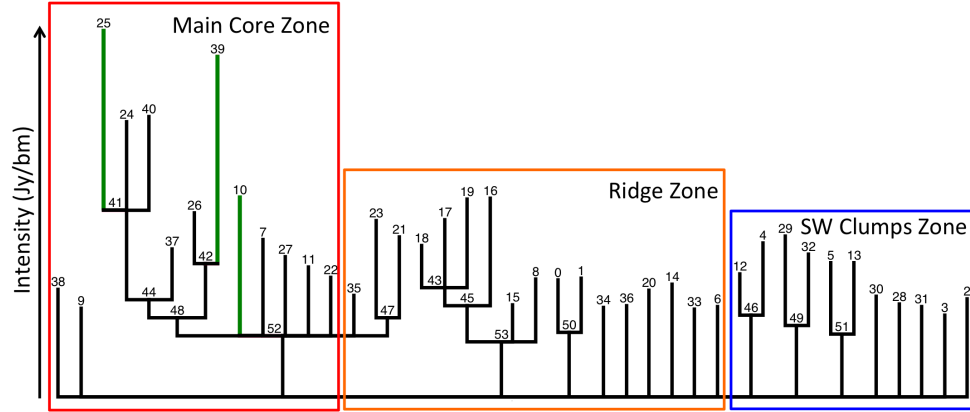


Figure 2.13: The non-binary dendrogram for Barnard 1 is shown; it represents the hierarchical structure of the N_2H^+ gas. There are 41 leaves (numbered 0 through 40), and 13 branches (numbered 41 through 53) on the dendrogram. The vertical axis represents the Jy beam^{-1} intensity for a given location within the gas hierarchy. Branching occurs in integer multiples of the $1\text{-}\sigma$ sensitivity of the binned data cube used in this analysis. The horizontal axis is ordered according to zone, though the order within a given zone has no physical meaning. Leaves 10, 25, and 39 (colored green) peak at least $6\text{-}\sigma$ above their first merge level.

We are using the $6\text{-}\sigma$ contrast criteria to highlight the strongest leaves before we are able to confidently discuss the virial boundedness of actual “cores” and “clumps”—defining bound cores requires accurate measurements of mass to go along with our high-resolution kinematic information, which is beyond the scope of this initial analysis. We chose a $6\text{-}\sigma$ contrast to highlight the gas in Barnard 1 that is located near existing compact continuum objects—this gas is likely bound. We will apply the same contrast cut to other CLASSy regions. While we cannot discuss boundedness of individual gas cores at this stage, we can discuss the properties of the strongest, highest-column density, dendrogram features and compare them to weaker features in the field. Leaves with $6\text{-}\sigma$ or greater contrast will be referred to as high-contrast leaves later in the chapter, and the rest of the leaves will be called low-contrast leaves.

The tree structure presented here captures the qualitative hierarchical nature of the dense gas in Barnard 1, but it does not give quantitative information about the

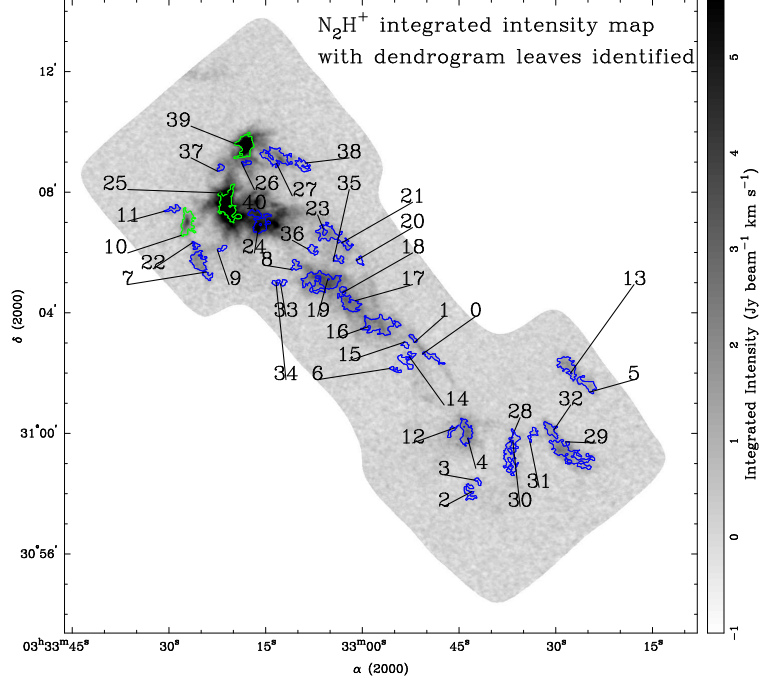


Figure 2.14: The N₂H⁺ integrated intensity map (Jy beam⁻¹ km s⁻¹) is shown in greyscale. The overplotted contours (green and blue) are two-dimensional representations of the three-dimensional (PPV) leaf structures found in Barnard 1. Green contours represent leaves with contrast greater than 6- σ . Each leaf is labeled with its number that can be referenced to Figure 2.13 and Table 2.5.

hierarchy or physical properties of the leaves and branches. Doing science with a dendrogram requires extracting tree statistics and physical properties of the leaves and branches, such as size, axis ratio, linewidth, mass, luminosity, etc. We present three simple tree statistics and the spatial and kinematic properties of leaves and branches in this chapter. In future papers, we will perform more detailed comparisons between dendrogram properties across multiple CLASSy regions.

2.6.2 Dendrogram Tree Statistics

Computation of tree statistics from a non-binary dendrogram is one method of quantifying a tree structure. Houllahan & Scalo (1992) were the first to develop tree statistics for the astronomy community in order to quantify the hierarchical

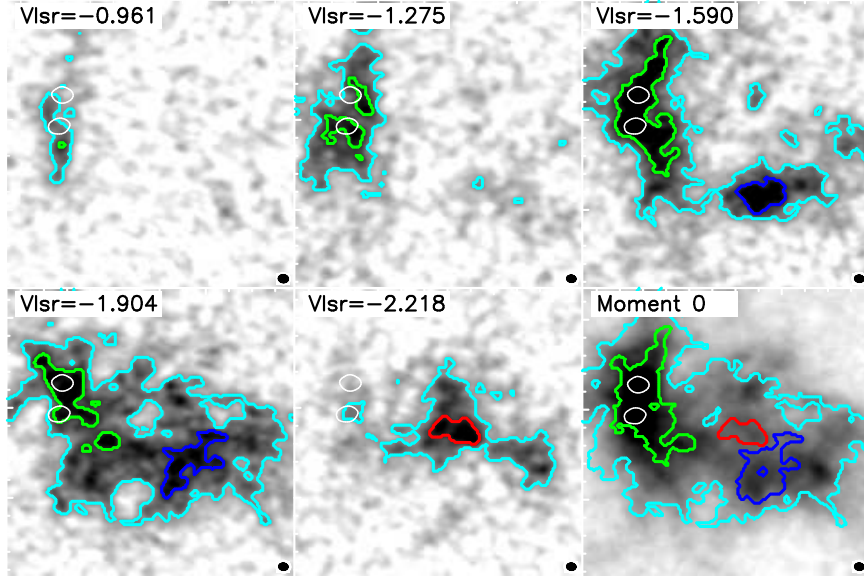


Figure 2.15: N_2H^+ emission surrounding the B1-b double core, viewed across five binned velocity channels used in the dendrogram analysis, and across the moment zero map. For the channel maps, the greyscale represents the intensity of emission (Jy beam^{-1}), and the colored contours (individually colored in the online version) represent the spatial extent of the dendrogram leaves and branches in that given channel. The single white contours in all maps represent the $4\text{-}\sigma$ detection level of the B1-b continuum sources. In the online version, leaf 25 is green, 40 is red, and 24 is blue, while branch 41 is cyan. For the moment zero map, the greyscale represents the integrated intensity of emission ($\text{Jy beam}^{-1} \text{ km s}^{-1}$), and the colored contours represent two-dimensional representations of the three-dimensional dendrogram structures seen in the channel maps.

nature of molecular cloud structure (see their discussion of “merged trees,” which are analogous to our non-binary trees). They describe several statistics that can be computed from non-binary trees; we describe three of the simplest statistics here.

The *maximum branching level* is the integer number of branching steps needed to reach the leaves at the top of the hierarchy. A region that has undergone a lot of hierarchical fragmentation will have more levels than a region that has not fragmented, or that has fragmented in a single step into several pieces with similar properties. Branching levels are defined upward from the base of the tree; the base (0 Jy beam^{-1} intensity) is considered level 0. An isolated leaf that sprouts

directly from the base is at level 0, while a leaf that grows from a branch one level above the base is at level 1. The maximum branching level in our Barnard 1 N_2H^+ dendrogram is level 4, where leaves 24, 25, and 40 merge together into branch 41 (see Figure 2.13). These leaves are in the main core zone, which is the only zone with detections of 3 mm compact continuum cores and Class 0/I YSOs. It is reasonable that the largest amount of fragmentation has occurred in the region with the most young star formation activity. That being said, the ridge zone and SW clumps zone have maximum branching levels of three and one, respectively, so we are dealing with small variations of this statistic within Barnard 1.

A related tree statistic is the *mean path length* of all segments in a dendrogram. The path length of a segment is defined as the number of branching steps required to go from a leaf to the bottom of the tree (there are as many path lengths in a dendrogram as there are leaves). For example, the path length of leaf 25 is four, while the path length of leaf 37 is three—the path length of leaf 30 is zero because it directly sprouts from the bottom of the tree. The mean path length in the whole Barnard 1 N_2H^+ dendrogram is 1.2 levels, while it is 2.0, 1.2, and 0.5 for the main core zone, ridge zone, and SW clumps zone, respectively. Again, it is logical that the main core zone, which is actively fragmenting into young stars, has the largest mean path length.

It is important to point out that these statistics would be different if we used the standard dendrogram algorithm instead of our non-binary one. The standard algorithm forces binary branching by introducing extra branching steps to ensure that only two objects merge at a time. For example, leaves 24, 25, and 40 would not all be allowed to merge into branch 41 even though that is what the data suggest is happening—leaves 24 and 25 would be merged into one branch, which would then be merged with leaf 40 into a second branch. This inflates the path length of leaves

24 and 25, and increases the maximum branching level of the tree. See Appendix B for more details about differences between the standard dendrogram algorithm and the new non-binary algorithm.

The third simple tree statistic is the *mean branching ratio* of all branches in a tree. The branching ratio for a single branch is defined as the number of substructures into which it fragments directly above it in the hierarchy. For example, the branching ratio of branch 41 is three, because it has three leaves directly above it. A very hierarchical region, where every object fragments into two nested objects, will have a mean branching ratio of 2, while a region that has fragmented in a single step into several pieces with similar properties will have a much larger mean branching ratio. The mean branching ratio in our Barnard 1 N₂H⁺ dendrogram is 3.9. We include the branching ratio for the base of the tree in this calculation, even though it is not explicitly defined with a branch number—this ensures that leaves that sprout directly from the base are factored in. (Note that the branching ratio above the tree base is always fixed at 2 for the standard dendrogram algorithm that forces binary branching.)

These simple statistics provide measures of the amount and type of fragmentation a given region has undergone; a region with a lot of hierarchical fragmentation will have more levels, a larger mean path length, and a smaller branching ratio, compared to a region that is just beginning to form strong overdensities. A caveat is that the absolute values of the branch statistics depend on algorithm parameters and choice of allowed branching steps (reminder that we restrict branching to intensity steps equal to integer values of the 1- σ sensitivity of the data instead of allowing branching at infinitely small intensity steps). However, the statistics can be compared across trees as a differential measurement if the same algorithm parameters and allowed branching steps are used; as pointed out by Houllahan & Scalo (1992), the power

of tree statistics is strongest when comparing regions with different star formation properties. We will compare the Barnard 1 tree statistics with the tree statistics of NGC 1333 and L1451 in Chapter 4 to explore whether the hierarchical complexity of dense gas represented by tree statistics correlates with the diversity of star formation activity in the western half of Perseus.

Another caveat arises from linking dendrogram hierarchical complexity to cloud fragmentation—tree statistics can be affected by projection effects. All observations suffer from projection effects when transforming the true position-position-position information of a molecular cloud to observable position-position-velocity information (for an in-depth discussion of projection effects in spectral line data, see Beaumont et al. 2013). Projection effects distort optically thick, space-filling emission more than optically thin emission concentrated in one part of the cloud. These effects are not overly concerning in our data because the isolated hyperfine component of N_2H^+ is optically thin, and the N_2H^+ emission is arising only from the densest parts of the cloud. If our data do suffer from projection effects, we assume that our large mapping areas create a big enough sample of dendrogram structures so that equal numbers of projection effects occur in each region we will compare.

2.6.3 Dendrogram Spatial Properties

The size of an object is one of its most fundamental properties, but defining the sizes of irregularly shaped objects in a uniform way is not trivial. This is one challenge of high-angular-resolution surveys of nearby molecular clouds—CLASSy resolves a rich morphology of structures with a range of irregular shapes.

When fitting for the size of a leaf or branch, we consider all pixels in its plane-of-sky footprint (as opposed to only considering the “onion-layer” emission of each individual branch, which is used to derive kinematic properties in the next section—

see Figures 2.16 and 2.17 for examples). We use the `regionprops` program in MATLAB to fit an ellipse to the integrated intensity footprint of each dendrogram object. All pixels are given equal weight so that the ellipse is preferentially fit to the largest scale of the object—this prevents strong emission at the center of an object from driving the fit towards a smaller scale. The fit is defined with an RA centroid, DEC centroid, major axis, minor axis, and position angle. The location, major axis, minor axis, and position angle are directly determined by the fit, and are listed in Columns 2–6 in Table 2.5. We do not report formal uncertainties on these values since the spatial properties of irregularly shaped objects are dependent on the chosen method, and we do not want to mislead the reader as to the “certainty” of these values.

To quantify the shape of an object, we use the axis ratio and filling factor of the fit (Columns 7 and 8 of Table 2.5). The axis ratio is defined as the ratio of the minor-to-major axis; a circular fit will have an axis ratio of one, and a highly elongated fit will have an axis ratio approaching zero. The filling factor is defined as the area of emission within the fitted ellipse divided by the area of the fitted ellipse; a circular object and an elliptical object will both have a filling factor near one, but an irregular object will likely have a filling factor much less than one, regardless of the axis ratio of the fitted ellipse. We lastly define an object size (Column 9 of Table 2.5) as the geometric mean of the major and minor axes. The values reported in Table 2.5 have been converted to parsecs, assuming a distance of 235 pc. Figure 2.16 shows example spatial property fitting results for leaves 26 and 39 and branch 42.

Histograms of the size, filling factor, and axis ratio for all leaves and branches are plotted in the top row of Figure 2.18. The trend in size is obvious—branches represent larger structures than the leaves that peak within them. Leaf sizes range

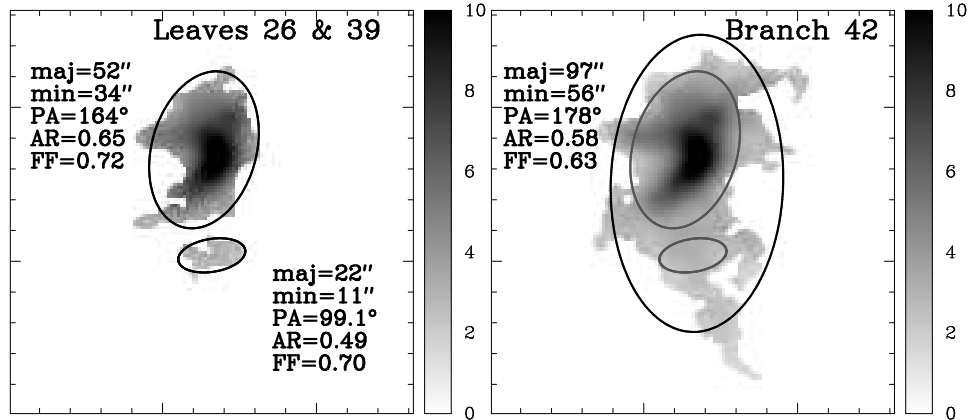


Figure 2.16: Example fits for the spatial properties of leaves and branches. The left panel shows the N_2H^+ integrated intensity ($\text{Jy beam}^{-1} \text{ km s}^{-1}$) within the two-dimensional footprints of leaves 26 and 39. We estimated the shape of these leaves with `regionprops` in MATLAB; the fits are shown with the solid black ellipses, and the fit parameters are listed. The axis ratio (AR) is the ratio of minor-to-major axis, and the filling factor (FF) is the number of greyscale pixels within the fitted ellipse divided by the total number of pixels within the ellipse. The right panel shows the N_2H^+ integrated intensity within the footprint of branch 42, with its ellipse fit shown in black, and the ellipse fits of the leaves in grey. When fitting for the size of a branch, we include emission from the branch itself and all objects above it in the dendrogram—this results in a filled-in integrated intensity map for the fitting process, whereas using the emission from a single branch would give an “onion-layer”-like structure.

from about 0.01 pc to 0.07 pc, while branch sizes range from about 0.08 pc to 0.34 pc. The high-contrast leaves are larger than the majority of low-contrast leaves. Nearly 25% of leaves have filling factors greater than 0.8, while all branches have filling factors less than 0.8. This shows that leaves are better fit as regular shapes compared to branches, but there is still a large population of irregularly-shaped leaves that are far from round or filamentary. The objects with the maximum axis ratios (leaf 14 and branch 46) are paired with filling factors below 0.8, indicating that they are not regularly shaped spheroids as the axis ratio alone might be interpreted. There are no obvious distinctions between high-contrast and low-contrast leaves in filling factor or axis ratio.

2.6.4 Dendrogram Kinematic Properties

One strength of CLASSy data is the kinematic information across a wide range of spatial scales. We can use the integrated intensity footprints of the dendrogram objects (leaf footprints shown in Figure 2.14) in combination with the centroid velocity and velocity dispersion maps in Figure 2.10 to determine the kinematic properties of leaves and branches. The four properties in Table 2.5 that we focus on are: the mean and rms centroid velocity ($\langle V_{\text{lsr}} \rangle$ and ΔV_{lsr} , respectively), and the mean and rms velocity dispersion ($\langle \sigma \rangle$ and $\Delta \sigma$, respectively).

We illustrate how we derive these properties for leaves and branches in Figure 2.17. For leaves, we mask the full N_2H^+ V_{lsr} and σ maps with the integrated intensity footprint of each leaf, and calculate the error weighted mean and standard deviation of the masked pixels within the masked footprints. For branches, we mask the full N_2H^+ V_{lsr} and σ maps with the integrated intensity footprint of each branch, excluding pixels associated with any leaves or branches inside the branch footprint. We calculate the error weighted mean and standard deviation of the remaining pixels belonging exclusively to the branch. By excluding leaf pixels, we are calculating the kinematic properties of branches only at the larger spatial scales that are not captured by the leaves within them—this method allows us to parse kinematics across different spatial scales, which enables a size-linewidth analysis in the next section. We only report kinematic properties of leaves and branches in Table 2.5 that have three or more synthesized beams worth of kinematic pixels; a low signal-to-noise feature may be strong enough to be selected as a dendrogram object, but still too weak to have enough kinematic data points based on our line fitting criteria discussed in Section 2.5.

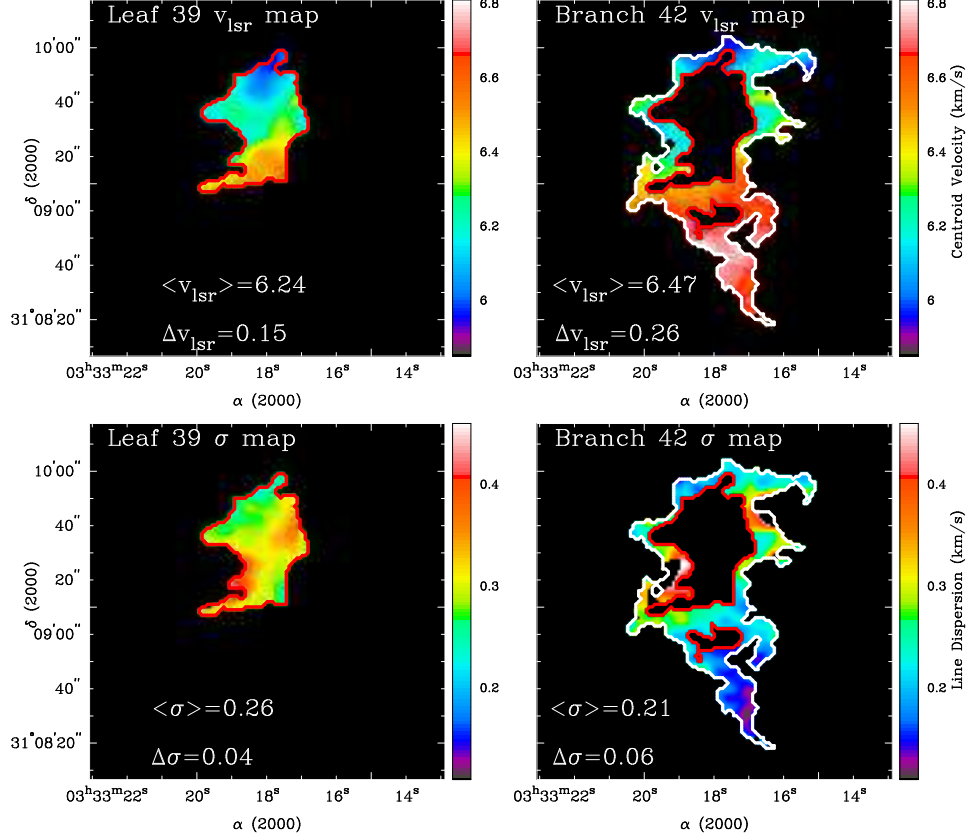


Figure 2.17: Examples of how we calculate the kinematic properties of leaves and branches, using the leaf emission towards B1-c, and the branch emission directly surrounding it. *Upper left:* The integrated intensity footprint of leaf 39 is represented by the contour (colored red). The best fit centroid velocities (V_{lsr}) from Figure 2.10 are shown within that contour; to find the mean centroid velocity ($\langle V_{\text{lsr}} \rangle$) for leaf 39, we calculate the weighted mean of those pixels (weighing according to fit error at each pixel), and to find the rms centroid velocity (ΔV_{lsr}) for leaf 39, we calculate the weighted standard deviation of those pixels. *Lower left:* We show the best fit velocity dispersions (σ , not FWHM) from Figure 2.10 within the contour, and calculate the weighted mean velocity dispersion ($\langle \sigma \rangle$) and rms velocity dispersion ($\Delta \sigma$) as we did for the V_{lsr} values in the upper left. *Upper right:* The integrated intensity footprint of branch 42 is represented by the outer contour (colored white), while those of leaf 39 and leaf 26 are represented by the inner contours (colored red). The best fit V_{lsr} from Figure 2.10 are shown only between the outer and inner contours. We are using information only at the branch spatial scales to calculate the kinematic properties of the branch—we exclude the kinematic properties of the leaves within the branch. As for the upper left figure, to find $\langle V_{\text{lsr}} \rangle$ for branch 42, we calculate the weighted mean of the shown pixels, and to find ΔV_{lsr} , we calculate the weighted standard deviation of the shown pixels. *Lower right:* The best fit σ for branch 42 are shown between the outer and inner contours.

Histograms of $\langle V_{\text{lsr}} \rangle$, ΔV_{lsr} , and $\langle \sigma \rangle$ are plotted in the bottom row of Figure 2.18. The distribution of $\langle V_{\text{lsr}} \rangle$ shows that most of the gas in Barnard 1 is near 6.5 km s^{-1} , while the gas from leaves 0 and 1 and branch 50 (representing the narrow filament in the ridge zone) is strongly redshifted.

There is a clear offset in the distribution of ΔV_{lsr} between leaves and branches: the majority of branches, which represent the largest objects, have larger ΔV_{lsr} than the smaller leaves. There are two effects that are likely causing this trend. The first effect is from organized velocity field motions (e.g., indicative of rotation or feedback from outflows) that exist towards a leaf and its surrounding branch. For example, the V_{lsr} field for the B1-c leaf and parent branch can be seen in Figure 2.17. The branch that directly surrounds B1-c has a larger ΔV_{lsr} compared to the B1-c leaf due to larger differences between the redshifted and blueshifted velocities in the rotating branch. However, the majority of leaf-branch pairs do not exhibit matching, well-ordered velocity fields. Therefore, turbulence is the second likely explanation for this trend. Turbulence has the property of causing scale-dependent spatial correlations within a velocity field—points separated by larger distances will have larger rms velocity differences between them than will points that are closer together (McKee & Ostriker 2007), meaning that branches will have larger ΔV_{lsr} values than leaves.

The high-contrast leaves are preferentially shifted to larger ΔV_{lsr} relative to the low-contrast leaves. The high-contrast leaves all have known protostellar objects within them, so their gas motions are most likely dominated by infall, rotation, or feedback from outflows, all of which increase the variation in the velocity field. The low-contrast leaves with the largest ΔV_{lsr} tend to have more organized centroid velocity patterns (manifested as gradients) than the low-contrast leaves with the smallest ΔV_{lsr} , indicating that they may represent gas around pre-stellar cores that

are more likely to form stars in the future.

The distribution of $\langle\sigma\rangle$ differs from the distribution of ΔV_{lsr} . The high-contrast leaves representing the gas around B1-b and B1-c have the largest $\langle\sigma\rangle$ in the entire field, and the majority of branches have $\langle\sigma\rangle$ that are similar to those of the majority of leaves. We would naively expect that if the branches represent the largest objects projected on the plane of the sky, then they should also represent the most extended objects along our lines of sight, and should therefore have the largest velocity dispersions (assuming velocity dispersion scales proportionally with length-scale, which is the case for a turbulent cloud; McKee & Ostriker 2007). We explore these results in more detail in Section 2.7, where we compare the sizes of structures to their ΔV_{lsr} and $\langle\sigma\rangle$ in order to probe the physical and turbulent nature of Barnard 1.

Table 2.5. N₂H⁺ Dendrogram Leaf and Branch Properties

No.	RA (h:m:s)	DEC (°:':")	Maj. Axis (")	Min. Axis (")	PA (°)	Axis Ratio	Filling Factor	Size (pc)	$\langle V_{\text{lsr}} \rangle$ (km s ⁻¹)	ΔV_{lsr} (km s ⁻¹)	$\langle \sigma \rangle$ (km s ⁻¹)	$\Delta \sigma$ (km s ⁻¹)	Pk. Int. (Jy beam ⁻¹)	Contrast (15)	Level (16)
(1)	(2)	(3)	(4)	(5)	(6)	(7)	(8)	(9)	(10)	(11)	(12)	(13)	(14)	(15)	(16)
Leaves															
0	03:32:49.1	+31:02:31.9	49.6	12.4	61.8	0.25	0.60	0.028	7.99(1)	0.02(0)	0.08(2)	0.04(1)	0.61	2.9	1
1	03:32:52.1	+31:03:09.3	22.9	8.3	41.1	0.36	0.84	0.016	7.98(1)	0.03(1)	0.08(1)	0.01(1)	0.62	3.0	1
2	03:32:43.4	+30:58:02.4	37.6	22.1	18.1	0.59	0.61	0.033	7.06(1)	0.02(1)	0.08(1)	0.01(0)	0.51	2.9	0
3	03:32:42.1	+30:58:24.3	19.9	9.1	36.7	0.46	0.82	0.015	0.42	2.0	0
4	03:32:43.9	+31:00:02.4	54.7	23.9	4.8	0.44	0.76	0.041	6.86(1)	0.03(0)	0.14(0)	0.02(0)	0.80	4.0	1
5	03:32:25.1	+31:01:36.9	48.5	20.0	55.1	0.41	0.68	0.035	6.99(1)	0.03(1)	0.12(1)	0.02(1)	0.70	4.0	1
6	03:32:54.9	+31:02:06.7	27.9	9.1	68.5	0.33	0.72	0.018	0.47	2.5	0
7	03:33:25.1	+31:05:36.7	66.7	27.8	30.7	0.42	0.67	0.049	6.88(1)	0.05(1)	0.07(0)	0.01(0)	0.82	5.3	1
8	03:33:10.3	+31:05:34.2	23.6	19.6	17.4	0.83	0.75	0.025	0.62	3.5	1
9	03:33:21.7	+31:06:07.8	22.9	8.9	118.2	0.39	0.82	0.016	0.46	2.4	0
10	03:33:27.1	+31:06:58.5	55.3	27.1	174.6	0.49	0.71	0.044	6.97(2)	0.10(1)	0.12(1)	0.03(0)	1.04	7.7	1
11	03:33:29.3	+31:07:26.1	32.5	13.4	101.7	0.41	0.68	0.024	7.02(1)	0.03(1)	0.10(1)	0.01(0)	0.68	3.8	1
12	03:32:46.2	+31:00:04.5	31.3	11.5	144.7	0.37	0.65	0.022	6.71(1)	0.03(1)	0.09(0)	0.01(0)	0.64	2.3	1
13	03:32:28.2	+31:02:13.1	53.1	27.7	37.2	0.52	0.74	0.044	6.66(2)	0.10(1)	0.10(1)	0.02(0)	0.70	4.0	1
14	03:32:53.1	+31:02:26.4	36.5	35.5	48.3	0.97	0.60	0.041	0.59	3.8	0
15	03:32:53.3	+31:02:55.7	16.6	11.4	55.9	0.69	0.83	0.016	0.48	2.1	1
16	03:32:57.3	+31:03:35.4	72.4	36.0	89.5	0.50	0.67	0.058	6.67(1)	0.04(0)	0.09(1)	0.03(0)	1.03	5.9	2
17	03:33:02.0	+31:04:18.4	49.0	26.2	55.7	0.53	0.72	0.041	6.61(1)	0.03(0)	0.15(0)	0.02(0)	0.92	3.8	3
18	03:33:03.0	+31:04:45.0	17.1	13.9	13.9	0.81	0.86	0.018	6.62(1)	0.02(1)	0.14(1)	0.01(0)	0.79	2.3	3
19	03:33:06.4	+31:05:02.2	80.3	40.1	88.8	0.50	0.67	0.065	6.64(1)	0.04(1)	0.13(1)	0.04(0)	1.03	4.9	3
20	03:33:00.3	+31:05:43.4	19.3	13.2	23.7	0.68	0.82	0.018	0.56	3.4	0
21	03:33:02.4	+31:06:15.5	25.8	17.0	38.6	0.66	0.68	0.024	6.67(1)	0.03(1)	0.13(1)	0.03(1)	0.83	4.5	2
22	03:33:25.9	+31:06:13.5	17.7	14.5	33.4	0.82	0.73	0.018	6.78(1)	0.02(1)	0.08(1)	0.01(1)	0.62	3.2	1
23	03:33:05.3	+31:06:38.3	51.4	33.5	69.5	0.65	0.60	0.047	6.60(1)	0.03(0)	0.11(0)	0.02(0)	0.92	5.4	2
24	03:33:15.7	+31:06:56.4	45.2	26.9	142.3	0.60	0.71	0.040	6.47(2)	0.10(2)	0.19(1)	0.03(0)	1.44	4.9	4
25	03:33:20.8	+31:07:33.0	72.7	38.7	11.4	0.53	0.58	0.060	6.62(2)	0.11(1)	0.29(1)	0.05(1)	1.91	9.9	4
26	03:33:18.0	+31:08:57.9	22.0	10.7	99.1	0.49	0.70	0.017	6.66(2)	0.03(1)	0.18(1)	0.02(1)	0.96	2.8	3
27	03:33:13.4	+31:09:10.2	61.2	32.8	73.1	0.54	0.66	0.051	6.51(1)	0.07(1)	0.17(1)	0.03(0)	0.73	4.4	1
28	03:32:37.1	+30:59:10.1	69.4	27.3	3.8	0.39	0.61	0.050	6.47(1)	0.04(1)	0.11(0)	0.02(0)	0.48	2.6	0
29	03:32:27.7	+30:59:18.2	101.8	34.5	59.8	0.34	0.59	0.068	6.44(1)	0.08(1)	0.16(0)	0.03(0)	0.84	5.0	1
30	03:32:36.4	+30:59:51.1	29.1	18.9	13.2	0.65	0.67	0.027	0.52	3.0	0
31	03:32:33.6	+30:59:59.1	32.0	15.4	151.7	0.48	0.58	0.025	0.47	2.5	0
32	03:32:30.8	+31:00:07.1	39.6	18.7	38.9	0.47	0.73	0.031	6.41(1)	0.04(1)	0.11(1)	0.03(0)	0.75	4.0	1
33	03:33:12.2	+31:04:59.9	15.4	10.3	144.5	0.67	0.87	0.014	0.46	2.3	0

Table 2.5 (cont'd)

No.	RA (h:m:s)	DEC (°:':")	Maj. Axis (")	Min. Axis (")	PA (°)	Axis Ratio	Filling Factor	Size (pc)	$\langle V_{\text{lsr}} \rangle$ (km s ⁻¹)	ΔV_{lsr} (km s ⁻¹)	$\langle \sigma \rangle$ (km s ⁻¹)	$\Delta \sigma$ (km s ⁻¹)	Pk. Int. (Jy beam ⁻¹)	Contrast (15)	Level (16)
(1)	(2)	(3)	(4)	(5)	(6)	(7)	(8)	(9)	(10)	(11)	(12)	(13)	(14)	(15)	(16)
34	03:33:13.4	+31:04:59.9	17.2	11.7	102.1	0.68	0.90	0.016	0.47	2.5	0
35	03:33:03.6	+31:05:46.4	25.6	14.7	75.3	0.57	0.72	0.022	6.42(2)	0.03(1)	0.13(1)	0.03(1)	0.53	2.2	1
36	03:33:07.7	+31:06:05.4	24.4	16.5	39.8	0.68	0.75	0.023	0.48	2.6	0
37	03:33:22.0	+31:08:53.6	16.5	13.2	139.6	0.80	0.87	0.017	6.32(2)	0.03(1)	0.14(1)	0.01(0)	0.77	2.8	3
38	03:33:09.2	+31:08:53.3	34.7	19.7	52.5	0.57	0.75	0.030	6.46(1)	0.03(1)	0.13(2)	0.04(1)	0.56	3.5	0
39	03:33:18.2	+31:09:32.2	52.1	34.0	164.4	0.65	0.72	0.048	6.24(3)	0.15(2)	0.26(1)	0.04(1)	1.77	11.5	3
40	03:33:16.7	+31:07:17.3	29.1	13.7	79.2	0.47	0.87	0.023	6.11(1)	0.04(1)	0.15(1)	0.02(0)	1.46	5.2	4
Branches															
41	03:33:18.2	+31:07:20.6	178.0	103.1	70.6	0.58	0.66	0.154	6.45(2)	0.24(1)	0.21(0)	0.06(0)	0.97	...	3
42	03:33:17.9	+31:09:21.3	96.6	56.0	178.0	0.58	0.63	0.084	6.47(4)	0.26(3)	0.21(1)	0.06(1)	0.69	...	2
43	03:33:04.6	+31:04:45.5	153.5	55.3	60.5	0.36	0.59	0.105	6.64(1)	0.04(0)	0.14(1)	0.04(0)	0.57	...	2
44	03:33:18.1	+31:07:23.5	197.6	116.9	67.0	0.59	0.68	0.173	6.51(2)	0.17(1)	0.17(1)	0.05(0)	0.51	...	2
45	03:33:01.9	+31:04:23.6	249.6	84.1	55.6	0.34	0.69	0.165	6.63(1)	0.06(0)	0.12(0)	0.04(0)	0.47	...	1
46	03:32:44.5	+31:00:00.4	79.2	75.1	81.4	0.95	0.76	0.088	6.80(1)	0.07(1)	0.12(0)	0.03(0)	0.43	...	0
47	03:33:04.9	+31:06:38.4	107.1	38.1	50.3	0.36	0.63	0.073	6.59(1)	0.06(1)	0.12(1)	0.03(1)	0.41	...	1
48	03:33:17.9	+31:07:47.8	237.1	177.5	17.5	0.75	0.64	0.234	6.54(2)	0.24(2)	0.16(1)	0.06(0)	0.41	...	1
49	03:32:28.3	+30:59:29.1	148.3	47.8	45.1	0.32	0.69	0.096	6.44(1)	0.07(1)	0.14(1)	0.04(0)	0.37	...	0
50	03:32:46.4	+31:02:45.5	103.4	18.9	47.8	0.18	0.56	0.050	7.99(2)	0.07(1)	0.12(4)	0.13(3)	0.34	...	0
51	03:32:27.0	+31:01:58.4	115.7	38.2	47.6	0.33	0.63	0.076	6.70(5)	0.17(4)	0.11(1)	0.03(1)	0.33	...	0
52	03:33:17.1	+31:07:34.2	324.8	267.3	73.1	0.82	0.50	0.336	6.67(2)	0.23(1)	0.12(0)	0.05(0)	0.32	...	0
53	03:33:01.8	+31:04:21.9	274.0	90.2	54.4	0.33	0.72	0.179	6.63(2)	0.10(1)	0.12(1)	0.04(0)	0.29	...	0

Note. — (2)–(6) The position, major axis, minor axis, and position angle were determined from `regionprops` in MATLAB. We do not report formal uncertainties of these values since the spatial properties of irregularly shaped objects is dependent on the chosen method.

(7) Axis ratio, defined as the ratio of the minor axis to the major axis.

(8) Filling factor, defined as the area of the leaf or branch inscribed within the fitted ellipse, divided by the area of the fitted ellipse.

(9) Size, defined as the geometric mean of the major and minor axes, for an assumed distance of 235 pc.

(10) The weighted mean V_{lsr} of all fitted values within a leaf or branch. Weights are determined from the statistical uncertainties reported by the IDL MPFIT program. The error in the mean is reported in parentheses as the uncertainty in the last digit. It was computed as the standard error of the mean, $\Delta V_{\text{lsr}}/\sqrt{N}$, where ΔV_{lsr} is the value in Column 11 and N is the number of beams' worth of pixels within a given object. We report kinematic properties only for objects that have at least three synthesized beams' worth of kinematic pixels.

(11) The weighted standard deviation of all fitted V_{lsr} values within a leaf or branch. The error was computed as the standard error of the standard deviation, $\Delta V_{\text{lsr}}/\sqrt{2(N-1)}$, assuming the sample of beams was drawn from a larger sample with a Gaussian velocity distribution.

(12) The weighted mean velocity dispersion of all fitted values within a leaf or branch. The error was computed as the standard error of the mean, $\Delta \sigma/\sqrt{N}$.

(13) The weighted standard deviation of all fitted velocity dispersion values within a leaf or branch. The error was computed as the standard error of the standard deviation, $\Delta \sigma/\sqrt{2(N-1)}$.

(14) For a leaf, this is the peak intensity measured in a single channel of our 2-channel binned dataset used in the dendrogram analysis. For a branch, this is the intensity level where the structures above it merge together.

(15) "Contrast" is defined as the difference between the peak intensity of a leaf and the height of its closest branch in the dendrogram, divided by the 1- σ sensitivity of the data.

(16) The branching level in the dendrogram. For example, the base of the tree is level 0, so an isolated leaf that grows directly from the base is considered to be at level 0. A leaf that grows from a branch one level above the base will be at level 1, etc.

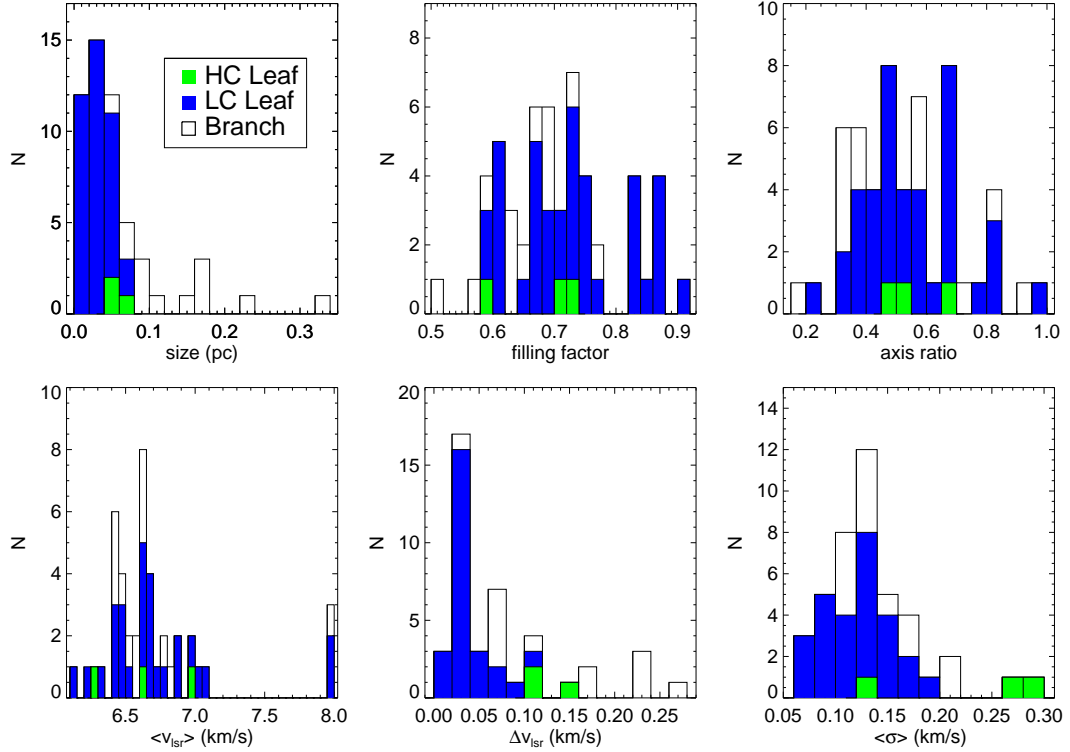


Figure 2.18: Histograms of dendrogram leaf and branch properties. High-contrast (HC) leaves, above $6\text{-}\sigma$ contrast, are represented by green; low-contrast (LC) leaves, below $6\text{-}\sigma$ contrast, are represented by blue; branches are represented by white. See the text in Sections 2.6.3 and 2.6.4 for a discussion of trends seen in these histograms.

2.7 A Connection Between Size-Linewidth Relations and Cloud Structure

This chapter presented the morphology and kinematics of the dense gas in Barnard 1, along with a dendrogram analysis of the N_2H^+ emission. We conclude with an analysis of the spatial and kinematic properties of dendrogram structures and what they can tell us about the turbulent and physical nature of the Barnard 1 region.

A turbulent cloud will have scale-dependent spatial correlations of its velocity field that take on power law forms over a wide enough range of spatial scales

(McKee & Ostriker 2007). Size-linewidth relations are commonly used to probe turbulence; there have been numerous studies of observed and simulated molecular clouds using a wide array of observational and statistical techniques, such as correlation plots (Larson 1981; Solomon et al. 1987), structure function and auto-correlation analysis (Miesch & Bally 1994; Ossenkopf & Mac Low 2002), principal component analysis (Brunt & Mac Low 2004; Heyer & Brunt 2004), and dendrograms (Rosolowsky et al. 2008b), to name a few. The overall result is that most galactic molecular clouds exhibit power-law scaling relations consistent with turbulence in a compressible medium, where supersonic motions and overlapping shocks are important (so-called “Burgers turbulence”). It is well accepted from these analyses that molecular clouds are turbulent, but there are new insights that can be gained by using size-linewidth relations derived from high angular resolution observations.

2.7.1 Total Linewidth of Dendrogram Structures

Our dendrogram analysis identified N_2H^+ structures in the Barnard 1 hierarchy as either leaves or branches, and we evaluated the size and kinematic properties of those objects in Section 2.6. Since the spatial scales of dendrogram structures in Barnard 1 range from ~ 0.01 – 0.3 pc, we can utilize these structures to investigate the turbulent properties of the cloud. Before discussing size-linewidth relations that use the full angular resolution of our observations, it is useful to consider a relation that uses the “total” linewidth of each dendrogram structure—this relation can be compared with classical size-linewidth relations from Larson (1981) and Solomon et al. (1987), in which the detailed kinematic variation within individual clouds was not resolved. We calculated a total linewidth for each structure by summing all the spectra assigned to it and fitting the velocity dispersion of the resulting spectrum (the σ , not FWHM,

of the line); for a visualization, see Figure 2.17, which shows the kinematic maps of an example leaf and branch. In that figure, all the spectra within the red contour of leaf 39, and all the spectra within the white contours of branch 42 (including the leaf emission), are summed to calculate the total linewidths of those respective structures.

Figure 2.19 shows plots of projected size versus total linewidth for all dendrogram structures that have kinematic values listed in Table 2.5, excluding the objects associated with the peculiar narrow filament in the ridge zone (leaves 0 and 1, branch 50). We separate structures in the main core zone (MCZ) from structures in the ridge and SW clumps zones (RSWZ) because the main core zone has a cluster of protostars driving outflows. Keeping the zones separate allows us to see whether or not they have different turbulent or physical properties. We also separately identify the few structures surrounding compact continuum cores, since their non-thermal gas motions are likely influenced by their central source.

The data in Figure 2.19 are scattered and could be fit by several functions. However, there does appear to be variation of total linewidth with size in both zones, with the linewidth varying more strongly with size in the MCZ. If we use a single power-law fit, the MCZ correlation is best fit with a slope of 0.37 ± 0.08 , and the RSWZ correlation slope is 0.16 ± 0.06 . The steeper slope in the MCZ could be due to outflows adding energy to the turbulence at these scales. The best-fit slope from the MCZ is consistent with the result (Larson 1981) that clouds ranging in size from 0.1 to 100 pc have a power-law slope of 0.38. However, we are probing the scaling relation across much smaller spatial scales than has typically been done, and unlike previous studies, we are using high-density molecular tracers that are sensitive to non-thermal motions near the sonic scale of the cloud. Therefore, directly comparing our results to studies that used larger scales and lower-density gas tracers, such as

^{12}CO , should be considered with caution.

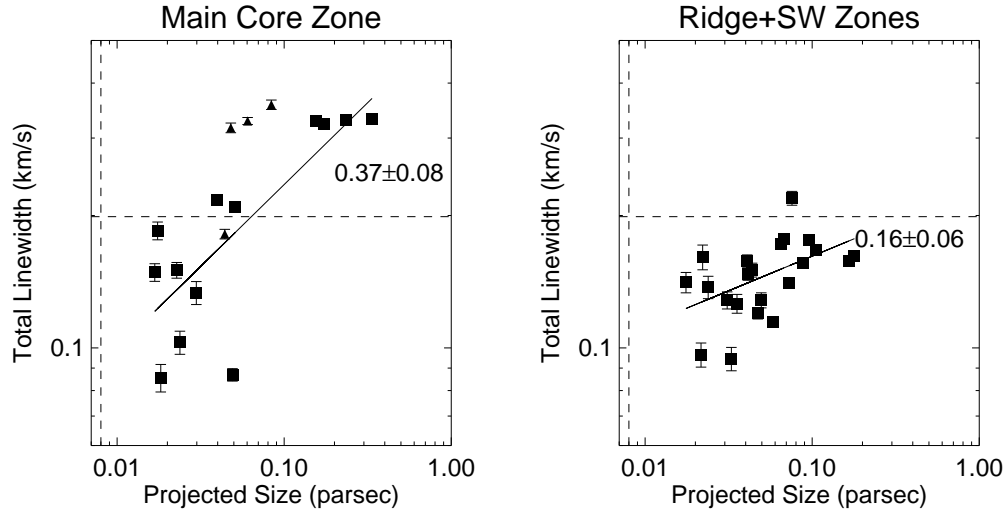


Figure 2.19: Scaling relations between projected structure size and total linewidth for the main core zone and the combined ridge and SW clumps zones. The projected size for each dendrogram structure is defined as the geometric mean of its best-fit major and minor axes. The majority of structures are labeled with squares, while the three leaves toward the three strongest compact continuum detections in main core zone are marked with triangles, along with the branch directly surrounding the B1-c leaf. The solid line represents a single power-law fit to the square points. The horizontal line represents the typical thermal speed for H_2 at gas kinetic temperatures near 11 K. The vertical line represents our spatial resolution of ~ 0.008 pc.

2.7.2 Resolved Linewidths of Dendrogram Structures

We have two kinematic measurements of leaves and branches in Table 2.5 that use the full angular resolution of our dataset—they complement the total linewidth and enable a different type of size-linewidth analysis. The first measurement is the V_{lsr} variation, ΔV_{lsr} . For a leaf or branch of size L , $\Delta V_{\text{lsr}}(L)$ is computed by measuring the rms variation of the (beam-scale) centroid velocity over the whole structure. The second measurement is the mean non-thermal velocity dispersion, $\langle \sigma \rangle_{\text{nt}}$. To calculate $\langle \sigma \rangle_{\text{nt}}$ from $\langle \sigma \rangle$ in Table 2.5, we remove the thermal velocity dispersion, σ_{th} , of 11 K N_2H^+ gas, which is the typical gas kinetic temperature across the entire

Barnard 1 region (Rosolowsky et al. 2008a): $\langle\sigma\rangle_{\text{nt}} = \sqrt{\langle\sigma\rangle^2 - \sigma_{\text{th}}^2}$. Recall that $\langle\sigma\rangle$ for a structure is defined by averaging all the individual velocity dispersions over the structure; each individual pointing captures the velocity dispersion along the line-of-sight for a given beam-width.

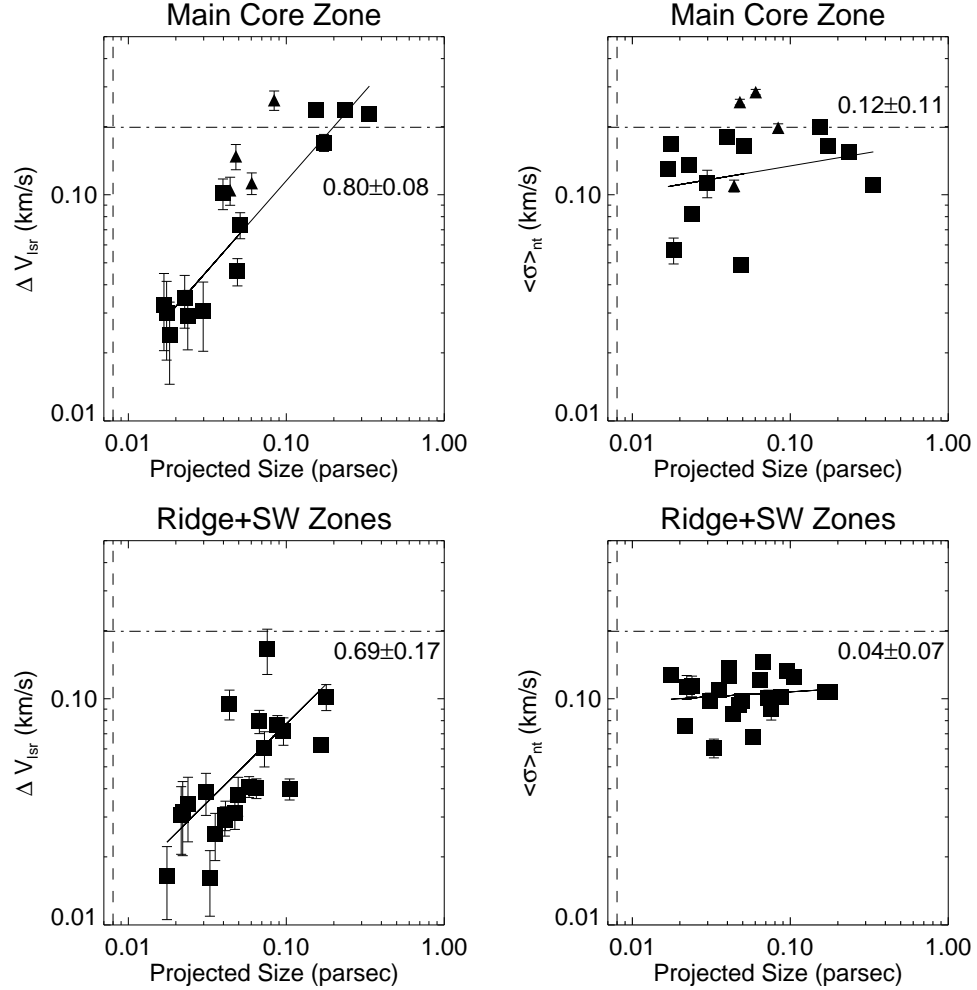


Figure 2.20: *Left*: Scaling relations between projected structure size and V_{lsr} variation (ΔV_{lsr}) for the main core zone and the combined ridge and SW clumps zones. *Right*: Scaling relations between projected structure size and mean non-thermal velocity dispersion ($\langle\sigma\rangle_{\text{nt}}$) for the main core zone and the combined ridge and SW clumps zones. The solid line represents a single power-law fit to the square points. The horizontal line represents the typical thermal speed for H_2 at gas kinetic temperatures near 11 K. The vertical line represents our spatial resolution of ~ 0.008 pc.

We compare the dependences of ΔV_{lsr} and $\langle\sigma\rangle_{\text{nt}}$ on projected structure size

in Figure 2.20. Size versus ΔV_{lsr} for the dendrogram structures in both zones is plotted on the left; the data appears to follow a power-law relation. There is a steep correlation in both regions, with power-law slopes of 0.80 ± 0.08 in the MCZ and 0.69 ± 0.17 in the RSWZ. The value of ΔV_{lsr} is very low for the smallest objects in all zones, and rises to the sound speed for the largest objects in the MCZ. Size versus $\langle \sigma \rangle_{\text{nt}}$ is plotted on the right side Figure 2.20. There is a much flatter correlation between size and $\langle \sigma \rangle_{\text{nt}}$ in both zones, with a power-law slope of 0.12 ± 0.11 in the MCZ and 0.04 ± 0.07 in the RSWZ. The mean non-thermal velocity dispersions are all sub-sonic to trans-sonic in the MCZ (though still superthermal). The two structures with largest $\langle \sigma \rangle_{\text{nt}}$ are surrounding B1-b and B1-c; it is likely that the non-thermal motions of the gas around them is boosted by rotation and/or outflows and is not purely turbulent. The $\langle \sigma \rangle_{\text{nt}}$ are all sub-sonic in the RSWZ.

Why are the dependences of $\langle \sigma \rangle_{\text{nt}}$ and ΔV_{lsr} on projected structure size so different? In the following section, we set up a theoretical framework that can explain this disparity in terms of differences between a structure’s projected size and its depth into the plane of the sky.

2.7.3 Inferring Cloud Depth from Resolved Size-Linewidth Relations

In this section, we assume that the observed non-thermal gas motions in our dendrogram structures are generated by isotropic, three-dimensional turbulence. In the previous section, we noted a few structures surrounding compact continuum cores that likely have non-thermal gas motions due to the influence of their central source; we exclude them from this analysis.

The total turbulent linewidth of a structure is most strongly influenced by the largest scale an observation encompasses, under the assumptions that the gas we

observe is isotropically turbulent, and optically thin with uniform excitation conditions. If the structure is wider across the plane of the sky than it is deep into the sky, then its turbulent linewidth will be most strongly influenced by its projected size. But if the structure is deeper into the sky than in either of the projected directions, then its turbulent linewidth will be most strongly influenced by its depth.

For a structure that is many resolution elements across (the case for all of our dendrogram structures), ΔV_{lsr} and $\langle \sigma \rangle_{\text{nt}}$ probe turbulence in different ways from the total linewidth. The value of V_{lsr} on any given line-of-sight is a measure of the mean motion of gas along that line-of-sight, which varies from one line-of-sight to another line-of-sight as a consequence of turbulence. The V_{lsr} variation, ΔV_{lsr} , is expected to increase with the projected scale of a structure if turbulence increases with scale, as is the case for the observed and simulated turbulent power spectra in molecular clouds. For any given line-of-sight, the turbulent contribution to $\langle \sigma \rangle$ will be set by the larger of the beam size and the structure depth. Since our beam size is very small (~ 0.008 pc), we expect that the linewidth along individual lines-of-sight will be dominated by structure depth, and thus $\langle \sigma \rangle_{\text{nt}}$ for a structure will depend primarily on the mean (unseen) depth of that structure into the sky. Statistically, along many lines-of-sight for a resolved structure, the comparison of linewidths set by the projected size of the structure (ΔV_{lsr}) to linewidths set by the depth of the structure ($\langle \sigma \rangle_{\text{nt}}$) should allow an estimation of the structure depth.

We can use a mathematical framework to explain how we can compare ΔV_{lsr} to $\langle \sigma \rangle_{\text{nt}}$ to learn about the typical depth of gas structures. In the full three dimensional turbulence, line-of-sight turbulent velocities ($v_{z,\text{turb}}$) can be written as

$$v_{z,\text{turb}}(x, y, z) = \sum_{k_x, k_y, k_z} v_p(k_x, k_y, k_z) \exp[i(k_x x + k_y y + k_z z)], \quad (2.4)$$

where $v_p(k_x, k_y, k_z)$ is the turbulent velocity power spectrum, $k_x = (2\pi/L_x)n_x$, $k_y = (2\pi/L_y)n_y$, and $k_z = (2\pi/L_z)n_z$. L_x is the size of an observed structure in the x

direction, and n_x is the number of full waves of a given turbulent velocity component that fit in the x -direction (the same is true for the y and z components in these equations). If the turbulent motions are Gaussian and isotropic, then $v_p(k_x, k_y, k_z)$ is drawn from a normal distribution whose standard deviation depends only on the magnitude of the k -vector, $|\mathbf{k}| = \sqrt{k_x^2 + k_y^2 + k_z^2}$. We assign the z direction as the line-of-sight, so that in Equation 2.4, $v_{z,\text{turb}}(x, y, z)$ is the z -component of the turbulence, and there are other independent components in the x and y directions.

In this framework, the total linewidth of a structure is the sum of components with non-zero k_x , k_y , or k_z . The resolved linewidths (ΔV_{lsr} and $\langle \sigma \rangle_{\text{nt}}$) are explained below with the aid of Figure 2.21.

The observed centroid velocity at a resolved projected position in the structure, $V_{\text{lsr}}(x, y)$, is the sum of components in Equation 2.4 that have $k_z=0$. The V_{lsr} dependence on spatial scale via $v_p(k_x, k_y; k_z = 0)$ is assumed to depend statistically only on $|\mathbf{k}|$ if the turbulence is isotropic. Therefore, $V_{\text{lsr}}(x, y)$ has the same statistical dependence on $|\mathbf{k}| = \sqrt{k_x^2 + k_y^2}$ (which we can measure) that the underlying turbulent velocity, $v_{z,\text{turb}}(x, y, z)$, has on $|\mathbf{k}| = \sqrt{k_x^2 + k_y^2 + k_z^2}$ (which we cannot measure). The $V_{\text{lsr}}(x, y)$ variation, ΔV_{lsr} , which is the standard deviation of $V_{\text{lsr}}(x, y)$ over all resolved positions in a structure, will scale with the (x, y) -size of the structure according to the turbulent scaling relation of the cloud (see Dickman & Kleiner (1985) for a discussion of spatial correlation properties of centroid velocity fields). To visualize this, we consider the structure on the left-side of Figure 2.21. We call the full 4-cell structure, structure A, and any contiguous 2-cell substructure within it, structure B. Structure A is wider than structure B in the (x, y) directions on the sky, so the minimum, non-zero k_x and k_y must be smaller in structure A than structure B. Assuming v_p has a (statistical) inverse power-law dependence on $|\mathbf{k}|$, this implies higher power in structure A, with a greater contribution to the V_{lsr} variation across

the (x, y) face of structure A compared to structure B.

The non-thermal velocity dispersion at each resolved position in a structure, $\sigma_{\text{nt}}(x, y)$, is obtained from the sum of turbulent components with all possible k_x and k_y , and non-zero k_z , along each line-of-sight. For a given (x, y) , the total line-of-sight velocity is a sum: $v_z(z) = v_{z,\text{turb}}(z) + v_{\text{th}}(z)$, where v_{th} is the thermal component of the velocity. The mean value of $v_{\text{th}}(z)$ is zero, and the mean value of $v_{z,\text{turb}}(z)$ is V_{lsr} . Thus, assuming that $v_{z,\text{turb}}(z)$ and $v_{\text{th}}(z)$ are uncorrelated, for a given line-of-sight, the square of the total velocity dispersion, $\sigma^2(x, y)$, is:

$$\sigma^2(x, y) = \langle v_z^2 \rangle - V_{\text{lsr}}^2 = \langle v_{z,\text{turb}}^2 \rangle - V_{\text{lsr}}^2 + \langle v_{\text{th}}^2 \rangle + 2\langle v_{z,\text{turb}} \rangle \langle v_{\text{th}} \rangle. \quad (2.5)$$

The last term in Equation 2.5 is zero because the mean value of $v_{\text{th}}(z)$ is zero. The second-to-last term in Equation 2.5 is equivalent to the square of the thermal velocity dispersion, σ_{th}^2 ; $\sigma^2 - \sigma_{\text{th}}^2$ is equal to the non-thermal component of the velocity variance, σ_{nt}^2 , which means that the first two terms Equation 2.5 contribute to the non-thermal velocity dispersion. The combination of the first two terms is

$$\langle \left| \sum_{k_x, k_y; k_z \neq 0} v_p(k_x, k_y, k_z) \exp(i\mathbf{k} \cdot \mathbf{x}) \right|^2 \rangle, \quad (2.6)$$

where the summation includes combinations with all k_x , k_y , and with all k_z except $k_z = 0$; \mathbf{k} is the wavenumber vector, and \mathbf{x} is the spatial vector. This shows that the mean non-thermal velocity dispersion for our structures, $\langle \sigma \rangle_{\text{nt}}$, defined as the mean of $\sigma_{\text{nt}}(x, y)$ at each resolved position, will scale with the z -depth of the structure according to the turbulent scaling relation of the cloud. Along any given line-of-sight, a larger L_z implies that the minimum nonzero $k_z = 2\pi/L_z$ is smaller, such that the contribution to Equation 2.6 would be larger (under the assumption that $v_p(\mathbf{k})$ statistically increases with decreasing $|\mathbf{k}|$). To visualize this, we can consider the structure on the right-side of Figure 2.21. We call the full 4-cell structure, structure A, and any contiguous 2-cell substructure within it, structure B. Structure A extends

deeper into the sky than structure B, so the minimum, non-zero k_z in structure A is smaller than the minimum, non-zero k_z in structure B. This implies higher power in structure A, with a larger contribution to $\sigma_{nt}(x, y)$ in structure A compared to structure B.

Based on the arguments above, the scaling relation between V_{lsr} variation and projected size, l , ($\Delta V_{lsr} \propto l^q$) should have the same power-law dependence as the scaling relation between mean non-thermal velocity dispersion and depth, d , into the sky ($\langle \sigma \rangle_{nt} \propto d^q$) if the turbulence is isotropic and we are observing all the gas along each line-of-sight. But we saw in Figure 2.20 that the dependences of ΔV_{lsr} and σ_{nt} on projected structure size are very different. The simplest explanation of this difference is that the projected size of an object need not be the same as its line-of-sight depth into the sky. The size axis in Figure 2.20 (right) is an estimate based on the geometric mean of the projected size. If every object, no matter its projected size, has the same depth, then we should measure a similar non-thermal velocity dispersion for those objects. Therefore, we interpret the shallow dependence of $\langle \sigma \rangle_{nt}$ with size as an indication that our collection of dendrogram structures have similar depths.

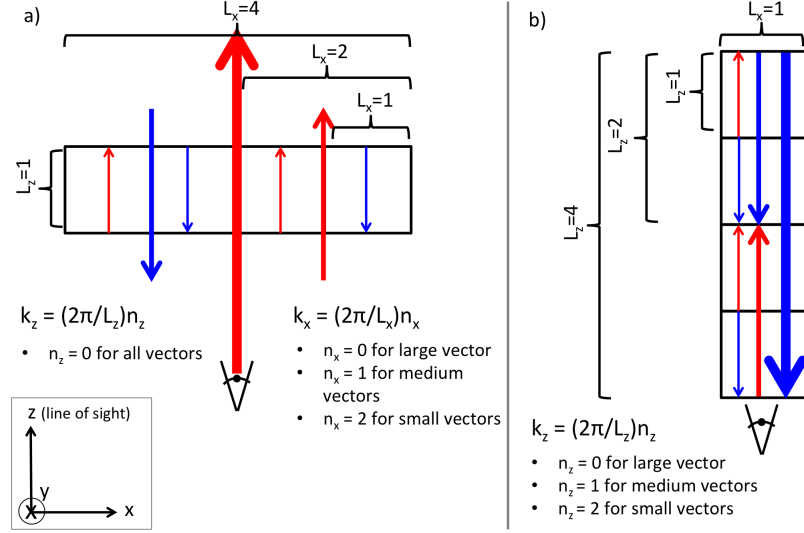


Figure 2.21: One-dimensional cartoons explaining our interpretation of the kinematics of spatially resolved dendrogram structures in the framework of isotropic turbulence. The spatial dimension of each structure is represented by four square cells, each one unit by one unit in area. The colored vectors in each figure represent turbulent velocity components along the line-of-sight (blue = blue-shifted velocity component, red = red-shifted velocity component). The length of the velocity vectors are not to scale, but are simply used to show that there is larger velocity power on the larger scales, and vice-versa. (a): We are looking across the resolved major axis (x -direction) of this filament, and down the minor axis (z -direction; line-of-sight). The V_{lsr} of the filament at each resolved $L=1$ cell is determined by the velocity of all vectors influencing the gas in that cell with $k_z = 0$. Since all vectors have $k_z = 0$, for example, the left-most cell has V_{lsr} contributions from a small red vector, a medium blue vector, and a large red vector, while the right-most cell has V_{lsr} contributions from a small blue vector, a medium red vector, and a large red vector. The V_{lsr} variation (ΔV_{lsr}) across the four resolved cells is the standard deviation of the V_{lsr} in each $L=1$ cell. If this structure were half as wide, then ΔV_{lsr} would decrease because each cell would only have contributions from a small and a medium vector. The non-thermal velocity dispersion along each resolved line-of-sight (σ_{nt}) is zero because there are no $k_z \neq 0$ vectors along the line of sight of each cell. The total velocity dispersion is a combination of vector components with $k \neq 0$, which is determined by small and medium vectors across x -direction. (b): We are looking down the major axis of this filament (z -direction; line-of-sight), through the single resolved spatial element in the x -direction. The V_{lsr} of the filament is determined by the velocity of the large vector because it is the only vector with $k_z = 0$; oscillations of the small and medium vectors average each other out along the line-of-sight, and they do not contribute to the V_{lsr} . The V_{lsr} variation (ΔV_{lsr}) is zero because there is only one resolved V_{lsr} value for this object. The non-thermal velocity dispersion (σ_{nt}) along the single line-of-sight is determined by the small and medium vectors, since both have $k_z \neq 0$. If this structure were half as deep, then σ_{nt} would decrease because it would be determined by the small vectors alone. The total velocity dispersion is a combination of vector components with $k \neq 0$, which is determined by small and medium vectors along the z -direction in this case; it equals σ_{nt} since there is only one resolved line-of-sight.

To illustrate these effects, we created a numerical realization of a three-dimensional, isotropic turbulent power spectrum, with power spectrum scaling $v^2 \propto k^{-4}$. Using an arbitrary length scale, L , the position-position-position box had x, y, z dimensions of $L \times L \times 2L$, where L corresponds to 512 pixels. We used this realization along with three sub-boxes with different L_z to demonstrate how $\langle \sigma \rangle_{\text{nt}}$ and ΔV_{lsr} depend on structure depth for a single turbulent realization. The original box had dimensions of $L \times L \times 2L$ (the “double depth” box), the first sub-box was $L \times L \times L$ (the “full depth” box), the second was $L \times L \times L/2$ (the “half depth” box), and the third was $L \times L \times L/4$ (the “quarter depth” box). For each of these sub-boxes (with uniform density), we created PPV cubes and then processed them similarly to the observations. The end products were centroid velocity and velocity dispersion maps across the $L \times L$ x, y surface of each numerical box. We segmented each $L \times L$ surface into equally sized square regions with side $L, L/2, L/4, L/8$, and calculated ΔV_{lsr} and $\langle \sigma \rangle_{\text{nt}}$ within each segment to show how they scale with size. The results for each box are shown in Figure 2.22. Evidently, $\langle \sigma \rangle_{\text{nt}}$ has no dependence on size, while ΔV_{lsr} increases with size, similar to the behavior seen in the observations in Figure 2.20. The size where ΔV_{lsr} crosses $\langle \sigma \rangle_{\text{nt}}$ corresponds well with the depth of the numerical cube.

If turbulence in the observed region has similar behavior to that in the isotropic turbulent realization, then we can use the correlation of V_{lsr} variation with size to estimate the depths of the Barnard 1 structures. For this correlation, we know the projected size is directly related to ΔV_{lsr} , so there is no size ambiguity as there is in the correlation between projected size and $\langle \sigma \rangle_{\text{nt}}$. To estimate the typical depth of the cloud, we can find the size scale at which the best-fit line for ΔV_{lsr} versus projected size is equal to the best-fit line for $\langle \sigma \rangle_{\text{nt}}$ versus projected size. This corresponds to ~ 0.11 pc for the MCZ, and ~ 0.18 pc for the RSWZ. Under the assumption that

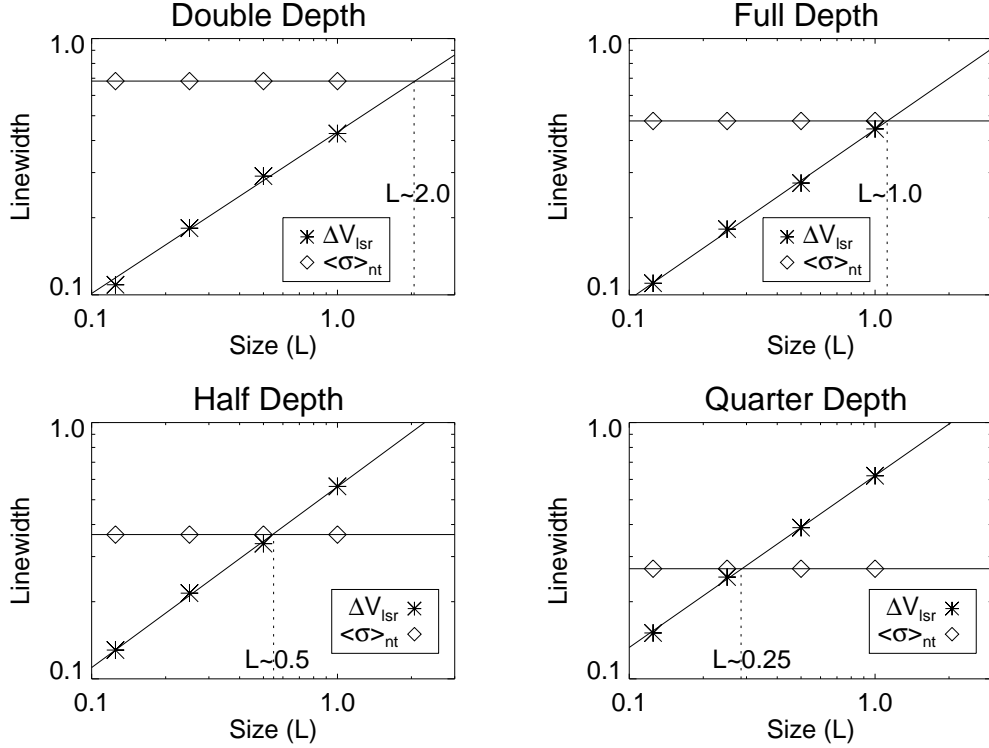


Figure 2.22: Size-linewidth relations from a numerical realization of an isotropic turbulent power spectrum. The four plots represent results from four different boxes taken from the realization: the “double depth” box is twice as deep as it is wide ($L \times L \times 2L$), the “full depth” box is cubic ($L \times L \times L$), the “half depth” box is half as deep as it is wide ($L \times L \times L/2$), etc. The vertical axis represents the two linewidths we discussed in text: $\langle \sigma \rangle_{\text{nt}}$ and ΔV_{lsr} (in arbitrary units). The horizontal axis represents the size-scale we sampled across the face of the box when calculating the linewidths: a size-scale of 1 represents sampling across the full $L \times L$ scale, a size-scale of 0.5 represents sampling across smaller-scale $L/2 \times L/2$ segments, etc. There are several things to notice in these panels: 1) $\langle \sigma \rangle_{\text{nt}}$ is independent of size, and its magnitude decreases by $\sqrt{2}$ as the box depth is halved from panel to panel, 2) ΔV_{lsr} increases with increasing size, 3) The magnitude of $\langle \sigma \rangle_{\text{nt}}$ and ΔV_{lsr} cross near the size that represents the depth of the box.

turbulence is isotropic, this implies that Barnard 1 is on the order of 0.1–0.2 pc deep, comparable to the largest projected width (~ 0.2 –0.3 pc) of individual structures.

Since the largest-scale dust structure in Barnard 1 extends over 1 pc on the sky, the overall region may be more flattened than spherical at the largest scales. Numerical simulations over the past 15 years have consistently shown that high-density

sheets and filaments are a generic result of strongly supersonic turbulence with parameters comparable to those in observed clouds (e.g., reviews by Elmegreen & Scalo 2004; Mac Low & Klessen 2004; McKee & Ostriker 2007). But measuring the depth of an individual structure in a molecular cloud is a difficult task. Comparison to realizations of turbulence suggests that the high angular resolution, large area observations from CLASSy allow us to estimate the physical depths of individual structures in molecular clouds, thus providing new observational insight into the true nature of those clouds³. Our observational result suggests that Barnard 1 is an over-dense region within the larger Perseus Molecular Cloud that could have formed a sheet-like geometry from supersonic turbulence. Lee et al. (2014) present the same size-linewidth relations using CLASSy observations of Serpens Main, and find similar behavior. We will compare the results from all our CLASSy regions in an upcoming cross-comparison paper.

2.8 Summary of Barnard 1 Results

We presented the CLASSy project overview with a focus on Barnard 1. CLASSy spectrally imaged over 800 total square arcminutes of the Perseus and Serpens Molecular Clouds at $7''$ angular resolution.

1. We spectrally imaged N_2H^+ , HCN, and HCO^+ ($J = 1 \rightarrow 0$) emission across 150 square arcminutes of Barnard 1. The final data products are position-position-velocity cubes with full line emission recovery obtained through joint

³We emphasize, however, that it is important to confirm the behavior seen in simple, isotropic turbulent realizations with fully-realistic turbulent simulations of clouds. For best comparison to observations, it will be valuable to create synthetic PPV data cubes via radiative transfer modeling, rather than assuming uniform excitation and optically thin conditions.

deconvolution with single-dish observations. The velocity resolution of the data is $\sim 0.16 \text{ km s}^{-1}$.

2. Four compact continuum sources were detected at $>5\text{-}\sigma$ at 3 mm, all in the main core zone. B1-c, B1-b South, and B1-b North were previously known; we report a new detection of compact emission towards the Per-emb 30 continuum source.
3. The N_2H^+ ($J = 1 \rightarrow 0$) gas morphology closely matches dust continuum observations of *Herschel*, while HCN and HCO^+ ($J = 1 \rightarrow 0$) emissions are weaker throughout most of the field and show less correlation with the long wavelength dust emission. HCN and HCO^+ also well-trace outflows in the main core zone.
4. Spectral line fitting of the molecular line data shows that the Barnard 1 main core is much more kinematically complex than the filaments and clumps that extend to its southeast; these filaments and clumps are characterized by more uniform centroid velocities and lower velocity dispersions.
5. We used dendrograms to identify N_2H^+ gas structures in Barnard 1. The motivation for using dendrograms instead of a more traditional clumpfinding algorithm was the need to analyze the morphological and kinematic structure of dense gas across the wide range of spatial scales captured in our CLASSy data. We found that dendrograms are better able to quantify that range of spatial scales. We created a new, non-binary adaptation to the standard, binary dendrogram algorithm to ensure that the dendrograms represent the true hierarchy of the emission within the noise limits of real data, and that tree statistics can be used to quantify that hierarchy.

6. The non-binary dendrogram of Barnard 1 contains 41 leaves and 13 branches. We calculated three simple tree statistics using the dendrogram: the maximum branching level, the mean path length, and the mean branching ratio. The tree structure representing the dense gas around the main core is the most complex, with four hierarchy levels and the highest contrast leaves. The tree statistics give insight into the type and amount of fragmentation a region has undergone, and will be used to compare the hierarchical complexity of the different CLASSy regions.

7. We characterized the spatial properties of the dendrogram structures and derived structure sizes ranging from ~ 0.01 to 0.34 pc. The high angular resolution data reveal a variety of irregular shapes, showing that star-forming gas is not composed of well ordered spheroids and filaments on the smallest scales. We also characterized the kinematic properties of the structures and found that, in general, branches have larger V_{lsr} variation, but similar mean velocity dispersion, compared to the leaves. The gas surrounding the most massive compact continuum cores have the largest velocity dispersions in the entire region.

8. Using the spatial and kinematic properties of the dendrogram leaves and branches, we estimated the depth of the Barnard 1 cloud to be ~ 0.1 – 0.2 pc. This estimate was made by comparing two size-linewidth relations: one using the mean non-thermal velocity dispersion of the dendrogram objects, which is sensitive to the depth of the cloud, and the other using the V_{lsr} variation of the objects, which is sensitive to the projected size of the cloud. The mean non-thermal velocity dispersion varied very little with structure size, while the V_{lsr} variation varied steeply with size. We interpreted this as an indication that

Barnard 1 is more flattened than spherical on the largest scales. This method is a powerful tool for observationally probing the structure of molecular clouds into the plane of the sky.

Chapter 3

Analysis of the Young L1451 Region Within Perseus

Abstract

We present spectral line images of HCO^+ , HCN , and N_2H^+ ($J = 1 \rightarrow 0$), and a continuum image at 3 mm, toward the L1451 region in the Perseus Molecular Cloud. These observations are part of the CARMA Large Area Star Formation Survey, which also imaged the Barnard 1 and NGC 1333 regions in Perseus. L1451 is the region of the survey with the lowest level of star formation activity; it contains no confirmed protostars, only a first hydrostatic core candidate source. All three dense gas tracer molecules are detected throughout the 150 square arcminute region, with HCO^+ the most spatially widespread. We detect molecular emission toward 90% of the area above $\text{N}(\text{H}_2)$ column densities of $1.9 \times 10^{21} \text{ cm}^{-2}$, where column densities are derived from *Herschel* observations. Our non-binary dendrogram algorithm reveals complex hierarchical structure in all three molecular lines, with similar trends of hierarchical fragmentation based on a comparison of tree statistics. Gas surrounding the candidate first hydrostatic core, L1451-mm, and other previously detected

single-dish continuum clumps show similar tree statistics, providing evidence that different sub-regions of L1451 are fragmenting on the pathway to forming young stars. Spectral line fitting reveals that HCO^+ has the broadest velocity dispersion, near 0.3 km s^{-1} on average, compared to $\sim 0.15 \text{ km s}^{-1}$ for the other molecules. A virial analysis using *Herschel*-derived column densities and CLASSy-derived kinematics shows that the most centrally-condensed dust structures are likely in virial equilibrium when considering effects including density stratification within a core, external confining pressure, and the systematic underestimation of column densities from fitting *Herschel* SEDs with a single-temperature component model. An analysis of N_2H^+ emission from L1451-mm and a newly identified centrally condensed feature, called L1451-west, shows that L1451-west is younger than L1451-mm, but more centrally condensed than a typical prestellar core, suggesting it could be another first hydrostatic core candidate. We determined the typical depth of molecular emission from L1451 structures to be $\sim 0.4 \text{ pc}$ and 0.1 pc for HCO^+ , and HCN and N_2H^+ , respectively; the comparison of these typical depths to the projected size of the largest dense gas features suggests that the dense gas in the L1451 region is not significantly flattened at the parsec-scales, and that the main features are more ellipsoidal than filamentary. These overall results point to L1451 being a young region that is forming its first generation of stars.

3.1 Introduction

The star formation process in a molecular cloud starts well before protostars are detectable at infrared wavelengths. In general, it begins with the formation of the molecular cloud that may span tens of parsecs (Evans 1999; Elmegreen & Scalo 2004; McKee & Ostriker 2007); it continues as structure and density enhancements

are created by the interaction of turbulence, gravity, and magnetic fields at parsec scales (McKee & Ostriker 2007; Crutcher 2012), and it progresses until prestellar core collapse occurs at 0.01–0.1 pc scales (di Francesco et al. 2007; Bergin & Tafalla 2007). Once a first generation of protostars is formed within those dense cores, the young stars can feed energy back into the cloud and impact subsequent star formation that may occur (Nakamura & Li 2007; Carroll et al. 2009; Nakamura & Li 2014). A full understanding of how turbulence, gravity, and magnetic fields control the star formation process requires observations that span cloud to core spatial scales at these distinct evolutionary stages.

An individual molecular cloud can be a great testbed for studying the star formation process across space and time if it is sufficiently close to get better than 0.1 pc resolution, and if it contains regions with distinct evolutionary stages. The Perseus Molecular Cloud is a nearby example of such a cloud. At a distance of 235 pc (Hirota et al. 2008, 2011), Perseus has several regions of clustered star formation that have been observed as part of large *Spitzer*, *Herschel*, and JCMT surveys. The regions with infrared detections of young stellar objects (YSOs) span a range of evolutionary epochs based on YSO statistics from the c2d Legacy project (Jørgensen et al. 2008; Evans et al. 2009). The IC 348 region has 121 YSOs, with 9.1% being Class I or younger; the NGC 1333 region has 102 YSOs, with 34% being Class I or younger; the Barnard 1 region had 9 YSOs, with 89% being Class I or younger; and, the L1448 region has five YSOs, with 100% being Class I or younger. Regions without current protostellar activity also exist within Perseus. The B1-E region may be forming a first generation of dense cores (Sadavoy et al. 2012), and the L1451 region has a single detection of a compact continuum core, which is a candidate first hydrostatic core (FHSC) (Pineda et al. 2011).

The CARMA Large Area Star Formation Survey (CLASSy) observed the dense

gas in three evolutionary distinct regions within Perseus (Storm et al. 2014) and two regions within Serpens (Lee et al. 2014; Fernández-López et al. 2014) with high angular and velocity resolution. From early to late stages of evolution (based on the ratio of Class II and older to Class I and younger YSOs), the Perseus regions are: L1451, Barnard 1, and NGC 1333. The observations enable a high resolution study of the structure and kinematics of star forming material at different epochs. The youngest region, L1451, probes conditions during the origin of clumps and stars; the more evolved Barnard 1 region probes conditions when a relatively small number of protostars are formed, and the active NGC 1333 region probes conditions when dozens of clustered protostars are driving outflows back into the cloud. Details of CLASSy, along with an analysis of Barnard 1, can be found in Chapter 2.

This chapter focuses on the L1451 region. L1451 is located ~ 5.5 pc to the southwest of NGC 1333 (see Figure 1.3). The region has been surveyed at a number of wavelengths. It contains no *Spitzer*-identified YSOs at IRAC or MIPS wavelengths (Jørgensen et al. 2008). Hatchell et al. (2005) and Kirk et al. (2006) did not identify any cores in their JCMT SCUBA 850 μm survey. There are four 1.1 mm sources identified in the Bolocam Survey (Enoch et al. 2006) that are classified as “starless” cores in Enoch et al. (2008): PerBolo 1, 2, 4, and 6. Pineda et al. (2011) showed that PerBolo 2 is not a starless core, but likely a core with an embedded YSO or a FHSC.

The Bolocam cores within L1451 are colder and less dense than the average Bolocam cores within Perseus. The visual extinction (A_v) of the four Bolocam sources ranges from 8 to 11 magnitudes, while the mean and median A_v for all Perseus sources are 24.6 and 12, respectively (Enoch et al. 2006). The mean particle density of the L1451 Bolocam sources ranges from 0.9×10^5 to $1.5 \times 10^5 \text{ cm}^{-3}$, which is lower than the mean density for all Perseus sources of 3.2×10^5 (Enoch et al. 2008).

The kinetic temperature of gas within the L1451 cores ranges from 9.1 to 10.3 K, which is lower than the mean for all Perseus cores of 11.0 (Rosolowsky et al. 2008a).

These statistics indicate that the dense cores forming within L1451 are, on average, a little colder and less dense than other star forming regions within Perseus, supporting the YSO statistics suggesting it is at an earlier evolutionary epoch than Barnard 1 and NGC 1333. The main science goals of our large-area, high-resolution, spectral line observations of this young region are: 1) to determine whether complex, hierarchical structure formation exists before the onset of star formation, as predicted by theories of turbulence-driven star formation, 2) to better understand how natal cloud material fragments on the pathway to star formation, by quantifying the hierarchical similarities and differences between different sub-regions of L1451, 3) to estimate the boundedness of the dense structures in young star forming regions, and 4) to potentially discover new young cores.

The chapter is organized as follows. Section 3.2 provides an overview of CLASSy observations of L1451. Properties of the L1451-mm continuum detection are in Section 3.3. Section 3.4 presents the dense gas morphology using integrated intensity and channel maps, and Section 3.5 presents the dense gas kinematic results from spectral line fitting. A dendrogram analysis of the HCO⁺, HCN, and N₂H⁺ data cubes is in Section 3.6. Section 3.7 shows how we calculate column density, dust temperature, and extinction maps using *Herschel* data, along with a dendrogram analysis of the extinction map. Section 3.8 uses the spectral line data in combination with the continuum data to assess the properties of structures in L1451, along with the typical depth of molecular emission from the region. We summarize our key findings in Section 3.9.

Table 3.1. Observation Summary

Array	Dates	Total Hours	Flux Cal.	Gain Cal.	Mean Flux (Jy)
DZ	October 2012	25	Uranus	3C84/3C111	18.6/2.6
	February - June 2013	50	Uranus	3C84/3C111	19.5/3.5
EZ	August - September 2012	25	Uranus	3C84/3C111	18.0/2.8
	July - August 2013	50	Uranus	3C84/3C111	17.5/4.2

3.2 Observations

The details of CLASSy observations, calibration, and mapping are found in Chapter 2 (Section 2.2); specifics related to L1451 are summarized here. We mosaicked a total area of ~ 150 square arcminutes in CARMA23 mode. The mosaic was made up of two adjacent rectangles, containing a total of 673 individual pointings with $31''$ spacing in a hexagonal grid (see Figure 3.1). The reference position of the mosaic is at the center of the eastern rectangle: $\alpha=03^{\text{h}}25^{\text{m}}17^{\text{s}}$, $\delta=30^{\circ}21'23''$ (J2000). The L1451-mm core (Pineda et al. 2011) is within the eastern rectangle. The region was observed for 150 total hours, evenly split between the DZ and EZ configurations, which provide projected baselines from about 1–40 k λ and 1–30 k λ , respectively. See Table 3.1 for a summary of observing dates, and calibrators. The mapped region covers roughly 1.1 pc by 0.6 pc with about 1700 AU (0.008 pc) spatial resolution.

The correlator setup is summarized in Table 3.2. N_2H^+ , HCO^+ , and $\text{HCN } J = 1 \rightarrow 0$ were simultaneously observed in 8 MHz bands, providing a velocity resolution of 0.16 km s $^{-1}$. We also used a 500 MHz band for continuum observations and calibration. Data were inspected and calibrated using MIRIAD (Multichannel Image Reconstruction, Image Analysis and Display; Sault et al. 1995). 3C84 was observed every 16 minutes for gain calibration; 3C111 was used for gain calibration when 3C84 transited above 80 degrees elevation. Uranus was observed for absolute flux calibration. The flux of 3C84 varied between 16 and 21 Jy over the observing

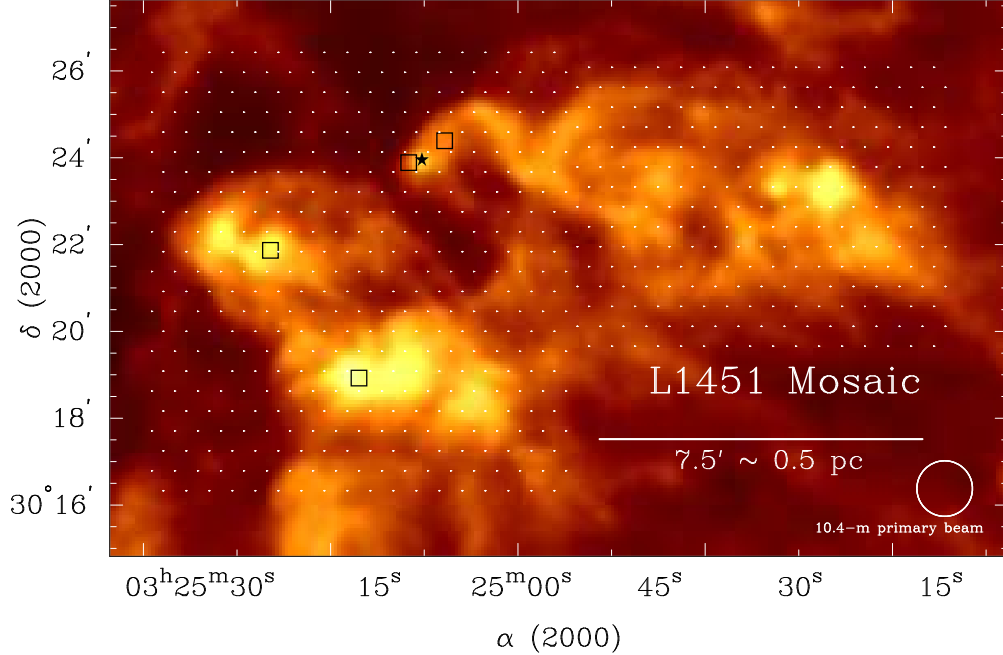


Figure 3.1: A *Herschel* image of the $250\ \mu\text{m}$ emission (yellow is brighter emission, red is fainter emission) from L1451 with the CLASSy mosaic pointing centers overlaid as white points. The spacing of the pointing centers is $31''$, and our total area coverage is ~ 150 square arcminutes. The locations of 1.1 mm Bolocam sources (Enoch et al. 2006) and the L1451-mm compact continuum core (Pineda et al. 2011) are marked with black squares and a black star, respectively.

Table 3.2. Correlator Setup Summary

Line	Rest Freq. (GHz)	No. Chan.	Chan. Width (MHz)	Vel. Coverage (km s^{-1})	Vel. Resolution (km s^{-1})	Chan. RMS (Jy beam^{-1})	Synth. Beam ^a
N_2H^+	93.173704 ^b	159	0.049	24.82	0.157	0.14	$8.6'' \times 6.8''$
Continuum	92.7947	47	10.4	1547	33.6	0.0013	$9.2'' \times 6.6''$
HCO^+	89.188518	159	0.049	25.92	0.164	0.12	$8.8'' \times 7.1''$
HCN	88.631847 ^c	159	0.049	26.10	0.165	0.12	$8.9'' \times 7.2''$

Note. — ^aIn principle, the synthesized beam is slightly different for each pointing center. Miriad calculates a synthesized beam for the full mosaic based on all of the pointings. ^bThe rest frequency of the band was set to the weighted mean frequency of the center three hyperfine components. ^cThe rest frequency of the band was set to the frequency of the center hyperfine component. See <http://splatalogue.net> for frequencies of the HCN and N_2H^+ hyperfine components.

period, while 3C111 varied between 2.6 and 4.5 Jy. The uncertainty in absolute flux calibration is about 10%. We will only report statistical uncertainties when quoting errors in measured values throughout the chapter.

To create spectral-line images which fully recover emission at all spatial scales, CARMA observed in single-dish mode during tracks with stable atmospheric opac-

ity. The OFF position for L1451 was $3.5'$ west and $13.7'$ south of the mosaic reference position. The single-dish data from the 10.4-m dishes was calibrated in MIRIAD using the `sinbad`, `sinpoly`, `varmaps`, and `imstack` commands. The antenna temperature rms in the final single-dish cubes was ~ 0.02 K for all three molecules. The spectral-line interferometric and single-dish data were combined with `mosmem`, a maximum entropy joint deconvolution algorithm in MIRIAD. The noise levels and synthesized beams for the final data cubes are given in Table 3.2. The rms noise in these lines correspond to brightness temperature rms of 0.34 K for N_2H^+ and 0.30 K for HCO^+ and HCN.

We created a 3 mm continuum map with the interferometric data from the 500 MHz window. The rms in the continuum map is ~ 1.3 mJy beam $^{-1}$ with a synthesized beam of $9.2'' \times 6.6''$. Single-dish continuum data can not be acquired at CARMA.

3.3 Continuum Results

We detected no compact continuum sources above the $5\text{-}\sigma$ level. One source was detected above $3\text{-}\sigma$ that could be confirmed with other observations; L1451-mm (Pineda et al. 2011) is detected at $4\text{-}\sigma$ with 5.2 mJy beam $^{-1}$. Figure 3.2 shows the 3 mm continuum image toward L1451-mm. The position, peak brightness, and lower-limit mass for our detection were calculated following the prescription described in Section 2.3 and are listed in Table 3.3. The position and peak brightness agree with 3 mm measurements from Pineda et al. (2011). Our image shows a possible secondary peak to the north of the brightest emission. However, this secondary peak is only within the $2\text{--}3\sigma$ contours, and does not appear in the higher sensitivity observations of Pineda et al. (2011). Pineda et al. (2011) detected a low-velocity

Table 3.3. Observed Properties of Continuum Detections

Source Name (1)	Position (h:m:s, d:':") (2)	Pk. Bright. (mJy beam ⁻¹) (3)	Mass (M _⊙) (4)
L1451-mm	03:25:10.38, +30:23:55.9	5.2 ± 1.3	0.10 ± 0.03

Note. — (3) Peak brightness, (4) Lower-limit mass using the peak brightness and assumptions outlined in Section 2.3.

CO ($J = 2 \rightarrow 1$) outflow in this area; we do not detect any HCN or HCO⁺ outflow emission near this source.

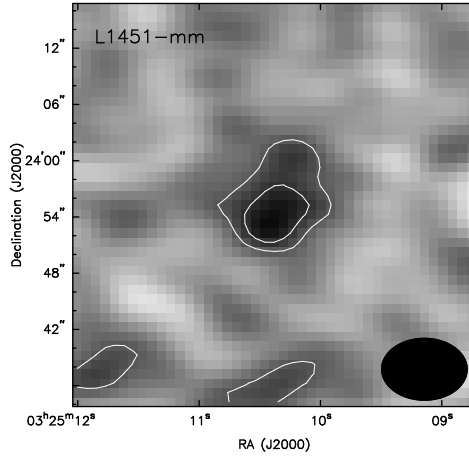


Figure 3.2: The single continuum detection in our field. The synthesized beam is $9.2'' \times 6.6''$, and the $1\text{-}\sigma$ sensitivity is $1.3 \text{ mJy beam}^{-1}$. The contour levels are 2, 3 times $1\text{-}\sigma$; no negative contours are present.

3.4 Morphology of Dense Molecular Gas

3.4.1 Integrated Intensity Emission

Figure 3.3 shows integrated intensity maps for HCO⁺, HCN, and N₂H⁺ $J = 1 \rightarrow 0$ ($\sim 7.5''$ angular resolution), along with a *Herschel* 250 μm image (18.1'' angular resolution) for a visual comparison between the dense gas and dust emission. The line maps were integrated over all channels with identifiable emission. HCO⁺ emission

was integrated from 5.316 to 3.018 km s⁻¹. HCN emission was integrated over all three hyperfine components from 9.945 to 7.962 km s⁻¹, 5.154 to 2.841 km s⁻¹, and -2.115 to -3.932 km s⁻¹. N₂H⁺ emission was integrated over all seven hyperfine components over velocity ranges from 11.542 to 8.714 km s⁻¹, 5.729 to 2.744 km s⁻¹, and -3.383 to -4.639 km s⁻¹. The rms of the maps are 0.08, 0.13, and 0.16 Jy beam⁻¹ km s⁻¹ for HCO⁺, HCN, and N₂H⁺, respectively.

The locations of the four Bolocam 1.1 mm sources (Enoch et al. 2006) and the one compact continuum core in L1451 are marked on each image of Figure 3.3. Four of the five sources are located near peaks of dense gas and dust emission. Kirk et al. (2006) showed possible evidence for dense cores being preferentially offset from the peak of their parent core due to the B0.5 V star, 40 Per, triggering star formation and sculpting Perseus material (Walawender et al. 2004; Kirk et al. 2006); we do not see evidence for this with our high-resolution observations.

While the molecules and dust are tracing similar features around those sources, the exact morphological details vary. Below, we describe the qualitative emission features, and refer to the colored rectangles in Figure 3.3 for reference.

All tracers show a curved structure surrounding L1451-mm and the two nearby Bolocam sources (see red rectangle in Figure 3.3), with a peak of integrated emission at the location of L1451-mm. The southwestern edge of the curved structure has a stream of emission that extends further to the southwest (see dark blue rectangle in upper left panel of Figure 3.3), which can be seen in all the maps, though it extends furthest in the HCO⁺, HCN, and dust maps. The two other Bolocam sources to the far east of L1451-mm are surrounded by significant molecular gas structure (see green rectangle in lower left panel). The HCO⁺ emission has the largest extent of strong emission in this region.

The integrated emission in the three lines is less similar across the western half

of L1451 compared to the eastern half. There is a strong, condensed N_2H^+ source (see orange rectangle in lower right panel) that does not appear in the HCN or HCO^+ maps, but that does correspond to a peak of emission in the dust map (see Section 3.8.3 for more details on this source). The strongest HCO^+ feature in the western half of the map has a weaker counterpart in the HCN map (see purple rectangle), which appears even weaker in N_2H^+ . Finally, there is HCO^+ emission to the northwest of the curved structure (see cyan rectangle) that closely mimics dust emission in that region; this emission is weakly detected in HCN, but not in N_2H^+ .

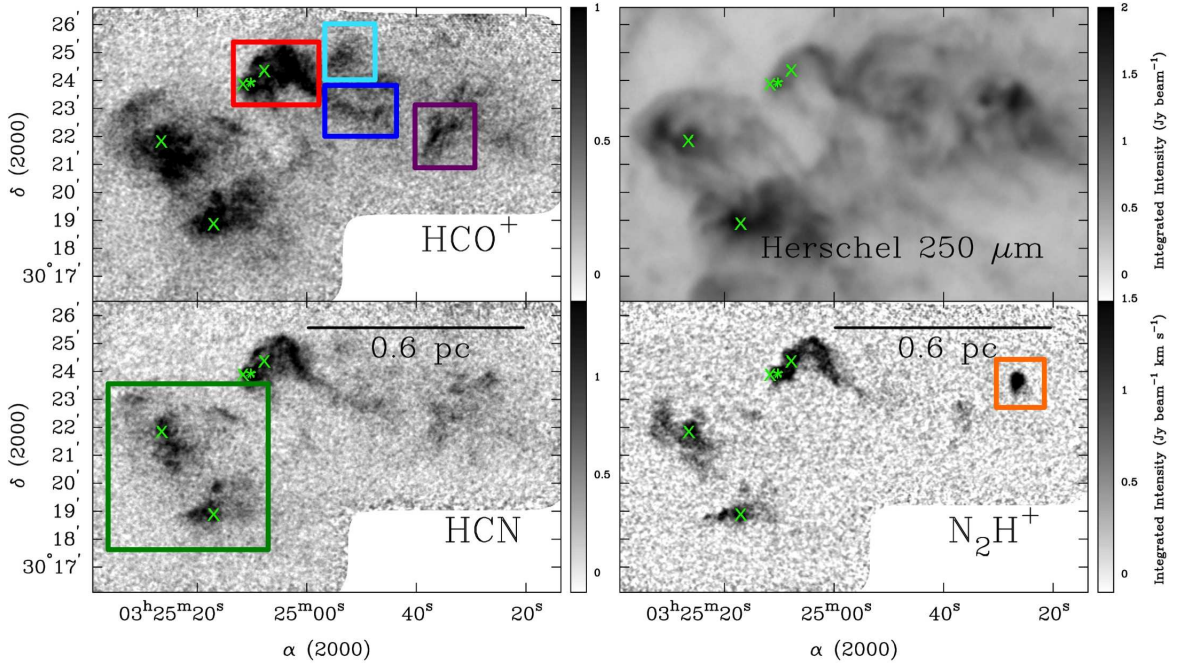


Figure 3.3: Integrated intensity maps of HCO^+ , HCN, and N_2H^+ , ($J = 1 \rightarrow 0$) emission toward L1451, along with a *Herschel* $250 \mu\text{m}$ map of the region. The four Bolocam 1.1 mm sources in this region are marked with “x” symbols, and the L1451-mm compact continuum core is marked with an asterisk. Colored rectangles show the locations of qualitative features discussed in Section 3.4.1.

3.4.2 Channel Emission

Figures 3.4, 3.5, and 3.6 show channel maps of HCO^+ , HCN , and N_2H^+ respectively, highlighting the bulk of the emission¹, which occurs from ~ 4.9 to 3.5 km s^{-1} . In general, it is clear from the maps that strong HCO^+ emission is more widespread compared to HCN emission, and particularly N_2H^+ emission (as was also evident in Figure 3.3). We labeled qualitative features in the HCO^+ channel maps, from A through I, in the order that they appear in velocity space (with eastern sources being labeled before western sources). We then placed those same labels on the HCN and N_2H^+ maps to aid a qualitative comparison of dense gas features, given below².

We detect no HCN or HCO^+ outflow emission in any channels, which suggests that L1451 is a young region with little to no protostellar activity. The strongest emission in the field is near the L1451-mm core; the peak brightness temperature for a single channel in a single synthesized beam is: 6.9 K, 6.3 K, and 3.9 K for HCO^+ (2.47 Jy beam⁻¹ to K conversion factor), HCN (2.46 Jy beam⁻¹ to K conversion factor), and N_2H^+ (2.42 Jy beam⁻¹ to K conversion factor), respectively.

Features A and C

Features A and C in the eastern half of the map are traced with all molecules, with varying strength. Feature A appears strongly in the first HCO^+ channel in Figure 3.4, faintly in the first HCN channel in Figure 3.5, and not until the third N_2H^+ channel in Figure 3.6. Even when it finally appears in the N_2H^+ channel, the

¹These figures do not show some of the highest and lowest velocity channels with emission; those channels can be viewed by downloading the publically available data cubes.

²The condensed structure labeled J in Figure 3.6 only appears in the N_2H^+ maps, so the J label is excluded from the HCO^+ and HCN maps.

emission is much more concentrated than what we observe in HCO^+ and HCN . This concentration is likely because the N_2H^+ ($J = 1 \rightarrow 0$) line traces higher-density, colder material compared to HCO^+ and HCN ($J = 1 \rightarrow 0$) lines. A 1.1 mm Bolocam core is located within Feature A, and corresponds with a peak in the N_2H^+ emission. Feature A moves from northeast to southwest as the first few channels progress from higher to lower velocity, and Feature C then appears to its southwest. Features A and C are possibly part of the same larger-scale structure, which will be explored in the next section when we analyze the kinematics of this region. Like Feature A, Feature C is more concentrated in N_2H^+ , and contains a 1.1 mm Bolocam source at an N_2H^+ peak of emission.

Figure 3.7 shows HCO^+ and HCN spectra from three locations across Feature A, along with an integrated intensity view of HCO^+ . The purpose of this figure is to demonstrate the complexity of HCO^+ and HCN emission in many parts of L1451. Location 1 shows a $\sim 6\text{-}\sigma$ dip between two peaks of HCO^+ emission. This could be a detection of a two component system, a signature of self-absorption, or a signature of infall. The HCN spectrum at this location shows a similar dip in the two higher-velocity hyperfine components, but no dip in the lowest-velocity component—this makes a two-component system unlikely. This feature is likely not due to infall, which predicts a stronger blue peak (Evans 1999), since the red peak is stronger. Double-peaked spectra from self-absorption can be due to several effects including: a foreground screen of lower-density HCO^+ , infall of material onto a dense core, and the spherical expansion of material (Zhou et al. 1993). The dotted line in each panel of Figure 3.7 indicates the N_2H^+ centroid velocity from our spectral line fitting in Section 3.5. The N_2H^+ spectra at these locations do not show evidence of double peaks. The best-fit centroid velocity of N_2H^+ at location 1 is 4.57 km s^{-1} , which is between the two HCO^+ and HCN peaks, thereby adding support to the case for

self-absorption at this location. Observations of optically thin tracers of HCO^+ and HCN species are needed to more definitively understand the emission.

The HCN spectrum at location 2 has all hyperfine components at a similar intensity—this is either a sign that part of the two higher opacity hyperfine components have been absorbed away, thereby matching the intensity of the lowest opacity hyperfine component, or that the line is optically thick and all components are saturated to the same intensity. The HCO^+ spectrum at location 2 has a weak, single-channel dip between two peaks of emission, which hints at self-absorption being the more likely cause of the matching HCN intensities at this location. Location 3 has a single-component HCO^+ spectrum, and a single-component HCN spectrum with hyperfine intensity ratios closer to the expected local thermodynamic equilibrium values, showing that spectra can vary on the scale of $\sim 30''$ when observations have high angular and velocity resolution.

Feature B

Feature B contains the L1451-mm compact continuum source. It appears strongly in all molecules, though it contains a prominent ridge of emission in the 4.82 km s^{-1} channel of HCO^+ and HCN that does not appear in the closest N_2H^+ channel.

Figure 3.8 shows an integrated intensity map of HCO^+ with HCO^+ and HCN spectra from a location in the eastern and western half of this feature. The HCO^+ spectrum from location 1 shows a double-peaked spectrum with a single-channel dip. The center hyperfine component of the HCN spectrum shows a remarkably similar shape to the HCO^+ spectrum, with a single-channel dip between two channels of significant emission. The full HCN spectrum shows a single-channel dip in the two higher-velocity hyperfine components, but not the lower-velocity component. It also shows similar component strengths for all three hyperfine lines. The N_2H^+ spectrum

at location 1 has no evidence of a second component along the line-of-sight. The N_2H^+ centroid velocity is 4.12 km s^{-1} (plotted as dotted line in Figure 3.8), closer to the HCO^+ dip near 4.0 km s^{-1} than the HCO^+ peaks at 3.87 and 4.30 km s^{-1} . All of this suggests that the dip in the HCO^+ and HCN spectra is from self-absorption.

The HCO^+ and HCN spectra from location 2 show a two-peak structure, where the bluer component is significantly stronger than the redder component. This feature appears in all HCN hyperfine components, unlike all the other spectra we looked at above. The N_2H^+ spectrum at location 2 does not show two components. The N_2H^+ centroid velocity is 4.32 km s^{-1} , closer to the HCO^+ dip near 4.45 km s^{-1} than the HCO^+ peaks at 4.14 and 4.75 km s^{-1} . These results are consistent with infall models, and suggest that the gas in this region may be undergoing collapse. This would require that the HCO^+ line and all three HCN hyperfine lines are optically thick. Similar spectra are seen at and around the peak of integrated emission nearest to location 2, as well as at the other two peaks of integrated emission to the north-east of location 2, suggesting that these could be young cores undergoing infall. As mentioned above, observations with optically thin tracers toward these sub-regions of L1451 are needed for a more complete understanding of the gas dynamics.

Features D Through J

Features D, E, F, G, H, and I are all identified based on the HCO^+ channel emission. N_2H^+ only shows faint emission in two channels for Feature G, while HCN emission appears weakly toward all features seen with HCO^+ . The descriptions below are based on HCO^+ .

Feature D appears to the west of Features A and C, and to the south of Feature B, in the 4.66 and 4.50 km s^{-1} channels as an elliptical feature not connected to larger-scale structure. Feature E appears as a prominent, round emission feature

in the 4.50 km s^{-1} channel, with more extended emission in channels surrounding the 4.50 km s^{-1} peak of emission. Feature F is emission that starts just to the northwest of Feature B in the 4.17 km s^{-1} channel, peaks in the 4.0 and 3.83 km s^{-1} channels, and then appears to get fainter while extending to the southwest in channel 3.67 km s^{-1} , while then brightening at the extended southwestern edge in the 3.51 km s^{-1} channel. Feature G emission peaks in the 3.83 km s^{-1} channel, and appears as a stream of emission to the east of Feature D. Feature H is a streamer to the southwest of Feature B and the south of Feature F, which first appears in the 3.83 km s^{-1} channel. It persists in both the 3.67 and 3.51 km s^{-1} channels shown in Figure 3.4, and more faintly extends into two bluer channels not shown in the figure. Feature I first appears in the 3.51 km s^{-1} channel, brightens in the two bluer channels not shown in the figure, and is not detectable at velocities lower than that.

Feature J, referred to as L1451-west in the rest of the chapter, is relatively round emission that only appears in the N_2H^+ data. It first appears in the 4.79 km s^{-1} channel of Figure 3.6, and extends across a total of four channels per hyperfine component (the structure can be seen repeating for another hyperfine component, starting in the 3.84 km s^{-1} channel). We discuss details of the structure and kinematics of L1451-west in Section 3.8.3.

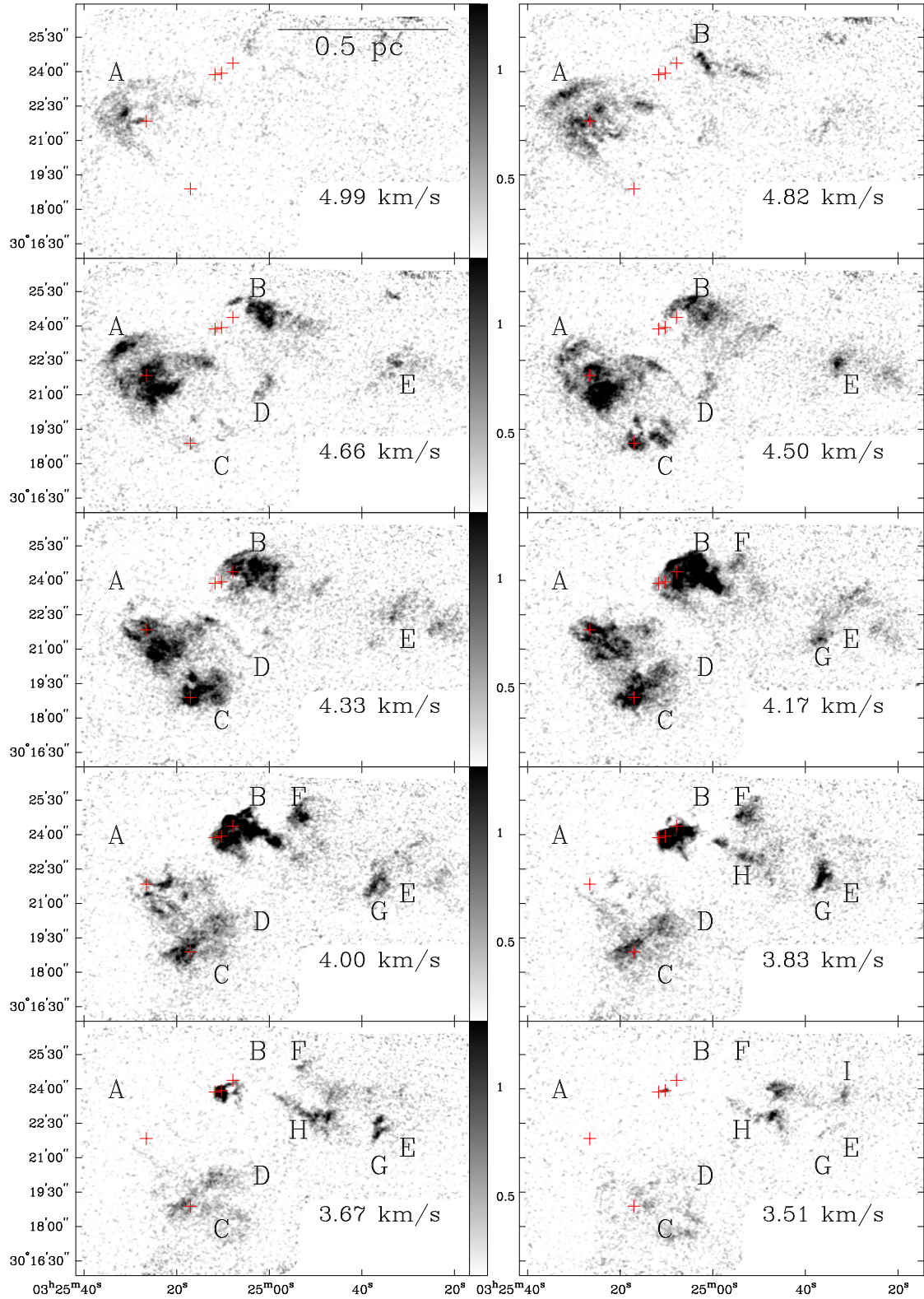


Figure 3.4: Ten HCO^+ channels maps. The rms in each channel is $0.12 \text{ Jy beam}^{-1}$, and the color intensity ranges from 0.12–1.3 Jy beam^{-1} . The red crosses represent the locations of the L1451-mm compact continuum core and the Bolocam sources. Features discussed in the text are identified with a letter in the first channel they appear.

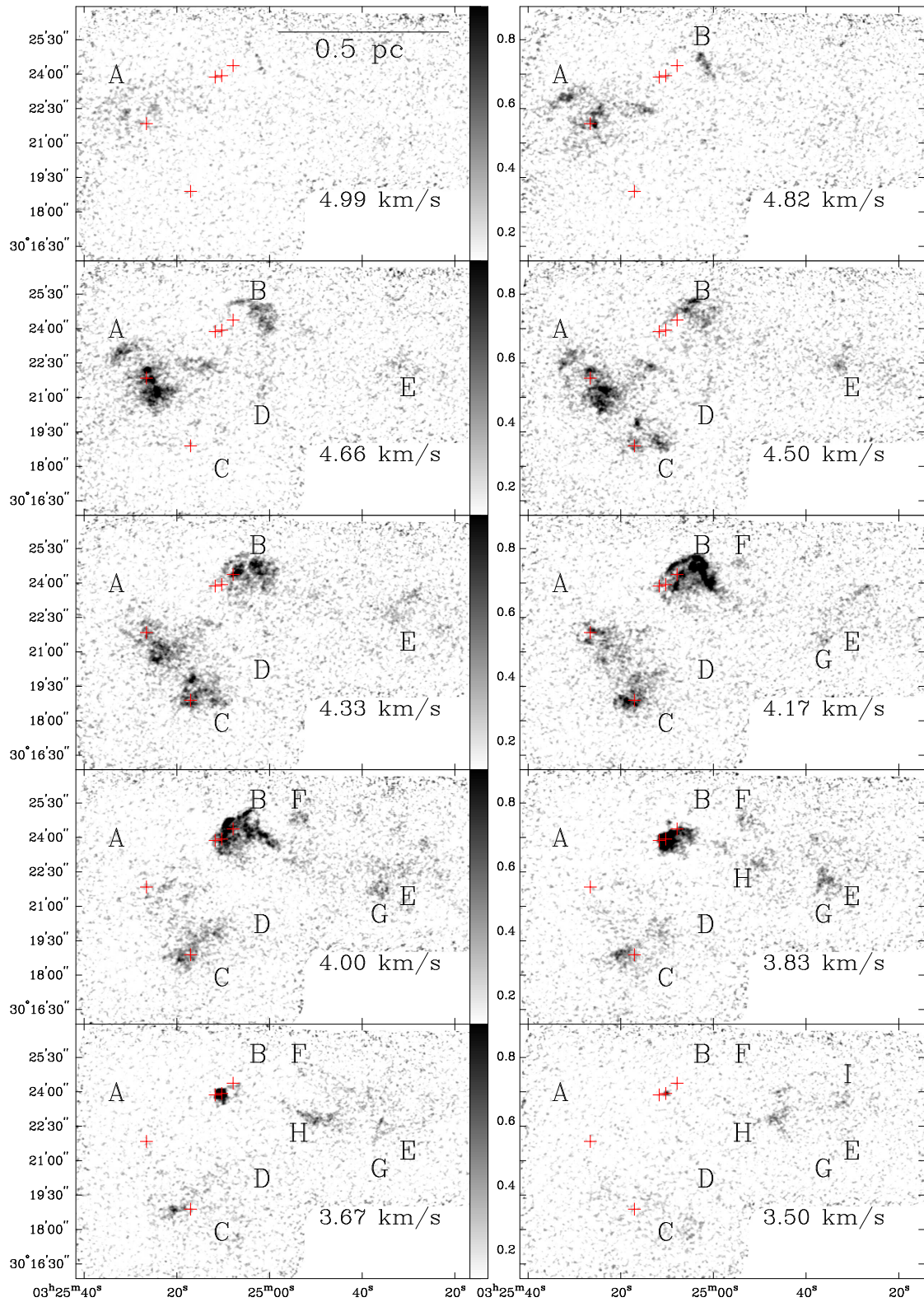


Figure 3.5: Similar to Figure 3.4, but for HCN. The rms in each channel is $0.12 \text{ Jy beam}^{-1}$, and the color intensity ranges from $0.12\text{--}0.9 \text{ Jy beam}^{-1}$. Feature labels from Figure 3.4 are overplotted in the same locations for aid in comparing the emission across molecules.

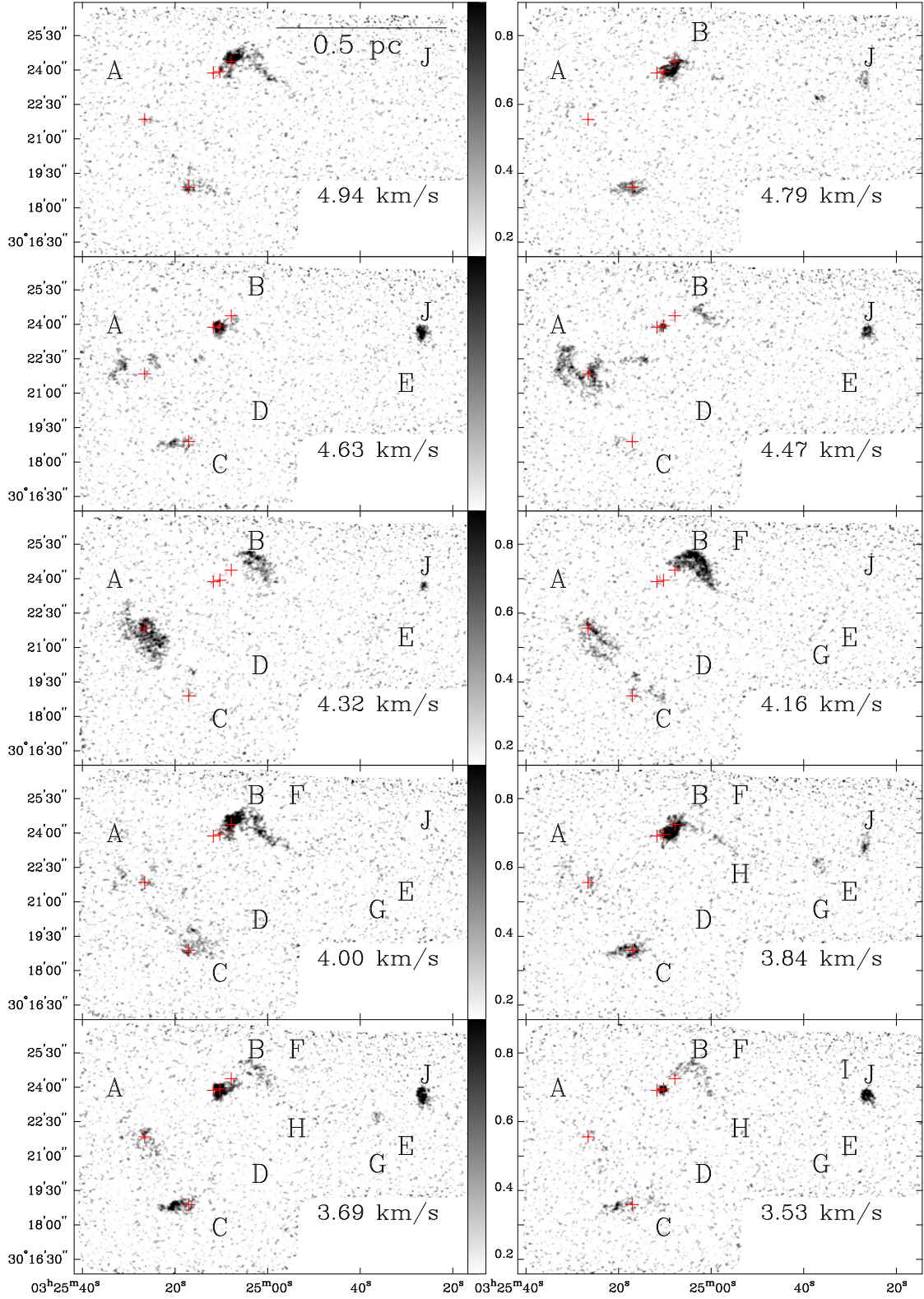


Figure 3.6: Similar to Figure 3.4, but for N_2H^+ . The rms in each channel map is $0.14 \text{ Jy beam}^{-1}$, and the color intensity ranges from 0.14 – 0.9 Jy beam^{-1} . Feature labels from Figure 3.4 are overlotted in the same locations for aid in comparing the emission across molecules. Feature J (also referred to as L1451-west) only appears in N_2H^+ , so it is only labeled in this figure.

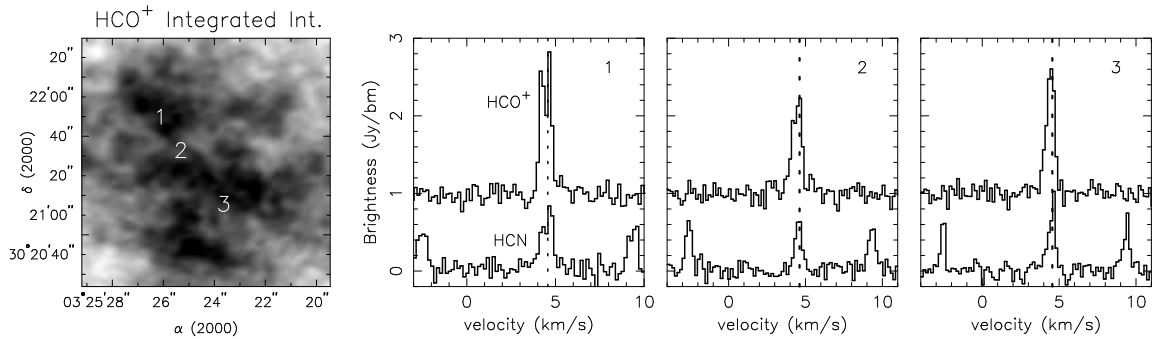


Figure 3.7: Example HCO⁺ and HCN spectra from three locations within Feature A (integrated intensity in greyscale on left), highlighting the varying spectra seen in CLASSy data toward L1451. Spectra are averaged over one synthesized beam at each location, and the HCO⁺ spectra are shifted by 1 Jy beam⁻¹ for visualization. The dashed line represents the centroid velocity of N₂H⁺ emission at each location.

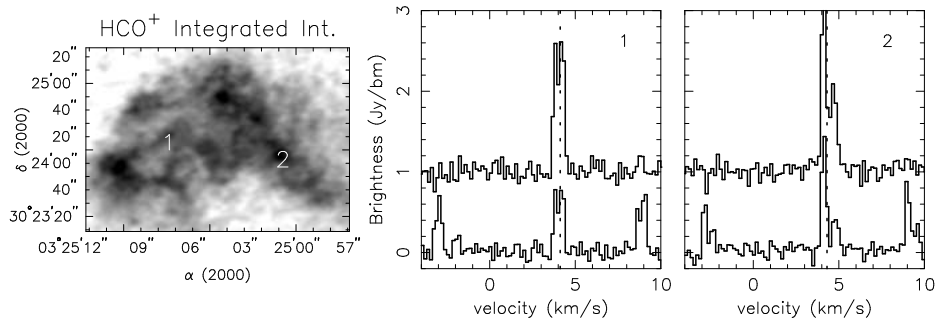


Figure 3.8: Example HCO⁺ and HCN spectra from two locations within Feature B. Spectra are averaged over one beam at each location, and the HCO⁺ spectra are shifted by 1 Jy beam⁻¹ for visualization. The dashed line represents the centroid velocity of N₂H⁺ emission at each location.

3.5 Kinematics of Dense Molecular Gas

We fitted the molecular line emission with gaussians as described in Chapter 2 (Section 2.5), and present the centroid velocity and line-of-sight velocity dispersion maps here. The N_2H^+ line was simple to fit relative to the other lines; there is only one velocity component along each line-of-sight and there is no sign of self-absorption. Examples of HCN and HCO^+ spectra with double peaks, which could be interpreted as self-absorption or two components along the line-of-sight, were shown in Figures 3.7 and 3.8. Since we cannot determine which of these scenarios is correct without H^{13}CN and H^{13}CO^+ observations at each cloud location, and since the available evidence points towards self-absorption being the dominant factor, we fit the HCN and HCO^+ lines with a single component across the entire field. Modeling the self-absorption across so many spectra is beyond the scope of this chapter. About 3% of HCO^+ spectra could be fit with two peaks separated by three or more channels, while about 0.2% could be fit with two peaks separated by five or more channels. By extrapolating self-absorbed spectra to a single peak, and measuring the full width at half of that peak, we estimate that the velocity dispersion is overestimated by $\sim 10\%$ toward these locations. Therefore, double-peaks have a relatively small overall impact on the results presented in this chapter.

There are no outflows affecting the line profiles. A low-velocity outflow from L1451-mm was previously detected in CO ($J = 2 \rightarrow 1$) by Pineda et al. (2011), but we do not detect any outflow signature in our HCN or HCO^+ ($J = 1 \rightarrow 0$) observations.

In Figure 3.9, we plot the fitted centroid velocity and velocity dispersion where: 1) the integrated intensity is greater than or equal to four times the rms of the integrated intensity map, and 2) the peak signal-to-noise of the spectrum is greater

than five. We will use these kinematic maps in the following section in order to interpret the hierarchical and turbulent nature of the cloud. Here we list some broad features of interest pertaining to the maps:

1. HCO^+ has systematically larger line-of-sight velocity dispersion compared to HCN and N_2H^+ , even if we account for an overestimation of velocity dispersion due to fitting self-absorbed spectra. Mean velocity dispersions across the maps are 0.29 ± 0.10 , 0.16 ± 0.07 , 0.12 ± 0.04 km s^{-1} , for HCO^+ , HCN, and N_2H^+ , respectively. If we assume that the typical temperature in this region is 10 K based on ammonia observations of Bolocam cores (Rosolowsky et al. 2008a), then the isothermal sound speed of the gas would be 0.20 km s^{-1} . The N_2H^+ velocity dispersions are subsonic everywhere, the HCN are subsonic most places, and the HCO^+ are transsonic to supersonic most places. Note that even though N_2H^+ and HCN are subsonic in many areas of L1451, they are not exhibiting purely thermal velocity dispersions, which would be ~ 0.05 km s^{-1} for 10 K gas.

The $J = 1 \rightarrow 0$ line of HCO^+ trace densities about an order of magnitude lower than that of HCN and N_2H^+ (see Shirley 2015, and Chapter 1). Therefore, we are likely observing the trend from supersonic to subsonic gas motions as gas goes from the larger, less-dense scales traced by HCO^+ to the smaller, more-dense scales traced by HCN and N_2H^+ . This is expected in a turbulent medium, where velocity dispersion scales proportionally with size (as is the case for observations of an optically-thin turbulent gas; McKee & Ostriker 2007).

2. All three molecules are tracing gas with centroid velocities ranging from ~ 3.8 – 4.7 km s^{-1} . However, the HCO^+ gas extends to lower velocities, due to the gas

in the feature H streamer, which appears in the HCN maps, but is not strong enough to provide reliable kinematic measurements. HCO^+ also extends to higher velocities, due to gas from the northeast part of feature A, which is noticeable in the first channel of Figure 3.4.

3. The HCO^+ centroid velocities for features A and C show a clear gradient from northeast to southwest. It is possible that this is a large, rotating piece of dense gas, which is fragmenting into denser components (e.g., the Bolocam 1 mm sources). It is also possible that the redshifted northeast section and the blueshifted southwest section represent independent components in the turbulent medium, or that they are merely projected along the same line of sight. Observations of optically thin tracers, and tracers of lower-density, larger-scale material are needed to help distinguish between these scenarios.
4. The gas in the eastern half of feature B shows an axial velocity gradient. It is most blueshifted at the southeastern end near the L1451-mm core, and becomes increasingly redshifted further away to the northwest. The gas immediately surrounding the L1451-mm compact continuum core has a centroid velocity pattern that is consistent with rotation (Pineda et al. 2011), and has velocity dispersions that increase toward the core center. L1451-west shows similar N_2H^+ kinematic features, and we compare these two sources in detail in Section 3.8.3.
5. Our measurements of N_2H^+ centroid velocity and velocity dispersion towards L1451-mm agree well with the results in Pineda et al. (2011), in terms of absolute values measured and gradients across the source.

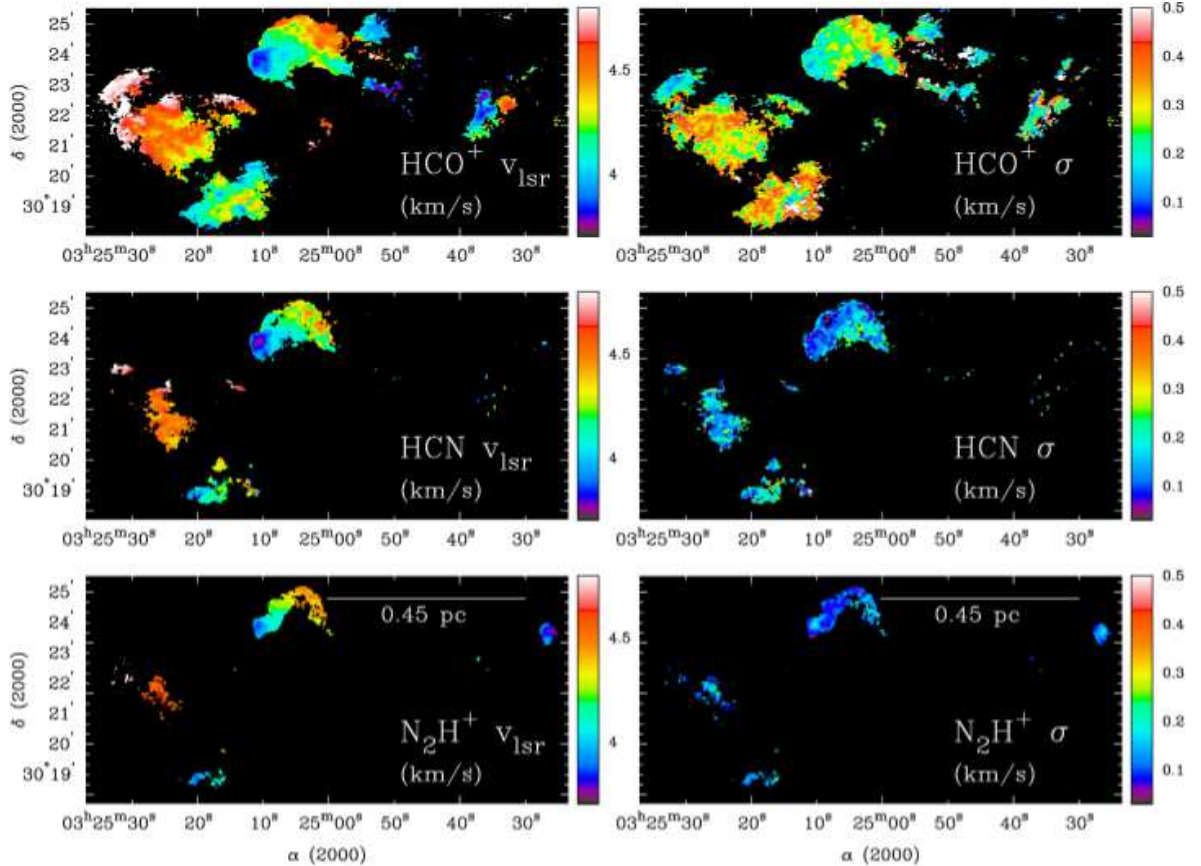


Figure 3.9: Kinematics of dense gas in L1451. *Left:* Centroid velocity maps of HCO^+ , HCN , and N_2H^+ ($J = 1 \rightarrow 0$) emission, from top to bottom. *Right:* Line-of-sight velocity dispersion maps of HCO^+ , HCN , and N_2H^+ ($J = 1 \rightarrow 0$) emission, from top to bottom. We masked these maps to visualize only statistically robust kinematic results (see Section 3.5 text). The color scales are the same across molecules.

3.6 Dendrogram Analysis of Molecular Emission

3.6.1 The Non-binary Dendrograms

We qualitatively described the dense gas morphology of L1451 in Section 3.4. Here we quantitatively identify dense gas structures in all three molecular tracers, and study the hierarchical nature of L1451 with the non-binary dendrogram algorithm described in Chapter 2 and Appendix B.

A dendrogram algorithm identifies emission peaks in a dataset, and keeps track of how those peaks merge together at lower emission levels. This method of identifying and tracking emission structures is advantageous compared to a watershed object-identification algorithm, such as CLUMPFIND (Williams et al. 1994), when the science goals include understanding how the morphology and kinematics of star-forming gas connects from large to small scales. A full discussion of the most widely used dendrogram algorithm can be found in Rosolowsky et al. (2008b); details of dendrograms and our non-binary version of the dendrogram algorithm are found in the Appendix A and B, along with a comparison with the results from using a more standard clump-finding algorithm on our CLASSy data.

We ran our non-binary dendrogram algorithm on the HCO^+ emission, the emission from the strongest HCN hyperfine line, and the emission from the strongest N_2H^+ hyperfine line. For other CLASSy regions, we limited our analysis to N_2H^+ emission because the HCO^+ and HCN lines were complicated by protostellar outflows and severe self-absorption effects. We also ran the algorithm on the isolated N_2H^+ hyperfine component in the other CLASSy regions because the stronger hyperfine components come in clusters of three and were not resolved in every location. The N_2H^+ hyperfine components in L1451 are resolved in all locations, letting us use the strongest component for our dendrogram analysis. A caveat is that some bluer emission from the higher-velocity, adjacent hyperfine component, and some redder emission from the lower-velocity, adjacent hyperfine component appear in the channels of the strongest component. Since there was no blending of hyperfine emission at the same location within the cloud, we masked the emission from the adjacent hyperfine components in the individual channels of the strongest hyperfine component in which they appeared. As an example, L1451-west (Feature J) appears in much bluer channels compared to Feature A, so L1451-west from the

higher-velocity, adjacent hyperfine component also appears in the reddest channel of the strongest hyperfine component that shows Feature A. For this example, we simply masked out L1451-west from this red channel of the strongest component.

We ran the algorithm with similar parameters used for the Barnard 1 analysis described in Chapter 2, while following the prescription for comparing data cubes with different noise levels presented in Appendix C. As in Chapter 2 (Section 2.6.1), we masked the channel emission of each PPV cube, only keeping pixels $\geq 4\sigma$ along with adjacent pixels of at least 2.5σ , where σ is the rms level of the data cube. For the `minpixel` noise-suppression parameter, we again required at least three synthesized beam areas of pixels for a leaf to be considered real. Appendix C shows that using uniform `minheight` and `stepsize` allows a proper comparison of dendrogram properties that is independent of noise-level differences between data cubes. Therefore, the `minheight` noise-suppression parameter required a local maximum to peak at least $2\sigma_n$ above the intensity where it merges with another local maximum for it to be considered a leaf, where σ_n is the rms level of the noisiest data cube (N_2H^+ at $\sim 0.14 \text{ Jy beam}^{-1}$, in this case). The `stepsize` parameter allowed branching at integer values of $1\sigma_n$.

Figures 3.10, 3.11, and 3.12 show HCO^+ , HCN , and N_2H^+ non-binary dendrograms for L1451, respectively. The vertical axis of the dendrograms represents the intensity range of the pixels belonging to a leaf or branch. The horizontal axis is arranged with the major features identified in Figures 3.4–3.6 progressing from east-to-west; we label certain branches that are associated with major features, and we provide the numeric label for structures referred to in the upcoming discussion. The isolated leaves are presented in numerical order. The horizontal dotted line in each dendrogram represents an intensity cut at $2.5\sigma_n$ that aids in cross-comparison of dendrogram statistics (see Appendix C), and is discussed in Section 3.6.3.

The HCO^+ dendrogram contains the largest number of structures, with 86 leaves and 27 branches. The HCN dendrogram contains 33 leaves and 13 branches, while the N_2H^+ dendrogram only contains 16 leaves and 6 branches. Leaves that peak at least $6\text{-}\sigma_n$ in intensity above the branch they merge directly into are colored green in Figures 3.13–3.15, and referred to as high-contrast leaves³. The strongest leaf for every molecule is at or near the location of L1451-mm in Feature B: Leaf 66 is the strongest structure in the HCO^+ dendrogram, with a peak intensity of $2.78 \text{ Jy beam}^{-1}$, leaf 30 is the strongest structure in the HCN dendrogram, with a peak intensity of $2.58 \text{ Jy beam}^{-1}$, and leaf 10 is the strongest structure in the N_2H^+ dendrogram, with a peak intensity of $1.62 \text{ Jy beam}^{-1}$.

3.6.2 Dendrogram Spatial and Kinematics Properties

The leaves and branches of each dendrogram represent molecular structures. We fit for the spatial properties of each structure, as we did in Chapter 2, using the `regionprops` program in MATLAB. This program fits an ellipse to the integrated intensity footprint of each dendrogram structure to determine its RA centroid, DEC centroid, major axis, minor axis, and position angle. Columns 2–6 in Tables 3.4–3.6 list the spatial properties of each structure. To quantify the shape of each structure, we use the axis ratio and filling factor of the fit (Columns 7 and 8 of Tables 3.4–3.6). We lastly define the structure size (Column 9 of Tables 3.4–3.6) as the geometric mean of the major and minor axes, assuming a distance of 235 pc when converting to parsec units.

Histograms of the size, filling factor, and axis ratio for all leaves and branches are plotted in the top rows of Figures 3.13–3.15. All HCO^+ and HCN leaves are

³We will use the definition of high-contrast leaves, first introduced in Chapter 2, as a way of comparing the properties of strong leaves across CLASSy clouds in future papers.

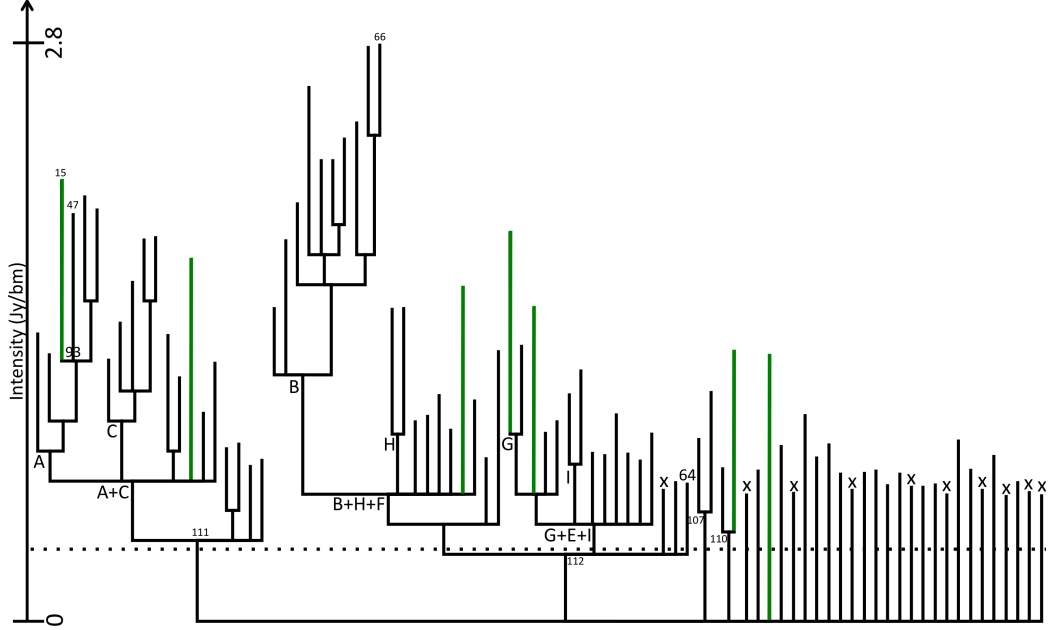


Figure 3.10: The HCO^+ non-binary dendrogram for L1451. The vertical axis represents the Jy beam^{-1} intensity for a given location within the gas hierarchy. The horizontal axis is ordered so that features identified in Section 3.4 are generally ordered from east to west. Leaves and branches discussed in the text are labeled with their numerical identifier, and branches associated with major features from Section 3.4 are marked with the feature letter. The leaves colored green peak at least $6\text{-}\sigma_n$ above their first merge level. The horizontal dotted line represents the $2.5\text{-}\sigma_n$ intensity cut above which we calculate tree statistics when comparing different dendrograms.

smaller than 0.11 pc, while all N_2H^+ leaves are smaller than 0.06 pc. HCO^+ branches are the largest of all molecules, peaking at 0.46 pc, while HCN branches peak at 0.24 pc, and N_2H^+ branches peak at 0.17 pc. This is expected since HCO^+ shows the most widespread emission in the channel and integrated emission maps. The filling factor for all molecular structures is between 0.45 and 0.95. The structures with filling factor closest to one are leaves, indicating that leaves are more likely to be elliptically shaped objects while branches are more likely to be irregularly shaped objects. The axis ratio for all structures is between 0.19 and 0.95, showing that there is a distribution from elongated to round structures, without differences between leaves and branches. There are no obvious differences between the high-

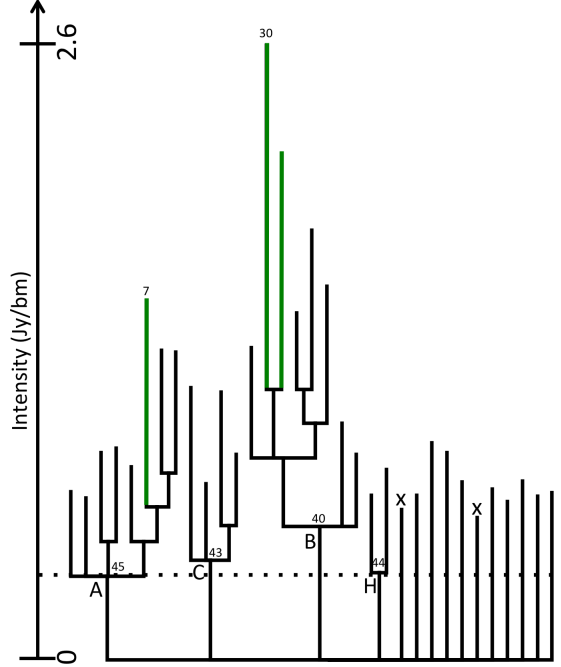


Figure 3.11: Same as Figure 3.10, but for the HCN non-binary dendrogram.

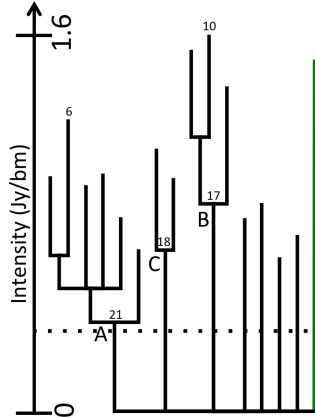


Figure 3.12: Same as Figure 3.10, but for the N_2H^+ non-binary dendrogram.

contrast leaves and the rest of the leaves.

We use the integrated intensity footprints of the dendrogram structures in combination with the centroid velocity and velocity dispersion maps to determine kinematic properties of leaves and branches. The four properties present in Tables 3.4–3.6 are: mean and rms centroid velocity ($\langle V_{\text{lsr}} \rangle$ and ΔV_{lsr} , respectively), and mean and rms velocity dispersion ($\langle \sigma \rangle$ and $\Delta \sigma$, respectively). We illustrated how to derive

these properties for leaves and branches in Chapter 2 (Section 2.6 and Figure 2.17).

Histograms of $\langle V_{\text{lsr}} \rangle$, ΔV_{lsr} , and $\langle \sigma \rangle$ are plotted in the bottom rows of Figures 3.13–3.15. HCO^+ traces larger variation in $\langle V_{\text{lsr}} \rangle$ compared to HCN and N_2H^+ . We attribute this to HCO^+ being sensitive to more widespread emission away from the densest regions of L1451, and therefore tracing more widespread centroid velocities relative to the systemic velocity of the most spatially compact gas. For all molecules, ΔV_{lsr} of the leaves generally extends from low to moderate velocities, while it is distributed from moderate to high velocities for the branches. This indicates a trend where ΔV_{lsr} is generally lower for smaller structures than larger structures. This trend was also seen for Barnard 1 gas structures, and we discussed explanations in Chapter 2 (Section 2.6.4); the primary reason was the scale-dependent nature of turbulence, which causes gas parcels separated by smaller distances to have smaller rms velocity differences between them (McKee & Ostriker 2007).

The distribution of $\langle \sigma \rangle$ is similar for leaves and branches, with neither distribution showing a preference to peak at high or low velocities. This trend was also seen in Chapter 2 for Barnard 1, indicating that $\langle \sigma \rangle$ does not strongly depend on the projected size of a structure. The peak $\langle \sigma \rangle$ for HCO^+ is higher compared to HCN and N_2H^+ : 0.42 km s^{-1} , 0.18 , and 0.13 km s^{-1} , respectively. Since HCO^+ traces effective excitation densities of an order of magnitude lower than HCN and N_2H^+ (Shirley 2015), we are likely observing emission from lower-density gas that is more extended along the line-of-sight. This could increase the line-of-sight velocity dispersions, which are expected to scale with cloud depth in a turbulent medium (McKee & Ostriker 2007). We note that although the HCO^+ velocity dispersion measurements are likely inflated by $\sim 10\%$ in regions with double-peaked spectra, this is not a large enough effect to produce the difference between HCO^+ and the other molecules. There are no obvious differences in these kinematic properties

between the high-contrast leaves and the rest of the leaves.

3.6.3 Tree Statistics

The dendrograms in Figures 3.10–3.12 show an apparently wide variety of hierarchical complexity between molecular tracers, and between sub-regions of L1451. In this section, we quantify the hierarchical nature of the gas with tree statistics that were introduced and explained in Chapter 2 so that the complexity between molecules and sub-regions can be quantitatively compared. Specifically, we calculate the maximum branching level, mean path length, and mean branching ratio of the entire L1451 region for each molecule in a uniform way that accounts for differences in the noise-level of each data cube (see Appendix C). We then calculate those same statistics for individual features within each dendrogram.

The path length, defined only for leaves, is the number of branching levels it takes to go from a leaf to the tree base. The branching ratio, defined only for branches, is the number of structures a branch splits into immediately above it in the dendrogram. We will be linking these tree statistics to cloud fragmentation in the discussion to follow. A more evolved region with a lot of hierarchical fragmentation will have a higher maximum branching level and larger mean path length than a young region that is starting to form overdensities and fragment. The branching ratio of a very hierarchical region will be smaller than a region fragmenting into many substructures in a single step. This is likely an overly simplistic view, since the molecular emission, and in turn, the dendrograms and tree statistics, can also be affected by projection effects and line opacity. We briefly discussed these effects in Chapter 2; since they are extremely difficult to accurately model over such a large area, we use the simple view that hierarchy comes from fragmentation⁴.

⁴Although a few regions within L1451 show double-peaked HCO⁺ spectra, which we attribute

The PPV cubes of all three molecules have slightly different noise levels, and we created the dendrograms by following the Appendix C discussion of how dendrogram structure and statistics depend on noise. Based on Appendix C, to compare the tree statistics of dendrograms derived from maps with different noise levels, we only count leaves and branches above a $2.5\text{-}\sigma_n$ intensity cut, where σ_n is the rms of the noisiest data cube. The N_2H^+ PPV cube has the highest noise level, at $\sim 0.14 \text{ Jy beam}^{-1}$, so the cut for each dendrogram is at $\sim 0.35 \text{ Jy beam}^{-1}$, and is represented as the horizontal dotted line in Figures 3.10–3.12. Only leaves that peak at least $2\text{-}\sigma_n$ above the cut are still considered in these statistics—all other leaves are marked with an “x” in the dendrogram. A branch below the cut is discounted, but if the leaf directly above it is more than $2\text{-}\sigma_n$ above the cut, then the leaf is counted as a leaf with a branching level of zero (e.g., leaf 64 in Figure 3.10). This comparison of tree statistics ensures that we can analyze the fragmentation of molecular emission independent of noise-level differences.

The tree statistics for the entire L1451 region are reported in the first section of Table 3.7. The mean branching ratios are 3.8, 3.3, and 3.0 for HCO^+ , HCN , and N_2H^+ , respectively. We interpret this to mean that each molecule is tracing physical structures that are fragmenting in a hierarchically similar way (e.g., a structure is most likely to fragment into about three to four sub-structures). The mean path length of HCO^+ is 1.0 level longer than that of HCN and N_2H^+ , and the maximum branching level of HCO^+ is two more than that of HCN and three more than that

primarily to self-absorption, the dendrogram algorithm rarely splits structures containing such spectral features in two. We searched the dendrogram structure cube and data cube by eye, and determined that only leaves 15 and 47 are likely split due to self-absorption. This has the effect of reducing the branching ratio of branch 93 from three to two, has no effect on the maximum branching level, and minimally impacts the other average tree statistics. Therefore, we do not consider the HCO^+ dendrogram to be contaminated by self-absorption.

of N_2H^+ . This trend in fragmentation levels is likely due to the ability of each tracer to detect material at different spatial scales and physical densities. As the effective excitation density of the tracer goes down from N_2H^+ to HCN to HCO^+ , our observations are more sensitive to more widespread emission, which means we are sensitive to more levels of fragmentation extending from the higher-density leaves (detectable with all tracers) to the lowest detectable branches (most detectable with HCO^+). Therefore, even though the dendrograms in Figures 3.10–3.12 look very different, a comparison of their tree statistics using a uniform noise-level cut, along with an understanding of what each molecule is tracing, produces a consistent picture of how L1451 is hierarchically fragmenting from parsec-scales into much smaller-scale structures.

Features A, B, and C are the only features with any hierarchical complexity in the N_2H^+ dendrogram, and are the ones with the most branching steps in the HCN and HCO^+ dendrograms. They are also the most likely sites for current and future star formation, since they account for emission surrounding the only continuum source detections in the field: Feature B surrounds L1451-mm, and Features A and C surround Bolocam 1 mm sources. Because of this, we next compare the tree statistics of these sub-regions in Table 3.7, along with a comparison to any other sub-region with hierarchical complexity (labeled as “others” in Table 3.7), using the original dendrograms of each molecular tracer. We do not use a noise-level cut because we are comparing different sub-regions of the same data cube. The sections of the dendrograms corresponding to individual features are marked in Figures 3.10–3.12 with letter identifiers, and we only consider structures above those identifiers in this comparison. For example, in the HCO^+ dendrogram, Feature A and C merge together at the branch labeled “A+C,” but we consider the statistics of the individual features only above labels “A” and “C”.

There is a trend of decreasing maximum branching level and mean path length from Feature B to A to C and then to the other remaining features. Feature A and B are more similar to one another than either is to the remaining other features, indicating that the gas in both features has fragmented a similar amount relative to the rest of the complex structure in the L1451 field. The mean path length and maximum branching level of Feature C bridge the gap between the maximum fragmentation amount seen in Feature A and B and the minimum fragmentation amount seen in the remaining other features.

We interpret the similarity in hierarchical branching levels between Features A and B to mean that these subregions have progressed to a similar stage along the evolutionary track of cloud fragmentation. We know a young star or first core (L1451-mm) is forming within Feature B at or near the location of the maximum intensity (leaf 66, 30, and 10 for HCO^+ , HCN, and N_2H^+ , respectively). For Feature A, PerBolo 6 is at or near the location of maximum intensity in Feature A (leaf 15, 7, and 6 for HCO^+ , HCN, and N_2H^+ , respectively). We argue that with Feature A and B showing very similar tree statistics, Feature B having a confirmed compact continuum detection at its hierarchical peak, and Feature A having a single-dish continuum detection at its hierarchical peak, that a star is likely to form within Feature A. This argument can be extended to Feature C being the next most likely place for current or future star formation, followed by the even less fragmented features. Follow-up observations of the single-dish cores and other column density enhancements in these features will be useful for testing this expectation. The mean branching ratios between all features are similar for all molecules, indicating that all structures are fragmenting into a similar number of sub-structures at each branching step, regardless how far a feature is along its evolution toward forming stars.

Table 3.4. HCO⁺ Dendrogram Leaf and Branch Properties

No.	RA	DEC	Maj. Axis	Min. Axis	PA	Axis	Filling	Size	$\langle V_{\text{lsr}} \rangle$	ΔV_{lsr}	$\langle \sigma \rangle$	$\Delta \sigma$	Pk. Int.	Contrast	Level
(1)	(h:m:s)	($^{\circ}$: $'$: $''$)	($''$)	($''$)	($^{\circ}$)	Ratio	Factor	(pc)	(km s ⁻¹)	(km s ⁻¹)	(km s ⁻¹)	(km s ⁻¹)	(Jy beam ⁻¹)	(15)	(16)
Leaves															
0	03:24:41.3	+30:26:06.4	33.0	6.4	98.3	0.19	0.67	0.017	0.88	2.4	1
1	03:24:39.5	+30:26:02.9	19.7	11.7	99.1	0.60	0.73	0.017	1.10	4.0	1
2	03:25:31.2	+30:22:13.1	33.1	19.8	138.7	0.60	0.86	0.029	5.03(2)	0.07(1)	0.16(2)	0.07(1)	1.39	3.9	3
3	03:25:19.6	+30:23:38.3	36.0	17.8	62.1	0.49	0.58	0.029	0.61	2.1	0
4	03:24:49.5	+30:26:05.1	31.2	20.4	109.1	0.65	0.50	0.029	0.72	2.9	0
5	03:24:28.7	+30:26:13.6	94.0	23.5	86.7	0.25	0.86	0.054	1.28	6.8	0
6	03:24:48.5	+30:26:22.2	20.6	8.1	103.8	0.39	0.81	0.015	0.85	3.8	0
7	03:24:35.5	+30:21:47.8	30.7	15.7	160.2	0.51	0.78	0.025	4.08(6)	0.13(5)	0.26(7)	0.16(6)	0.81	2.4	2
8	03:25:15.7	+30:22:34.7	31.9	14.7	92.3	0.46	0.71	0.025	4.77(1)	0.04(1)	0.24(1)	0.04(1)	1.17	2.4	3
9	03:24:52.7	+30:23:59.2	33.1	22.9	95.1	0.69	0.81	0.031	4.77(4)	0.10(3)	0.22(4)	0.12(3)	0.99	2.6	3
10	03:24:54.4	+30:24:13.2	40.1	10.8	130.4	0.27	0.75	0.024	0.96	2.4	3
11	03:24:36.7	+30:25:25.5	26.8	10.9	159.7	0.41	0.64	0.019	0.74	2.1	1
12	03:25:35.5	+30:20:44.9	47.6	27.3	134.2	0.57	0.48	0.041	0.62	2.2	0
13	03:25:31.6	+30:21:34.6	18.1	14.7	105.5	0.81	0.86	0.019	4.72(2)	0.04(2)	0.21(2)	0.04(2)	1.29	2.2	4
14	03:25:01.2	+30:21:13.7	140.5	65.4	139.4	0.47	0.62	0.109	4.63(2)	0.09(2)	0.21(2)	0.07(1)	0.99	4.8	0
15	03:25:26.1	+30:21:54.4	56.7	42.0	134.6	0.74	0.71	0.056	4.55(1)	0.05(1)	0.30(1)	0.05(1)	2.12	6.0	5
16	03:25:31.1	+30:22:56.5	117.4	53.9	121.4	0.46	0.75	0.091	4.76(1)	0.06(0)	0.17(0)	0.04(0)	1.74	7.4	2
17	03:24:55.8	+30:24:31.8	22.8	13.1	81.8	0.57	0.86	0.020	4.46(3)	0.06(2)	0.41(1)	0.03(1)	1.09	3.3	3
18	03:24:33.9	+30:25:25.8	83.2	41.1	78.3	0.49	0.52	0.067	1.30	6.0	1
19	03:24:23.9	+30:26:05.6	19.9	13.0	67.9	0.65	0.64	0.018	0.79	3.4	0
20	03:24:25.3	+30:26:11.1	22.3	16.5	42.6	0.74	0.57	0.022	0.85	3.8	0
21	03:25:24.8	+30:20:47.6	37.9	26.3	60.9	0.70	0.85	0.036	4.45(1)	0.06(1)	0.28(1)	0.03(1)	1.98	3.1	6
22	03:25:23.3	+30:21:16.3	61.8	28.6	82.9	0.46	0.76	0.048	4.52(1)	0.05(1)	0.28(0)	0.03(0)	2.05	3.5	6
23	03:24:33.4	+30:21:51.4	16.5	11.8	77.1	0.71	0.95	0.016	0.91	2.0	3
24	03:25:33.2	+30:22:00.4	16.7	10.0	12.9	0.60	0.79	0.015	1.01	2.3	2
25	03:24:32.9	+30:22:23.2	45.8	40.6	107.3	0.89	0.80	0.049	4.55(2)	0.08(1)	0.24(2)	0.08(1)	1.51	6.2	3
26	03:24:28.1	+30:22:23.4	21.4	14.5	122.1	0.68	0.70	0.020	0.80	2.3	2
27	03:24:55.0	+30:22:45.3	16.4	13.5	174.7	0.82	0.87	0.017	0.78	2.2	2
28	03:24:47.4	+30:23:56.4	25.1	12.6	83.8	0.50	0.81	0.020	0.92	2.2	3
29	03:25:04.3	+30:25:07.5	24.6	18.8	104.6	0.77	0.78	0.025	4.40(2)	0.06(2)	0.33(2)	0.05(1)	1.83	4.5	4
30	03:25:16.3	+30:18:43.7	30.0	9.1	107.0	0.30	0.83	0.019	4.30(1)	0.03(1)	0.28(2)	0.04(1)	1.85	2.1	5
31	03:25:25.2	+30:18:48.8	26.6	13.5	161.9	0.51	0.68	0.022	0.71	2.8	0
32	03:25:11.4	+30:18:58.2	32.8	11.4	101.8	0.35	0.73	0.022	4.35(3)	0.07(2)	0.24(3)	0.07(2)	1.44	2.3	4
33	03:25:10.9	+30:19:44.6	29.0	17.5	52.5	0.60	0.66	0.026	4.19(2)	0.07(2)	0.35(1)	0.04(1)	1.26	2.0	3
34	03:25:16.4	+30:19:45.1	25.9	23.8	4.4	0.92	0.92	0.028	4.28(1)	0.05(1)	0.27(1)	0.05(1)	1.64	3.6	4
35	03:25:07.6	+30:21:15.2	55.4	40.0	58.9	0.72	0.65	0.054	0.63	2.3	0
36	03:24:13.5	+30:21:11.5	29.7	9.4	41.8	0.32	0.64	0.019	0.71	2.8	0
37	03:24:22.8	+30:21:53.0	98.6	42.2	85.8	0.43	0.64	0.074	4.32(2)	0.06(1)	0.30(3)	0.07(2)	1.00	3.7	2
38	03:25:12.9	+30:22:16.9	46.8	18.8	67.8	0.40	0.81	0.034	4.55(2)	0.08(1)	0.24(1)	0.04(1)	1.38	3.9	3
39	03:24:34.1	+30:23:38.8	52.1	17.6	79.0	0.34	0.60	0.034	0.63	2.1	1
40	03:24:58.9	+30:24:29.8	20.8	14.7	100.0	0.70	0.87	0.020	4.44(1)	0.02(1)	0.25(1)	0.03(1)	1.51	2.2	4
41	03:25:22.3	+30:16:09.9	26.5	18.8	116.1	0.71	0.69	0.025	0.72	2.9	0
42	03:25:18.2	+30:18:47.6	21.6	12.1	83.3	0.56	0.74	0.018	4.21(3)	0.07(3)	0.32(1)	0.02(1)	1.84	2.0	5
43	03:24:51.8	+30:19:51.7	17.2	9.4	129.5	0.55	0.89	0.014	0.65	2.4	0
44	03:24:20.8	+30:21:04.1	17.2	8.8	34.5	0.51	0.84	0.014	0.67	2.4	1
45	03:24:36.6	+30:21:25.7	27.3	11.5	82.8	0.42	0.78	0.020	4.18(1)	0.03(1)	0.15(2)	0.04(1)	1.33	2.9	4
46	03:25:15.9	+30:21:50.6	71.0	42.4	69.2	0.60	0.66	0.063	4.34(2)	0.10(1)	0.25(1)	0.05(1)	1.24	3.9	2
47	03:25:25.2	+30:21:50.4	60.2	19.5	66.7	0.32	0.74	0.039	4.46(1)	0.05(1)	0.34(1)	0.03(0)	1.96	4.9	5

Table 3.4 (cont'd)

No.	RA	DEC	Maj. Axis	Min. Axis	PA	Axis Ratio	Filling Factor	Size	$\langle V_{\text{lsr}} \rangle$	ΔV_{lsr}	$\langle \sigma \rangle$	$\Delta \sigma$	Pk. Int.	Contrast	Level
(1)	(h:m:s) (2)	($^{\circ}$: $'$: $''$) (3)	($''$) (4)	($''$) (5)	($^{\circ}$) (6)	(7)	(8)	(pc) (9)	(km s^{-1}) (10)	(km s^{-1}) (11)	(km s^{-1}) (12)	(km s^{-1}) (13)	(Jy beam^{-1}) (14)	(15)	(16)
48	03:24:30.1	+30:23:20.9	86.6	20.9	112.2	0.24	0.47	0.048	4.15(5)	0.14(4)	0.28(5)	0.13(3)	0.96	2.4	3
49	03:24:26.7	+30:23:51.0	13.7	11.3	76.9	0.82	0.83	0.014	0.81	2.3	2
50	03:25:00.5	+30:23:55.9	37.4	30.2	42.0	0.81	0.88	0.038	4.20(1)	0.05(1)	0.17(1)	0.06(1)	2.58	5.6	6
51	03:25:06.7	+30:24:19.6	19.2	13.2	115.2	0.69	0.91	0.018	4.12(1)	0.02(1)	0.25(1)	0.03(1)	2.02	2.7	5
52	03:25:04.3	+30:24:43.1	28.5	17.2	156.4	0.60	0.78	0.025	4.28(2)	0.05(1)	0.27(1)	0.04(1)	2.33	2.9	7
53	03:25:08.9	+30:24:35.9	42.9	19.9	147.7	0.46	0.65	0.033	4.14(1)	0.04(1)	0.19(1)	0.02(1)	2.40	4.4	6
54	03:25:02.5	+30:24:36.9	17.2	16.0	178.1	0.93	0.89	0.019	4.39(2)	0.04(1)	0.30(1)	0.03(1)	2.22	2.2	7
55	03:24:40.4	+30:25:00.0	28.1	18.3	35.7	0.65	0.72	0.026	0.71	2.8	0
56	03:24:25.1	+30:25:03.9	24.5	18.4	74.5	0.75	0.70	0.024	0.65	2.4	0
57	03:24:22.0	+30:22:20.8	34.6	16.8	76.4	0.48	0.68	0.027	0.77	2.1	2
58	03:25:03.9	+30:24:08.4	39.9	22.9	74.2	0.57	0.62	0.034	4.14(1)	0.03(1)	0.24(1)	0.02(0)	2.22	3.1	6
59	03:24:32.1	+30:24:11.2	24.2	12.6	147.2	0.52	0.76	0.020	0.65	2.4	0
60	03:24:53.2	+30:24:48.7	82.0	60.1	117.8	0.73	0.73	0.080	3.99(1)	0.08(1)	0.19(1)	0.07(1)	1.61	6.9	3
61	03:24:47.2	+30:25:28.6	19.9	10.6	50.9	0.53	0.76	0.017	0.66	2.4	0
62	03:25:05.8	+30:16:38.0	16.4	13.4	42.1	0.81	0.81	0.017	0.61	2.1	0
63	03:25:05.7	+30:19:44.2	34.0	14.0	135.1	0.41	0.62	0.025	0.75	2.5	1
64	03:24:43.5	+30:21:38.6	63.3	23.5	79.1	0.37	0.52	0.044	0.66	2.3	1
65	03:24:36.6	+30:22:06.6	92.5	37.6	156.8	0.41	0.62	0.067	3.86(1)	0.09(1)	0.19(1)	0.06(1)	1.87	6.7	4
66	03:25:10.3	+30:23:49.1	19.1	13.1	176.4	0.69	0.79	0.018	3.84(1)	0.02(1)	0.18(1)	0.03(1)	2.78	3.0	7
67	03:24:38.4	+30:23:55.8	19.6	18.3	25.7	0.93	0.86	0.022	0.90	3.0	2
68	03:25:09.7	+30:24:04.5	25.9	11.5	100.4	0.45	0.71	0.020	3.88(1)	0.02(1)	0.17(1)	0.02(1)	2.77	2.9	7
69	03:24:50.6	+30:25:32.0	21.1	12.2	134.6	0.58	0.85	0.018	1.06	3.1	3
70	03:25:24.7	+30:16:00.1	35.5	14.3	108.0	0.40	0.83	0.026	0.87	3.9	0
71	03:24:56.9	+30:16:09.8	31.3	19.5	173.1	0.62	0.45	0.028	0.73	2.9	0
72	03:25:23.9	+30:16:33.6	49.5	31.7	7.7	0.64	0.58	0.045	0.63	2.3	0
73	03:24:50.5	+30:22:48.1	42.9	26.0	78.5	0.61	0.60	0.038	3.71(2)	0.06(1)	0.16(1)	0.05(1)	1.51	4.2	4
74	03:24:18.4	+30:26:02.3	18.8	12.9	179.1	0.69	0.66	0.018	0.80	3.4	0
75	03:25:09.0	+30:17:32.7	26.7	18.5	84.3	0.69	0.65	0.025	0.83	2.1	2
76	03:25:05.4	+30:17:42.7	26.4	17.5	51.8	0.66	0.72	0.025	0.86	2.2	2
77	03:25:05.1	+30:18:31.4	94.4	41.7	76.3	0.44	0.66	0.071	0.78	2.7	1
78	03:25:05.3	+30:19:04.0	37.8	29.0	135.8	0.77	0.56	0.038	0.60	2.1	0
79	03:24:47.3	+30:22:48.2	32.1	22.6	136.4	0.70	0.84	0.031	3.61(1)	0.03(1)	0.17(1)	0.03(1)	1.51	4.2	4
80	03:24:45.6	+30:23:51.5	74.6	62.8	104.7	0.84	0.76	0.078	3.53(2)	0.11(1)	0.18(1)	0.09(1)	1.30	5.8	2
81	03:25:14.7	+30:17:32.2	21.8	13.8	7.6	0.63	0.77	0.020	0.67	2.5	0
82	03:24:26.3	+30:23:26.4	17.6	13.7	122.4	0.78	0.80	0.018	0.62	2.2	0
83	03:24:31.9	+30:23:38.8	39.6	16.6	144.4	0.42	0.72	0.029	3.41(2)	0.07(1)	0.19(2)	0.06(1)	1.21	3.1	3
84	03:25:16.2	+30:17:51.8	18.0	10.4	103.0	0.58	0.89	0.016	0.61	2.1	0
85	03:24:32.9	+30:23:15.7	19.0	10.1	80.2	0.53	0.85	0.016	3.34(8)	0.16(6)	0.22(9)	0.17(7)	1.09	2.3	3
Branches															
86	03:25:09.8	+30:23:52.9	47.6	42.9	118.3	0.90	0.73	0.051	3.89(1)	0.06(1)	0.19(1)	0.03(0)	2.35	...	6
87	03:25:03.4	+30:24:39.6	50.3	38.0	54.4	0.75	0.65	0.050	4.32(2)	0.07(1)	0.29(1)	0.04(1)	1.91	...	6
88	03:25:02.7	+30:24:17.9	110.8	59.8	49.9	0.54	0.68	0.093	4.20(2)	0.10(1)	0.26(1)	0.05(1)	1.77	...	5
89	03:25:09.3	+30:24:03.8	89.4	53.3	161.4	0.60	0.65	0.079	4.03(2)	0.11(2)	0.21(1)	0.03(1)	1.77	...	5
90	03:25:05.0	+30:24:13.9	186.3	102.2	93.1	0.55	0.75	0.157	4.18(1)	0.16(1)	0.24(0)	0.04(0)	1.62	...	4
91	03:25:23.9	+30:21:03.6	90.0	64.9	112.9	0.72	0.80	0.087	4.48(1)	0.07(1)	0.29(1)	0.04(0)	1.54	...	5
92	03:25:16.4	+30:19:02.3	119.7	48.7	112.1	0.41	0.76	0.087	4.23(1)	0.10(1)	0.28(1)	0.07(1)	1.54	...	4
93	03:25:24.1	+30:21:21.4	151.6	111.6	57.7	0.74	0.81	0.148	4.48(1)	0.15(1)	0.29(0)	0.06(0)	1.26	...	4
94	03:25:04.4	+30:24:09.9	215.8	132.0	97.1	0.61	0.80	0.192	4.27(2)	0.21(1)	0.24(0)	0.06(0)	1.19	...	3
95	03:25:15.9	+30:19:06.8	134.7	81.6	104.8	0.61	0.68	0.119	4.18(2)	0.12(1)	0.30(1)	0.08(1)	1.11	...	3

Table 3.4 (cont'd)

No.	RA	DEC	Maj. Axis	Min. Axis	PA	Axis	Filling	Size	$\langle V_{\text{lsr}} \rangle$	ΔV_{lsr}	$\langle \sigma \rangle$	$\Delta \sigma$	Pk. Int.	Contrast	Level
(1)	(h:m:s) (2)	($^{\circ}$: $'$: $''$) (3)	($''$) (4)	($''$) (5)	($^{\circ}$) (6)	Ratio (7)	Factor (8)	(pc) (9)	(km s^{-1}) (10)	(km s^{-1}) (11)	(km s^{-1}) (12)	(km s^{-1}) (13)	(Jy beam^{-1}) (14)	(15)	(16)
96	03:25:24.5	+30:21:22.5	182.1	120.7	70.4	0.66	0.82	0.169	4.57(2)	0.19(1)	0.29(1)	0.07(1)	0.97	...	3
97	03:25:14.6	+30:19:17.8	192.1	105.2	116.2	0.55	0.77	0.162	4.12(1)	0.11(1)	0.34(1)	0.08(0)	0.97	...	2
98	03:24:50.0	+30:22:51.2	137.1	46.5	80.4	0.34	0.59	0.091	3.76(2)	0.12(1)	0.21(1)	0.09(1)	0.90	...	3
99	03:24:36.5	+30:21:57.1	110.9	58.5	165.0	0.53	0.76	0.092	4.07(2)	0.13(2)	0.24(2)	0.10(1)	0.90	...	3
100	03:25:24.8	+30:21:24.4	210.0	136.1	68.4	0.65	0.78	0.193	4.58(2)	0.22(2)	0.29(1)	0.09(1)	0.82	...	2
101	03:25:14.4	+30:22:24.0	100.0	30.1	70.9	0.30	0.74	0.063	4.70(3)	0.11(2)	0.22(2)	0.08(1)	0.82	...	2
102	03:24:32.2	+30:23:34.1	67.4	29.3	147.4	0.43	0.79	0.051	0.76	...	2
103	03:25:21.1	+30:20:58.9	451.6	252.0	51.7	0.56	0.79	0.384	4.60(6)	0.25(4)	0.24(2)	0.10(2)	0.68	...	1
104	03:24:59.0	+30:23:59.2	387.5	181.2	80.4	0.47	0.62	0.302	3.79(7)	0.25(5)	0.23(4)	0.14(3)	0.61	...	2
105	03:24:34.3	+30:22:19.7	199.4	78.4	135.2	0.39	0.71	0.142	0.61	...	2
106	03:25:07.7	+30:17:42.2	107.0	48.3	91.2	0.45	0.58	0.082	0.53	...	1
107	03:24:40.2	+30:26:01.8	67.0	29.9	58.9	0.45	0.59	0.051	0.53	...	0
108	03:24:30.5	+30:22:29.5	321.6	195.3	84.3	0.61	0.60	0.286	0.47	...	1
109	03:24:56.7	+30:23:50.0	422.3	208.9	80.5	0.49	0.74	0.338	0.47	...	1
110	03:24:34.7	+30:25:24.6	103.5	54.5	91.0	0.53	0.49	0.086	0.43	...	0
111	03:25:19.3	+30:20:38.4	528.3	268.5	50.4	0.51	0.81	0.429	0.39	...	0
112	03:24:46.8	+30:23:17.4	775.1	211.0	77.8	0.27	0.66	0.461	0.32	...	0

Note. — (2)–(6) The position, major axis, minor axis, and position angle were determined from `regionprops` in MATLAB. We do not report formal uncertainties of these values since the spatial properties of irregularly shaped objects is dependent on the chosen method.

(7) Axis ratio, defined as the ratio of the minor axis to the major axis.

(8) Filling factor, defined as the area of the leaf or branch inscribed within the fitted ellipse, divided by the area of the fitted ellipse.

(9) Size, defined as the geometric mean of the major and minor axes, for an assumed distance of 235 pc.

(10) The weighted mean V_{lsr} of all fitted values within a leaf or branch. Weights are determined from the statistical uncertainties reported by the IDL MPFIT program. The error in the mean is reported in parentheses as the uncertainty in the last digit. It was computed as the standard error of the mean, $\Delta V_{\text{lsr}}/\sqrt{N}$, where ΔV_{lsr} is the value in column 11 and N is the number of beams' worth of pixels within a given object. We report kinematic properties only for objects that have at least three synthesized beams' worth of kinematic pixels.

(11) The weighted standard deviation of all fitted V_{lsr} values within a leaf or branch. The error was computed as the standard error of the standard deviation, $\Delta V_{\text{lsr}}/\sqrt{2(N-1)}$, assuming the sample of beams was drawn from a larger sample with a Gaussian velocity distribution.

(12) The weighted mean velocity dispersion of all fitted values within a leaf or branch. The error was computed as the standard error of the mean, $\Delta \sigma/\sqrt{N}$.

(13) The weighted standard deviation of all fitted velocity dispersion values within a leaf or branch. The error was computed as the standard error of the standard deviation, $\Delta \sigma/\sqrt{2(N-1)}$.

(14) For a leaf, this is the peak intensity measured in a single channel of our 2-channel binned dataset used in the dendrogram analysis. For a branch, this is the intensity level where the leaves above it merge together.

(15) "Contrast" is defined as the difference between the peak intensity of a leaf and the height of its closest branch in the dendrogram, divided by the 1- σ sensitivity of the data.

(16) The branching level in the dendrogram. For example, the base of the tree is level 0, so an isolated leaf that grows directly from the base is considered to be at level 0. A leaf that grows from a branch one level above the base will be at level 1, etc.

Table 3.5. HCN Dendrogram Leaf and Branch Properties

No.	RA	DEC	Maj. Axis	Min. Axis	PA	Axis	Filling	Size	$\langle V_{\text{lsr}} \rangle$	ΔV_{lsr}	$\langle \sigma \rangle$	$\Delta \sigma$	Pk. Int.	Contrast	Level
(1)	(h:m:s)	($^{\circ}$: $'$: $''$)	($''$)	($''$)	($^{\circ}$)	Ratio	Factor	(pc)	(km s^{-1})	(km s^{-1})	(km s^{-1})	(km s^{-1})	(Jy beam^{-1})	(15)	(16)
Leaves															
0	03:25:31.1	+30:22:16.0	39.5	20.1	149.3	0.51	0.71	0.032	0.70	2.5	1
1	03:25:02.2	+30:21:05.5	17.1	14.1	110.1	0.83	0.90	0.018	0.63	2.3	0
2	03:25:02.8	+30:24:49.4	25.0	17.2	135.3	0.69	0.70	0.024	4.31(4)	0.10(3)	0.12(2)	0.06(2)	0.86	2.1	1
3	03:24:32.3	+30:25:16.6	26.6	17.3	95.6	0.65	0.73	0.024	0.69	2.7	0
4	03:24:27.2	+30:26:21.3	20.3	10.6	137.4	0.52	0.83	0.017	0.91	4.3	0
5	03:25:24.1	+30:21:03.2	71.4	41.7	162.3	0.58	0.59	0.062	4.49(1)	0.05(1)	0.13(1)	0.03(0)	1.29	3.5	4
6	03:25:25.4	+30:21:45.4	27.1	19.7	82.7	0.73	0.86	0.026	4.56(2)	0.06(1)	0.15(1)	0.04(1)	1.30	3.6	4
7	03:25:26.3	+30:22:10.6	37.0	20.7	112.3	0.56	0.80	0.031	4.60(2)	0.06(1)	0.13(1)	0.06(1)	1.51	6.0	3
8	03:25:31.6	+30:22:59.0	53.1	29.1	101.8	0.55	0.72	0.045	4.73(1)	0.04(1)	0.11(1)	0.04(1)	0.89	2.7	2
9	03:25:28.4	+30:23:09.9	46.9	26.4	18.9	0.56	0.57	0.040	0.68	2.3	1
10	03:25:11.8	+30:19:01.5	45.7	24.1	36.6	0.53	0.65	0.038	4.42(2)	0.08(2)	0.10(2)	0.07(1)	0.86	2.1	2
11	03:25:15.0	+30:22:22.2	125.9	44.1	85.4	0.35	0.68	0.085	4.68(3)	0.07(2)	0.13(1)	0.04(1)	0.87	4.0	0
12	03:25:32.5	+30:22:25.3	30.0	17.4	143.5	0.58	0.67	0.026	0.87	2.6	2
13	03:25:04.3	+30:25:10.1	35.0	13.0	93.5	0.37	0.86	0.024	4.31(2)	0.05(1)	0.13(1)	0.03(1)	0.99	3.0	1
14	03:25:16.7	+30:19:48.3	45.9	35.9	102.7	0.78	0.77	0.046	4.33(1)	0.05(1)	0.13(1)	0.04(1)	1.14	5.0	1
15	03:25:06.8	+30:24:24.7	27.7	19.7	112.1	0.71	0.83	0.027	4.15(2)	0.06(1)	0.12(1)	0.02(0)	1.31	3.2	2
16	03:25:17.9	+30:18:54.4	90.7	41.7	101.4	0.46	0.65	0.070	4.06(2)	0.12(1)	0.12(1)	0.07(1)	1.12	3.9	2
17	03:25:27.2	+30:21:27.7	29.4	15.1	83.2	0.51	0.80	0.024	4.42(1)	0.03(1)	0.07(2)	0.05(2)	0.81	2.2	2
18	03:24:29.3	+30:23:27.6	112.3	29.2	119.0	0.26	0.60	0.065	0.74	3.1	0
19	03:25:00.9	+30:23:59.9	25.5	25.2	62.7	0.99	0.85	0.029	4.17(1)	0.04(1)	0.12(1)	0.03(1)	1.57	4.0	3
20	03:25:02.5	+30:24:43.2	56.3	23.7	13.9	0.42	0.65	0.042	4.24(1)	0.05(1)	0.10(1)	0.04(1)	1.80	4.6	4
21	03:25:04.4	+30:24:42.6	19.7	17.6	0.2	0.90	0.81	0.021	4.21(2)	0.06(2)	0.13(2)	0.04(1)	1.46	2.2	4
22	03:24:40.8	+30:25:03.4	29.0	17.6	87.6	0.61	0.58	0.026	0.60	2.1	0
23	03:25:11.3	+30:19:47.2	32.0	14.0	59.3	0.44	0.80	0.024	0.74	2.2	1
24	03:25:08.9	+30:24:40.1	31.6	12.7	128.3	0.40	0.93	0.023	4.08(1)	0.03(1)	0.10(1)	0.03(1)	2.12	6.8	3
25	03:24:53.6	+30:24:49.0	69.6	37.0	83.9	0.53	0.69	0.058	0.71	2.9	0
26	03:24:38.3	+30:23:54.9	37.6	22.7	22.6	0.60	0.71	0.033	0.66	2.6	0
27	03:24:50.8	+30:22:51.8	77.4	29.7	71.1	0.38	0.54	0.055	0.80	3.0	1
28	03:24:34.9	+30:22:10.8	122.5	88.2	136.7	0.72	0.66	0.118	3.97(7)	0.18(5)	0.18(4)	0.09(3)	0.75	3.2	0
29	03:24:46.4	+30:22:47.3	64.3	33.9	95.8	0.53	0.52	0.053	0.69	2.3	1
30	03:25:09.9	+30:23:57.1	53.6	35.5	137.5	0.66	0.81	0.050	3.83(1)	0.07(1)	0.09(0)	0.02(0)	2.58	10.0	3
31	03:24:46.2	+30:23:58.9	23.4	9.5	110.0	0.41	0.85	0.017	0.69	2.7	0
32	03:24:32.3	+30:23:33.2	68.2	30.8	142.8	0.45	0.72	0.052	0.70	2.8	0
Branches															
33	03:25:03.0	+30:24:41.8	58.4	46.1	37.9	0.79	0.67	0.059	4.30(2)	0.08(2)	0.15(1)	0.05(1)	1.14	...	3
34	03:25:09.5	+30:24:03.4	92.4	47.2	158.3	0.51	0.78	0.075	4.00(2)	0.10(1)	0.11(0)	0.03(0)	1.14	...	2
35	03:25:02.7	+30:24:32.7	112.1	44.4	37.4	0.40	0.68	0.080	4.28(2)	0.11(2)	0.15(1)	0.05(1)	0.99	...	2
36	03:25:05.6	+30:24:16.7	180.1	100.9	103.4	0.56	0.75	0.154	4.17(1)	0.14(1)	0.12(1)	0.06(0)	0.85	...	1
37	03:25:24.6	+30:21:11.0	98.8	64.4	21.4	0.65	0.65	0.091	4.50(1)	0.06(1)	0.14(1)	0.04(0)	0.78	...	3
38	03:25:24.5	+30:21:22.5	139.4	85.0	26.9	0.61	0.70	0.124	4.56(2)	0.15(2)	0.09(1)	0.07(1)	0.64	...	2
39	03:25:16.0	+30:18:58.4	163.4	65.0	95.7	0.40	0.64	0.117	4.12(4)	0.15(3)	0.10(2)	0.07(1)	0.56	...	1
40	03:25:04.9	+30:24:08.9	201.4	141.8	101.7	0.70	0.77	0.193	4.31(5)	0.17(4)	0.13(2)	0.05(1)	0.56	...	0
41	03:25:31.9	+30:22:47.4	86.1	60.1	117.7	0.70	0.62	0.082	0.50	...	1
42	03:25:24.2	+30:21:22.2	168.6	120.2	44.7	0.71	0.66	0.162	0.50	...	1
43	03:25:15.3	+30:19:14.6	187.4	113.6	110.7	0.61	0.72	0.166	0.42	...	0
44	03:24:48.4	+30:22:50.0	150.6	55.3	86.5	0.37	0.57	0.104	0.36	...	0
45	03:25:25.3	+30:21:43.3	278.2	156.8	58.0	0.56	0.62	0.238	0.35	...	0

Note. — Same at Table 3.4.

Table 3.6. N_2H^+ Dendrogram Leaf and Branch Properties

No.	RA	DEC	Maj. Axis	Min. Axis	PA	Axis	Filling	Size	$\langle V_{\text{lsr}} \rangle$	ΔV_{lsr}	$\langle \sigma \rangle$	$\Delta \sigma$	Pk. Int.	Contrast	Level
(1)	(h:m:s)	($^{\circ}$: $'$: $''$)	($''$)	($''$)	($^{\circ}$)	Ratio	Factor	(pc)	(km s^{-1})	(km s^{-1})	(km s^{-1})	(km s^{-1})	(Jy beam^{-1})	(15)	(16)
Leaves															
0	03:25:30.8	+30:21:27.9	38.2	25.2	97.4	0.66	0.58	0.035	0.69	2.1	1
1	03:25:32.9	+30:21:59.9	18.0	12.1	73.7	0.67	0.83	0.017	0.97	3.0	2
2	03:25:30.9	+30:22:12.7	40.2	23.1	58.8	0.57	0.61	0.035	1.02	3.4	2
3	03:25:14.7	+30:22:28.0	33.1	21.0	89.9	0.64	0.84	0.030	0.83	3.2	0
4	03:25:31.3	+30:22:53.2	28.1	13.1	88.0	0.47	0.83	0.022	0.83	2.1	2
5	03:25:23.5	+30:21:12.8	33.8	18.5	51.9	0.55	0.68	0.028	4.54(1)	0.03(1)	0.10(1)	0.01(0)	1.01	2.3	3
6	03:25:26.0	+30:21:44.0	51.1	36.0	30.7	0.70	0.66	0.049	4.57(1)	0.04(1)	0.13(1)	0.03(1)	1.25	4.0	3
7	03:25:03.9	+30:25:00.3	36.8	19.6	89.7	0.53	0.68	0.031	4.45(1)	0.03(1)	0.09(1)	0.02(0)	1.40	3.5	1
8	03:25:16.1	+30:19:47.4	35.7	28.9	54.8	0.81	0.68	0.037	0.89	3.7	0
9	03:24:55.8	+30:23:23.3	19.3	11.6	61.8	0.60	0.77	0.017	0.66	2.1	0
10	03:25:07.3	+30:24:32.1	38.5	21.1	96.6	0.55	0.71	0.032	4.24(1)	0.03(1)	0.08(0)	0.01(0)	1.62	3.0	2
11	03:25:18.3	+30:19:00.4	16.7	10.9	62.7	0.65	0.68	0.015	1.00	2.1	1
12	03:24:36.7	+30:22:42.4	36.4	28.9	114.2	0.79	0.67	0.037	0.75	2.7	0
13	03:25:09.3	+30:23:53.3	59.5	17.0	113.1	0.29	0.66	0.036	4.03(2)	0.08(1)	0.10(1)	0.03(0)	1.55	2.5	2
14	03:25:20.1	+30:18:51.6	36.6	18.0	123.7	0.49	0.81	0.029	3.93(1)	0.04(1)	0.12(0)	0.01(0)	1.13	3.0	1
15	03:24:26.3	+30:23:33.7	60.4	44.6	12.1	0.74	0.78	0.059	3.86(1)	0.06(1)	0.11(0)	0.03(0)	1.51	7.9	0
Branches															
16	03:25:08.5	+30:24:11.8	101.3	38.3	136.7	0.38	0.71	0.071	4.11(2)	0.12(1)	0.10(0)	0.02(0)	1.18	...	1
17	03:25:04.8	+30:24:18.4	196.1	108.9	95.0	0.56	0.62	0.166	4.26(2)	0.17(1)	0.11(0)	0.03(0)	0.90	...	0
18	03:25:17.7	+30:18:54.8	141.7	42.6	101.8	0.30	0.65	0.088	4.08(2)	0.07(2)	0.13(1)	0.04(1)	0.69	...	0
19	03:25:25.6	+30:21:34.2	96.5	65.4	41.1	0.68	0.62	0.091	4.58(1)	0.04(1)	0.10(1)	0.02(0)	0.67	...	2
20	03:25:27.2	+30:21:45.9	200.6	100.1	53.0	0.50	0.56	0.161	0.53	...	1
21	03:25:27.2	+30:21:44.0	204.3	105.2	54.6	0.51	0.58	0.167	0.38	...	0

Note. — Same as Table 3.4.

Table 3.7. Tree Statistics

Line (Sub-region)	Total No. ^a	Max Level ^b	Mean PL ^c	Mean BR ^d
Comparison Across Tracers^e				
HCO ⁺	113	6	2.3	3.8
HCN	46	4	1.3	3.3
N ₂ H ⁺	22	3	1.3	3.0
Comparison of Sub-Regions^f				
HCO ⁺ (A)	10	6	4.8	2.3
HCO ⁺ (B)	16	7	5.9	2.5
HCO ⁺ (C)	8	5	4.2	2.3
HCO ⁺ (others)	9	4	3.7	2.0
HCN (A)	13	4	2.4	2.4
HCN (B)	13	4	2.6	2.4
HCN (C)	6	2	1.5	2.5
HCN (others)	6	1	1.0	2.0
N ₂ H ⁺ (A)	9	3	2.2	2.7
N ₂ H ⁺ (B)	5	2	1.7	2.0
N ₂ H ⁺ (C)	3	1	1.0	2.0
N ₂ H ⁺ (others)	NA	NA	NA	NA

Note. — ^a Total number of leaves and branches. ^b Maximum branching level. ^c Mean path length. ^d Mean branching ratio. ^e Using method to compare dendrograms from data with different noise levels. ^f Using original dendrograms.

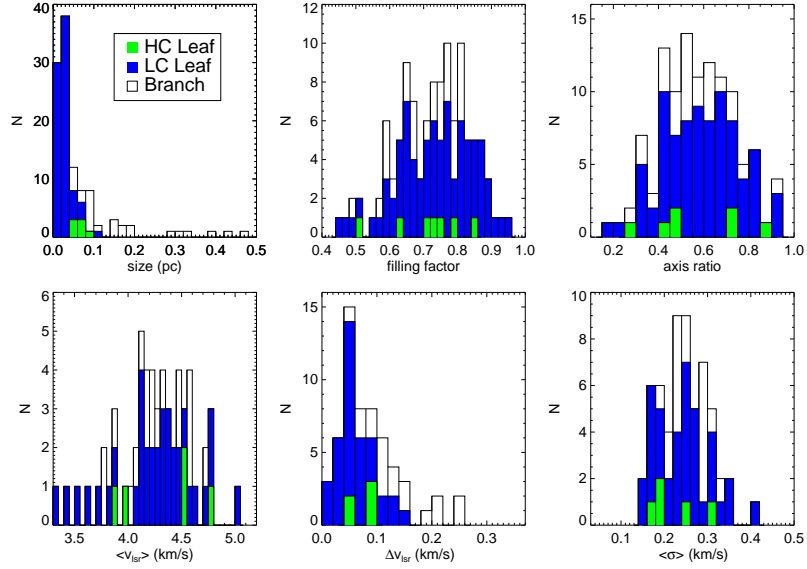


Figure 3.13: Histograms of HCO^+ dendrogram leaf and branch properties. High-contrast (HC) leaves, above $6\text{-}\sigma_n$ contrast, are represented by green; low-contrast (LC) leaves, below $6\text{-}\sigma_n$ contrast, are represented by blue; branches are represented by white. See the text in Section 3.6.2 for a discussion of trends seen in these histograms.

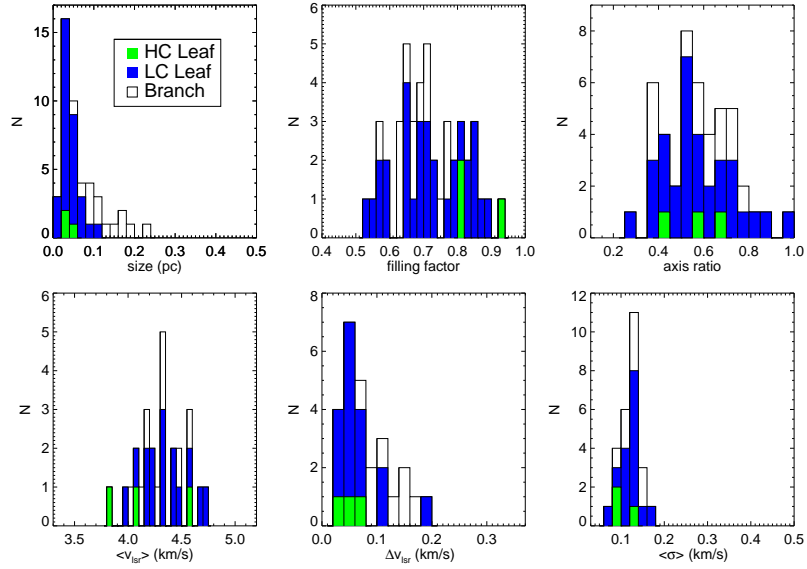


Figure 3.14: Same as Figure 3.13, but for HCN.

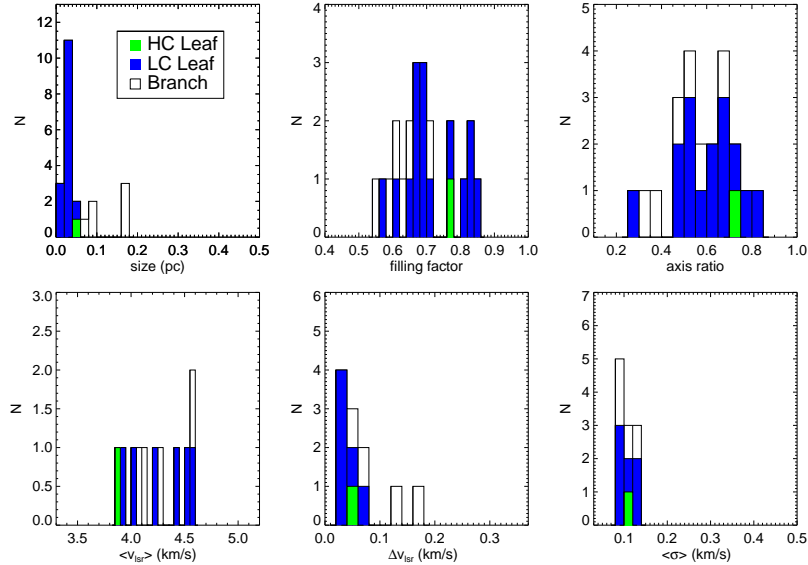


Figure 3.15: Same as Figure 3.13, but for N_2H^+ .

3.7 Dust in L1451

The CLASSy observations provide excellent measurements of gas structure and kinematics, but are less reliable for column density or mass information due to large uncertainties in relative abundance and opacity of the molecular emission. For this, we turned to *Herschel* observations.

3.7.1 L1451 Column Density and Temperature

We used *Herschel* 160, 250, 350, and 500 μm observations of L1451 to derive the column density and temperature of the dust. The *Herschel* images were corrected for the zero-level offset based on a comparison with *Planck* and DIRBE/IRAS data (Meisner & Finkbeiner 2015). The images were convolved to the angular resolution of the *Herschel* 500 μm band ($\sim 36''$) using the convolution kernels from Aniano et al. (2011), and were regridded to a common pixel size of $10''$. The fitting was performed on a pixel-by-pixel basis with a modified blackbody spectrum

of $I_\nu = \kappa_\nu B(\nu, T)\Sigma$, where κ_ν is the dust mass opacity coefficient at frequency ν , $B(\nu, T)$ is the Planck function at temperature T , and $\Sigma = \mu m_p N(H_2)$ is the gas mass column density for a mean molecular weight of $\mu = 2.8$ (e.g. Kauffmann et al. 2008) assuming a gas-to-dust ratio of 100:1. We assume $\kappa_\nu = 0.1 \times (\nu/10^{12} \text{ Hz})^\beta \text{ cm}^2 \text{ g}^{-1}$ (Beckwith & Sargent 1991), and $\beta = 1.7$.

The resulting column density and temperature maps are shown in Figures 3.16 and 3.17, respectively. We validated our SED fitting procedure by comparing our derived optical depth to that of the Planck Collaboration et al. (2014) model. Specifically, we re-ran our SED fits after smoothing the *Herschel* input maps to match the Planck Collaboration et al. (2014) resolution of $5'$, and found that our derived $300 \mu\text{m}$ optical depth agrees with that of the *Planck*-based model to within 5% on average. The mean column density of L1451 that is enclosed within the $2.0 \times 10^{21} \text{ cm}^{-2}$ contour in Figure 3.16 (the white contour that encircles all of the high column density regions) is $3.7 \times 10^{21} \text{ cm}^{-2}$ with a standard deviation of $1.7 \times 10^{21} \text{ cm}^{-2}$. The peak column density of $1.2 \times 10^{22} \text{ cm}^{-2}$ occurs at the location of the Bolocam source, Per-Bolo 4. The mean temperature within the 15.0 K contour of Figure 3.17 is 14.0 K, with a standard deviation of 0.7 K. A minimum temperature of 11.9 K occurs at the location of L1451-mm.

We have independent temperature measurements toward the four Bolocam sources in the field from Rosolowsky et al. (2008a) ammonia observations. Those temperatures are $\sim 2\text{--}3.5$ K lower than we find by fitting the *Herschel* SEDs. Our results, and those from Planck Collaboration et al. (2014) that we compared to, assume emission from a single cloud layer. However, there will always be a warmer layer of foreground and background material surrounding a dense, cold star-forming region. This warmer cloud component can drive the fitted temperature up and fitted column density down when only doing a single component fit. To estimate the systematic

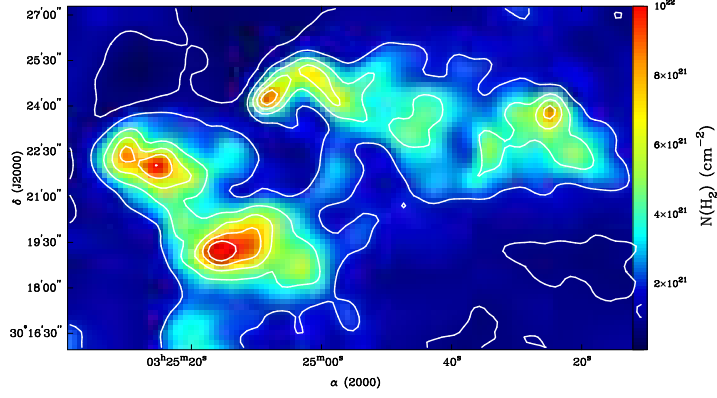


Figure 3.16: Column density map of L1451 derived from *Herschel* 160, 250, 350, and 500 μm data. The white contours corresponds to $N(\text{H}_2)=[0.8, 2.0, 4.0, 6.0, 8.0, 10.0]\times 10^{21} \text{ cm}^{-2}$. The measured column densities toward the densest regions are likely systematically underestimated by half from the true values; see the discussion in the text.

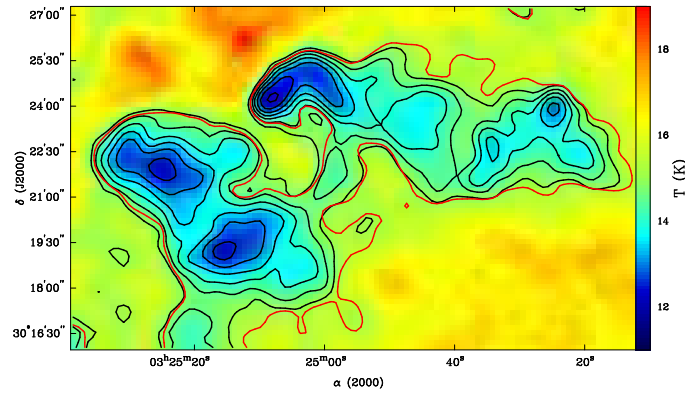


Figure 3.17: Temperature map of L1451 derived from *Herschel* 160, 250, 350, and 500 μm data. The black contours represent 12 to 15 K, in 0.5 K increments. The red contour represents a column density of $2.0\times 10^{21} \text{ cm}^{-2}$, for comparison to Figure 3.16. The temperatures toward the densest regions are likely overestimated by a few Kelvin; see text for discussion.

overestimation of temperatures and underestimation of column densities toward the densest regions of clouds, we created a simple radiative transfer model with a cold layer at 9 K (representing L1451) between two warmer layers at 17 K (representing foreground and background cloud material). If the warm layers have A_V of 0.4, then the temperature in cold layer regions with $A_V \gtrsim 2$ is overestimated by ~ 2.5 –5.5 K when using a single component fit (e.g., 12 K instead of 9 K). This matches

the differences between our temperatures and the temperatures from the ammonia data. Furthermore, measured column density values of a cold, dense region are predicted to be half of the true values in regions where the warm layers have A_V of 0.4 and the cold layer has $A_V \gtrsim 2$. If the lower-resolution *Herschel* beam is not filled in regions of cold, dense gas, then this could further bias temperatures to be too warm, and column densities to be too low. In Section 3.8, we will discuss how these systematic uncertainties can affect our energy balance results. An upcoming paper will present a detailed comparison of single-layer and two-layer SED fitting across Perseus, showing the improvement that is achieved for cold, dense regions when considering the hot, diffuse component along the line-of-sight (Lee et al., in preparation).

3.7.2 Dendrogram Analysis of Dust

The column density results in the previous section are angular resolution limited compared to our CLASSy maps, so it is not possible to estimate the mass within the smallest molecular structures we identified using the dendrogram analysis in Section 3.6. Therefore, we take the approach of first defining structures based on the dust data, and then using the kinematic information within those structures to explore energy balance. A virial analysis is presented in Section 3.8.

We converted the N_{H_2} column density map to an extinction map using a conversion factor of $N_{\text{H}_2}/A_V = (1/2) \times 1.87 \times 10^{21} \text{ cm}^{-2} \text{ mag}^{-1}$ (Draine 2003). We then ran our non-binary dendrogram algorithm on the extinction map to define dust structures in the field. We used an rms and branching step of $0.2 A_V$, and required that local maxima peak at least $0.4 A_V$ above the merge level to be considered a real leaf. The algorithm identified 8 leaves and 6 branches in the region where we have molecular line data.

Table 3.8. Dust Structure Properties

No.	RA	DEC	Size	$\langle T \rangle$	$\langle N_{H_2} \rangle$	M_{tot}	$\sigma_{\text{tot, HCN}}$	$\sigma_{\text{tot, N}_2\text{H}^+}$
(1)	(h:m:s) (2)	($^{\circ}$: $'$: $''$) (3)	(pc) (4)	(K) (5)	(10^{21} cm $^{-2}$) (6)	(solar) (7)	(km s $^{-1}$) (8)	(km s $^{-1}$) (9)
Leaves								
0	03:25:13.3	+30:19:05.8	0.23	13.6	5.1	5.1	0.39	0.34
1	03:25:00.2	+30:21:22.1	0.08	14.4	2.8	0.2	0.41	...
2	03:25:27.2	+30:21:43.6	0.17	13.2	5.0	3.1	0.29	0.27
3	03:24:35.5	+30:22:09.5	0.07	13.6	4.4	0.4	0.34	0.37
4	03:24:47.0	+30:23:11.2	0.14	13.9	4.0	1.4	0.54	...
5	03:24:26.8	+30:22:47.7	0.17	13.9	4.6	2.0	0.44	0.28
6 ^a	03:25:08.7	+30:24:09.5	0.07	12.2	7.2	0.5	0.25	0.25
7	03:25:01.5	+30:24:27.9	0.07	12.7	6.4	0.5	0.28	0.26
Branches								
8	03:25:01.5	+30:24:12.9	0.21	13.7	4.1	3.0	0.33	0.33
9	03:25:17.8	+30:20:07.0	0.41	14.2	3.1	13.1	0.47	0.44
10	03:24:29.2	+30:22:26.8	0.27	14.2	3.6	4.5	0.45	0.35
11	03:24:54.2	+30:23:38.9	0.33	14.1	3.3	6.2	0.39	0.34
12	03:24:43.1	+30:23:04.4	0.46	14.3	3.1	12.4	0.43	0.39
13	03:25:17.1	+30:19:52.8	0.51	14.3	3.0	14.9	0.50	0.47

Note. — (4) Geometric mean of major and minor axis fit to structure (used as diameter of structure). (5) Weighted mean temperature within structure. (6) Weighted mean column density of H_2 within structure. (7) Total mass within structure. (8) HCN velocity dispersion calculated from integrated spectrum across structure. (9) N_2H^+ velocity dispersion calculated from integrated spectrum across structure. ^a L1451-mm is located within this structure.

The extinction map, with dendrogram-identified structures, is shown in Figure 3.18. Properties of the dendrogram structures are listed in Table 3.8, including their coordinate, size, weighted mean temperature and column density, and total mass. The mean temperature and column density, and total mass of each structure considers all of the emission interior to the structure (e.g., branch 9 includes emission from branch 9 and leaves 0 and 2). To calculate the total mass within each structure, we first converted the column density at each pixel to a solar mass unit as:

$$M(\alpha, \delta) = \mu_{H_2} m_H N_{H_2}(\alpha, \delta) A, \quad (3.1)$$

where μ_{H_2} is the molecular weight per hydrogen molecule (2.8), m_H is the mass of a hydrogen atom, $N_{H_2}(\alpha, \delta)$ is the column density at a pixel location, and A is the pixel area. As before, the assumed distance is 235 pc. We then totaled the mass enclosed within each structure. The mass of leaves ranges from 0.2 to 5.1 M_{\odot} , and the mass enclosed within branches ranges from 3.0 to 15.9 M_{\odot} . The mass interior to the yellow and purple contour in Figure 3.18 is 14.9 M_{\odot} and 12.4 M_{\odot} , respectively.

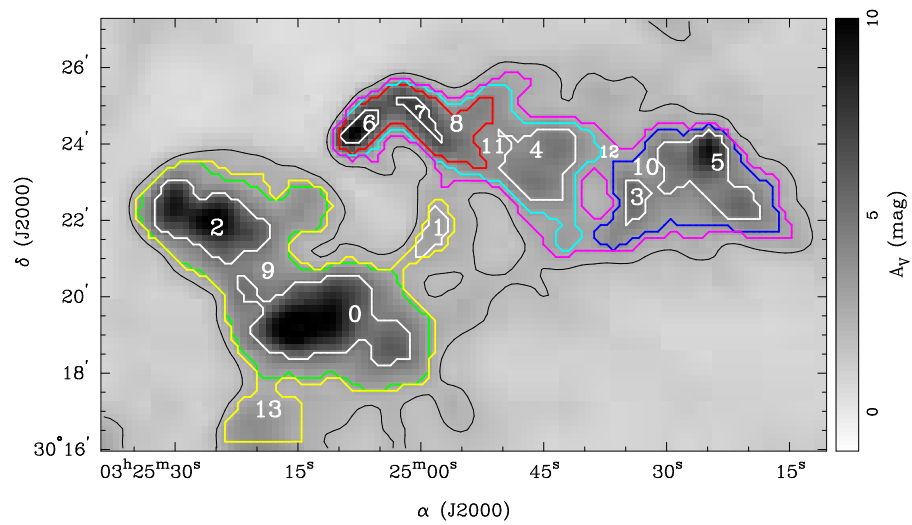


Figure 3.18: Visual extinction map of L1451 (greyscale), as derived from the column density map in Figure 3.16. The solid black contour represents $A_V=2$, and the mean extinction within that contour is 3.8 mag with a 1.8 mag standard deviation. Dendrogram-derived dust structure boundaries are shown with colored contours. The peak extinction is ~ 13 mag within structure 0.

3.8 Understanding Star Formation in L1451

We selected L1451 as a CLASSy region because of its very low star formation activity. There are no confirmed protostar detections, and only one confirmed compact continuum core. This is very different from the other CLASSy regions, which have many protostars and outflows. We wanted to use L1451 to study cloud structure and kinematics in the densest regions of clouds before star formation activity feeds back into the cloud.

We now explore the following questions. What column density threshold are we capturing with our spectral line observations, and do dendrogram-identified structures trace actual column density features that can inform structure formation in a young cloud? If so, will any structures go on to form stars? We address these questions in this section by exploring the correspondence between molecular line and continuum emission, with a virial analysis of L1451 structures, and by describing the similarities and differences between L1451-mm and L1451-west. We conclude with an analysis of the three-dimensional morphology of L1451 on the largest scales.

3.8.1 Connecting molecular structures to physical cloud structures

L1451 is the one CLASSy region with strong, widespread HCO⁺ and HCN that is not affected by outflows and severe self-absorption. This enabled a dendrogram analysis of all three molecules, instead of just N₂H⁺, and lets us compare the identified molecular structures to the column density structure of L1451. Figures 3.19 and 3.20 have the dendrogram footprints of the lowest-level branches, and all the leaves, respectively, overplotted on column density derived from *Herschel* data. We combined the footprints of all the contoured emission in Figures 3.19 and 3.20 to

create a mask for the column density map for determining how well the molecular emission captures material at different column densities.

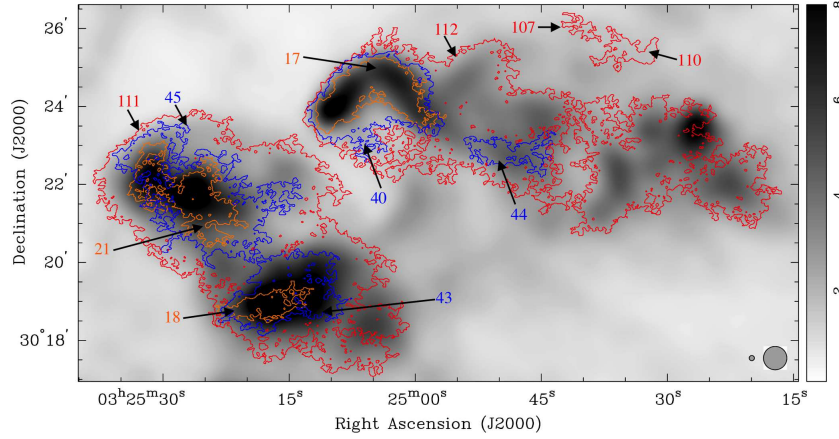


Figure 3.19: Dendrogram lowest-level branch footprints for all molecules, overplotted on the column density from Figure 3.16 that was regridded to match the CLASSy pixel scale (beams for column density ($36''$) and molecular ($7''$) maps are in the lower right). Red = HCO^+ , blue = HCN , and orange = N_2H^+ . We label each branch with its number corresponding to most Tables 3.4–3.6.

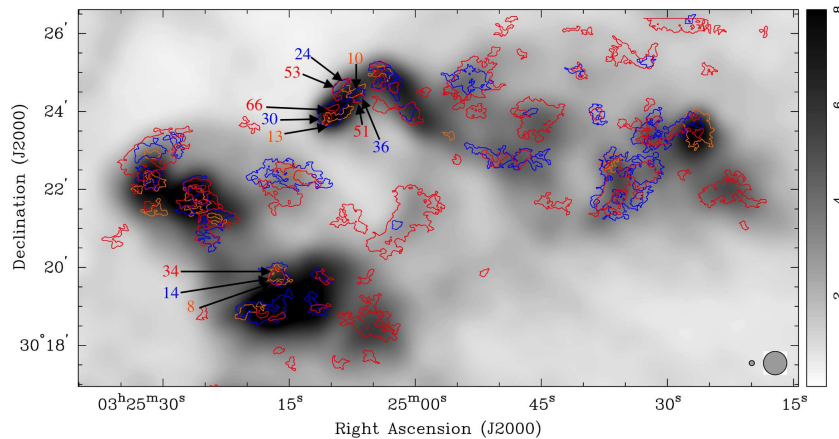


Figure 3.20: Dendrogram leaf footprints for all molecules, overplotted on the column density from Figure 3.16 that was regridded to match the CLASSy pixel scale (beams for column density ($36''$) and molecular ($7''$) maps are in the lower right). Red = HCO^+ , blue = HCN , and orange = N_2H^+ . We label a few examples where leaves where emission from all tracers coincides with numbers corresponding to Tables 3.4–3.6.

A threshold for star formation above $A_V \sim 8$, or an H_2 column density of $7.5 \times 10^{21} \text{ cm}^{-2}$, has been postulated based on the distribution of prestellar cores and protostars

within the densest regions of molecular clouds (André et al. 2014, and references therein). Figure 3.21 shows cumulative distribution functions for column density where we detect dense gas and where we do not detect dense gas. Only 0.002% of dust regions without a molecular gas detection are above the threshold column density if we take our derived column densities as correct. If our measured column densities are uniformly underestimated by half from the true values, as was discussed in Section 3.7.1, still only 1% of dust regions without a molecular gas detection are above the threshold column density. 90% of the regions where we detect molecules are at column densities above $1.9 \times 10^{21} \text{ cm}^{-2}$, with a maximum of $1.3 \times 10^{22} \text{ cm}^{-2}$, and minimum of $8.9 \times 10^{20} \text{ cm}^{-2}$. 90% of the regions where we do not detect molecules are below $2.4 \times 10^{21} \text{ cm}^{-2}$, with a maximum of $7.8 \times 10^{21} \text{ cm}^{-2}$, and minimum of $3.6 \times 10^{20} \text{ cm}^{-2}$. This shows that spectral line observations using our suite of dense-gas tracer molecules is a great probe of the star forming material in young regions above the threshold for star formation and down to column densities of a few $\times 10^{21} \text{ cm}^{-2}$.

We demonstrated that the branches in Figure 3.19 are fragmenting to form the leaves in Figure 3.20 in a similar hierarchical fashion for each molecule (see Section 3.6.3). This consistent fragmentation story between molecules, combined with the result of molecular emission capturing most of the cloud material near and above threshold of star formation, shows that the dendrogram-identified molecular fragmentation is tracing physical structure, accounting for some biases due to chemistry and extinction. This provides observational evidence that structure formation precedes star formation in molecular clouds, which supports turbulence-driven star formation theories that predict the turbulence cascade from large-scale flows leads to the formation of complex morphological structure in clouds before the onset of star formation (Klessen & Hennebelle 2010, and reference therein). Other theories

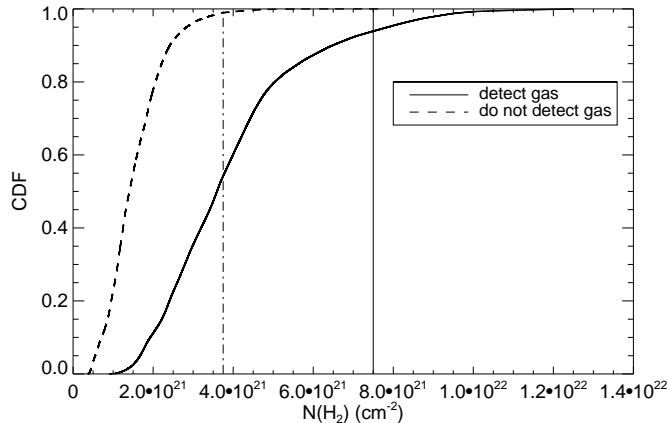


Figure 3.21: Cumulative distribution functions for the areas of the L1451 column density map where we have detected molecular emission (solid curve), and the areas where we have not detected molecular emission (dashed curve). The solid vertical line marks the column density threshold for star formation (André et al. 2014, and references therein), while the dashed-dotted vertical line represents that threshold if our measured column densities are underestimated by half from the true column densities.

for the production of cloud structure consider internally-driven turbulence from protostellar feedback; protostars can inject energy and momentum back into molecular clouds to impact cloud structure and dynamics (Carroll et al. 2009; Federrath et al. 2014; Nakamura & Li 2014). Our result helps to disentangle externally and internally driven structure, which it is important for demonstrating an observational case of complex, hierarchical cloud structure existing at an epoch before internal feedback can impact the natal cloud environment.

3.8.2 Energy balance of structures

We next use a virial analysis to assess whether structures in L1451 are gravitationally bound and on the pathway to star formation. We know one star is currently forming in L1451, based on the detection of compact 3 mm emission at L1451-mm. Showing that other gas and dust structures in the field are gravitationally

bound would add support to L1451 being a region at the onset of star formation. For the virial analysis, we use the dust results in combination with the molecular data. In Section 3.7, we derived column densities and temperatures across L1451 at the angular resolution of the longest wavelength *Herschel* band (36"). We also found dendrogram-identified dust structures in the extinction map. In this section, we use that information for dust leaves, along with CLASSy kinematic data from Section 3.5, to assess the energy balance of structures in L1451.

The virial theorem is useful for describing the energy balance of structures. There are several approaches for applying the virial theorem to molecular cloud observations in the literature (e.g., Larson 1981; Bertoldi & McKee 1992; McKee & Zweibel 1992; Ballesteros-Paredes 2006; Kauffmann et al. 2013). We follow the formalism of McKee & Zweibel (1992), who derive a time-averaged Eulerian form of the virial theorem that contains surface pressure terms for both thermal and turbulent pressure. Equation (4.15) of McKee & Zweibel (1992) writes the virial theorem as

$$\frac{1}{2}\ddot{I}_{\text{cl}} = 3(\bar{P}_{\text{cl}} - c_{\text{pr}}P_{\text{ic}})V_{\text{cl}} + \mathcal{M} + \mathcal{W} \quad (3.2)$$

where \ddot{I}_{cl} is the second-derivative of the moment of inertia of the cloud of interest, \bar{P}_{cl} is the mean total pressure in the cloud (including thermal and turbulent pressure), P_{ic} is the total pressure in the intercloud medium (intercloud medium being the gas and dust between discrete clouds), c_{pr} is a dimensionless factor of order unity (expected to be $0.5 \lesssim c_{\text{pr}} \lesssim 1.0$) that accounts for the surface pressure of the intercloud medium on the cloud being at lower pressure than the average intercloud pressure, V_{cl} is the total cloud volume, \mathcal{M} is the net magnetic energy of the cloud, and \mathcal{W} is the gravitational potential energy of the cloud.

A steady-state cloud in virial equilibrium will have $\ddot{I}_{\text{cl}} = 0$. We ignore \mathcal{M} since there are not adequate magnetic field data to assess its magnitude. What remains is a balance of two confining terms and one dispersive term, all which can be estimated

using our observational data. The confining terms are the gravitational potential energy of the cloud and the pressure term from the intercloud medium on the surface of the cloud. The dispersive term is the mean total pressure in the cloud. A structure is said to satisfy the virial theorem if the confining and dispersive terms are equal. The virial expression in Equation 3.2 can technically be satisfied for a source without any self-gravity if it is contained only by external pressure balancing internal pressure. Thus, it is important to note that satisfying the virial theorem in Equation 3.2 does not automatically mean a structure is gravitationally bound.

The confining term of surface pressure is often ignored in the literature. In this case, the widely used virial parameter, α , is defined for a spherical source by only considering gravitational potential energy and internal kinetic energy:

$$\alpha = 5 \frac{1 - \frac{2k}{5} \frac{R_{cl}\sigma_{cl}^2}{GM_{cl}}}{1 - \frac{k}{3}} \quad (3.3)$$

where R_{cl} and M_{cl} are the cloud radius and total cloud mass, respectively; σ_{cl} is the one-dimension velocity dispersion of cloud gas, and k is the exponent of the density distribution within the cloud. For a source with a uniform density distribution ($\rho(r) \propto r^{-k}$, with $k = 0$), the virial parameter becomes the widely used: $5R_{cl}\sigma_{cl}^2/GM_{cl}$. A cloud is said to satisfy the virial theorem if $\alpha = 1$, and is bound if $\alpha \lesssim 2$ (Kauffmann et al. 2013). McKee & Zweibel (1992) discuss how the effects of external confining-pressure, non-uniform cloud density, and magnetic fields all tend to compensate each other, making this balance of gravitational potential energy and total internal pressure most important.

Although the external confining-pressure term is traditionally ignored, it can be important for young star forming regions (Lada et al. 2008; Seo et al. 2015). Therefore, we will discuss the magnitude of this extra energy term to determine if L1451 structures satisfy the virial theorem with the addition of external confining pressure. Finally, it should be noted that this approach assumes an isolated spherical

cloud with no tidal gravitational field from sources of gravity other than the cloud. Since all of the identified structures are nearby other structures and embedded within larger structures, the tidal forces may be non-negligible. One approach which includes these effects is to compute the total gravitational potential from the column density map (e.g., using the GRID-core algorithm from Gong & Ostriker 2011); that analysis is beyond the scope of this work and will be explored in the future.

For the traditional virial parameter in Equation 3.3, R_{cl} , is half of the size reported in Column 4 of Table 3.8, and M_{cl} is reported in Column 7 of Table 3.8. The σ_{cl} of each structure includes thermal and non-thermal support against collapse. The thermal component of the velocity dispersion was calculated as:

$$\sigma_{th} = \sqrt{\frac{kT}{\mu m_H}}, \quad (3.4)$$

where T is the mean temperature of the dust within the structure, μ is the mean molecular weight (2.33), and m_H is the hydrogen atomic mass. The non-thermal component of the velocity dispersion was calculated for each molecular tracer separately, as:

$$\sigma_{nth,tracer} = \sqrt{\sigma_{obs,tracer}^2 - \sigma_{th,tracer}^2} \quad (3.5)$$

where $\sigma_{obs,tracer}^2$ is the observed velocity dispersion of the molecular emission within the structure, and $\sigma_{th,tracer}$ is the thermal velocity dispersion of the molecule at the mean temperature found within the structure:

$$\sigma_{th,tracer} = \sqrt{\frac{kT}{\mu_{tracer} m_H}}. \quad (3.6)$$

We determined $\sigma_{obs,tracer}^2$ by masking the CLASSy data cubes of N_2H^+ and HCN using the boundaries of each dust structure, generating an integrated spectrum for each molecule, and fitting for the velocity dispersion of that integrated spectrum.

The final $\sigma_{total,tracer}$ value was then calculated as:

$$\sigma_{cl,tracer} = \sqrt{\sigma_{th}^2 + \sigma_{nth,tracer}^2} \quad (3.7)$$

Table 3.9. Virial Parameters

No.	N ₂ H ⁺				HCN			
	k=0		k=2		k=0		k=2	
	No	P _{ext}	No	P _{ext}	No	P _{ext}	No	P _{ext}
(1)	(2)	(3)	(4)	(5)	(6)	(7)	(8)	(9)
0	3.0	1.4	1.8	0.8	4.0	2.1	2.4	1.3
1	28.5	20.0	17.1	12.0
2	2.3	0.9	1.4	0.5	2.8	1.2	1.7	0.7
3	15.3	12.0	9.2	7.2	13.0	7.5	7.8	4.5
4	17.5	13.5	10.5	8.1
5	3.8	0.5	2.2	0.3	9.3	3.7	5.6	2.2
6 ^a	4.4	2.9	2.6	1.7	4.5	3.0	2.7	1.8
7	6.2	3.5	3.7	2.1	6.8	4.1	4.1	2.5

Note. — (1) No. from Table 3.8. (2) Virial parameter calculated using Equation 3.3 with the N₂H⁺ velocity dispersion and $k = 0$. (3) Virial parameter calculated using Equation 3.8 with the N₂H⁺ velocity dispersion and $k = 0$. (4) Virial parameter calculated using Equation 3.3 with the N₂H⁺ velocity dispersion and $k = 2$. (5) Virial parameter calculated using Equation 3.8 with the N₂H⁺ velocity dispersion and $k = 2$. (6-9) Same as Columns 2-5, but using HCN for the velocity dispersion. ^a L1451-mm is located within this structure.

and is reported in Columns 8 and 9 of Table 3.8 for HCN and N₂H⁺, respectively. We do not analyze the HCO⁺ in this analysis because it has significantly larger velocity dispersion than the other molecules, likely because it is tracing more extended, lower-density emission compared to HCN and N₂H⁺ (see Section 3.5).

Columns 2 and 6 of Table 3.9 list the virial parameters of dust leaves when using N₂H⁺ and HCN to determine the velocity dispersion, respectively, under the assumption of uniform density and ignoring surface pressure. Structures 1, 3, and 4 have $\alpha > 10$ when considering the N₂H⁺ or HCN velocity dispersion. These structures have the weakest dense gas emission from HCN and N₂H⁺ of leaves in the field, so it is sensible that they appear to be the least bound. Considering the N₂H⁺ velocity dispersion, the other structures have virial parameters between 2.3 and 6.2. This range of virial parameters suggests that none of the structures are

bound. But does this mean that L1451 will not form stars? Since we know a star is forming at L1451-mm, and since there are centrally condensed structures in the dust and molecular line maps (in Features A, B, C, and J), it is likely that some of the structures are at least marginally bound.

The coefficient in the virial theorem used in Equation 3.3 assumes a density profile of $\rho(r) \propto r^{-k}$, with $k = 0$, representing a constant density structure. If a structure is centrally condensed, an exponent of $k = 2$ leads to a lower coefficient that produces a factor of 1.67 decrease in the virial parameter (MacLaren et al. 1988): $3R_{cl}\sigma_{cl}^2/GM_{cl}$. Columns 4 and 8 of Table 3.9 report values for $k = 2$ to highlight this point. Now considering the N_2H^+ velocity dispersion, the structures discussed above have virial parameters dropping from $2.3 < \alpha < 6.2$ to $1.4 < \alpha < 3.7$. Structures 0 and 2 are at least marginally gravitationally bound with $\alpha < 2$; they appear in the *Herschel* maps as centrally condensed dust structures with Bolocam cores within them.

Two major sources of systematic uncertainty in the measured virial parameters, regardless of density profile, are the column density and temperature values derived from the *Herschel* SED fitting in Section 3.7.1. We discussed how using a single temperature model (ignoring the warmer foreground and background component surrounding the colder L1451 region) for fitting the *Herschel* SEDs leads to estimated column densities that are about half of the true column densities and estimated temperatures that are ~ 2.5 – 5 K higher than true temperatures. If the measured column densities are half of the true column densities, this directly leads to an α overestimate by a factor of 2. The temperature overestimate systematically increases the thermal component of the internal velocity dispersion of each structure, thereby increasing the dispersive term used to calculate α . The temperature error is less significant than the column density error, but still contributes a $\sim 7\%$ system-

atic increase in the virial parameter if the temperature is overestimated by 2.5 K. Work has been done on the galactic scale to estimate dust mass underestimation due to spatial resolution and temperature mixing in *Herschel* data; Galliano et al. (2011) found that *Herschel*-derived dust masses can be $\sim 30\%$ underestimated in the Large Magellanic Cloud (LMC). Our observations have much higher spatial resolution than observations of the LMC, but the warm-cold temperature contrast in local clouds like L1451 may be more extreme than on galactic scales, explaining our larger correction factor. If the values in Table 3.9 are reduced by a factor of two, then more dust leaves would appear to be in virial equilibrium.

The virial analysis from Equation 3.3 ignores the surface pressure term of Equation 3.2, $3c_{\text{pr}}P_{\text{ic}}V_{\text{cl}}$, which can be important for young star forming regions. If a structure is not bound according to the balance of gravitational potential energy and internal kinetic energy, it may still satisfy the virial theorem if the surface pressure is enough to confine the structure in the presence of its internal energy. As we noted above, confinement by surface pressure can satisfy the virial theorem, but it does not mean a structure is gravitationally bound—the structure may form a star in the future if it collapses, it may remain a persistent structure, or it may disperse if the external pressure decreases.

We calculated the energy from surface pressure that is exerted on each dendrogram structure from the dendrogram structure immediately surrounding it (e.g., branch 9 adding confining pressure to leaves 0 and 2). The c_{pr} term is considered unity to assess the maximum possible confining pressure. The P_{ic} term is calculated as $\rho_{\text{branch}}\sigma_{\text{branch}}^2$, where ρ_{branch} is the density of the confining structure (measured from the mean column density and size of the confining structure), and σ_{branch} is the quadrature sum of thermal and non-thermal velocity dispersion of the gas in the

confining structure. The modified virial parameter is then:

$$\alpha = 5 \frac{1 - \frac{2k}{5}}{1 - \frac{k}{3}} \frac{R_{cl}(M_{cl}\sigma_{cl}^2 - \rho_{branch}\sigma_{branch}^2 V_{cl})}{GM_{cl}^2}. \quad (3.8)$$

Columns 3, 5, 7, and 9 in Table 3.9 consider external confining pressure for the different molecular tracers and density profiles. As an example, the virial parameter of structure 0 is reduced by about a factor of two when considering external confining pressure. This means that the external confining energy from the surrounding branch on the dust leaf is about 50% the internal energy of the dust leaf. Since the gravitational potential energy of the dust leaf is comparable to the energy from external confining pressure, this structure is likely confined by a combination of self-gravity and external pressure. Overall, with the addition of this confining term, for a $k = 2$ density profile, the majority of the sources have virial parameters of $\alpha \lesssim 2$. If we then consider the column density underestimation discussed above, the values would be reduced even further. We will explore these results in more detail in upcoming work.

Considering external pressure, the uncertainties in the density profile, and the uncertainties in column density of the structures, most of the dust structures in L1451 appear on the threshold of satisfying the virial theorem, and at least two structures (0, 2) appear to be gravitationally bound as long as their density profile is not uniform.

It is clear that even with the improved data from telescopes like CARMA and *Herschel*, uncertainties still make it difficult to find a definite result with this type of analysis. Therefore, we conclude that although the traditional virial analysis, which only considers the balance of internal kinetic energy to gravitational potential energy, suggests that most L1451 leaves are not bound, considerations of surface pressure, density profiles, and column density underestimation suggest that several of the dust structures satisfy the virial theorem and may be at the precipice of star formation. In

particular, structures 0, 2, 5, 6, and 7 are all candidates for being bound. All of these structures appear centrally condensed: structure 0 contains Per Bolo 4, structure 2 contains Per Bolo 6, structure 5 contains L1451-west, structure 6 contains L1451-mm, and structure 7 is a leaf adjacent to L1451-mm. This supports these structures (or at least the central parts of these structures) being bound.

We will extend this type of virial analysis in upcoming work and will compare virial parameters across CLASSy regions. This way, even if there are systematic and statistical uncertainties, all structures will have been observed and analyzed in the same way, making a relative comparison of virial parameters across clouds at different stages of evolution possible.

3.8.3 Closer Look at L1451-mm and L1451-west

In this section, we explore the properties of the two centrally condensed, roughly spherical cores in L1451. One is L1451-mm, which we know is a compact object containing a YSO or a FHSC (Pineda et al. 2011). The other is L1451-west, which has been discovered with these observations. We summarize the morphology and kinematics of L1451-mm below, and then describe the properties of L1451-west and how they compare to L1451-mm.

The top row of Figure 3.22 shows molecular and continuum features of L1451-mm. L1451-mm is the only confirmed compact continuum core in L1451, and all molecules trace strong emission near, and surrounding its location. N_2H^+ shows a peak of integrated emission at the location of L1451-mm, while HCN and HCO^+ show peaks that are slightly offset. The surrounding emission is more concentrated for N_2H^+ , and more widespread for HCN and HCO^+ . The N_2H^+ centroid velocity field shows a gradient across the core, which Pineda et al. (2011) modeled as a rotating and infalling envelope using slightly higher angular resolution data ($5''$); we

measure a gradient of about $6 \text{ km s}^{-1} \text{ pc}^{-1}$ through the peak of integrated emission at a position angle of 120 deg east of north (see white line in the top row panels of Figure 3.22). The velocity dispersion field is narrowest around the edges of the core with minima $\sim 0.07 \text{ km s}^{-1}$, and it shows an increase toward the core location, with a peak $\sim 0.2 \text{ km s}^{-1}$. See Pineda et al. (2011) for detailed discussion and modeling of the possibility that L1451-mm is a dense core with a central YSO and disk, or a dense core with a central FHSC.

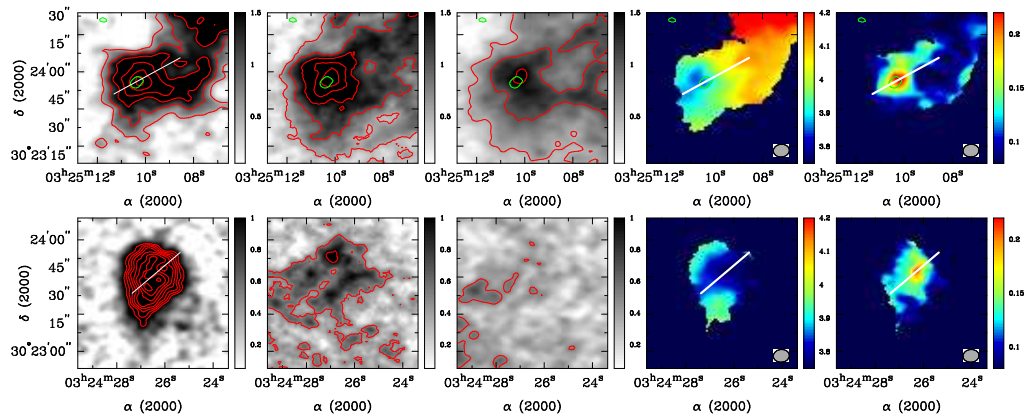


Figure 3.22: The top and bottom rows show properties of L1451-mm and L1451-west, respectively. From left-to-right, the panels are: N_2H^+ , HCN, and HCO^+ integrated intensity ($\text{Jy beam}^{-1} \text{ km s}^{-1}$), N_2H^+ centroid velocity (km s^{-1}), and N_2H^+ velocity dispersion (km s^{-1}). The kinematic maps of each source are on the same color scale. The velocity dispersion is expressed as Gaussian σ (FWHM/2.355 in km s^{-1}). The green $0.0039 \text{ mJy beam}^{-1}$ contour represents our L1451-mm compact continuum detection. The red contours are used to accentuate specific features in the greyscale maps. The white lines represent the direction of the measured velocity gradient through each source.

The bottom row of Figure 3.22 shows molecular and continuum features of L1451-west. The N_2H^+ integrated intensity map does not have a single peak of integrated emission at the center of the structure. Instead, there are two peaks in the southern half of the source $\sim 2.5 \text{ Jy beam}^{-1} \text{ km s}^{-1}$, and one peak in the northern half of the source $\sim 2.4 \text{ Jy beam}^{-1} \text{ km s}^{-1}$ (the red contours in the bottom-left panel of Figure 3.22 represent $1.1\text{--}2.5 \text{ Jy beam}^{-1} \text{ km s}^{-1}$ in $0.2 \text{ Jy beam}^{-1} \text{ km s}^{-1}$ increments).

The source is considerably weaker in HCN, and not detected in HCO⁺. This is an indication that this might be a very cold, dense region of L1451, where CO is depleted. If CO is frozen out onto dust grains, then it is not able to destroy N₂H⁺, leading to an increased abundance of N₂H⁺. Likewise, if CO is frozen out, it is not available to create HCO⁺ through collisions with H₃⁺ (Prasad & Huntress 1980). Our temperature map in Figure 3.17 does not suggest that dust around L1451-west is significantly colder than L1451-mm, but the systematic uncertainties in that temperature map discussed in Section 3.7.1 leave room for lower temperatures than we derived.

The N₂H⁺ centroid velocity field of L1451-west shows a relatively complex structure compared with L1451-mm, with higher velocity emission in the southern and northeastern sections of the core, and lower velocity emission toward the center and west of the core. Since the higher velocity emission at both ends of the source is bridged with intermediate velocity emission along the eastern edge, we consider the simplest case to be the source rotating in a northwest-southeast direction, marked by the white line in the bottom row panels. We measure a velocity gradient of $\sim 2.5 \text{ km s}^{-1} \text{ pc}^{-1}$ along that direction.

The velocity dispersion field of L1451-west is narrowest around the edges of the core with minima $\sim 0.07 \text{ km s}^{-1}$, and it peaks near $\sim 0.2 \text{ km s}^{-1}$ at the location of lowest velocity emission in the central part of the source. The axis of rotation that we chose intersects this peak of velocity dispersion and runs between the three peaks of N₂H⁺ integrated emission, as seen in the bottom-left panel. It is possible that infall is producing the increased velocity dispersion. Infall would broaden the molecular emission toward the core center, with the blue shifted emission being brighter than the redshifted emission if the N₂H⁺ emission is optically thick. This could explain why the peak of velocity dispersion is at the location with the bluest

centroid velocity. The signal-to-noise of the detectable HCN spectra are too low to look for evidence of infall motions, so this needs to be followed up with deeper observations of optically thick and thin lines.

There is no compact continuum emission detected in data toward L1451-west. The $3\text{-}\sigma$ flux density limit for a point source ($\lesssim 3'' = 700$ AU) in our observations is 3.9 mJy, corresponding to a mass limit of $0.08 M_{\odot}$ for the conversion from mJy to M_{\odot} discussed in Chapter 2 (Section 2.3). We use the location of peak velocity dispersion as a proxy for the location of a compact continuum core, if it exists; this peak is offset from the peak in the *Herschel*-derived column density map by about $16''$.

We estimated the size, physical density, total mass, and virial mass of L1451-mm and L1451-west for a more detailed comparison. To determine the size, we used the MIRIAD `imfit` routine to fit a two-dimensional gaussian to the N_2H^+ integrated intensity map. The geometric mean of the major and minor axes are $37''$ and $32''$ for L1451-mm and L1451-west, respectively. To determine the maximum physical density, we took the peak column density of each source within the fitted gaussian, and assumed their depth was the same extent as their geometric mean across the plane of the sky. For both sources, the physical density is $7\text{--}8 \times 10^4 \text{ cm}^{-3}$ in the $7''$ beam. This density is sensible, considering that we observe N_2H^+ , HCN ($J = 1 \rightarrow 0$) in L1451, which are molecular transitions with effective excitation densities on the order of 10^5 cm^{-3} .

To estimate the total mass associated with each source, we summed the *Herschel*-determined mass within the two-dimensional gaussian. L1451-mm and L1451-west have a total mass of ~ 0.25 and $\sim 0.16 M_{\odot}$, respectively. To estimate the virial mass from the sizes measured above and the masses listed here, we calculated the velocity dispersion of N_2H^+ within each two-dimensional gaussian as described in

Section 3.8.2, and used Equation 3.3 with $k = 2$ to account for these objects being approximated as centrally condensed spheres instead of uniform-density spheres. L1451-mm and L1451-west have a virial mass of ~ 0.70 and $\sim 0.59 M_{\odot}$, respectively. Although this would imply that the material in these sources is not gravitationally bound, we know that a young star is forming in L1451-mm. Considering the systematic uncertainties discussed in the previous section, along with uncertainties in κ_{ν} and our choice of $\beta = 1.7$, the mass of these sources could be double what we measure here—in that case, the ratio of virial mass to total mass comes closer to one, indicating structures that are consistent with being gravitationally bound.

We also compared the mass within 4200 AU ($18''$ at $d=235$ pc) to the intrinsic radius at 70% of peak intensity, following the analysis of starless cores presented in Kauffmann et al. (2008). We measured the mass using the *Herschel* data, and got 0.22 and 0.23 for L1451-mm and L1451-west, respectively. We measured the radius using the N_2H^+ integrated intensity, since the dust data is not as well resolved to derive accurate radius measurements. L1451-mm measured $7''$, and L1451-west measured $12''$ at 70% of the peak intensity. Compared to the sample of starless cores in Kauffmann et al. (2008), L1451-mm is more compact than starless, while L1451-west is at the upper limit of compactness seen in starless objects.

All of these observational results point to L1451-west being similar to, but slightly less evolved than, L1451-mm, yet more evolved than a prestellar core. Deep continuum and spectral line observations will be needed to determine the true nature of these sources. But these two cores are the best evidence that L1451 is a region that is just starting to form its first stars. L1451-mm was the target of an ALMA Cycle 1 project that was observing a sample of five FHSC candidates, and we put in an ALMA Cycle 3 proposal to observe L1451-west. These new observations will build on the results presented here and in Pineda et al. (2011).

3.8.4 Depth of L1451 Structures: A Non-Filamentary Region

Comparing the projected size of cloud structure to its depth along the line-of-sight gives a better understanding of the three-dimensional geometry of a region where stars are forming (e.g., a region that is primarily planar/sheet-like versus one that is more spherical). We described a statistical method to estimate the typical line-of-sight depth of cloud structures in Chapter 2 (Sections 2.7.2 and 2.7.3). The method uses the spatial and kinematic properties of dendrogram objects presented in Tables 3.4–3.6. It assumes that the V_{lsr} variation (ΔV_{lsr} ; Column 11) of a structure scales with its projected size (Column 9) in a turbulent medium. It also assumes that the mean non-thermal velocity dispersion ($\langle\sigma\rangle_{\text{nt}}$) of a dendrogram structure scales with its depth along the line-of-sight in a turbulent medium. We calculate $\langle\sigma\rangle_{\text{nt}}$ for each structure in all three molecular tracers by subtracting the thermal velocity dispersion of 10 K gas of the given tracer from the value reported in Column 12 of Tables 3.4–3.6: $\langle\sigma\rangle_{\text{nt}} = \sqrt{\langle\sigma\rangle^2 - \sigma_{\text{th}}^2}$. With those assumptions, we create two size-linewidth relations using all the dendrogram structures (one with projected size versus $\langle\sigma\rangle_{\text{nt}}$, and the other with projected size versus ΔV_{lsr}), and take the spatial scale where they cross as the typical depth of the region. See Chapter 2 (Section 2.7.3) for the theoretical framework and numerical results that justify this method.

We used the method in previous papers to argue that the typical depth of the N_2H^+ emission in the CLASSy Barnard 1 and Serpens Main regions was 0.1–0.2 pc (see Section 2.7.3 and Lee et al. (2014)). Figure 3.23 shows the size-linewidth relations for each molecule. As in the analysis of Barnard 1 in Chapter 2 and Serpens Main in (Lee et al. 2014), the projected size- ΔV_{lsr} for each molecule has a positive

slope (which is expected for a turbulent medium), while the projected size- $\langle\sigma\rangle_{\text{nt}}$ relationship has a flatter slope (which is expected if all structures have a similar depth along the line-of-sight, independent of their projected size). The best-fit lines to the relations cross at a size-scale 0.11 and 0.10 pc for N_2H^+ and HCN, respectively, indicating that those molecules are tracing structures ~ 0.1 pc in depth. The HCO^+ fits cross near 0.40 pc, indicating that it is tracing structures with larger line-of-sight depths compared to the other molecules. This is consistent with HCO^+ detecting larger-scale, lower density gas than the other molecules.

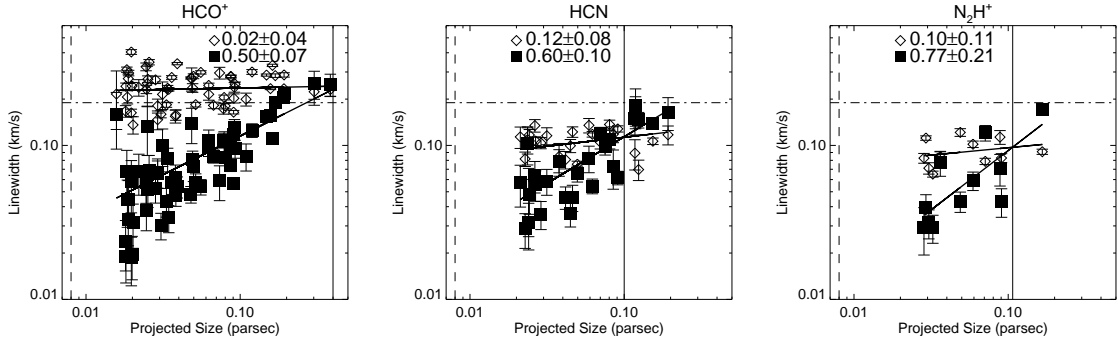


Figure 3.23: Scaling relations between projected structure size and V_{lsr} variation (ΔV_{lsr} ; solid squares), and projected structure size and mean non-thermal velocity dispersion ($\langle\sigma\rangle_{\text{nt}}$; open diamonds), for each molecule. The solid lines represent single power-law fits to the data points. The horizontal line represents the typical thermal speed for H_2 at gas kinetic temperatures near 11 K. The vertical dashed line represents our spatial resolution of ~ 0.008 pc. The vertical solid line represents the spatial scale where the power-law fits intersect.

These results show that the N_2H^+ emission in L1451 has similar depth as it does in Barnard 1 and Serpens Main. However, there are differences between L1451 and the other regions that lead us to different conclusions about the large-scale structure of L1451. In Chapter 2 (Section 2.7.3), we said that the depth of Barnard 1 (0.1–0.2 pc) is comparable to the largest size of individual N_2H^+ dendrogram structures identified from the isolated N_2H^+ hyperfine component (0.2–0.3 pc). But we followed up by discussing how the Barnard 1 has contiguous N_2H^+ structure at parsec-scales

when considering the full N_2H^+ emission instead of just the isolated hyperfine component. We used the estimated 0.1–0.2 pc depth and observed parsec projected size of Barnard 1 to conclude that the region is flattened at the largest scales with filamentary substructure (such as the B1 Ridge) forming within the large-scale sheet. A similar argument was made for Serpens Main in (Lee et al. 2014).

In projection, the full N_2H^+ emission, sub-millimeter continuum emission, and other molecular emission from L1451 region does not appear to have contiguous structure across parsec scales like the other CLASSy regions. Instead, the emission is concentrated in a few major features, sub-parsec in size, that were identified in Section 3.4. Because of this, we argue that the L1451 is not a flattened, sheet-like region of dense gas and dust at parsec-scales with connected substructure. It appears more like a loose collection of dense concentrations that are ~ 0.2 pc projected on the sky and ~ 0.1 pc deep.

The physical density of the regions of L1451 with N_2H^+ emission can be estimated from the cloud depth and column density. For a 0.1 pc depth of N_2H^+ emission and a mean $N(\text{H}_2)$ of $6 \times 10^{21} \text{ cm}^{-2}$ measured from the *Herschel* data, the derived physical density is $2 \times 10^4 \text{ cm}^{-3}$ in the regions of L1451 with N_2H^+ emission. This is lower than the $\sim 10^5 \text{ cm}^{-3}$ estimate for the physical density needed to excite N_2H^+ ($J = 1 \rightarrow 0$) to ~ 1 K, which was discussed in Chapter 1. This is not an inconsistency, since it is possible to excite N_2H^+ at a range of physical densities, where the range depends on the molecular column density (and thus relative abundance of N_2H^+ to H_2), the gas kinetic temperature, and the linewidth of emission. Using the RADEX program (van der Tak et al. 2007), we find that N_2H^+ ($J = 1 \rightarrow 0$) can reach 1 K brightness temperatures with a physical density of $2.7 \times 10^4 \text{ cm}^{-3}$ if the gas kinetic temperature is 12 K, the molecular column density of N_2H^+ is $6 \times 10^{12} \text{ cm}^{-2}$, and the linewidth of emission is 0.3 km s^{-1} . This physical density is

essentially the same as derived from our depth and column density measurements.

We can compare the typical depth of the molecular emission to the projected size of the largest-scale structures of each molecule in Figure 3.19 to infer the three-dimensional morphology of the individual molecular structures. The projected size of N_2H^+ structure 21 (lowest level branch of Features A) is ~ 0.17 pc, structure 18 (lowest level branch of Features C) is ~ 0.09 pc, and structure 17 (lowest level branch of Features B) is ~ 0.17 pc. For a typical N_2H^+ depth of 0.11 pc, these structures have axis ratios of 1.5:1 and 0.8:1, with a mean of 1.3:1. The projected size of HCN structure 45 (lowest level branch of Feature A) is ~ 0.24 pc, structure 43 (lowest level branch of Feature C) is ~ 0.17 pc, and structure 40 (lowest level branch of Feature B) is ~ 0.19 pc. For a typical HCN depth of 0.10 pc, these structures have axis ratios between 2.4:1 and 1.7:1, with a mean axis ratio of 2.0:1. The projected size of HCO^+ structure 111 (lowest level branch connecting Features A and C) is ~ 0.43 pc, and structure 112 (lowest level branch connecting Features B, H, F, G, E, and I) is ~ 0.46 pc. For our derived typical HCO^+ depth of 0.40 pc, these structures have axis ratios of 1.1:1 and 1.2:1.

With axis ratios between 0.8:1 and 2.4:1 for individual structures that do not connect at larger scales, these results support the L1451 region being composed of discrete, high-density structures that are approximated as ellipsoids. In addition to not having contiguous, flattened structure at parsec scales like the other CLASSy regions, none of the large-scale structures of L1451 appear to have clear filamentary substructure like was the case in the other CLASSy regions. These results differentiate L1451 in a way beyond the lack of protostars and outflows.

We take these results as an indication that not everything in a molecular cloud is filamentary, or required to be filamentary, for star formation to begin. This pushes against the universality of filamentary cloud structure that has taken a hold in

the past few years (André et al. 2014). The *Herschel* Gould Belt Survey team has suggested a paradigm for star formation where complex networks of filaments, with filaments lengths from ~ 1 pc up to tens of parsecs, are formed within clouds, followed by prestellar core formation that occurs due to fragmentation of the highest column density filaments (André et al. 2010). However, the L1451 region within Perseus is markedly not filamentary in *Herschel* and CLASSy data, with relatively ellipsoidal dust and gas structures a few tenths of parsecs across found within the parsec-scale region, and yet it is still beginning to form stars. Where does L1451 stand in the paradigm mentioned above and why are we drawing a different conclusion from the *Herschel* Gould Belt team?

The major differences between CLASSy and the *Herschel* Gould Belt Survey are with spatial area coverage, angular resolution, and density sensitivity. The *Herschel* survey has covered approximately 145 square degrees spanning a dozen molecular clouds, compared to the smaller CLASSy area coverage of about 800 square arcminutes (0.22 square degrees) encompassing five regions within two molecular clouds. The *Herschel* survey can map cloud column density and temperature structure with $36''$ angular resolution, compared to CLASSy that can map the denser gas ($n > 10^4 \text{ cm}^{-3}$ and $N(\text{H}_2) > \text{few} \times 10^{21} \text{ cm}^{-2}$) structure and kinematics with $7''$ angular resolution.

Overall, the differences mentioned above mean that the *Herschel* Gould Belt Survey has captured a relatively macroscopic view of star formation across molecular cloud complex scales throughout the Gould Belt, while CLASSy has captured a relatively in-depth view of the dense gas in five parsec-scale regions of star formation. The *Herschel* view of the entire Perseus Molecular Cloud is undoubtedly filamentary on the macroscopic scale of several parsecs, with many filaments being well-traced by *Herschel* continuum images. In the western half of Perseus, NGC 1333, Barnard 1,

and L1448 are the most active sites of star formation and have filamentary structure that appears strong in the *Herschel* bands; there are also weaker emission filamentary regions detected by *Herschel* between these active sites. However, we have seen that some parts of Perseus, such as L1451, are not filamentary, and those exceptions need to be accounted for in any global picture of star formation.

The morphology of *Herschel* continuum structure and CLASSy N_2H^+ structure are remarkably similar where both have detectable emission, and L1451 appears non-filamentary in both datasets. It is highly likely that many other non-filamentary regions within “macroscopically filamentary” clouds can be identified and studied as interesting sights of star formation. L1451 was chosen to be one of the five CLASSy regions because it appeared to have different properties from the more well-studied regions within Perseus and Serpens, and it is important that these parts of clouds do not get ignored.

If L1451 is not a flattened, sheet-like region at parsec-scales (unlike other CLASSy regions), if it does not have filamentary structure (unlike other CLASSy regions), and if it has less active star formation than other CLASSy regions, then it is natural to question what caused these differences. A cloud complex, like Perseus, that spans tens of parsecs will have different turbulent energies in different parts of the cloud. Simulations of turbulence-driven star formation with supersonic turbulence (e.g., Federrath & Klessen 2012) show that star formation within several-parsec scale clouds is clustered in regions where material has been compressed to high densities, leaving voids of star formation in other parts of the cloud. The L1451 region of Perseus may not have been as compressed as strongly by supersonic turbulence to form an overdense sheet-like structure at parsec-scales like may have happened several parsecs away near the cloud regions that became Barnard 1 and NGC 1333. Without a comparable push to high-density that other more active regions of Perseus

got, the L1451 region could have been predisposed to forming fewer stars.

3.9 Summary of L1451 Results

We presented observations and analysis of the L1451 region of the CARMA Large Area Star Formation Survey. We summarize the key findings below.

1. Only one compact continuum source is detected at 3 mm, down to a $3\text{-}\sigma$ limit of $3.9 \text{ mJy beam}^{-1}$ ($0.08 M_{\odot}$ limit) in a $9.2'' \times 6.6''$ beam. The detected source is L1451-mm, which has previously been identified as a FHSC candidate.
2. We detect widespread HCO^+ , HCN, and N_2H^+ ($J = 1 \rightarrow 0$) emission in L1451. The HCO^+ emission covers the largest area of the cloud, which we attribute to HCO^+ tracing lower-density material than the other molecules. HCN emission morphology is nearly identical to HCO^+ , although it is weaker and less spatially extended in most regions. The N_2H^+ emission has the smallest spatial extent, with morphology that differs from the other molecules at the smallest scales; N_2H^+ traces denser, colder material than the other molecules, as supported by comparison to *Herschel*.
3. We derived column density and temperature maps from *Herschel* observations at 160, 250, 350, and 500 μm . The values were derived using modified black-body spectrum fits to the data, and column densities agree to within 5% of *Planck* results when compared at the same angular resolution. The temperatures toward the densest regions are $\sim 2\text{--}3$ K warmer than kinetic temperatures derived from single-pointing ammonia observations toward dense cores. We attribute this difference to a limitation of using a single-component fit when modeling SEDs from cold, dense regions of molecular clouds. A simple two-layer model shows that having warm, 17 K foreground emission in front of

cold, 9 K cloud emission, can cause temperatures to be overestimated by a few K, and column densities to be underestimated by half from the true value. We use the single-component values in the analysis of this chapter, and discuss how the uncertainties effect the subsequent virial analysis. We will present a detailed comparison of single- and double-component fits using all CLASSy regions in a future paper.

4. The structure of the star-forming material in L1451 that is traced by the sum of all our molecular emission is very similar to column density structure that we derived from *Herschel* observations. All of the cloud locations that are above the $A_v \sim 8$ threshold for star formation are detected, and 90% of the molecular emission is at column densities above $1.9 \times 10^{21} \text{ cm}^{-2}$. This shows that high-resolution observations of this suite of spectral lines over large areas of molecular clouds are an excellent probe of the structure and kinematics of star forming material in young regions.
5. We use our non-binary dendrogram algorithm to identify dense gas structures in the HCO^+ , HCN, and N_2H^+ data cubes. Slight differences in the noise-level of each data cube are accounted for to ensure a uniform comparison of tree statistics. The HCO^+ dendrogram has the largest number of leaves and branches. A comparison of tree statistics shows that all tracers are identifying structures that are fragmenting in a similar way, even though we detect more HCO^+ branching levels compared to than HCN or N_2H^+ ; the increase in levels is likely due to HCO^+ being more sensitive to widespread emission from lower-density regions of the cloud. We show that tree statistics of the gas structure surrounding L1451-mm (a confirmed young protostar or FHSC) is very similar to that of the gas surrounding Per Bolo 6 (a single-dish continuum detection),

and argue this is an indication that star formation is proceeding in a similar fashion in both regions, with Per Bolo 6 a likely site of future star formation.

6. All molecules trace gas at similar systemic velocities, but the velocity dispersion of the HCO^+ emission is significantly larger than that of HCN or N_2H^+ : mean dispersions are 0.29, 0.16, and 0.12 km s^{-1} , respectively. This is likely due to HCO^+ tracing lower-density gas at larger scales than the other two molecules; in a turbulent medium, there is more power on larger scales, which will produce larger velocity dispersions.
7. A traditional virial analysis, comparing the kinetic and gravitational potential energy of dense structures assuming uniform density profiles, resulted in virial parameters of all structures being near or above two. We discussed how the virial parameter can be overestimated by about a factor of two from the systematic underestimation of column densities from our *Herschel* SED fitting, by assuming uniform density instead of stratified density profiles for the dust structures, or by neglecting the effects of external confining pressure. Several structures in L1451 satisfy the virial theorem when considering one, or a combination of these effects. We will explore these effects in more detail in upcoming works that do a uniform comparison of structures in all CLASSy regions.
8. We detect two strong, centrally condensed N_2H^+ structures: L1451-mm, and a newly identified source that we label L1451-west. L1451-mm was characterized by Pineda et al. (2011) as a FHSC candidate or young protostar. Our data shows that L1451-west is similar to, but likely younger than L1451-mm. It has strong emission from N_2H^+ but is depleted in HCO^+ , unlike L1451-mm which has strong emission from both molecules; this could indicate that L1451-west

is colder than L1451-mm. It is less centrally condensed than L1451-mm, but more centrally condensed than the typical prestellar core; this indicates that L1451-west is at an evolutionary state between the prestellar core phase and the FHSC or early protostellar phase of L1451-mm. Follow-up observations will determine if L1451-west is a viable FHSC candidate.

9. We used our size-linewidth analysis presented in Chapter 2 to show that the dense gas in L1451 is not flattened at the largest scales like the Barnard 1 and Serpens Main CLASSy regions studied in previous chapters and papers, and that its dense gas structures are more ellipsoidal than filamentary. Typical inferred line-of-sight depths for HCO^+ structures are 0.40 pc with projected sizes ~ 0.45 pc, and typical HCN and N_2H^+ line-of-sight depths are 0.10 pc with projected sizes of ~ 0.20 to 0.14 pc, respectively. This suggests that sheet-like geometry at parsec-scales with filamentary substructure is not a prerequisite for star formation, but that the lack of a sheet-like geometry may be an explanation for why L1451 has formed fewer stars than the other CLASSy regions.
10. Overall, these observations support turbulent star formation theories that argue that externally driven turbulence can create complex, hierarchical structure in molecular clouds (regardless of whether that structure is filamentary), without internal feedback from protostars. The molecular emission from L1451 shows a lot of complex structure, even though there is very little existing star formation in the region. We cannot say that individual structures within L1451 are definitively gravitationally bound based on our virial analysis, but that several structures are consistent with satisfying the virial theorem within the uncertainties in the data; we also know at least one star is forming in the

region. This supports external supersonic turbulence being the driver of the first structure within the densest regions of molecular cloud complexes; those structures then become the dense, fertile grounds for the future formation of stars.

Chapter 4

Comparing CLASSy Regions to Understand Pathways to Star Formation

Abstract

We present a comparison of the dense gas emission, hierarchical complexity, and young stellar content of all five regions from the CARMA Large Area Star Formation Survey. The goals are to compare fragmentation properties of dense gas at different stages of evolution, and how, if at all, the young stellar content of those regions is linked to that fragmentation. We construct a non-binary dendrogram from the integrated intensity map of each region, using a uniform set of algorithm parameters to ensure a proper cross-comparison of region properties. The more evolved regions, including Serpens Main, Serpens South, and NGC 1333, show more levels of fragmentation in their dendrograms relative to Barnard 1, while the least evolved L1451 region shows little hierarchical complexity in this uniform compari-

son. Despite the differences in hierarchical depth between the regions, all regions have a similar mean branching ratio; this shows that fragmentation is similar across all stages of star formation. We find that the Class 0 sources in each region are primarily located within dendrogram leaves, which represent the peaks of the dense gas hierarchy in each region. This shows that the youngest protostars tend to form where gas has become the most hierarchically complex. The more evolved Class II sources are preferentially found further from leaves. This shows that more evolved protostars migrate away from their natal core as they accrete cloud material, or that they may consume or disperse their natal core.

4.1 Introduction

A branching hierarchy is a general term for a system that contains objects with at least two direct subordinates. One example of a branching hierarchy is in academia, where a professor may have two postdoctoral subordinates, and each postdoctoral scientist may have three graduate and undergraduate student subordinates. Observations have shown that the structure of the molecular ISM is a branching hierarchy, which begins on the largest scale with molecular clouds, extends down in scale to many clumps (overdensities within clouds), then to multiple cores (regions within clumps where individual or multiple protostars may form), and then finally to protostars (Williams et al. 2000). This is a conceptual view of the hierarchical nature of star formation, illustrated in Figure 4.1, which highlights the fact that smaller, denser structures are born within larger, less dense structures. This is predicated on an ordered relationship between clouds, cores, clumps, and stars, as is generally accepted in the scientific community. However, observational limitations of clouds (poor angular resolution, limited area coverage, limited types of dust and gas trac-

ers) have not allowed a detailed assessment of the linkage through molecular cloud branching hierarchies to stars that are born with the clouds.

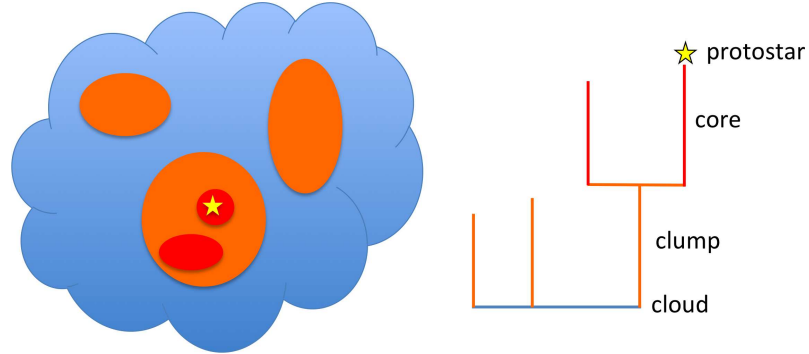


Figure 4.1: *Left:* A cartoon molecular cloud, where the blue emission is from the large-scale cloud, the orange emission is from clumps forming within the cloud, the red emission is from cores that fragmented from the clumps, and the yellow star represents a protostar forming within a core. *Right:* A cartoon dendrogram representation of the cloud on the left. The cloud represents the parent structure that all substructures higher in the tree form from. The cloud fragments into three clumps, and one clump fragments further into two cores. One core forms a protostar, which sits at the top of the cartoon hierarchy.

In this chapter, we use our CLASSy data and catalogs of stellar content in each region to assess the importance of fine-scale hierarchical fragmentation in the star formation process. We do not classify structures in terms of clouds, clumps, and cores—we instead map the full hierarchical nature of the regions from cloud-to-core scales, quantify the hierarchies using tree statistics, and quantify the relationship between the hierarchy and stellar content by comparing the spatial distribution of stars and cloud structures. It is possible that parsec-scale regions of dense gas fragment in a similar hierarchical fashion in most regions of clustered star formation, with youngest stars always being found at hierarchical peaks of volume and column density. Alternatively, clouds may fragment in a hierarchically similar way, but with young stars forming in relatively random locations relative to hierarchical peaks. Another possibility is that fragmentation and young star location differs from cloud-to-cloud.

CLASSy data are able to address the relationship between hierarchical dense gas structure and current star formation. We observed N_2H^+ ($J = 1 \rightarrow 0$) with high angular resolution ($\sim 7''$) across five large regions with diverse star formation properties. By having this sample of diverse regions within the Perseus and Serpens clouds, we can explore the similarities and differences of dense gas fragmentation at different evolutionary stages and environments. We can also explore whether the stellar content is closely associated with peaks¹—does star formation care about the fine-scale hierarchical structure of dense gas? As a reminder, we discussed in Chapter 1 (Section 1.5) how N_2H^+ is a tracer of high density, cold gas, which means we are tracing cloud regions that are viable locations for star formation. In the discussions that follow, we will assume that high (low) integrated intensity means high (low) dense gas column density.

The following is a breakdown of this chapter. In Section 4.2, we present the N_2H^+ integrated intensity maps of each region, and demonstrate that relative N_2H^+ integrated intensity is a good proxy for relative dense gas column density. The young stellar content of each region is summarized in Section 4.3, using *Spitzer* catalogs and *Herschel* observations for YSO identification. We use our non-binary dendrogram algorithm in Section 4.4 to assess the hierarchy of each N_2H^+ integrated intensity map in a uniform way, accounting for differences in region distance and noise-level. Section 4.5 compares the tree statistics of each region to determine the relative hierarchical complexity and fragmentation properties of each CLASSy region. Section 4.6 connects YSOs to dendrogram-identified structures to determine if hierarchical structure formation is linked to the formation of young stars. We summarize key findings in Section 4.7.

¹We are tracing gas denser than $\sim 10^5 \text{ cm}^{-3}$ with observations of N_2H^+ ($J = 1 \rightarrow 0$), but we are not able to distinguish between column density and density peaks with just one observed line.

4.2 Integrated Intensity Maps Across Regions

Figure 4.2 shows all CLASSy regions with the same N_2H^+ ($J = 1 \rightarrow 0$) integrated intensity color-scale. Serpens Main, Serpens South, and NGC 1333 have the strongest emission, peaking at ~ 22 , 21, and 16 $\text{Jy beam}^{-1} \text{ km s}^{-1}$, respectively. Barnard 1 has weaker emission peaking at ~ 11 $\text{Jy beam}^{-1} \text{ km s}^{-1}$. L1451 has the weakest emission, peaking at ~ 3 $\text{Jy beam}^{-1} \text{ km s}^{-1}$. This trend of integrated intensity shows that the two Serpens regions and NGC 1333 have the largest concentration of relatively high dense gas column density amongst the CLASSy regions, with L1451 having the lowest dense gas column density.

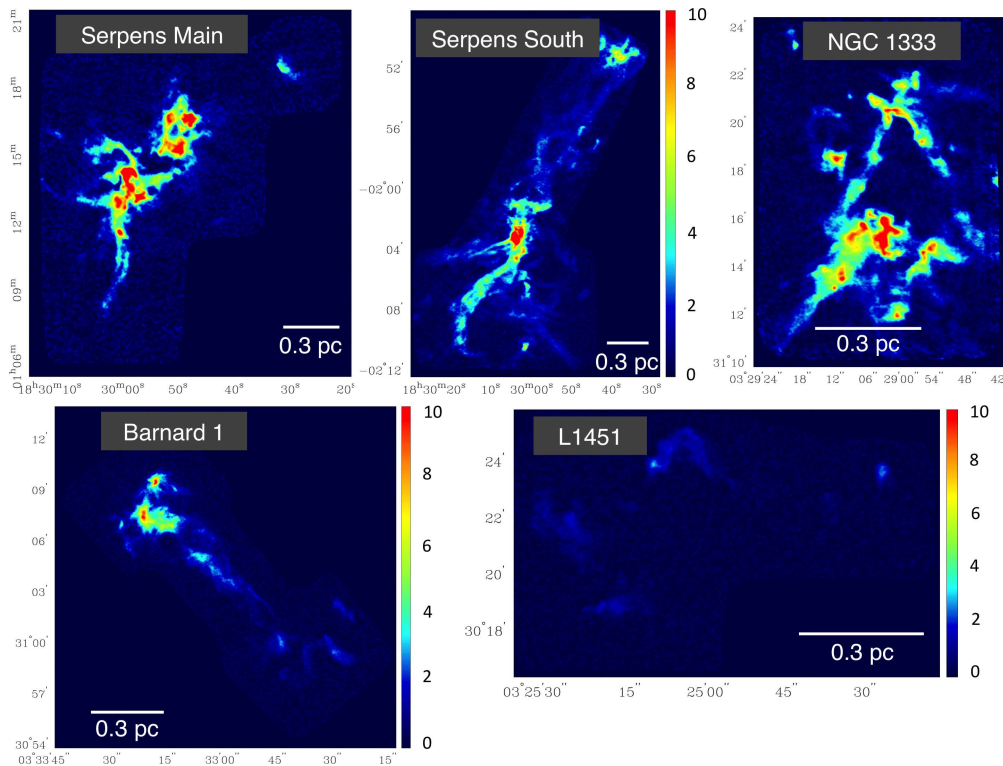


Figure 4.2: N_2H^+ integrated intensity maps ($\text{Jy beam}^{-1} \text{ km s}^{-1}$) for all five CLASSy regions on the same intensity scale.

To support the view of relative integrated intensity as a proxy for relative dense gas column density, we can first compare the *Herschel*-based column density map of

L1451 presented in Chapter 3 and that of Barnard 1 seen in Figure 4.3 (provided by K. Lee, priv. communication) to the N_2H^+ emission; *Herschel*-based maps for the other CLASSy regions have not been made yet. We know from Chapter 3 that 90% of our detected molecular emission in L1451 is at $\text{N}(\text{H}_2)$ above a few $\times 10^{21} \text{ cm}^{-2}$, peaking at $1.3 \times 10^{22} \text{ cm}^{-2}$. With the so-called threshold for star formation at $7.5 \times 10^{21} \text{ cm}^{-2}$ (André et al. 2014, and references therein), these column densities show that L1451 has some sub-regions with gas above the threshold. The column density map for Barnard 1 peaks at around $8 \times 10^{22} \text{ cm}^{-2}$, with nearly the entire ridge structure having column densities above the L1451 maximum, and above the threshold for star formation. This shows that Barnard 1 has much higher column density than L1451, which agrees with what we were inferring from the comparison of N_2H^+ integrated intensity between the regions. Note that the area-weighted surface density (as defined in Leroy et al. 2013) of Barnard 1 and L1451 are about 105 and $65 M_\odot \text{ pc}^{-2}$, respectively, above $\text{N}(\text{H}_2) \simeq 1.4 \times 10^{21} \text{ cm}^{-2}$. Heiderman et al. (2010) report the mean surface gas density of the entire Perseus Molecular Cloud as $90 \pm 33 M_\odot \text{ pc}^{-2}$, indicating that Barnard 1 and L1451 are above and below the mean surface density of the cloud, respectively.

For a quantitative comparison of integrated intensity and dense gas column density maps, we convolved the integrated intensity of Barnard 1 and L1451 to the *Herschel* angular resolution ($36''$) and matched the pixel scale of the two maps. Figure 4.4 shows a general trend of increasing N_2H^+ integrated intensity with increasing column density (for *Herschel*) in both regions. The lack of a perfect correlation is not concerning since measured continuum column density and N_2H^+ integrated intensity respond differently to changes in density and temperature—regions with the same column density but different density or temperature can have different N_2H^+ emission properties (see discussion in Chapter 1, Section 1.5). Also, different N_2H^+

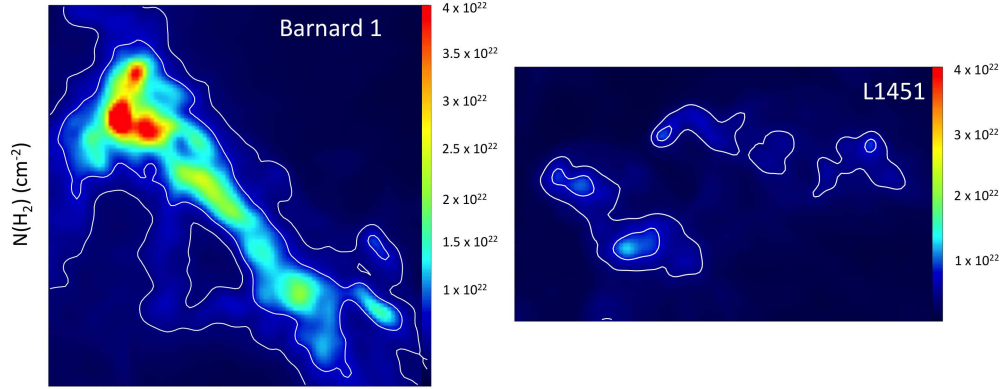


Figure 4.3: Column density maps for Barnard 1 (left) and L1451 (right) derived from *Herschel* SED fitting (see Chapter 3 for discussion of method). The maps are on the same color scale, from $1.0 \times 10^{20} \text{ cm}^{-2}$ to $4.0 \times 10^{22} \text{ cm}^{-2}$. The inner contour represents the threshold for star formation at $7.5 \times 10^{21} \text{ cm}^{-2}$, and the outer contour represents half that value. In Chapter 3, we discussed how our measured column densities are likely half of the true values towards lines of sight with $A_V > 2$.

abundances across a single region can lead to differences in N_2H^+ emission strength within that region that are independent of H_2 column density.

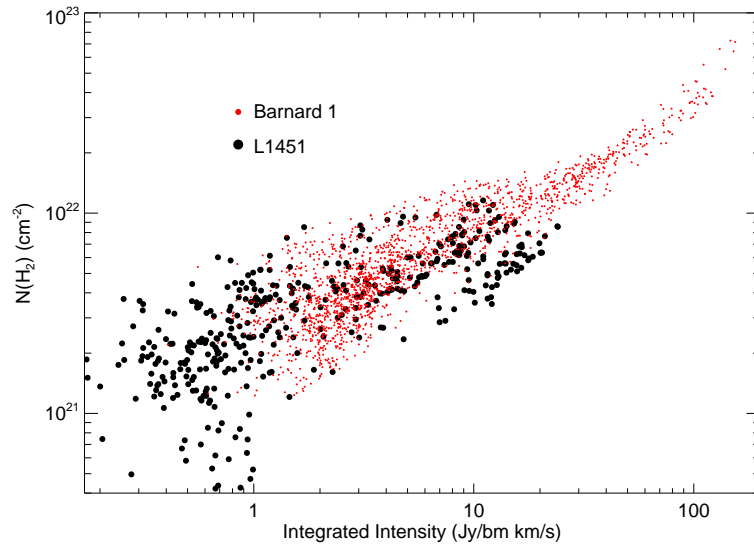


Figure 4.4: Pixel-by-pixel comparison of N_2H^+ integrated intensity and *Herschel*-derived column density for Barnard 1 and L1451. The original integrated intensity maps were convolved to match the angular resolution of the column density maps, and then regridded to the same pixel scale. Each point represents one beam.

4.3 YSO Statistics Across Regions

Table 4.1 summarizes the YSO statistics in each CLASSy region, listing Class II, Flat, and Class I YSOs from the *Spitzer* c2d Legacy Project (Evans et al. 2009, and references therein). The classifications are based on the SED spectral indices, α . The spectral index classification from c2d follows the convention from Greene et al. 1994, where Class II is $-1.6 \leq \alpha < -0.3$, Flat is $-0.3 \leq \alpha < 0.3$, and Class I is $\alpha \geq 0.3$. Class III sources commonly have weak infrared excesses. Therefore, the Class III numbers from *Spitzer* surveys are extremely incomplete, which has been confirmed by X-ray surveys of molecular clouds (Winston et al. 2010). We will not consider Class III sources in our analysis. The lifetime of the Class I and Flat phases is about 0.5 Myr each, while the Class II phase is observed to last for ~ 2 Myr (Evans et al. 2009).

The Class 0 stage was not recognized by c2d as a separate Class, since it requires a proper understanding of longer wavelength emission and viewing angle to help determine whether a source is Class 0 or Class I. For our analysis, we complemented the c2d sample in each region with sources visible in *Herschel* 70 or 100 μm images that were not classified as YSOs by c2d. We classify any source identifiable at 70 and/or 100 μm , but not at 24 μm or shorter wavelengths, as a Class 0 source. Sources identified at 70 and/or 100 μm , and also detected at 24 μm or shorter wavelengths are added to the Class I category; these sources may not have been classified as YSOs by c2d due to saturation, or incomplete SEDs. Appendix D contains a complete listing of new YSOs for each CLASSy region. *Herschel*-identified Class I sources not classified by *Spitzer* are arbitrarily given $3 > \alpha > 4$ to distinguish them from the highest- α *Spitzer* Class I YSOs. *Herschel*-identified Class 0 sources are arbitrarily given $\alpha > 5$ to distinguish them from the other YSOs.

Our mapped regions of Serpens Main, Serpens South, and NGC 1333 have the largest number of YSOs within them (between 69 and 89 sources), followed by Barnard 1 (with 16 sources), and then L1451 with no confirmed YSO detections from *Spitzer* or *Herschel*. We classify L1451-mm as a Class 0-like YSO for the purposes of this analysis since we know it has a slow CO ($J = 2 \rightarrow 1$) outflow (Pineda et al. 2011) that must be driven by a protostellar source or first hydrostatic core. Even though we do not use a similar criteria for finding more Class 0-like YSOs in the other CLASSy regions, such a criteria would have a relatively minor impact on the YSO statistics of those other regions, while it is the difference between zero and one YSO for L1451.

The ratio of (Class 0 + I)-to-(Flat + Class II) sources in Table 4.1 is 0.57, 0.60, 0.85, 2.2, and 1-to-0 for NGC 1333, Serpens Main, Serpens South, Barnard 1, and L1451, respectively. Evans et al. (2009) utilizes a similar ratio as a youth indicator for star forming regions: higher values are younger. This sets the order of evolution in the discussion in the following sections, with NGC 1333 and Serpens Main being the most evolved regions, followed by Serpens South, Barnard 1, and finally L1451.

4.4 N_2H^+ Dendrograms Across Regions

A goal of this chapter is to compare the hierarchical complexity, and its link to star formation, across the five regions. To uniformly compare the dendrograms of different regions, it is important to define the algorithm parameters used for dendrogram creation so they account for differences in distance and the noise-level of each region. Appendix C has details and examples for each of these considerations, and we already had an example of comparing dendrograms from data cubes with different noise levels in Chapter 3 (Section 3.6.1).

Table 4.1. YSO Statistics in CLASSy Regions

Region	Class II (c2d)	Flat (c2d)	Class I (c2d)	Class I (<i>Herschel</i>)	Class 0 (<i>Herschel</i>)
Serpens Main	30	13	21	1	4
Serpens South	33	15	20	20	1
NGC 1333	40	14	23	8	0
Barnard 1	4	1	8	1	2
L1451	0	0	0	0	1 ^a

Note. — Source statistics are only counting sources in our mapped region. The Class II, Flat, and I (c2d) sources are based on the *Spitzer* c2d catalogs (Evans et al. 2009). Class I (*Herschel*) sources are those identified by eye in *Herschel* 70 or 100 μm maps that have a corresponding *Spitzer* 24 μm detection. Class 0 (*Herschel*) sources are those identified by eye in *Herschel* 70 or 100 μm maps that do not have a corresponding *Spitzer* 24 μm detection. ^aThis represents L1451-mm, which is not detected by either *Spitzer* or *Herschel*, but which has a CO ($J = 2 \rightarrow 1$) outflow detection (Pineda et al. 2011).

We ran our non-binary dendrogram algorithm on the N_2H^+ integrated intensity maps of all CLASSy regions shown in Figure 4.2. The emission of each input map is masked down to the $2.5\text{-}\sigma$ level, where σ is the rms of each individual map. We account for differences in distance by contouring the data in units of $\text{Jy beam}^{-1} \text{ km s}^{-1}$ (conserved with distance), and ensuring that the `minpixel` parameter for each region corresponds to the same *spatial* area instead of the same angular area. The squared ratio of distances between Serpens and Perseus is 3.12, so we require a minimum of 4 and 12.5 beams worth of pixels for Serpens and Perseus structures to be considered leaves, respectively. We account for differences in noise level by setting the `minheight` parameter to be $2\text{-}\sigma_n$, where σ_n is the rms of the noisiest integrated intensity map, by setting the `stepsize` parameter to be $1\text{-}\sigma_n$, and by calculating tree statistics of each dendrogram above a cut at $2.5\text{-}\sigma_n$. The Serpens Main map has the largest integrated intensity rms, at $0.30 \text{ Jy beam}^{-1} \text{ km s}^{-1}$. Therefore, the absolute values of parameters are: `minheight` of $0.60 \text{ Jy beam}^{-1} \text{ km s}^{-1}$,

stepsize of $0.30 \text{ Jy beam}^{-1} \text{ km s}^{-1}$, and a cut for calculating tree statistics at $0.75 \text{ Jy beam}^{-1} \text{ km s}^{-1}$.

By contouring the data and defining noise-suppression parameters in absolute units of integrated intensity units, the hierarchical structure derived for every region is based on a uniform set of physical properties that can be linked to star formation; integrated intensity units are a proxy for dense gas column density, which we demonstrated in Section 4.2. This is instead of contouring the data and setting noise-suppression parameters in terms of the noise-level of each individual map. That would lead to regions branching at different step sizes and having different requirements for what it takes to be considered a true leaf, and it would make a uniform comparison between regions impractical (demonstrated in Appendix C).

Figures 4.5–4.9 show the resulting non-binary dendrograms for each region. The vertical axis of all the dendrograms represents integrated intensity and the relative heights of the axes are to scale. Serpens South has the most structures (75), which is about 60% more than the region with the next most structures. This is likely due to a combination of Serpens South having the largest mapped area of all CLASSy regions, and having significant amount of dense gas at high column densities. We observed all of the strongest emitting areas in each selected region (guided by existing lower-resolution maps of cool dust or other molecular tracers), so it is not the case that we merely missed parts of Serpens Main or NGC 1333, but rather that Serpens South has dense gas that covers the largest area on the sky. L1451 has the fewest structures, all branching from the tree base with no hierarchical complexity, with a mapping area that matches Barnard 1 and Serpens Main. This indicates that there is not as much high-density material to form many identifiable structures in this young region when contouring the data in a uniform way between regions. Note from Chapter 3 that L1451 does have hierarchical structure when analyzed with

different branching step and leaf requirements—this is discussed in more detail in the next section, where we use tree statistics for a comparison of the dense gas hierarchies in each region.

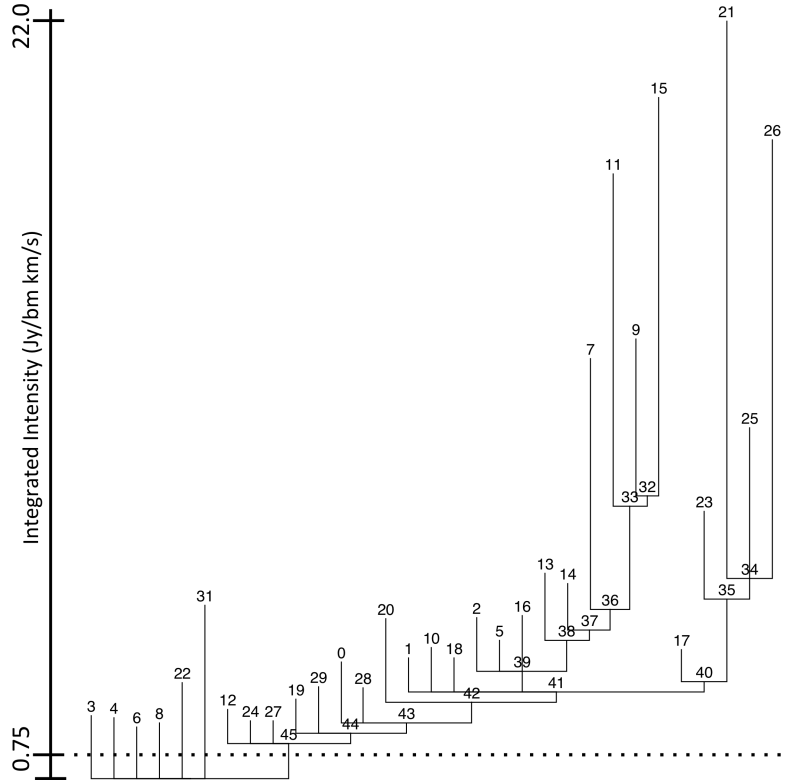


Figure 4.5: Non-binary dendrogram of N_2H^+ integrated intensity in Serpens Main. The vertical axis represents the $\text{Jy beam}^{-1} \text{ km s}^{-1}$ integrated intensity for a given location within the gas hierarchy. The horizontal axis has no physical meaning. The horizontal dotted line represents the noise limit for emission used in the dendrogram analysis ($2.5\text{-}\sigma_n$, where $\sigma_n=0.30 \text{ Jy beam}^{-1} \text{ km s}^{-1}$).

4.5 Statistical Comparison of Hierarchies

Table 4.2 lists region-averaged tree statistics for all five non-binary dendrograms. All statistics are calculated only using structures above the horizontal dotted line in Figures 4.5–4.9. The dotted line represents the noise limit for emission used in the analysis of Serpens Main, which is our noisiest map ($2.5\text{-}\sigma_n = 0.75 \text{ Jy beam}^{-1} \text{ km s}^{-1}$).

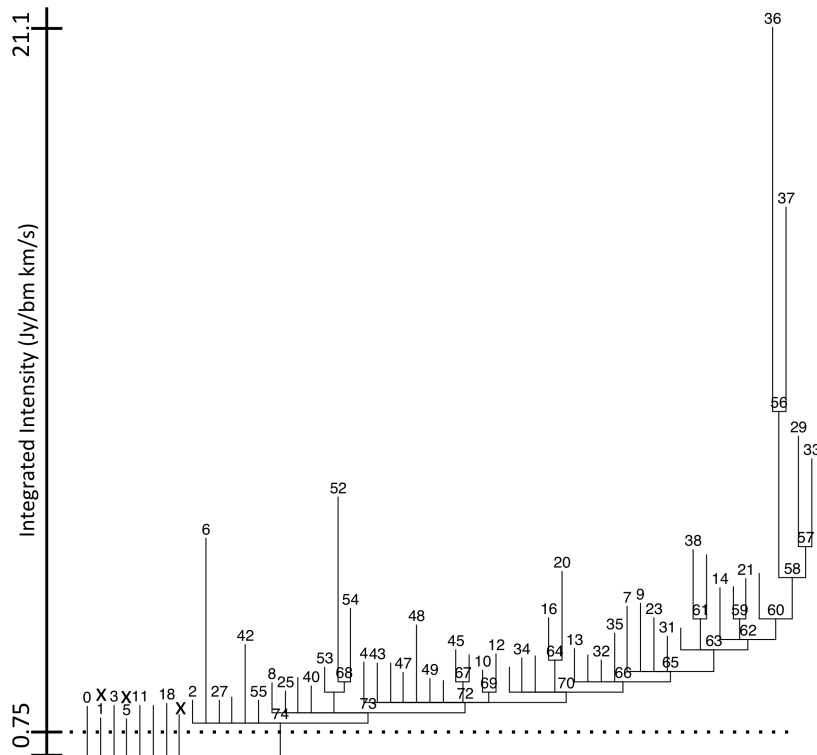


Figure 4.6: Same as Figure 4.5, but for Serpens South. The dotted line represents the noise limit used for Serpens Main, since Serpens Main had the largest noise limit of all five regions. Leaves that do not peak at least $0.60 \text{ Jy beam}^{-1} \text{ km s}^{-1}$ above the dotted line are marked with an “x” and not included in the calculation of tree statistics.

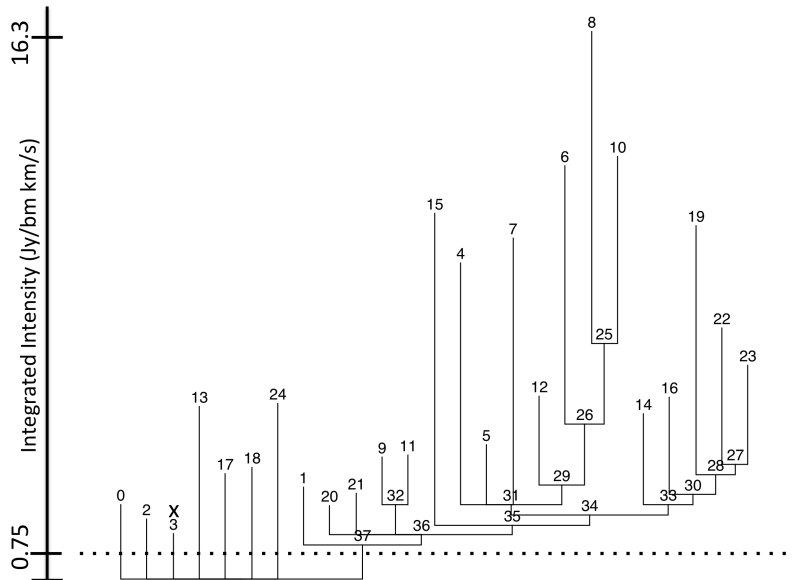


Figure 4.7: Same as Figure 4.6, but for NGC 1333.

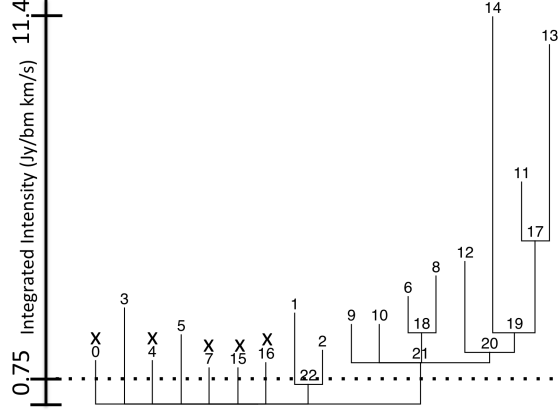


Figure 4.8: Same as Figure 4.6, but for Barnard 1. Branch 22 is below the noise limit of the noisiest map, and is not included in the calculation of tree statistics. Leaves 1 and 2 become leaves at branch level 0 instead of branch level 1.

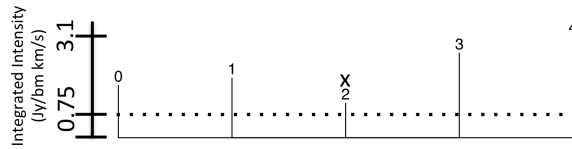


Figure 4.9: Same as Figure 4.5, but for L1451.

For regions less noisy than Serpens Main, we do not want to analyze any structures that would not be identifiable in Serpens Main. Therefore, all leaves must peak at least $0.60 \text{ Jy beam}^{-1} \text{ km s}^{-1}$ above the dotted line to be counted, and any branch that is below the dotted line is discounted, with its leaves then considered to be sprouting directly from the tree base.

The two Serpens regions have the highest maximum branching level of 11, followed by NGC 1333 at 8, Barnard 1 at 4, and L1451 at 0. The mean path length shows a similar trend, with the two Serpens regions on top, followed by NGC 1333 at about a half level lower on average, then Barnard 1 at about three levels lower on average, and L1451 with a 0 level average. This indicates that the dense gas in the two Serpens regions has fragmented to the most levels, with NGC 1333 not far behind. NGC 1333 and the two Serpens regions were classified as the most evolved regions in Section 4.3 based on their YSO statistics—the ratio of young-to-old pro-

Table 4.2. Tree Statistics

Region	Total No. ^a	Max Level ^b	Mean PL ^c	Mean BR ^d
Serpens Main	46	11	4.5	3.1
Serpens South	75	11	4.3	3.6
NGC 1333	37	8	3.8	2.6
Barnard 1	18	4	1.5	2.8
L1451	4	0	0	NA

Note. — ^a Total number of leaves and branches. ^b Maximum branching level. ^c Mean path length. ^d Mean branching ratio.

tostars are from 0.57 to 0.85 for the three regions. Barnard 1 is a much younger region, with a ratio of young-to-old protostars of 2.2. The maximum branching level and mean path length of Barnard 1 are much lower than the more evolved regions. This suggests that the number of branching levels is correlated with the evolution and range of dense gas column density in a region. This makes sense—if all regions start with a base-level of weak emission early in their evolution, the regions that have evolved to have the stronger emission on top of that base will have likely fragmented in more steps along their evolution to reach those strong emission peaks. L1451, which has the weakest emission of all regions, and only one Class 0-like source, has yet to fragment in appreciable amounts relative to the other regions.

Even though the regions show a large diversity in levels of fragmentation, the mean branching ratios for each region are similar. All regions, except for L1451, have a mean branching ratio between 2.6 and 3.6, meaning that each branch structure fragments into ~ 3 sub-structures as the hierarchy is built. This similarity is interesting, since the regions differ in their integrated intensity and protostellar outflow properties. In terms of protostellar outflows, the N_2H^+ emission from NGC 1333 and Serpens Main regions is overlapping with numerous outflows that we detect in HCO^+ and HCN. However, Serpens South has outflows primarily concentrated in

its central “hub” region, and Barnard 1 has a few outflows in its main core zone. This shows that the average dense gas fragmentation properties of a region is not strongly correlated with the stellar feedback in a region; regions that are dominated by outflows (e.g., NGC 1333 and Serpens Main) have similar fragmentation to regions where outflows are limited to a small percentage of the dense gas area (e.g., Barnard 1 and Serpens South). We cannot distinguish between structure formed from protostellar feedback induced fragmentation or original cloud fragmentation, but if some fragmentation near outflows was triggered by the protostellar feedback, then this could mean the initial fragmentation of dense gas in a region before the first generation of star formation is similar to subsequent fragmentation that is triggered from protostellar feedback.

What about L1451? We do not present a mean branching ratio for L1451, since it only has leaves sprouting from the tree base, and lacks hierarchical structure. Although L1451 appears simple in this comparison of integrated intensity maps contoured at the same levels, that does not mean L1451 is fragmenting with no hierarchically complexity. Star formation is set by physical processes, and is linked to high volume and column density regions of clouds. L1451 has lower amount of high density gas compared to other CLASSy regions, so it is has not yet evolved to the point where it can efficiently form stars. Even so, we know from Chapter 3 that there is detectable hierarchical structure in the HCO^+ , HCN , and N_2H^+ PPV cubes, and we calculated mean branching ratios for all molecules ~ 3 – 4 . This means that cloud fragmentation starts before a region has reached high enough densities to efficiently forms stars. This fragmentation is likely seeded from initial supersonic turbulence present in the cloud. Since the L1451 analysis in Chapter 3 revealed mean branching ratios similar to those found in this chapter for the more evolved regions, it shows that the hierarchical nature of the initial cloud fragmentation from

the cascade of large-scale turbulence is similar to the fragmentation that occurs once material has enough time to reach higher densities to collapse to form stars.

Putting this all together, it appears that dense gas fragments in a similar hierarchical fashion from the first stage of fragmentation that we see in the L1451 PPV cubes, to the second stage of fragmentation that occurs when densities are high enough to start forming stars, to the potential third stage of fragmentation that may occur when protostellar feedback injects additional energy into the cloud. The main difference between a region like L1451 and a region like NGC 1333 is not how the gas is fragmenting, but how much high density material has formed, and how many distinct fragmentation levels have formed.

4.6 Linking Stellar Content to Hierarchies

The previous section showed how the dense gas in all five CLASSy regions is fragmenting in a hierarchically similar way, even though each region is at a different evolutionary stage in terms of amount of dense gas, type of YSOs, and number of branching levels. Here we explore the connection between N_2H^+ hierarchy and the young stars in the four CLASSy regions with *Spitzer* and *Herschel* YSO detections to determine if star formation is correlated with the fine-scale hierarchical structure of dense gas.

Figures 4.10–4.13 show the location of YSOs, color-coded by spectral index, overlaid on a greyscale representation of the N_2H^+ dendrogram-identified structures for Serpens Main, Serpens South, NGC 1333, and Barnard 1, respectively. The darker grey structures are leaves, while the surrounding, lighter grey structures are the branches.

The dendrogram leaves represent peaks of the emission hierarchy, and can be

considered the regions with highest dense gas column density in the region. A few things are apparent by eye. First, it appears that many YSOs do not reside within the boundaries of leaves, and many leaves have no associated YSOs. We quantify those statements in Tables 4.3 and 4.4, respectively. Barnard 1 has 50% of its YSOs within leaves, with 88% of those sources being Class I or 0. The more evolved regions have between 25 and 31% of their YSOs overlapping leaf boundaries, and about 75% of those sources being Class I or 0. This shows that if a YSO is found to be within a leaf, it is likely to be a younger YSO. It also shows that the less evolved Barnard 1 region is the most likely to have a YSOs found within a leaves; this makes sense since it has the largest percentage of Class 0 and I sources.

Looking at the leaf-YSO connection the other way, all regions have a relatively similar percentage of leaves containing YSOs, with the Serpens regions at 28–29%, and the Perseus regions at 35–40%. Barnard 1 does not have a larger percentage of leaves with YSOs relative to the other regions, while it did have the largest percentage of YSOs found within leaves relative to other regions by about 50%. This is not contradictory, since a region can have many density peaks with no stars forming in them—those peaks can either be on the verge of star formation, or density enhancements that will never form stars. The fact that two Serpens regions and the two Perseus regions have nearly identical percentages of leaves with YSOs could indicate an inherent “leaf efficiency” for a cloud, where leaves have certain efficiency-to-date for turning mass into stars; Serpens regions may be producing stars from density enhancements at a leaf efficiency of about 38%, while Perseus regions are doing so at a leaf efficiency of about 29%. The rest of the leaves might form stars later in the life of the cloud, or fail to produce stars before getting disrupted and dispersed.

The second apparent property of Figures 4.10–4.13 is that Class II sources are

Table 4.3. YSOs Found Within Leaves

Region (1)	YSOs in Leaves(% of Total) (2)	Class II(L0) (3)	Flat(L0) (4)	Class I(L0) (L5)	Class 0(L0) (6)
Serpens Main	22(31%)	4(1)	1(1)	14(0)	3(0)
Serpens South	22(25%)	3(2)	3(0)	15(0)	1(0)
NGC 1333	24(29%)	4(0)	2(1)	18(2)	0(0)
Barnard 1	8(50%)	1(1)	0(0)	5(1)	2(0)

Note. — (2) Number of YSOs that are found within the boundary of a leaf, and the percentage of the total number of YSOs this represents in parenthesis. (3–6) Number of the YSOs that are found within the boundary of a leaf that are of this Class. The number in parentheses is the number of YSOs of this Class that are at branching level 0.

Table 4.4. Leaves With YSOs

Region (1)	Leaves with YSOs(% of Total) (2)	No. Leaves at L0 (Class of YSOs) (3)
Serpens Main	9(28%)	1 (F/II)
Serpens South	16(29%)	2 (II, II)
NGC 1333	10(40%)	2 (F/I, I)
Barnard 1	6(35%)	2 (I, II)

Note. — (2) Number of leaves that have a YSO within their boundaries, and the percentage of the total number of leaves this represents in parenthesis. (3) The number of leaves that have a YSO that are at branching level 0, along with the Class of YSOs that are found within those leaves.

less preferentially found near dendrogram leaves, compared with younger sources. To quantify this relationship between YSO location and dendrogram leaves, we calculate the distance between each YSO and the centroid position of the nearest dendrogram leaf, and plot the results as a function of classification in Figure 4.14. A zero arcsecond separation means a YSO resides within a leaf boundary. All regions have Class II sources distributed near and far from leaves. However, about 75% of the Class II sources are separated from their nearest leaf by more than 10,000 AU ($\sim 43''$ for Perseus and $25''$ for Serpens) in all regions: 3/4 in Barnard 1, 30/40 in NGC 1333, 24/33 in Serpens South, and 22/30 in Serpens Main. For Serpens

Main, no Flat or Class I sources are found more than $50''$ from a leaf, while about a dozen Class II sources are found at 50 and $200''$ separation. Above zero separation, Barnard 1 shows the most consistent trend of decreasing YSO-leaf separation with increasing α . Serpens South and NGC 1333 are different from the other regions, with many Class I and Flat sources found at larger separations than seen in other regions.

What might these trends mean? Having Class II YSOs generally distributed further from hierarchy peaks than less evolved sources could be an indication that some protostars are migrating away from their natal core, or dispersing/consuming their natal core. The Class I and Flat phases last about 0.5 Myr each, and the Class II lifetime is ~ 2 Myr (Evans et al. 2009). Protostars can move with velocities up to $\sim 0.1 \text{ km s}^{-1}$ relative to their natal core (Walsh et al. 2004; Ayliffe et al. 2007), so we can make a conservative estimate for how far a new Class II source may have moved from its natal core in 1 Myr, if we ignore the Class 0 stage. If a star is formed with a 0.1 km s^{-1} velocity relative to its natal core, it can move 0.1 pc per 1 Myr, which would put it about $50''$ and $80''$ from its original position in Serpens and Perseus, respectively. This could explain the wide distribution of Class II separations with hierarchy peaks—some protostars may remain within their natal core, while others might have small relative velocities that take them outside of the core by the time they reach the Class II stage, and others still might have depleted or dispersed their natal core.

One interesting cluster of YSOs that may have dispersed or depleted the dense gas from a natal core is found in the southeastern part of Serpens South. This cluster rivals the cluster in the Serpens South “hub” region, with four Class I, three Flat, and five Class II YSOs. However, unlike the hub, this region is void of significant N_2H^+ , HCO^+ , or HCN emission. Since we are not seeing HCN or HCO^+ , which

would remain in gas phase if this region were too warm for N_2H^+ emission, it is likely that the dense gas has been dispersed or consumed. It is possible that the Class I sources are actually Flat or Class II sources viewed at an angle causing their SEDs to have larger spectral indices indicative of younger sources. This uncertainty in YSO classification could explain why there are Class I and Flat sources distributed as much as Class II sources in Serpens South and NGC 1333.

In Figure 4.14, all regions show a wide distribution of classes at zero arcsecond separation from leaves, from Class II to Class 0. However, it is always the case that the majority of the sources at zero separation are less evolved, as we saw in Table 4.3 and the discussion above. This relates to the discussion of migration above—the younger sources with zero separation were likely born within those leaves, and the more evolved sources with zero separation may have been born with zero relative velocity to the core. It appears that Class 0 YSOs are only found near N_2H^+ hierarchical peaks. The one Class 0 source in Serpens South, the two Class 0 sources in Barnard 1, and three of the four Class 0 sources in Serpens Main are found at zero separation. The only Class 0 source not within a leaf boundary is in Serpens Main, and it is less than 10,000 AU from the nearest leaf centroid. We interpret this trend to mean that regions form their first generation of protostars embedded in dense gas hierarchical peaks.

It is apparent from Figures 4.10–4.13 that even the YSOs that lie within leaf boundaries are not always located at the leaf center. We counted any YSO within leaf boundaries as having “zero” separation from the leaf in Figure 4.14, but if we calculate the distance of those YSOs from the centroid position of the leaves, only $\sim 30\%$ of YSOs are within $10''$ of the leaf centroid. What could this mean? A gravitationally collapsing spheroid or ellipsoid would naturally form a star at its center, not off to one side. We saw in Chapters 2 and 3 that dendrogram structures

are not perfectly uniform spheroids or ellipsoids, so this suggests that irregularly-shaped leaves containing YSOs could be fragmenting at even small scales and higher densities to form one or multiple stars at positions off-center from the N_2H^+ leaf centroid.

In addition to analyzing the separation of YSOs from leaves, we classified the branching level at each YSO location, and plot the spectral index as a function of branching level in Figure 4.15. In these plots, level “-1” refers to YSOs that are located at a position with no dense gas. To complement Figure 4.15, Tables 4.3 and 4.4 show how many YSOs in leaves are at level zero, and how many leaves with YSOs are at level zero, respectively.

The Class II sources are distributed across branching levels for the two Serpens regions and NGC 1333, similar to how they were distributed over a wide range of separations in Figure 4.14. Serpens Main shows a weak trend of increasing hierarchy level with decreasing evolutionary stage, with all Classes being represented at high levels, but only evolved sources being represented at low levels. Serpens South and NGC 1333 show the full range of Classes across all levels of the hierarchy. However, Barnard 1 has all Class II sources at level zero or “-1” and shows a trend of increasing hierarchy level with decreasing evolutionary stage.

It appears that Class 0 YSOs are only found in hierarchically complex regions; no sources are found at level 0 or “-1”. A small number of Class I sources are found at level 0 (one out of five in Barnard 1, two out of 18 in NGC 1333), while the wide majority are found at higher levels. This means that in the regions of clustered star formation, hierarchically fragmented dense gas is more likely to be the birthplace of a young YSO, compared to isolated clumps of dense gas.

The overall results from this analysis, including all regions, is that: 1) not all hierarchical peaks of dense gas are associated with young stellar content, and not

all young stellar content is found in hierarchical peaks, 2) most Class 0 YSOs are forming at the location of hierarchical peaks, while more evolved YSOs can be distributed anywhere in a cloud, and 3) star formation is most efficient in locations of rich hierarchy.

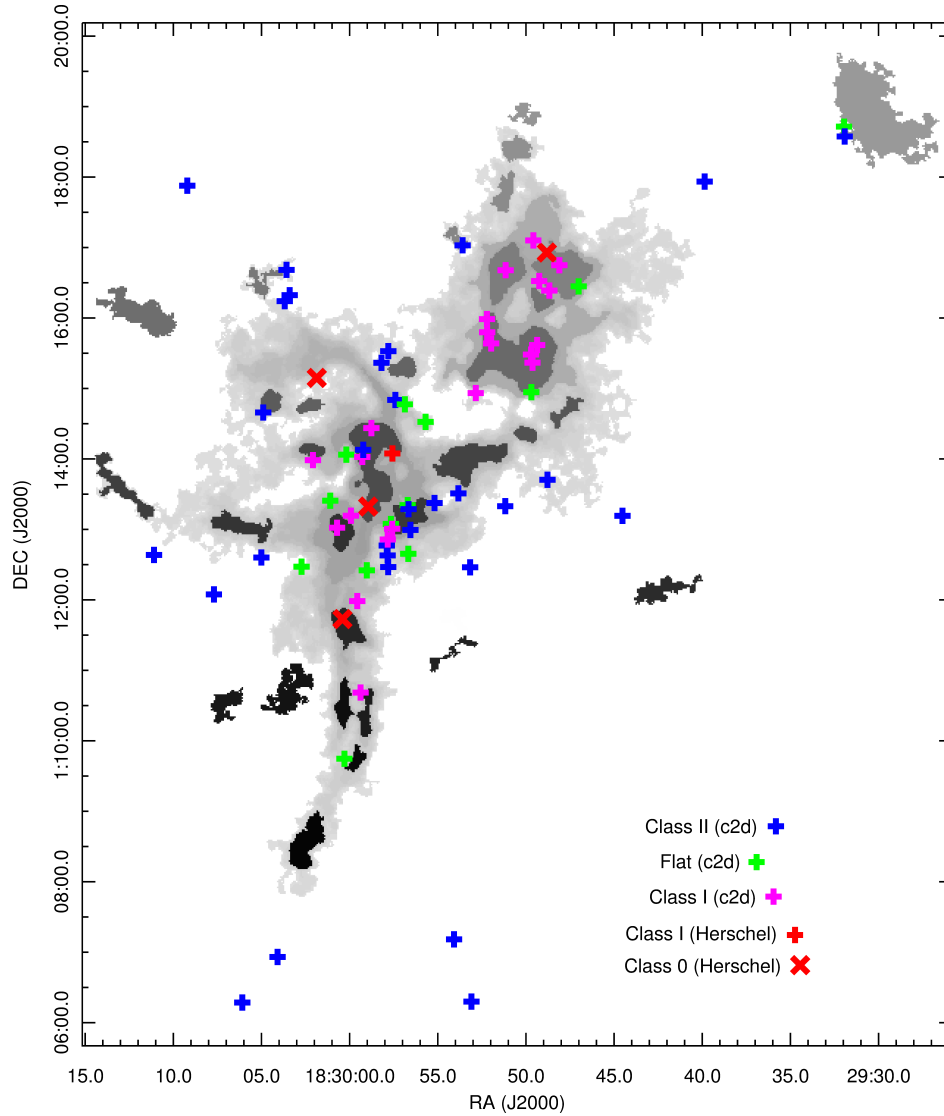


Figure 4.10: Serpens Main dendrogram structures (greyscale) with overplotted locations of YSOs. The different greyscale levels correspond to the distinct numeric identifier associated with each dendrogram leaf and branch; leaves have lower numbers and appear as darker grey structures and branches have higher numbers and appear as lighter grey structures. YSOs are colored by evolutionary state, with Class II, Flat, and Class I sources from *Spitzer* $c2d$ being blue, green, and magenta crosses, respectively. Sources not identified by *c2d* as YSOs, but with *Spitzer* $24\ \mu\text{m}$ and either *Herschel* $70\ \mu\text{m}$ or $100\ \mu\text{m}$ detections, are classified as Class I sources and marked with red crosses. Sources not identified by *c2d* as YSOs, and with no *Spitzer* $24\ \mu\text{m}$ and either *Herschel* $70\ \mu\text{m}$ or $100\ \mu\text{m}$ detections, are classified as Class 0 sources and marked with red Xs. Class III sources identified by *c2d* are not shown here, for reasons explained in the text.

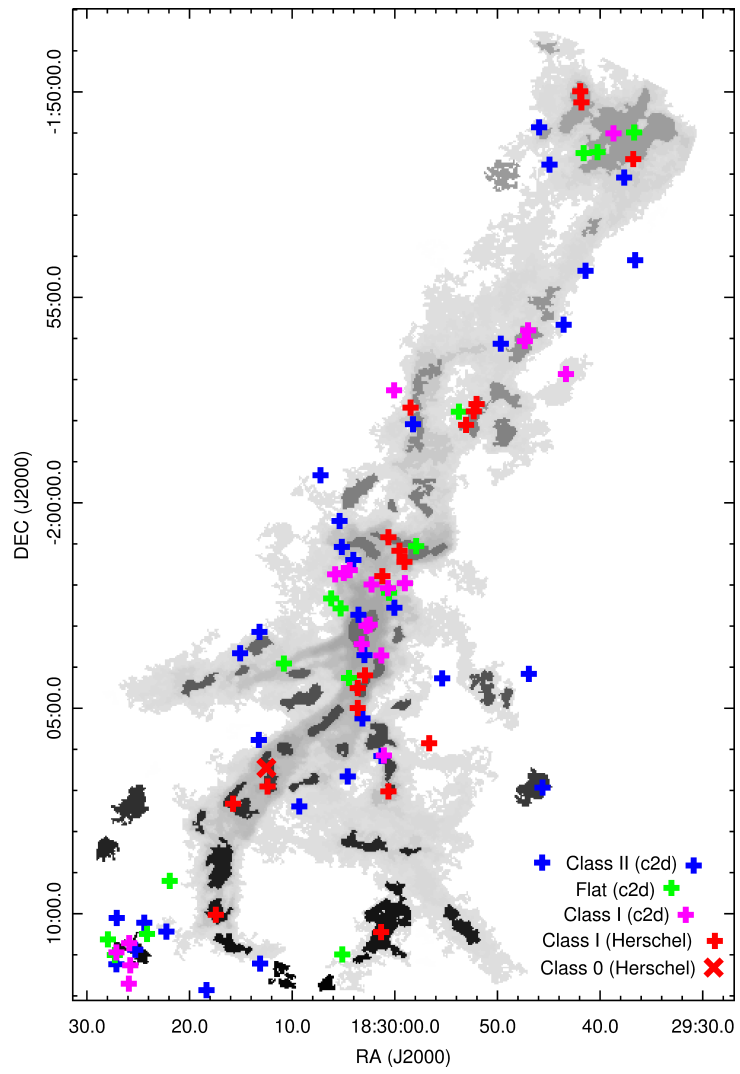


Figure 4.11: Same as Figure 4.10, but for Serpens South.

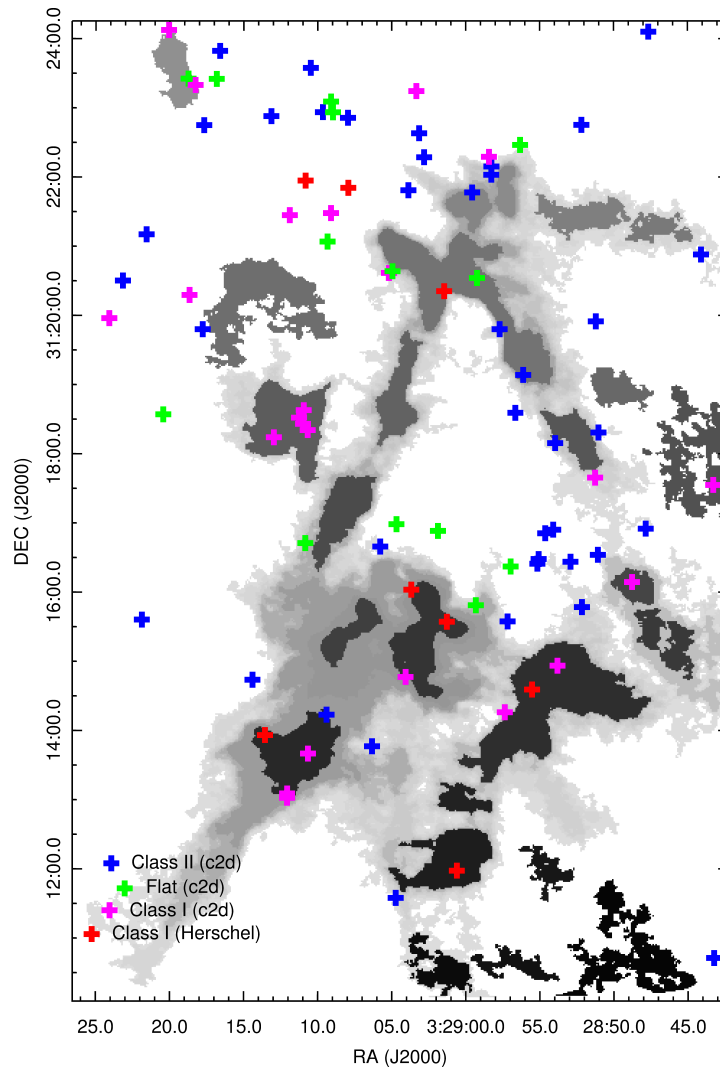


Figure 4.12: Same as Figure 4.10, but for NGC 1333.

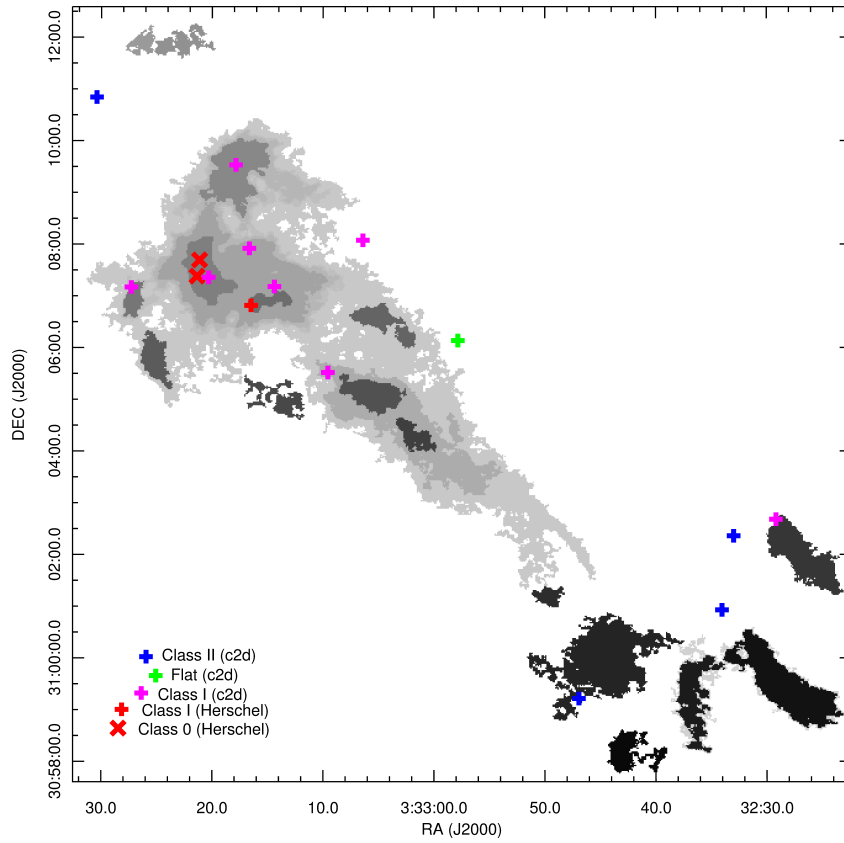


Figure 4.13: Same as Figure 4.10, but for Barnard 1.

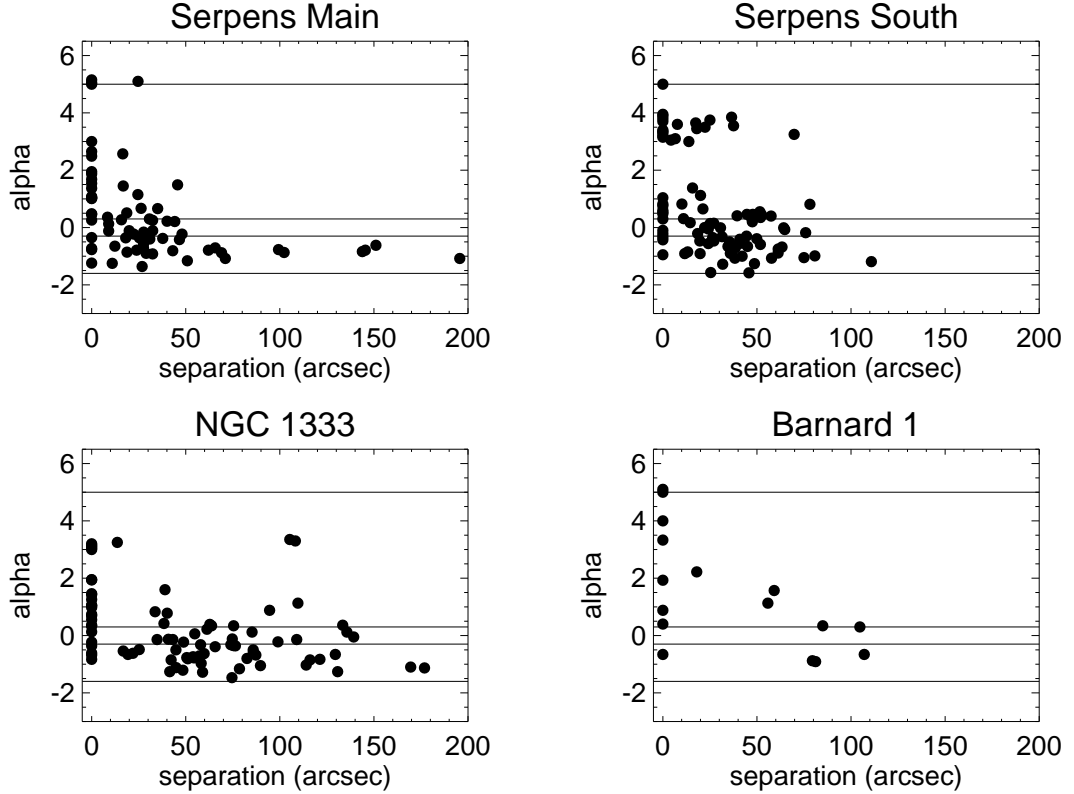


Figure 4.14: YSO classification (represented by the spectral index, α), as a function of minimum separation between a YSO and its nearest leaf. If a YSO overlaps with any portion of a leaf, the separation is considered zero; otherwise, the separation is the minimum distance between a YSO and the centroid position of the nearest leaf. The horizontal lines mark the separation between Classes discussed in the text. L1451 is not represented because it contains no *Spitzer* or *Herschel*-identified YSOs.

4.7 Summary

We presented a uniform comparison of N_2H^+ integrated intensity maps using our non-binary dendrogram algorithm, and compared dendrogram-identified structures to the young stellar content in each region. We summarize key findings below.

1. Molecular clouds are known to have hierarchical structure. The high angular-resolution and large-area of CLASSy observations allow a study of the fine-

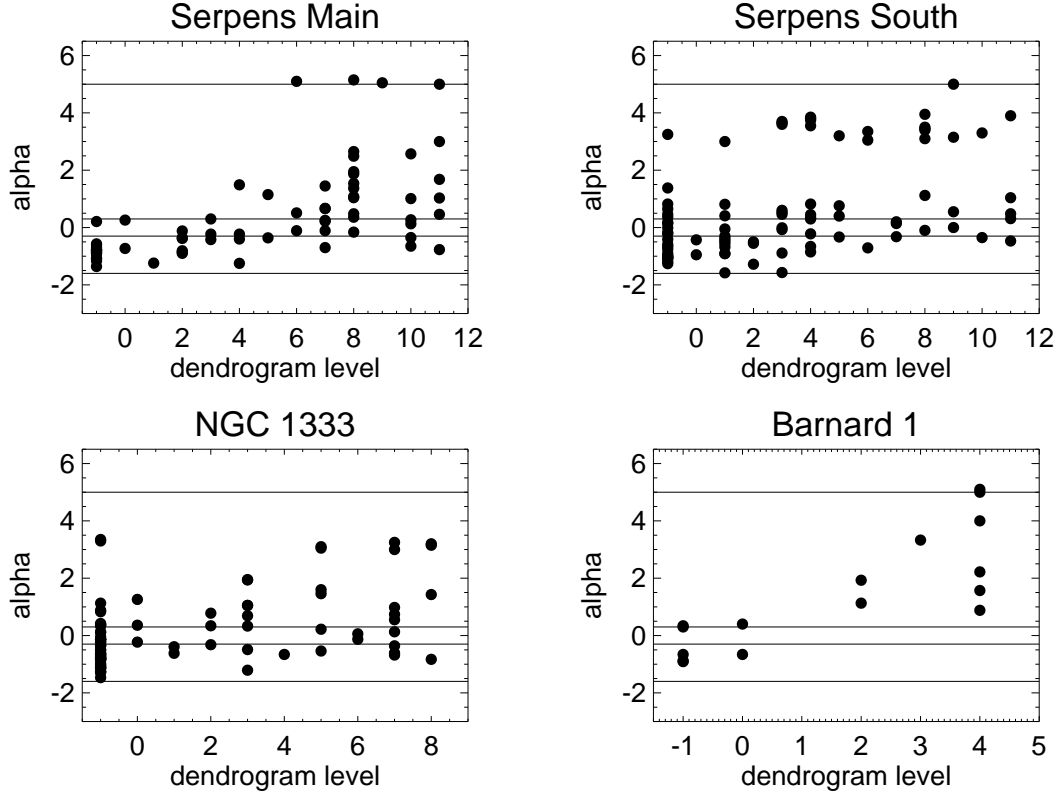


Figure 4.15: YSO classification (represented by the spectral index, α), as a function of dendrogram branching level. The branching level of a YSO is the branching level of the leaf or branch at the position of the YSO. A “-1” level means the YSO is located at a position that does not overlap with any dense gas dendrogram structure. The horizontal lines mark the separation between Classes discussed in the text. L1451 is not represented because it contains no *Spitzer* or *Herschel*-identified YSOs.

scale hierarchical structure of dense gas in clouds from the parsec to the ~ 0.01 pc scale. We use N_2H^+ integrated intensity as a proxy for dense gas column density in CLASSy regions, and use our non-binary dendrogram algorithm to determine the hierarchical structure of each region in a uniform way to allow us to compare regions.

2. Serpens Main and Serpens South have the largest peak integrated intensities, followed by NGC 1333, Barnard 1, and finally L1451. The non-binary dendrograms of all regions, except for L1451, show complex structure when analyzed

uniformly. Serpens South has the most leaves and branches, due to having the largest area of high-density gas.

3. A comparison of tree statistics across regions show that the more evolved regions with higher integrated intensity are fragmenting to more levels than the less evolved regions. However, the mean branching ratio of all dendrograms is similar, meaning that the dense gas is fragmenting in a similar way in each region; each parent fragments into ~ 3 sub-structures on average. Even though L1451 shows no hierarchical structure in this uniform comparison of integrated intensity maps, we know from Chapter 3 that the HCO^+ , HCN , and N_2H^+ emission shows hierarchical structure, with a mean branching ratio ~ 3 . This shows that fragmentation is similar during all stages of star formation, from the initial fragmentation in a region like L1451 that is just beginning to form density enhancements, to the later fragmentation in a region like NGC 1333 that has gathered gas and dust to high densities and is efficiently forming stars.
4. We compare the dense gas hierarchy to the young stellar content of Serpens Main, Serpens South, NGC 1333, and Barnard 1, ignoring L1451 since it has only one Class 0-like source (L1451-mm). We find that most Class 0 sources are forming within leaves, and at branching levels high in the dendrogram, suggesting that the youngest stars preferentially form within hierarchical peaks of dense gas within clouds. Class II sources are distributed throughout the region, mostly away from hierarchical peaks. This trend could be due to migration if a YSO is born with a non-negligible velocity relative to its natal core, or due to the YSO consuming or dispersing its natal core. Not all dendrogram leaves have a YSO forming within them, and not all YSOs are found within den-

drogram leaves. The two Serpens regions have embedded YSOs within $\sim 29\%$ of leaves, and the two Perseus regions have embedded YSOs within $\sim 38\%$ of leaves, suggesting a distinct efficiency-to-date for leaves in each cloud.

Chapter 5

Key Findings, Summary, and Future Work

5.1 Key Findings of Thesis

I highlight six important outcomes of this thesis below. A more complete summary of the thesis is given in Section 5.2.

1. I developed a non-binary dendrogram algorithm that calculates the hierarchical structure of an emission map or position-position-velocity cube within the noise limits of the data. The non-binary algorithm is an improvement over the standard dendrogram algorithm, which forces binary branching structure, because it permits a quantitative and more physically meaningful assessment of the hierarchical properties of molecular clouds using tree statistics.
2. I showed that a proper comparison of dendrograms for star-forming regions that are observed with different noise-levels and that are at different distances requires using algorithm parameters that are based on absolute, physical units, rather than based on the sensitivity or angular resolution of an individual

dataset.

3. The non-binary dendrograms of all CLASSy regions reveal hierarchical fragmentation. The mean branching ratio tree statistic is ~ 3 for all regions, meaning that, on average, larger structures fragment into about three smaller substructures during the earlier stages of star formation before protostars have formed, as well as during the later stages of star formation when regions contain feedback from protostars. The identified structures tend to be irregularly shaped, implying that forming cores grow in non-spherically symmetric environments.
4. The areas within Barnard 1 and L1451 with the strongest emission and the most hierarchical levels contain the majority of embedded Class 0/I YSOs and prestellar sources in those regions. A uniform comparison of N_2H^+ emission and tree statistics across all CLASSy regions shows a similar trend, with the more evolved regions having fragmented to the most hierarchical levels and having the strongest N_2H^+ integrated intensity (proxy for dense gas column density). A spatial analysis of the dendrogram structures and young stellar content shows that the youngest protostars are preferentially found near hierarchical peaks of dense gas emission located at high branching levels in the dendrogram. This shows that regions with large clusters of star-forming cores must have first accumulated enough dense gas column density to fragment to many distinct hierarchy levels.
5. Our high-angular resolution, large-area spectral line observations allowed us to create two size-linewidth relations sensitive to two distinct spatial properties of CLASSy regions: the depth of the gas structures in the region, and the projected size of the gas structures in the region. We developed a frame-

work to estimate the typical line-of-sight depth of the dense gas using these relations. We found that the more evolved CLASSy regions are sheet-like at parsec scales, with N_2H^+ depths ~ 0.15 pc, and with filamentary substructure within the sheet that is commonly found in numerical simulations of supersonic turbulence. We found that the dense gas in the L1451 region is better characterized as a collection of distinct ellipsoidal structures than a contiguous region of flattened gas and dust. It is possible that L1451 is the least evolutionary advanced region in terms of star formation because it was not compressed to high enough densities to efficiently fragment into many bound cores.

6. There is an extraordinary correspondence in L1451 between the observed cumulative emission from the HCO^+ , HCN, and N_2H^+ ($J = 1 \rightarrow 0$) transitions and the H_2 column density derived from *Herschel* continuum observations. The differences in the observed emission structure and kinematics between individual molecules can be understood based on their chemical and excitation properties, and the combination of molecules captures the kinematics of star-forming material that could not be traced with continuum observations. The HCO^+ and HCN ($J = 1 \rightarrow 0$) emission in the more evolved CLASSy regions suffered from self-absorption effects and were better at tracing dense gas outflows from protostars than the global structure and kinematics of cloud material. Future studies of these more evolved star formation regions should use different molecular transitions to complement N_2H^+ ($J = 1 \rightarrow 0$) to build a more complete picture of the dense gas in these regions.

5.2 Summary of Thesis

This thesis presented the methodology and results from CLASSy, which used CARMA to spectrally image dense gas in nearby molecular clouds with an unprecedented combination of area coverage, angular resolution, and velocity resolution. CLASSy observed N_2H^+ , HCO^+ , and HCN ($J = 1 \rightarrow 0$) emission across five evolutionarily distinct regions within the Perseus and Serpens Molecular Clouds: NGC 1333, Barnard 1, L1451, Serpens Main, and Serpens South. These observations capture the structure and kinematics of star-forming regions from cloud-to-core scales. When combined with catalogs of young stellar content and maps of continuum emission, they provide the most complete picture to-date of how dense gas in nearby molecular clouds fragments on the pathway to core and star formation.

5.2.1 CLASSy Observations

We presented details of CLASSy observations and mapping in Chapter 2. Observations were done in compact CARMA array configurations using the 23-element mode, providing a synthesized beam $\sim 7\text{--}8''$ and improved sensitivity to larger structures compared to the standard 15-element observing mode. The largest-scale structure—up to 1–2 pc—of each region was captured with large-area mosaics utilizing the combination of interferometric and single-dish data from CARMA. We used a newly developed “continuous integration” technique to improve on-source efficiency for large mosaics; for example, the Barnard 1 mosaic was composed of 743 individual pointings, and on-source efficiency reached about 48%. The final molecular line data cubes were made by jointly deconvolving the interferometric and single-dish data cubes. The typical rms was $\sim 0.13 \text{ Jy beam}^{-1}$ per 0.16 km s^{-1} channel. We also obtained interferometric-only $\lambda=3 \text{ mm}$ continuum observations of

each cloud region down to a sensitivity of ~ 1.3 mJy beam $^{-1}$.

5.2.2 The Barnard 1 and L1451 Regions

The two younger CLASSy regions in Perseus, Barnard 1 and L1451, were analyzed in Chapters 2 and 3, respectively. These regions provide a look at cloud conditions before feedback from existing star formation has a chance to significantly influence cloud structure, such as what is happening in the more evolved NGC 1333 and Serpens Main regions, and to a lesser extent the Serpens South region. Serpens Main was analyzed in detail in Lee et al. (2014), and an analysis of Serpens South filaments is in Fernández-López et al. (2014).

Barnard 1 is more evolved than L1451, based on the identification of over a dozen YSOs by *Spitzer* and *Herschel* in Barnard 1 compared to only one Class 0-like protostar identified in L1451 based on millimeter detections of compact continuum emission and a slow molecular outflow (Pineda et al. 2011). This was supported by the CLASSy $\lambda=3$ mm continuum observations that detected four compact continuum sources in Barnard 1 above $5\text{-}\sigma$, compared to no sources in L1451 above that limit. Three of the Barnard 1 detections were from the known B1-c, B1-bN, and B1-bS sources, while one was a new detection toward the Per-emb 30 $\lambda=1$ mm continuum source (Enoch et al. 2009). In L1451, we did detect weak emission above $3\text{-}\sigma$ ($0.08 M_{\odot}$ limit) towards L1451-mm, which is a candidate first hydrostatic core (Pineda et al. 2011).

All three molecules were detected in each region, with the N_2H^+ morphology most closely matching the morphology of cold dust observed by *Herschel* in both cases. In Barnard 1, the strongest HCO^+ and HCN emission was associated with protostellar outflows in the main core, while the non-outflow emission was relatively weak compared to N_2H^+ (possibly due to self-absorption from low-density gas along

the line-of-sight). In L1451, no HCO^+ or HCN outflows were detected, but the bulk emission from those lines was stronger than was seen in Barnard 1. An orderly progression of N_2H^+ to HCN to HCO^+ emission was seen from the most compact to the most widespread spatial scales. This progression is expected since HCO^+ traces about an order of magnitude lower densities than HCN and N_2H^+ , and the N_2H^+ abundance should be highest in the coldest, densest regions of the cloud.

We developed a new non-binary dendrogram algorithm to quantitatively analyze the dense gas structure in each cloud region. We discussed the benefits of dendrogram over clump-finding algorithms in Chapter 2 and Appendix A—dendrograms trace cloud structure from large-to-small scales instead of forcing emission into distinct clumps that may not have physical meaning. The benefits of our non-binary algorithm were also discussed in Chapter 2 and Appendix B—allowing dendrogram structure to branch into more than two sub-structures allows for the quantification of hierarchical complexity with tree statistics, and lets us present the actual observable emission hierarchy within the noise limits of the data.

The non-binary dendrogram algorithm was applied to the N_2H^+ position-position-velocity (PPV) cube of Barnard 1. Tree statistics showed that the main core of Barnard 1 is the most hierarchically complex, with the largest maximum branching level and mean path length. Since the main core is the location of current star formation in Barnard 1, this suggested that star formation is correlated with hierarchical complexity of the dense gas.

For L1451, we created non-binary dendrograms for all three molecules in PPV space since the HCO^+ and HCN emission was not impacted by outflows or significant self-absorption features as they were in the more evolved CLASSy regions. This allowed us to compare tree statistics between subregions as well as between molecules. All three dendrograms showed hierarchical complexity, with the gas the most hier-

archically complex around L1451-mm. This is an indication, as seen in Barnard 1, that star formation occurs in regions that have achieved high hierarchical complexity. L1451-mm is the only detected source of current star formation in the region. Other continuum condensations were detected at $\lambda=1$ mm by Enoch et al. (2006). The tree statistics of the gas surrounding these condensations is very similar to the gas surrounding L1451-mm, which we argue means that the condensations are likely sites of very early stages of star formation.

The dendrogram of each molecule observed in L1451 showed a similar mean branching ratio, which tracks how many substructures each structure breaks into, indicating that each molecule is tracing physical structures fragmenting in a hierarchically similar way. The HCO^+ dendrogram had the largest mean path length and maximum branching level, followed by HCN, and then by N_2H^+ . Since all molecules peak near the same high-intensity structures (e.g., near the gas surrounding the bright L1451-mm core), the difference in branching level was attributed to the varying sensitivity to low-intensity levels of fragmentation— HCO^+ is able to detect low-density, more extended emission than the other molecules, so we are able to identify additional low-intensity branching levels not seen in the other molecules. We interpreted the complex hierarchical nature of L1451 as supportive of turbulent star formation theories that argue that externally driven turbulence can create the first complex, hierarchical structure in molecular cloud regions. Those early structures are the seeds that form the over-dense, fertile grounds for the formations of the first generation of stars.

In addition to quantifying the structure of the cloud emission, we fit the spectral lines in each region to determine the kinematic properties of the dense gas. In L1451, the mean velocity dispersion of HCO^+ , HCN, and N_2H^+ was 0.29, 0.16, and 0.12 km s^{-1} , respectively, meaning that the HCO^+ was tracing trans-sonic to

supersonic gas in most areas, while the other molecules were tracing mostly sonic-to-subsonic motions. The N_2H^+ emission in Barnard 1 subregions with no young stars had subsonic velocity dispersions, while the gas in the main core reached up to 0.5 km s^{-1} .

We measured the spatial and kinematic properties of each dendrogram structure to understand how larger branches may differ from smaller leaves. The spatial measurements revealed that leaves and branches are irregularly shaped structures, showing that star-forming gas does not fragment into orderly spheroidal or ellipsoidal structures on the pathway to star formation. The kinematic measurements showed that branches (larger structures) tend to have larger rms variation of their velocity compared to leaves (smaller structures)—this can be understood based on the scale-dependent nature of turbulence, where gas separated by larger distances will have larger rms velocity differences between them. However, we found that the distribution of mean line-of-sight velocity dispersion was similar for branches and leaves. Since the line-of-sight velocity dispersion is sensitive to the line-of-sight depth of emission in a turbulent medium, we interpreted this to mean that the depth of emission was not closely linked to the projected size of a dendrogram structure.

We constructed two size-linewidth relations using the spatial and kinematic properties of dendrogram-identified structures discussed above, and used them to estimate the typical depth of molecular emission from each region. The assumption for this analysis was that observed non-thermal gas motions are generated by isotropic, three-dimensional turbulence in the cloud. For each region, and each molecule, the first relation showed that rms variation in centroid velocity increased with projected structure size. The second relation showed that non-thermal line-of-sight velocity dispersion varied weakly with projected structure size. We showed, using a theoretical framework and support from numerical realizations of turbulence, that the

projected structure size where the two size-linewidth relations cross gives an estimate for the typical line-of-sight depth of emission.

We determined that the typical depth of Barnard 1 N_2H^+ structures are ~ 0.15 pc. Compared to the parsec-scale size of Barnard 1 projected on the sky, this indicated that the parsec-scale region is flattened at largest scales, and that the flattened gas is fragmenting hierarchically as it forms stars in the Barnard 1 main core. A similar result was found in an analysis of the Serpens Main region (Lee et al. 2014). These results are consistent with numerical simulations that show high-density sheets and filaments being generic results of supersonic turbulence.

Using this method, all three molecules for L1451 appear to be tracing line-of-sight depths that are similar to the projected sizes of individual molecular features that are not contiguous across the parsec-scale of the entire region. This suggests that the dense gas in L1451 is more ellipsoidal than flattened at largest scales. Since L1451 does not appear to have filamentary structure in projection, this shows that not every star-forming region in a molecular cloud needs to be flattened and filamentary for star formation to proceed. However, it is possible that L1451's status as the least-active CLASSy region is linked to the fact that it is the only one without flattened, large-scale, high-density structure and filamentary substructure. A lack of flattened, high-density structure could indicate that this region of Perseus has not been strongly compressed by turbulent flows to create a sheet-like geometry and strong density enhancement needed to bring gas to high enough density and column density to efficiently form stars.

5.2.3 A Closer Look At L1451

L1451 was the first CLASSy region where we used *Herschel* data to construct column density and temperature maps, which allowed us to quantify how well our dense gas observations captured material above the threshold for star formation, and to estimate the gravitational boundedness of structures in this young region. Katherine Lee and Aaron Meisner led the construction of the column density and temperature maps by fitting modified blackbody curves to *Herschel* SEDs, and found that our derived column densities matched *Planck* results to within 5% when smoothed to matching angular resolutions. One major systematic uncertainty came from using a single-temperature fit for modeling the SEDs from cold, dense regions—comparing our results to a simple two-layer model with a warm and cold component showed that single-component fits can underestimate column densities in cold regions by a factor of two. This result will be presented in detail in future work, and the remainder of the thesis analysis took the uncertainty into account.

We found that 90% of the total molecular emission detected in L1451 overlapped with regions above H_2 column densities of $1.9 \times 10^{21} \text{ cm}^{-2}$. With the threshold for star formation near densities of $7.5 \times 10^{21} \text{ cm}^{-2}$, this shows that the suite of molecular lines observed by CLASSy captures the gas structure and kinematics of young regions within clouds.

The non-binary dendrogram algorithm was applied to the column density map to identify dust structures. A virial analysis of those structures, using the column density information from *Herschel* and the CLASSy kinematic data, showed that many structures are near the critical value for satisfying the virial theorem. However, several uncertainties of a factor of two limit conclusive interpretations of gravitational boundedness.

Although the conclusiveness of the virial results was limited, it is known that a star is currently forming within L1451-mm. L1451-mm is a candidate FHSC Pineda et al. (2011) and appeared in the molecular maps as a strongly centrally condensed feature. We detected another strong, centrally condensed N_2H^+ structure in the west of L1451, and we named this new source L1451-west. L1451-west is likely colder than L1451-mm, because it has N_2H^+ emission but lacks detectable HCO^+ emission. We estimated that L1451-west is less centrally condensed than L1451-mm, but more so than the typical prestellar core, making it another potential candidate FHSC.

5.2.4 Comparing All CLASSy Regions

In Chapter 4, we compared the N_2H^+ emission, hierarchical structure, and young stellar content of all five CLASSy regions to understand how gas is fragmenting at different evolutionary stages in clouds, and if the protostars are connected to that fragmentation.

We applied our non-binary dendrogram algorithm to each N_2H^+ integrated intensity map in a uniform way across regions, accounting for differences in map noise and cloud distance that are further explored in Appendix C. All regions, except for L1451, showed complex hierarchical structure with the uniform comparison. Tree statistics showed that the more evolved regions with stronger integrated intensity fragmented to more branching levels than the less evolved regions with weaker integrated intensity. This simply means that as a region evolves to higher intensities (or dense gas column densities), the gas fragments along the evolutionary path to form more distinct hierarchy levels. All regions, except for L1451, had a mean branching ratio ~ 3 in this uniform comparison, which showed that even though more evolved regions may fragment to more levels, the type of fragmentation at each stage of

evolution is similar. Although L1451 lacked hierarchical complexity in the uniform comparison between regions, we noted that the region did have hierarchical structure in Chapter 3, with mean branching ratios ~ 3 for each molecular dendrogram, supporting this idea of similar fragmentation from early to late stages of evolution.

Finally, we compared the hierarchical structures to the YSOs identified in each region from *Spitzer* and *Herschel* observations—this analysis excluded L1451 since its one candidate YSO was identified only at millimeter wavelengths. Not all hierarchical gas peaks contained a YSO, and not all YSOs were found at hierarchical peaks. We showed that the youngest YSOs are preferentially located within leaves high in the emission hierarchy, while the most evolved Class II YSOs are more evenly distributed throughout regions. This indicates that star formation in these dense regions is most likely to occur once a very dense, hierarchically complex subregion has been created.

5.3 Looking Forward

CLASSy made an important step toward mapping large areas of star formation with high angular and velocity resolution. There are many paths to continue moving this type of mapping forward. We highlight a few here.

The new W-band ($\sim 85\text{--}115$ GHz) receiver, ARGUS, on the GBT will provide an exciting opportunity for studying dense gas across a larger sample of clouds than was feasible with CARMA. GBT and ARGUS will open the door to efficiently mapping molecular gas in nearby clouds with sub-core angular resolution ($\sim 7''$ angular resolution, which corresponds to ~ 0.004 , 0.008 , and 0.02 pc at the distances of Taurus, Perseus, and Orion, respectively). CLASSy demonstrated the potential use of mapping large areas of molecular clouds with enough angular resolution to

see below core scales and with enough velocity resolution to resolve below the sonic scale of the dense gas. We discovered complex hierarchical structure, and evidence that many overall regions are sheet-like at parsec scales. These discoveries warrant follow-up observations of N_2H^+ ($J = 1 \rightarrow 0$) in other nearby clouds to create a statistical study of the properties of their densest regions and cores; this large, sensitive observational dataset can then be used to constrain theoretical models of filament, core, and star formation in turbulent molecular clouds. GBT and ARGUS will achieve similar spectral line sensitivity to our CLASSy data with a factor of 30 less integration time, and it can be used to build on CLASSy results.

One limitation of CLASSy is that we are only sensitive to densities $\sim 10^{4-6} \text{ cm}^{-3}$ with N_2H^+ , HCO^+ , and $\text{HCN } J = 1 \rightarrow 0$. A more complete analysis of clouds will include high-resolution maps of different CO isotopologues to probe the structure and kinematics of the lower-density gas that contains the bulk of the cloud mass and large-scale turbulent energy. The CarmaOrion project (PI: John Carpenter) started this work, using CARMA to map one square degree of the Orion Molecular Cloud.

We also need to extend to even higher densities and smaller scales to understand if the identified N_2H^+ leaves are fragmenting further. ALMA can be used for very high angular resolution observations of the densest gas and dust within dense cores, which can then be connected to the larger scales detected by CARMA and GBT. With this combination of data, we will be able to investigate the influence of the host cluster on properties of the gas and dust at smaller scales and higher physical densities, by tracing mass flow from the large-scale cluster onto the cores, and then mass accretion from cores onto protostars. With ALMA's ability to resolve disks, we can also study how larger-scale dense gas relates to disk orientation, velocity field, and angular momentum.

Appendix A

Differences Between Clump-finding and Dendrograms for CLASSy Data

We use the Cloudprops algorithm (Rosolowsky & Leroy 2006) and an IDL dendrogram algorithm (Rosolowsky et al. 2008b) to identify N_2H^+ emission structures in our CLASSy data cubes. The goal is to compare clump-finding and dendrogram object identification methods when applied to nearby star forming regions observed with high angular resolution. Both algorithms analyze the emission in position-position-velocity cube to segment the emission into structures. Figure A.1 shows Cloudprops (top) and dendrogram (bottom) contours for identified structures, overlaid on two N_2H^+ velocity channels around the B1-b continuum cores. The common color contours represent the same structures in the left and right panels. There are clearly major differences in the number and shapes of the identified structures between the two methods.

We find that the Cloudprops algorithm forces emission into small-scale clumps,

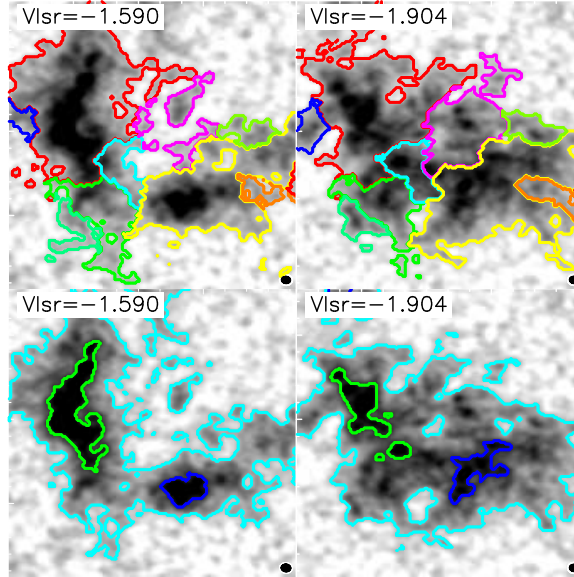


Figure A.1: Two N_2H^+ channel maps of the B1-b region for a comparison of Cloudprops (top) and dendrogram (bottom) object identification results. Each Cloudprops and dendrogram object is contoured with a unique color—this particular region is broken up into nine distinct Cloudprops objects, and three dendrogram objects. Cloudprops tends to put all emission into smaller-scale, independent clumps, while dendrograms identifies peaks of emission as leaves (green and blue contours in the online version), and then identifies lower intensity contour(s) that surround them as branches (cyan contour in the online version). We argue that the dendrogram approach is the more appropriate one for high angular resolution studies of nearby molecular clouds, since it captures the hierarchical nature of the gas emission across the wide range of spatial scales that exists in those regions.

even when the data does not show clear regions with strong intensity enhancements. When visually inspecting the emission channels in Figure A.1, there is no physical reason to think that the plateau of emission west of the B1-b cores is made up on several, independent clumps of dense gas that are separated with orderly borders. The technical reason for the clumpy breakdown is that Cloudprops first locates the highest level, local closed isocontours. Next, the algorithm steps down in intensity dividing the lower intensity emission between the stronger peaks according to a nearest-neighbor algorithm. This division of lower intensity emission across a fairly uniform emission plateau leads to the arbitrary borders seen in the top row of Figure A.1. Cloudprops and other clump-finding algorithms work best for sparse

fields that have resolved separations between objects—identifying giant molecular clouds in an extragalactic source is one example of where they work well. But attempting to decompose nearby, well-resolved, molecular gas emission into many small clumps with fairly straight borders does not have good physical motivation. Similar conclusions were found in Goodman et al. (2009), where the authors showed that CLUMPFIND (Williams et al. 1994) makes artificial attempts to fill in the structure between meaningful clumps.

Instead of partitioning all of the emission into individual clumps according to a nearest-neighbor scheme, it makes more physical sense to interpret it as lower intensity structure surrounding the peaks within it. For example, the peaks could represent gas that fragmented from the lower intensity emission surrounding them. This scenario considers that small-scale features can form from existing large-scale features, and is a hierarchical way of thinking about the data. If we accept that molecular clouds are hierarchical, then this is a more physical way to interpret the emission, and it requires an algorithm that can track the emission structure as a function of contour level intensity—a dendrogram algorithm does just that.

How does a dendrogram algorithm work? We quickly review the basic dendrogram procedure using a one-dimensional emission profile seen in Figure A.2 (from Rosolowsky et al. 2008b). (See that paper for more discussion of this example and the extension to two- and three-dimensions.) A one-dimensional, horizontal contour can be started at the absolute maximum of the emission profile and stepped downward to the base of emission. During this process, the peaks and merge levels of the three local maxima are identified and represented in a dendrogram (seen inset within the emission profile and repeated on the right with labels).

A dendrogram is composed of leaves and branches. In our example, the three leaves of the dendrogram correspond to the three local maxima in the emission profile

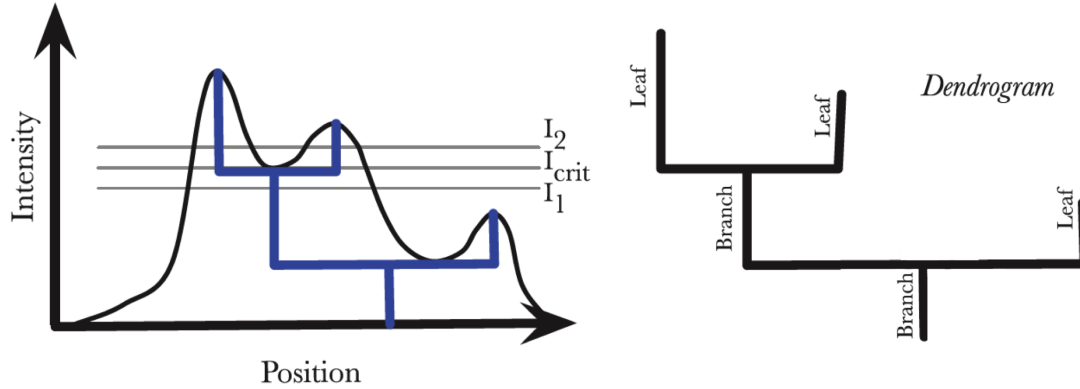


Figure A.2: This figure is taken from Rosolowsky et al. (2008b). The left image shows a one-dimensional, three-peak emission profile with the dendrogram representation as an inset. The dendrogram is reproduced on the right with the tree features labeled (the labels differ slightly from Rosolowsky et al. (2008b) to accommodate the naming conventions used in this thesis). The dendrogram is formed by keeping track of the emission structure as a function of intensity level. For example, contouring the emission profile at the I_1 level produces a single object, while contouring at I_2 produces two objects—the I_{crit} contour represents the level where the two strongest peaks in the emission profile merge together. In the dendrogram, this contour level is represented by a horizontal line connecting the two strongest leaves into the branch. Readers should see the original paper for a detailed discussion on dendrograms in all three dimensions.

that do not break up into any substructure. The peak intensity of a leaf represents the peak intensity of its corresponding local maximum, while the lowest intensity of a leaf represents the intensity where the corresponding local maximum merges with another local maximum. The two branches of the dendrogram correspond to lower-intensity emission that breaks up into substructure at higher intensities. The upper branch represents the lower-intensity emission that seeds the two strongest leaves, and the lower branch represents even lower-intensity emission that encompasses all of the emission peaks. The peak intensity of a branch represents the intensity where the leaves above it merge together, while the lowest intensity of a branch represents the intensity where it merges with another leaf or branch (the case of the left branch) or where it reaches the lowest measured intensity (the case of the lower branch). This algorithm can be extended from one-dimension to two- and three-dimensions to operate on position-position or position-position-velocity datasets.

All of our object identification for CLASSy clouds was done in three-dimensions, even if we occasionally represent the identified objects as two-dimensional contours for visualization simplicity.

Going back to our example in Figure A.1, the dendrogram identified objects in the two N_2H^+ channels are shown on the bottom row of the figure. Two peaks of emission (leaves) are identified with isolated contours (green and blue contours), and then get joined at a lower intensity level within a larger scale contour (a branch shown as the cyan contour).

To summarize, the dendrogram identification method is more appropriate for our data and science goals. Our data capture small-scale dense gas structures due to the high-angular resolution of the interferometer, and they capture large-scale dense gas features because of the large-area mosaicing and full emission reconstruction with single-dish data. Our science goals involve studying how small-scale gas features connect to the large-scale cloud features. The dendrogram approach lets us investigate the physical and kinematic properties of the dense gas across the wide range of spatial scales probed by our CLASSy data in a way that purely small-scale, clumpfind-like segmentation would not allow.

Appendix B

A New Non-binary Dendrogram

Procedure

The standard dendrogram algorithm forms a purely binary tree – thinking about a tree growing from the base upward, every branch terminates in either two leaves, a leaf and a branch, or two branches. A single branch is not allowed to directly sprout three leaves, even if the leaves merge into the branch at exactly the same level. In this three leaf example, two of the leaves would get merged into a branch, and then that branch would merge with the remaining leaf into another branch. We refer to this as “phantom branching” because an artificial branch was introduced only to enforce a binary merger requirement, as opposed to being motivated by the true nature of the data being modeled. This makes interpreting the true hierarchical nature of the data difficult, and makes a quantitative assessment of the dendrogram using tree statistics impossible (see Houlahan & Scalo (1992) for the use of tree statistics to interpret the hierarchical nature of emission). Going back to our example, we set out to allow all three leaves to merge into a single branch—we set out to allow non-binary mergers.

Non-binary dendrograms are useful for two reasons: 1) they provide a collection of branches that respect the noise inherent in real data, and 2) they allow the user to quantitatively compare the hierarchical complexity of different emission regions, and correlate that complexity with properties of those regions (e.g., star formation efficiency, column density, etc.).

The three-leaf example we used to motivate non-binary dendrograms is artificial; it is extremely unlikely for a real dataset to have three leaves merging at exactly the same intensity. Typical behavior seen in real data sets may have two leaves merge into a branch at the 1.0 Jy beam^{-1} level, and then merge with a third leaf into another branch at the $0.98 \text{ Jy beam}^{-1}$ level. Our key argument is that these three leaves should merge into a single branch, *if* the sensitivity of the dataset is lower than the branching difference. For example, the sensitivity of our Barnard 1 dataset is $0.13 \text{ Jy beam}^{-1}$, and the standard dendrogram algorithm produces branching in increments less than $0.13 \text{ Jy beam}^{-1}$ to ensure binary mergers—this produces a collection of branches that is not meaningful within the noise limits of the data, and limits the quantitative interpretation of the hierarchy. Our new method alleviates the binary merger requirement and allows branches to sprout an unrestricted amount of leaves and/or branches.

The key technical differences between our new non-binary method and the standard method are: 1) we restrict branching to intensity steps equal to integer values of at least the $1\text{-}\sigma$ sensitivity of the data, instead of allowing branching at infinitely small intensity steps, 2) we have an algorithm that can cluster more than two objects into a single group, instead of being restricted to clustering two objects at a time. Another way to think about the difference is that the standard dendrogram code yields the one emission hierarchy that represents the one realization of the noise applied to the true emission being observed. Our modified dendrogram code

instead represents an observable emission hierarchy within the noise limits of the data.

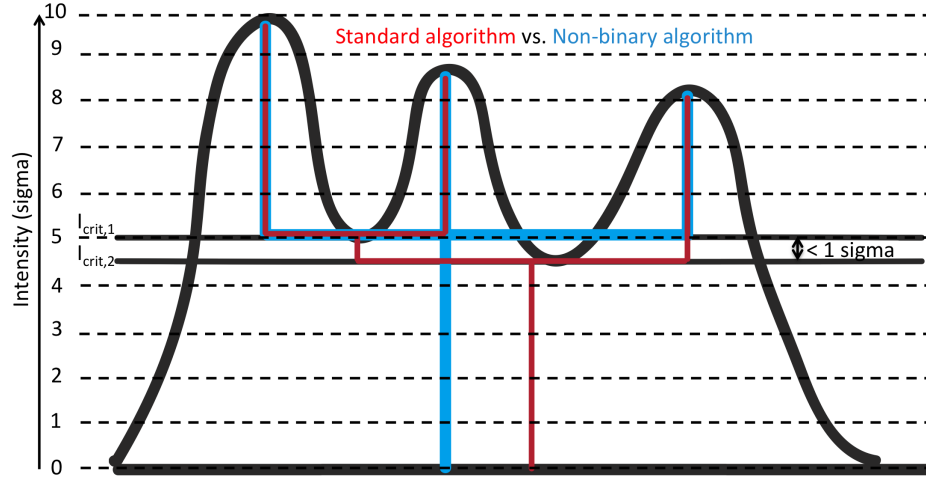


Figure B.1: Cartoon example of the difference between the standard dendrogram algorithm, and our new non-binary algorithm. The standard algorithm (red tree in the online version) forces binary mergers of dendrogram leaves and branches—the left and center peaks are first merged into a branch at the $I_{\text{crit},1}$ contour level, and that branch is then merged with the right peak at the $I_{\text{crit},2}$ contour level. Since the two merger levels are separated by less than the 1-sigma sensitivity of the data, we argue that the branch between $I_{\text{crit},1}$ and $I_{\text{crit},2}$ is not motivated by the data, but by the requirement of binary mergers. Our new non-binary algorithm (cyan in the online version) merges all three peaks at the highest merger level, and assigns the remaining emission between $I_{\text{crit},1}$ and $I_{\text{crit},2}$ to a single branch. This represents an observable emission hierarchy within the noise limits of the data.

A cartoon example of the difference is shown in Figure B.1. The cartoon shows a one-dimensional intensity profile, where the intensity axis is quoted in terms of the sigma sensitivity units of the data. Under the standard algorithm (red tree), the two leftmost peaks merge together at the level of the first saddle point ($I_{\text{crit},1}$, which represents an intensity level of 5-sigma) into a branch. The algorithm then merges that first branch with the rightmost peak at the level of the second saddle point ($I_{\text{crit},2}$, which is less than 1-sigma lower than $I_{\text{crit},1}$) into a second branch. Our algorithm (cyan tree) merges all three peaks into a single branch at the 5-sigma level since the two saddle points are separated by less than the 1-sigma sensitivity of the data.

Our algorithm comes with one obvious caveat. The resulting dendrogram depends on the discrete contouring of the data (which occurs in $1\text{-}\sigma$ steps in the example above and in Chapter 2); if branching levels are shifted slightly higher or lower, then the dendrogram can change. For example, consider a dataset in Kelvin units (for visual simplicity), with 0.10 K sensitivity, two leaves that peak at 4.00 K and merge together at 1.00 K, and a third leaf that peaks at 3.00 K and merges with the other leaves at 0.98 K. If the data is being contoured in $1\text{-}\sigma$ steps, our algorithm would set $1\text{-}\sigma$ branching levels in 0.10 K steps starting from the 4.00 K peak, which means that 1.00 K is an available merge level. All three leaves would be merged into a single branch at 1.00 K using our non-binary algorithm. But if the peak intensity is 3.98 K instead of 4.00 K, then 1.00 K is not an available branching level anymore—but 1.08 K and 0.98 K are. For that case, the two strongest leaves would merge at 1.08 K, and then merge with the third leaf at 0.98 K. This simple example shows how our dendrograms, and the tree statistics derived from them, can be slightly altered by shifts in the discrete contouring of the data. We went from a dendrogram with one branching level, a branching ratio of three, and a mean path length of one, to a dendrogram with two branching levels, a mean branching ratio of two, and a mean path length of 1.66.

This caveat produces only small changes in the dendrogram and tree statistics when tested on the actual Barnard 1 data presented in Chapter 2, Section 2.6. We shifted the $1\text{-}\sigma$ branching levels by $0.33\text{-}\sigma$; compared to the results presented in Section 2.6.2, the mean branching ratio changed from 3.9 to 3.8, and the mean path length and maximum branching level were unchanged. We argue that the benefits of this new non-binary algorithm outweigh this caveat, particularly when science goals include: 1) correlating the physical properties of several star forming regions with differences in dendrogram structure (by comparing tree statistics of different

regions, which is not possible with the standard algorithm), and 2) comparing the structure and kinematics of large-scale and small-scale structures within a single region (by comparing the spatial and kinematic properties of leaves and branches, which is more difficult for the end-user if the branch list is contaminated by phantom branching from the standard algorithm).

Appendix C

How to Compare Non-Binary Dendrograms of Different Regions

We need to be able to compare the dendrograms of different clouds that were observed with different noise levels and that are at different distances. In Chapter 2, we analyzed a single non-binary dendrogram for the PPV cube of the isolated hyperfine component of N_2H^+ in Barnard 1, which is the simplest case of one cloud distance and one noise level. In Chapter 3, we analyzed the non-binary dendrograms for the PPV cubes of the strongest hyperfine components of N_2H^+ and HCN, and the single component of HCO^+ in L1451; there was a noise difference of 15% between those cubes, so this was a slightly more complex scenario. In Chapter 4, we analyzed the non-binary dendrograms for integrated intensity maps of each CLASSy region, which have different distances (Serpens at 415 pc, and Perseus at 235 pc), and different noise levels (e.g., Serpens Main at $0.30 \text{ Jy beam}^{-1} \text{ km s}^{-1}$ and Barnard 1 at $0.17 \text{ Jy beam}^{-1} \text{ km s}^{-1}$); this is the most complex scenario.

The goal of this section is to establish how we can compare dendrogram structure and statistics between clouds that have significantly different observational noise-

levels and that are located at different distances. We will argue in this appendix that the key is to construct the dendrograms using physically meaningful units for the algorithm parameters first introduced in Chapter 2 (Section 2.6.1), including the parameters for: 1) the minimum height for a local maximum to peak above the level where it merges with adjacent local maxima to be considered a real leaf (`minheight`), 2) the minimum area covered by a leaf for it to be considered real (`minpixel`), and 3) the minimum allowed branching step height between adjacent levels in the dendrogram (`stepsize`).

C.1 Noise Dependence of Dendrogram Structure and Statistics

The goal of this section is to demonstrate a method for comparing regions with different noise levels. We want to ensure that lowering the noise-level of a map will not significantly change the dendrogram structure or tree statistics derived from the emission.

To illustrate the problem, we start by imagining a scenario where we observe a cloud for one hour, and make a map. We then observe it again for nine hours, and make a second map that has the noise reduced by a factor of three compared to the first map. We would then run our dendrogram algorithm on these two maps and see if and how the structure and statistics change.

Although we do not have maps of the same cloud with different noise, an easy way to mimic this scenario with existing data is to use the hyperfine components in the N_2H^+ PPV cube. The N_2H^+ ($J = 1 \rightarrow 0$) transition is split into seven resolvable hyperfine components, which have the same velocity dispersion and excitation condition but different peak intensity. We can integrate over different com-

binations of hyperfine components to create moment maps with different signal-to-noise ratio (SNR). Signal is proportional to the number of channels with emission, N , and is dependent on the strength of the emission in each channel. Integrating over only the lowest-velocity component will give lower signal than integrating over all velocity components. Integrating over the lowest-velocity component will give slightly lower noise (σ_{LV}) in emission-free regions compared to integrating over all of the velocity components, since noise scales as $\sqrt{N}\sigma$, where N is the number of channels, and σ is the noise in a single channel. For a real example, the noise levels of the Barnard 1 lowest-velocity and full-velocity component maps are 0.09 and 0.15 Jy beam⁻¹ km s⁻¹, respectively, with peak signals of 1.8 and 11.4 Jy beam⁻¹ km s⁻¹, respectively—the peak SNR are then 20 and 76, respectively.

The questions we want to answer hinge on what happens to dendrogram structure and statistics when we *reduce the noise* in a map while keeping the signal the same. In the paragraph above, we created two maps with different SNR, but the difference came from different noise levels and even more disparate peak signals. To turn these into maps with similar peak signal and different noise, we first normalize the full-velocity component map to the low-velocity component map at locations where the low-velocity component map has emission greater than $6\sigma_{LV}$; this ensures that the regions with strong emission have matching signal (e.g., a pixel at 11.4 Jy beam⁻¹ km s⁻¹ in the full-velocity component map with a corresponding pixel at 1.8 Jy beam⁻¹ km s⁻¹ in the low-velocity component map will be reduced by a factor of 6.3 in the normalized map). In weaker regions (less than $6\sigma_{LV}$ in the low-velocity component map), we scale the full-velocity component map down by a factor of 7, which is the mean normalization factor in regions of strong signal. We then calculate the rms of the normalized full-velocity component map, σ_{NFV} , which

is $0.03 \text{ Jy beam}^{-1} \text{ km s}^{-1}$ compared to $\sigma_{LV} = 0.09 \text{ Jy beam}^{-1} \text{ km s}^{-1}$. The result is a new map with similar signal to the low-velocity component map but with three times lower noise; this is the scenario we want to test our dendrogram algorithm on.

We ran our non-binary dendrogram algorithm on the Barnard 1 versions of these two maps in two different ways. First, we allowed each dendrogram to have a `stepsize` and `minheight` based on the rms of each map: `stepsize` = $1\text{-}\sigma_{NFV}$ and `minheight` = $2\text{-}\sigma_{NFV}$ for the normalized full-velocity component map, and `stepsize` = $1\text{-}\sigma_{LV}$ and `minheight` = $2\text{-}\sigma_{LV}$ for the lowest-velocity component map. Second, we forced each dendrogram to have the same `stepsize` and `minheight` based on the noisier map: `stepsize` = $1\text{-}\sigma_{LV}$ and `minheight` = $2\text{-}\sigma_{LV}$ for both maps. Using absolute units across maps as in this second case could be beneficial because absolute units are linked with physical properties of a cloud, while noise units are linked with the properties of the observations. For example, if a study wants to link fragmentation properties of column density structure in different clouds to the properties of star formation in those clouds, it would be more sensible to define an absolute unit, such as a minimum mass or column density that is always the same across clouds, for branching and leaf identification, rather than a noise unit, such as $1\text{-}\sigma$, which can be different for different clouds.

For the first case, where we allowed the `stepsize` and `minheight` parameters to be based on the noise-level of the individual map, the resulting dendrogram-identified structures for the two Barnard 1 maps are shown in Figure C.1, and the dendrograms are shown in Figures C.2. Two of the strongest peaks in the region are similarly identified in both maps (structures 9 and 11 in the low-velocity component map are 27 and 31 in the full-velocity component map). However, some leaves break up into multiple structures when lowering the noise of the map and also lowering the absolute threshold for creating a leaf and a branching step (structure 6 in the low-

velocity component map becomes structures 22, 23, 25, and 28 in the full-velocity component map).

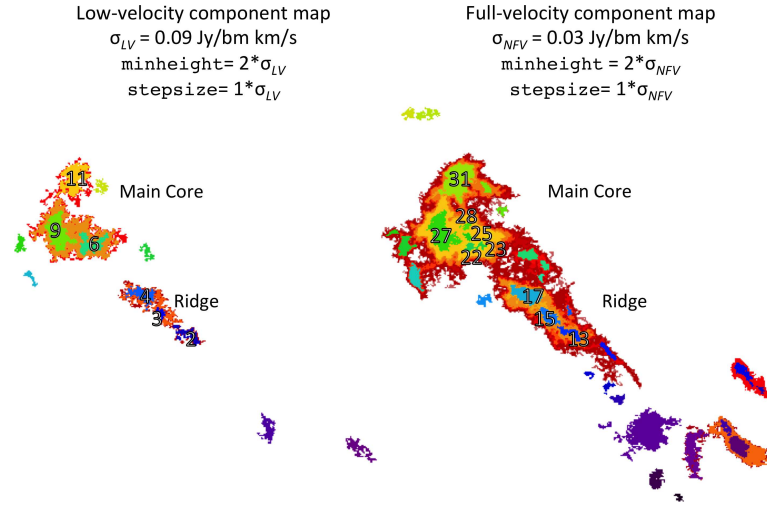


Figure C.1: Structures identified by our non-binary dendrogram algorithm from the integrated intensity map made from the lowest-velocity hyperfine component (left) and a scaled-down map made using all velocity components (right). The dendrogram algorithm parameters are listed in the figure, and are based on the noise level of the individual maps. Structures are labeled with numbers that correspond to leaves and branches in Figure C.2.

This shows that the hierarchical structure of two maps of the same region that have different noise can significantly change if `minheight` and `stepsize` are kept in terms of the sensitivity of each individual map. This makes sense if we consider an extreme limit of very low noise maps that may soon be produced by ALMA. If the noise in a map is extremely reduced, structures peaking $2\text{-}\sigma$ above a merger level with other structures would likely not represent physically relevant features, but small-scale variations on top of physical meaningful features. In this case of extremely low noise, it would make more sense to define a physically relevant minimum unit for studying structure, such as a minimum mass.

For the second case, we used the values of the noisier map for `stepsize` and `minheight` for the construction of both dendrograms. That meant that each dendrogram could branch in $0.09 \text{ Jy beam}^{-1}$ steps, and leaves needed to be $0.18 \text{ Jy beam}^{-1}$

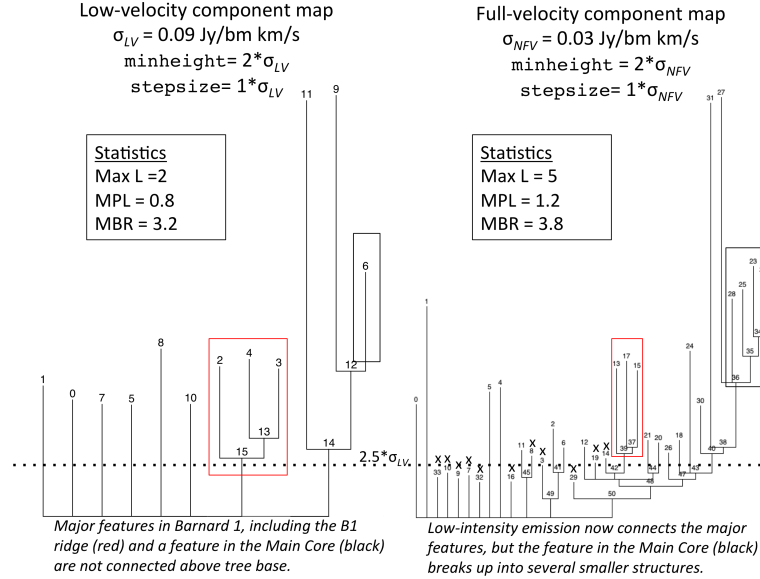


Figure C.2: Non-binary dendrograms from the integrated intensity map made from the lowest-velocity hyperfine component (left) and a scaled-down map made from using all velocity components (right) using the dendrogram algorithm parameters listed in the figure.

above their merge level to be considered real—these were our minimum physically relevant units to study structure across these two maps with different noise. The resulting dendrogram-identified structures for the two Barnard 1 maps are shown in Figure C.3, and the dendrograms are shown in Figure C.4. The main take-away from these figures is that lowering the noise but keeping the same absolute units for studying structure results in very similar dendrograms. A large-scale, low-intensity branch (structure 16 in the full-velocity component map) is added around smaller-scale, higher-intensity structures found in the noisier map, and some leaves that branched directly from the tree base in the low-velocity component map now branch from one level up due to the addition of the large-scale, low-intensity branch (e.g., leaf 8 becomes leaf 7). The strongest peaks in the region are similarly identified in both maps (structures 6, 9, and 11 in the low-velocity component map are 6, 8, 10 in the full-velocity component map); lowering the noise did not cause these structures to break up. This provides evidence that if the noise in a map is lowered,

and the `stepsize` and `minheight` parameters are kept constant, the hierarchical structure will not significantly change—you mainly add lower-intensity branching structure to connect parts of the emission hierarchy not previously connected.

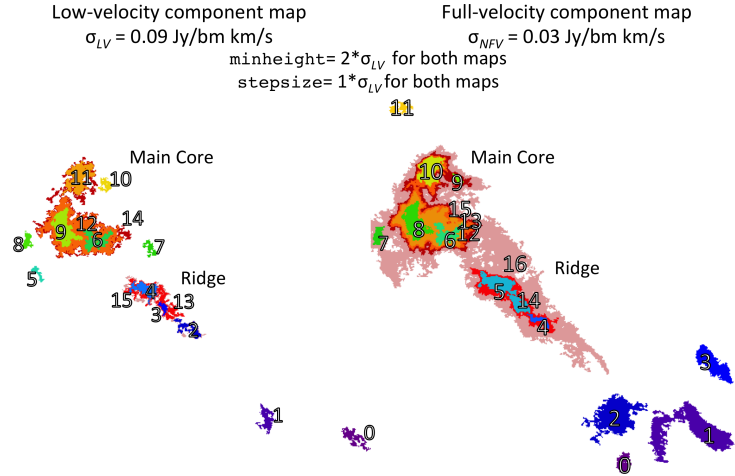


Figure C.3: Structures identified by our non-binary dendrogram algorithm from the integrated intensity map made from the lowest-velocity hyperfine component (left) and a scaled-down map made from using all velocity components (right). The dendrogram algorithm parameters are listed in the figure, and are the same for each map. Structures are labeled with numbers that correspond to leaves and branches in Figure C.4.

Another important test is how the tree statistics change between the dendrograms. We calculate the tree statistics of the low-velocity component map in both cases as described in Chapter 2, and list the statistics as insets of Figures C.2 and Figure C.4. To properly compare statistics between the two maps, we need to only consider the dendrogram structures in the full-velocity component map above the mask level applied to the low-velocity component map. The dendrogram of the lowest-velocity component map has a minimum integrated intensity of $0.21 \text{ Jy beam}^{-1} \text{ km s}^{-1}$ (set by the $2.5\text{-}\sigma_{LV}$ mask limit to the data input to the dendrogram algorithm). Since the full-velocity component map extends to lower emission levels set by a $2.5\text{-}\sigma_{NFV}$ mask limit, we calculate the statistics for that dendrogram above a cut corresponding to the same $2.5\text{-}\sigma_{LV}$ limit of the low-velocity

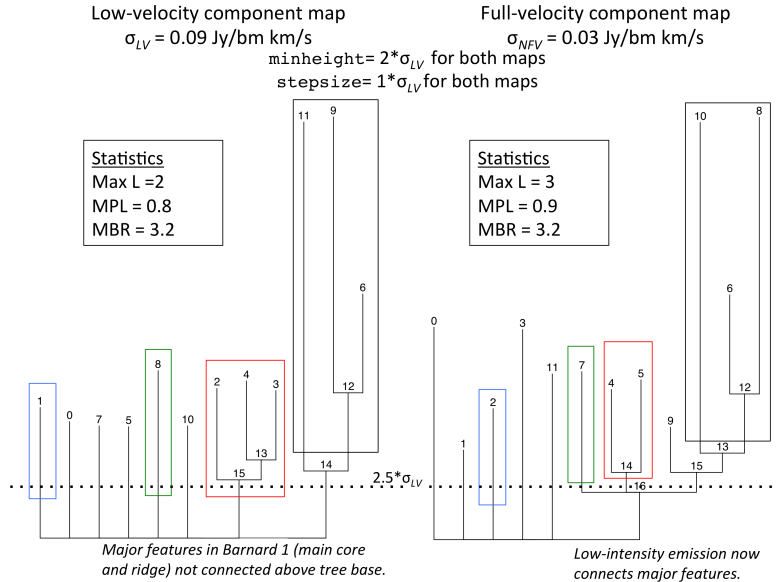


Figure C.4: Non-binary dendrograms from the integrated intensity map made from the lowest-velocity hyperfine component (left) and a scaled-down map made from using all velocity components (right) using uniform dendrogram algorithm parameters listed in the figure for each map.

component map (the cut is represented in Figures C.2 and C.4 by the horizontal dashed line). This means that leaves from the full-velocity component map must peak $2\text{-}\sigma_{NFV}$ or $2\text{-}\sigma_{LV}$ above the noisier mask level to be considered real, for the first and second case, respectively. The leaves that do not meet this requirement are marked with an “x” in Figures C.2 and C.4. Any branch below this noisier mask level is removed, and structures above it are lowered one level.

For the first case, where we set `stepsize` and `minheight` based on the noise-level of the individual map, the lower-noise dendrogram has a maximum branching level three levels higher than the higher-noise dendrogram, a mean path length about half a level larger than the higher-noise dendrogram, and a mean branching ratio 0.6 higher than the higher-noise dendrogram. The differences in maximum branching level and mean path length can be explained by the lower-noise map having a lower absolute threshold for what can be considered a leaf compared to the higher-noise map (`minheight` of $0.06 \text{ Jy beam}^{-1} \text{ km s}^{-1}$ vs. $0.18 \text{ Jy beam}^{-1} \text{ km s}^{-1}$),

and allowing branching steps at smaller absolute units compared to the higher-noise map (`stepsize` of $0.03 \text{ Jy beam}^{-1} \text{ km s}^{-1}$ vs. $0.09 \text{ Jy beam}^{-1} \text{ km s}^{-1}$); when it is easier to break emission into leaves and to define new branching levels, there will be more hierarchical structure in the dendrogram.

For the second case, where we set `stepsize` and `minheight` based on a minimum relevant $\text{Jy beam}^{-1} \text{ km s}^{-1}$ amount, the mean path lengths agree to a tenth of a level, the mean branching ratios are identical, and the maximum branching levels differ by only one level. This demonstrates how tree structure can be defined so that lowering the noise of a map will not alter the calculated tree statistics significantly. When comparing different clouds with different noise-levels, it will be important to use a minimum relevant amount so that the emission in each cloud has the same absolute threshold for what can be considered a leaf and what can be considered a significant branching step.

In conclusion, the dendrograms of clouds observed with different noise can be uniformly compared if the comparison uses absolute units for the dendrogram contouring and leaf requirements instead of units based on the noise-level of each individual map, and if the comparison of tree statistics only analyzes structures above the intensity level set by the noisiest map.

C.2 Comparing Regions at Different Distances

In comparing clouds at different distances, there are two effects to consider: 1) a fixed angular resolution covers a different spatial scale at different distances, and 2) the emission measurement unit could depend on distance.

CLASSy can resolve slightly smaller spatial structures in Perseus ($d=235 \text{ pc}$) than it can in Serpens ($d=415 \text{ pc}$) with its uniform angular resolution, but doing

so would create an imbalance in the comparison of tree statistics across clouds. To account for this, we ensure that we match the minimum *spatial* size that a dendrogram leaf can be in each region using the `minpixel` parameter.

To account for the second effect, if a physical measurement of each cloud, such as mass, is not available, then using a measured value conserved with distance, such as specific intensity, is a good option. Specific intensity, I_ν , is a fundamental property of radiation that describes how much energy is passing through a detector of some area, per time interval, per frequency interval, per observed solid angle on a source. It is written as

$$I_\nu = \frac{dE}{dA dt d\nu d\Omega}, \quad (\text{C.1})$$

with units of $\text{erg s}^{-1} \text{cm}^{-2} \text{Hz}^{-1} \text{Sr}^{-1}$. I_ν is conserved for non-cosmological distances where the frequency of radiation is not changing. This is because if you move a source to a greater distance, d , its flux density ($\text{erg s}^{-1} \text{cm}^{-2} \text{Hz}^{-1}$) will decrease by $1/d^2$, while its solid angle as perceived by the observer will also decrease by a factor of $1/d^2$. For a fixed telescope beam and a uniform, extended source, another way of thinking about this conservation is that as the source moves twice as far away, the collected flux density decreases by a factor of four, but the telescope beam is covering four times more physical area of emission.

Interferometric data are in units of Jy beam^{-1} , which are analogous to I_ν , and which are conserved with distance for a uniform, extended source. The flux density (in units of Janskys) at a given position in a uniform, extended cloud will decrease with the square of the distance, while a fixed beam area will cover a spatial area that increases by the square of the distance.

In summary, we ensure a proper comparison of hierarchical structure for cloud regions at different distances by using a matching minimum spatial area requirement for leaves and constructing our dendrograms in Jy beam^{-1} or $\text{Jy beam}^{-1} \text{km s}^{-1}$

units.

C.3 Summary

In astronomy, we are constantly comparing objects at different distances that have been observed with different noise properties. To understand the state of star formation in each cloud, it is most insightful to analyze cloud structure using physical and spatial units, such as mass or column density and parsecs, since star formation is controlled by physical processes that act on collections of mass at different spatial scales. At a certain scale, very small pieces of cloud mass, or very low columns of material, will have no effect on the global star formation picture of a cloud, so getting more sensitive and high-resolution observations will have no impact on the overall picture of fragmentation. If future observations become sensitive to such small variations in a cloud, an analysis using a uniform set of physical units can restrict dendrogram branching to meaningful quantities of mass or column density that can be related to the physics controlling the star formation and compared across clouds.

Since we do not have access to reliable, high-resolution maps in physical units such as column density, we contour the data in the conserved units of Jy beam^{-1} (for PPV cubes) or $\text{Jy beam}^{-1} \text{ km s}^{-1}$ (for integrated intensity maps) in this thesis¹. We then use a uniform set of physical units for dendrogram algorithm parameters when comparing the hierarchical structure of cubes or maps with different noise levels or distances so that the resulting hierarchies can be properly compared.

¹We discuss how intensity measurements of dense gas tracers can be used as a proxy for dense gas column density in Chapter 1.

Appendix D

Herschel-identified YSOs

Table D.1. Non-c2d YSOs Identified with *Herschel*

Region (1)	RA (2)	DEC (3)	Detections (4)
NGC 1333	52.2313	31.2432	24, 70, 100 μm
NGC 1333	52.2525	31.1996	24, 70, 100 μm
NGC 1333	52.2553	31.2595	24, 70, 100 μm
NGC 1333	52.2561	31.3392	24, 70, 100 μm
NGC 1333	52.2653	31.2673	24, 70, 100 μm
NGC 1333	52.2831	31.3641	24, 70, 100 μm
NGC 1333	52.2951	31.3658	24, 70, 100 μm
NGC 1333	52.3065	31.2323	24, 70, 100 μm
Barnard 1	53.3187	31.1136	24, 70, 100 μm
Barnard 1	53.3381	31.1282	100 μm
Barnard 1	53.3391	31.1230	100 μm
Serpens Main	277.4534	1.2822	70, 100 μm
Serpens Main	277.4899	1.2346	24, 70, 100 μm
Serpens Main	277.4956	1.2221	70, 100 μm
Serpens Main	277.5017	1.1955	100 μm
Serpens Main	277.5078	1.2525	100 μm
Serpens South	277.5056	-2.1741	24, 70, 100 μm
Serpens South	277.5727	-2.1671	24, 70, 100 μm
Serpens South	277.5657	-2.1221	24, 70, 100 μm
Serpens South	277.5517	-2.1150	24, 70, 100 μm
Serpens South	277.5521	-2.1075	100 μm
Serpens South	277.5026	-2.1171	24, 70, 100 μm
Serpens South	277.4861	-2.0975	24, 70, 100 μm
Serpens South	277.5121	-2.0700	24, 70, 100 μm
Serpens South	277.5051	-2.0297	24, 70, 100 μm
Serpens South	277.5026	-2.0140	24, 70, 100 μm
Serpens South	277.4981	-2.0195	24, 70, 100 μm
Serpens South	277.4961	-2.0240	24, 70, 100 μm
Serpens South	277.4936	-1.9614	24, 70, 100 μm
Serpens South	277.4711	-1.9684	24, 70, 100 μm
Serpens South	277.4680	-1.9629	24, 70, 100 μm
Serpens South	277.4668	-1.9599	24, 70, 100 μm
Serpens South	277.4248	-1.8331	24, 70, 100 μm
Serpens South	277.4243	-1.8376	24, 70, 100 μm
Serpens South	277.4032	-1.8606	24, 70, 100 μm
Serpens South	277.5151	-2.0751	24, 70, 100 μm
Serpens South	277.5151	-2.0832	24, 70, 100 μm

Note. — (1) CLASSy region. (2,3) J2000 RA and DEC position of source, determined by eye. (4) Bands in which the source was detected, among *Spitzer* 24 μm and *Herschel* 70 and 100 μm bands.

Bibliography

Adams, W. S. 1941, *ApJ*, 93, 11

André, P., Di Francesco, J., Ward-Thompson, D., Inutsuka, S.-I., Pudritz, R. E., & Pineda, J. E. 2014, *Protostars and Planets VI*, 27

André, P., Men'shchikov, A., Bontemps, S., Könyves, V., Motte, F., Schneider, N., Didelon, P., Minier, V., Saraceno, P., Ward-Thompson, D., di Francesco, J., White, G., Molinari, S., Testi, L., Abergel, A., Griffin, M., Henning, T., Royer, P., Merín, B., Vavrek, R., Attard, M., Arzoumanian, D., Wilson, C. D., Ade, P., Aussel, H., Baluteau, J.-P., Benedettini, M., Bernard, J.-P., Blommaert, J. A. D. L., Cambrésy, L., Cox, P., di Giorgio, A., Hargrave, P., Hennemann, M., Huang, M., Kirk, J., Krause, O., Launhardt, R., Leeks, S., Le Penec, J., Li, J. Z., Martin, P. G., Maury, A., Olofsson, G., Omont, A., Peretto, N., Pezzuto, S., Prusti, T., Roussel, H., Russeil, D., Sauvage, M., Sibthorpe, B., Sicilia-Aguilar, A., Spinoglio, L., Waelkens, C., Woodcraft, A., & Zavagno, A. 2010, *A&A*, 518, L102

Aniano, G., Draine, B. T., Gordon, K. D., & Sandstrom, K. 2011, *PASP*, 123, 1218

Arce, H. G., Borkin, M. A., Goodman, A. A., Pineda, J. E., & Halle, M. W. 2010, *ApJ*, 715, 1170

Ayliffe, B. A., Langdon, J. C., Cohl, H. S., & Bate, M. R. 2007, *MNRAS*, 374, 1198

Bacmann, A., Lefloch, B., Ceccarelli, C., Castets, A., Steinacker, J., & Loinard, L.

- 2002, *A&A*, 389, L6
- Ballesteros-Paredes, J. 2006, *MNRAS*, 372, 443
- Bally, J., Walawender, J., Johnstone, D., Kirk, H., & Goodman, A. The Perseus Cloud, ed. B. Reipurth, 308
- Barnard, E. E. 1913, *ApJ*, 38, 496
- Beaumont, C. N., Offner, S. S. R., Shetty, R., Glover, S. C. O., & Goodman, A. A. 2013, *ApJ*, 777, 173
- Beckwith, S. V. W. & Sargent, A. I. 1991, *ApJ*, 381, 250
- Beckwith, S. V. W., Sargent, A. I., Chini, R. S., & Guesten, R. 1990, *AJ*, 99, 924
- Bergin, E. A. & Langer, W. D. 1997, *ApJ*, 486, 316
- Bergin, E. A. & Tafalla, M. 2007, *ARA&A*, 45, 339
- Bertoldi, F. & McKee, C. F. 1992, *ApJ*, 395, 140
- Bigiel, F., Leroy, A., Walter, F., Brinks, E., de Blok, W. J. G., Madore, B., & Thornley, M. D. 2008, *AJ*, 136, 2846
- Blake, G. A., Sutton, E. C., Masson, C. R., & Phillips, T. G. 1987, *ApJ*, 315, 621
- Boger, G. I. & Sternberg, A. 2005, *ApJ*, 632, 302
- Briggs, D. S., Schwab, F. R., & Sramek, R. A. 1999, in *Astronomical Society of the Pacific Conference Series*, Vol. 180, *Synthesis Imaging in Radio Astronomy II*, ed. G. B. Taylor, C. L. Carilli, & R. A. Perley, 127
- Brunt, C. M. & Mac Low, M.-M. 2004, *ApJ*, 604, 196
- Buckle, J. V., Davis, C. J., Francesco, J. D., Graves, S. F., Nutter, D., Richer, J. S., Roberts, J. F., Ward-Thompson, D., White, G. J., Brunt, C., Butner, H. M., Cavanagh, B., Chrysostomou, A., Curtis, E. I., Duarte-Cabral, A., Etxaluze, M., Fich, M., Friberg, P., Friesen, R., Fuller, G. A., Greaves, J. S., Hatchell, J., Hogerheijde, M. R., Johnstone, D., Matthews, B., Matthews, H., Rawlings, J. M. C., Sadavoy, S., Simpson, R. J., Tothill, N. F. H., Tsamis, Y. G., Viti, S.,

- Wouterloot, J. G. A., & Yates, J. 2012, MNRAS, 422, 521
- Carroll, J. J., Frank, A., Blackman, E. G., Cunningham, A. J., & Quillen, A. C. 2009, ApJ, 695, 1376
- Caselli, P., Benson, P. J., Myers, P. C., & Tafalla, M. 2002, ApJ, 572, 238
- Caselli, P., Myers, P. C., & Thaddeus, P. 1995, ApJ, 455, L77
- Chen, C.-Y. & Ostriker, E. C. 2014, ApJ, 785, 69
- Chen, X., Arce, H. G., Zhang, Q., Bourke, T. L., Launhardt, R., Jørgensen, J. K., Lee, C.-F., Foster, J. B., Dunham, M. M., Pineda, J. E., & Henning, T. 2013, ApJ, 768, 110
- Collings, M. P., Dever, J. W., Fraser, H. J., McCoustra, M. R. S., & Williams, D. A. 2003, ApJ, 583, 1058
- Crutcher, R. M. 2012, ARA&A, 50, 29
- Daniel, F., Cernicharo, J., Roueff, E., Gerin, M., & Dubernet, M. L. 2007, ApJ, 667, 980
- di Francesco, J., Evans, II, N. J., Caselli, P., Myers, P. C., Shirley, Y., Aikawa, Y., & Tafalla, M. 2007, Protostars and Planets V, 17
- Dickman, R. L. 1985, in Protostars and Planets II, ed. D. C. Black & M. S. Matthews, 150–174
- Dickman, R. L. & Kleiner, S. C. 1985, ApJ, 295, 479
- Djupvik, A. A., André, P., Bontemps, S., Motte, F., Olofsson, G., Gålfalk, M., & Florén, H.-G. 2006, A&A, 458, 789
- Dobbs, C. L., Krumholz, M. R., Ballesteros-Paredes, J., Bolatto, A. D., Fukui, Y., Heyer, M., Low, M.-M. M., Ostriker, E. C., & Vázquez-Semadeni, E. 2014, Protostars and Planets VI, 3
- Draine, B. T. 2003, ARA&A, 41, 241
- Dzib, S., Loinard, L., Mioduszewski, A. J., Boden, A. F., Rodríguez, L. F., & Torres,

- R. M. 2010, *ApJ*, 718, 610
- Eiroa, C., Djupvik, A. A., & Casali, M. M. The Serpens Molecular Cloud, ed. B. Reipurth, 693
- Elmegreen, B. G. & Scalo, J. 2004, *ARA&A*, 42, 211
- Enoch, M. L., Evans, II, N. J., Sargent, A. I., & Glenn, J. 2009, *ApJ*, 692, 973
- Enoch, M. L., Evans, II, N. J., Sargent, A. I., Glenn, J., Rosolowsky, E., & Myers, P. 2008, *ApJ*, 684, 1240
- Enoch, M. L., Young, K. E., Glenn, J., Evans, II, N. J., Golwala, S., Sargent, A. I., Harvey, P., Aguirre, J., Goldin, A., Haig, D., Huard, T. L., Lange, A., Laurent, G., Maloney, P., Maukopf, P., Rossinot, P., & Sayers, J. 2006, *ApJ*, 638, 293
- Erickson, K. L., Wilking, B. A., Meyer, M. R., Kim, J. S., Sherry, W., & Freeman, M. 2015, *AJ*, 149, 103
- Evans, II, N. J. 1999, *ARA&A*, 37, 311
- Evans, II, N. J., Dunham, M. M., Jørgensen, J. K., Enoch, M. L., Merín, B., van Dishoeck, E. F., Alcalá, J. M., Myers, P. C., Stapelfeldt, K. R., Huard, T. L., Allen, L. E., Harvey, P. M., van Kempen, T., Blake, G. A., Koerner, D. W., Mundy, L. G., Padgett, D. L., & Sargent, A. I. 2009, *ApJS*, 181, 321
- Federrath, C. & Klessen, R. S. 2012, *ApJ*, 761, 156
- Federrath, C., Schrön, M., Banerjee, R., & Klessen, R. S. 2014, *ApJ*, 790, 128
- Fernández-López, M., Arce, H. G., Looney, L., Mundy, L. G., Storm, S., Teuben, P. J., Lee, K., Segura-Cox, D., Isella, A., Tobin, J. J., Rosolowsky, E., Plunkett, A., Kwon, W., Kauffmann, J., Ostriker, E., Tassis, K., Shirley, Y. L., & Pound, M. 2014, *ApJ*, 790, L19
- Ferrière, K. M. 2001, *Reviews of Modern Physics*, 73, 1031
- Friesen, R. K., Di Francesco, J., Shimajiri, Y., & Takakuwa, S. 2010, *ApJ*, 708, 1002
- Galliano, F., Hony, S., Bernard, J.-P., Bot, C., Madden, S. C., Roman-Duval, J.,

- Galametz, M., Li, A., Meixner, M., Engelbracht, C. W., Lebouteiller, V., Misselt, K., Montiel, E., Panuzzo, P., Reach, W. T., & Skibba, R. 2011, *A&A*, 536, A88
- Genzel, R. & Stutzki, J. 1989, *ARA&A*, 27, 41
- Gong, H. & Ostriker, E. C. 2011, *ApJ*, 729, 120
- Goodman, A. A., Rosolowsky, E. W., Borkin, M. A., Foster, J. B., Halle, M., Kauffmann, J., & Pineda, J. E. 2009, *Nature*, 457, 63
- Gould, B. A. 1874, *Proceedings of the American Association for Advanced Science*, 115
- Gutermuth, R. A., Bourke, T. L., Allen, L. E., Myers, P. C., Megeath, S. T., Matthews, B. C., Jørgensen, J. K., Di Francesco, J., Ward-Thompson, D., Huard, T. L., Brooke, T. Y., Dunham, M. M., Cieza, L. A., Harvey, P. M., & Chapman, N. L. 2008, *ApJ*, 673, L151
- Harvey, P., Merín, B., Huard, T. L., Rebull, L. M., Chapman, N., Evans, II, N. J., & Myers, P. C. 2007, *ApJ*, 663, 1149
- Hatchell, J., Richer, J. S., Fuller, G. A., Qualtrough, C. J., Ladd, E. F., & Chandler, C. J. 2005, *A&A*, 440, 151
- Heiderman, A., Evans, II, N. J., Allen, L. E., Huard, T., & Heyer, M. 2010, *ApJ*, 723, 1019
- Heyer, M. H. & Brunt, C. M. 2004, *ApJ*, 615, L45
- Hiramatsu, M., Hirano, N., & Takakuwa, S. 2010, *ApJ*, 712, 778
- Hirano, N., Kamazaki, T., Mikamxi, H., Ohashi, N., & Umemoto, T. 1999, in *Star Formation 1999*, ed. T. Nakamoto, 181–182
- Hirano, N., Kameya, O., Mikami, H., Saito, S., Umemoto, T., & Yamamoto, S. 1997, *ApJ*, 478, 631
- Hirota, T., Bushimata, T., Choi, Y. K., Honma, M., Imai, H., Iwadate, K., Jike, T., Kameya, O., Kamohara, R., Kan-Ya, Y., Kawaguchi, N., Kijima, M., Kobayashi,

- H., Kuji, S., Kurayama, T., Manabe, S., Miyaji, T., Nagayama, T., Nakagawa, A., Oh, C. S., Omodaka, T., Oyama, T., Sakai, S., Sasao, T., Sato, K., Shibata, K. M., Tamura, Y., & Yamashita, K. 2008, PASJ, 60, 37
- Hirota, T., Honma, M., Imai, H., Sunada, K., Ueno, Y., Kobayashi, H., & Kawaguchi, N. 2011, PASJ, 63, 1
- Houlahan, P. & Scalo, J. 1992, ApJ, 393, 172
- Huang, Y.-H. & Hirano, N. 2013, ApJ, 766, 131
- Jørgensen, J. K., Harvey, P. M., Evans, II, N. J., Huard, T. L., Allen, L. E., Porras, A., Blake, G. A., Bourke, T. L., Chapman, N., Cieza, L., Koerner, D. W., Lai, S.-P., Mundy, L. G., Myers, P. C., Padgett, D. L., Rebull, L., Sargent, A. I., Spiesman, W., Stapelfeldt, K. R., van Dishoeck, E. F., Wahhaj, Z., & Young, K. E. 2006, ApJ, 645, 1246
- Jørgensen, J. K., Johnstone, D., Kirk, H., & Myers, P. C. 2007, ApJ, 656, 293
- Jørgensen, J. K., Johnstone, D., Kirk, H., Myers, P. C., Allen, L. E., & Shirley, Y. L. 2008, ApJ, 683, 822
- Kauffmann, J., Bertoldi, F., Bourke, T. L., Evans, II, N. J., & Lee, C. W. 2008, A&A, 487, 993
- Kauffmann, J., Pillai, T., & Goldsmith, P. F. 2013, ApJ, 779, 185
- Kennicutt, R. C. & Evans, N. J. 2012, ARA&A, 50, 531
- Kim, M. K., Hirota, T., Honma, M., Kobayashi, H., Bushimata, T., Choi, Y. K., Imai, H., Iwadate, K., Jike, T., Kamenno, S., Kameya, O., Kamohara, R., Kan-Ya, Y., Kawaguchi, N., Kuji, S., Kurayama, T., Manabe, S., Matsui, M., Matsumoto, N., Miyaji, T., Nagayama, T., Nakagawa, A., Oh, C. S., Omodaka, T., Oyama, T., Sakai, S., Sasao, T., Sato, K., Sato, M., Shibata, K. M., Tamura, Y., & Yamashita, K. 2008, PASJ, 60, 991
- Kirk, H., Johnstone, D., & Di Francesco, J. 2006, ApJ, 646, 1009

- Kirk, H., Myers, P. C., Bourke, T. L., Gutermuth, R. A., Hedden, A., & Wilson, G. W. 2013, *ApJ*, 766, 115
- Klessen, R. S. & Hennebelle, P. 2010, *A&A*, 520, A17
- Krumholz, M. R., McKee, C. F., & Tumlinson, J. 2008, *ApJ*, 689, 865
- Kutner, M. L., Tucker, K. D., Chin, G., & Thaddeus, P. 1977, *ApJ*, 215, 521
- Lada, C. J., Muench, A. A., Rathborne, J., Alves, J. F., & Lombardi, M. 2008, *ApJ*, 672, 410
- Lada, C. J. & Reid, M. J. 1978, *ApJ*, 219, 95
- Larson, R. B. 1981, *MNRAS*, 194, 809
- Lee, K. I., Fernández-López, M., Storm, S., Looney, L. W., Mundy, L. G., Segura-Cox, D., Teuben, P., Rosolowsky, E., Arce, H. G., Ostriker, E. C., Shirley, Y. L., Kwon, W., Kauffmann, J., Tobin, J. J., Plunkett, A. L., Pound, M. W., Salter, D. M., Volgenau, N. H., Chen, C.-Y., Tassis, K., Isella, A., Crutcher, R. M., Gammie, C. F., & Testi, L. 2014, *ApJ*, 797, 76
- Leroy, A. K., Lee, C., Schrubba, A., Bolatto, A., Hughes, A., Pety, J., Sandstrom, K., Schinnerer, E., & Walter, F. 2013, *ApJ*, 769, L12
- Leroy, A. K., Walter, F., Brinks, E., Bigiel, F., de Blok, W. J. G., Madore, B., & Thornley, M. D. 2008, *AJ*, 136, 2782
- Mac Low, M.-M. & Klessen, R. S. 2004, *Reviews of Modern Physics*, 76, 125
- MacLaren, I., Richardson, K. M., & Wolfendale, A. W. 1988, *ApJ*, 333, 821
- Markwardt, C. B. 2009, in *Astronomical Society of the Pacific Conference Series*, Vol. 411, *Astronomical Data Analysis Software and Systems XVIII*, ed. D. A. Bohlender, D. Durand, & P. Dowler, 251
- Matthews, B. C., Hogerheijde, M. R., Jørgensen, J. K., & Bergin, E. A. 2006, *ApJ*, 652, 1374
- McCall, B. J., Geballe, T. R., Hinkle, K. H., & Oka, T. 1999, *ApJ*, 522, 338

- McKee, C. F. & Ostriker, E. C. 2007, *ARA&A*, 45, 565
- McKee, C. F. & Zweibel, E. G. 1992, *ApJ*, 399, 551
- McKellar, A. 1940, *PASP*, 52, 187
- Meisner, A. M. & Finkbeiner, D. P. 2015, *ApJ*, 798, 88
- Miesch, M. S. & Bally, J. 1994, *ApJ*, 429, 645
- Morris, M. & Rickard, L. J. 1982, *ARA&A*, 20, 517
- Nakamura, F. & Li, Z.-Y. 2007, *ApJ*, 662, 395
- . 2014, 783, 115
- Nakamura, F., Sugitani, K., Tanaka, T., Nishitani, H., Dobashi, K., Shimoikura, T., Shimajiri, Y., Kawabe, R., Yonekura, Y., Mizuno, I., Kimura, K., Tokuda, K., Kozu, M., Okada, N., Hasegawa, Y., Ogawa, H., Kamenno, S., Shinnaga, H., Momose, M., Nakajima, T., Onishi, T., Maezawa, H., Hirota, T., Takano, S., Iono, D., Kuno, N., & Yamamoto, S. 2014, *ApJ*, 791, L23
- Ossenkopf, V. & Mac Low, M.-M. 2002, *A&A*, 390, 307
- Perrot, C. A. & Grenier, I. A. 2003, *A&A*, 404, 519
- Pineda, J. E., Arce, H. G., Schnee, S., Goodman, A. A., Bourke, T., Foster, J. B., Robitaille, T., Tanner, J., Kauffmann, J., Tafalla, M., Caselli, P., & Anglada, G. 2011, *ApJ*, 743, 201
- Planck Collaboration, Abergel, A., Ade, P. A. R., Aghanim, N., Alves, M. I. R., Aniano, G., Armitage-Caplan, C., Arnaud, M., Ashdown, M., Atrio-Barandela, F., & et al. 2014, *A&A*, 571, A11
- Prasad, S. S. & Huntress, Jr., W. T. 1980, *ApJS*, 43, 1
- Rebull, L. M., Stapelfeldt, K. R., Evans, II, N. J., Jørgensen, J. K., Harvey, P. M., Brooke, T. Y., Bourke, T. L., Padgett, D. L., Chapman, N. L., Lai, S.-P., Spiesman, W. J., Noriega-Crespo, A., Merín, B., Huard, T., Allen, L. E., Blake, G. A., Jarrett, T., Koerner, D. W., Mundy, L. G., Myers, P. C., Sargent, A. I., van

- Dishoeck, E. F., Wahhaj, Z., & Young, K. E. 2007, *ApJS*, 171, 447
- Ridge, N. A., Di Francesco, J., Kirk, H., Li, D., Goodman, A. A., Alves, J. F., Arce, H. G., Borkin, M. A., Caselli, P., Foster, J. B., Heyer, M. H., Johnstone, D., Kosslyn, D. A., Lombardi, M., Pineda, J. E., Schnee, S. L., & Tafalla, M. 2006, *AJ*, 131, 2921
- Roman-Duval, J., Jackson, J. M., Heyer, M., Rathborne, J., & Simon, R. 2010, *ApJ*, 723, 492
- Rosolowsky, E. & Leroy, A. 2006, *PASP*, 118, 590
- Rosolowsky, E. W., Pineda, J. E., Foster, J. B., Borkin, M. A., Kauffmann, J., Caselli, P., Myers, P. C., & Goodman, A. A. 2008a, *ApJS*, 175, 509
- Rosolowsky, E. W., Pineda, J. E., Kauffmann, J., & Goodman, A. A. 2008b, *ApJ*, 679, 1338
- Rybicki, G. B. & Hummer, D. G. 1978, *ApJ*, 219, 654
- Sadavoy, S. I., di Francesco, J., André, P., Pezzuto, S., Bernard, J.-P., Bontemps, S., Bressert, E., Chitsazzadeh, S., Fallscheer, C., Hennemann, M., Hill, T., Martin, P., Motte, F., Nguyen Luong, Q., Peretto, N., Reid, M., Schneider, N., Testi, L., White, G. J., & Wilson, C. 2012, *A&A*, 540, A10
- Sadavoy, S. I., Di Francesco, J., Johnstone, D., Currie, M. J., Drabek, E., Hatchell, J., Nutter, D., André, P., Arzoumanian, D., Benedettini, M., Bernard, J.-P., Duarte-Cabral, A., Fallscheer, C., Friesen, R., Greaves, J., Hennemann, M., Hill, T., Jenness, T., Könyves, V., Matthews, B., Mottram, J. C., Pezzuto, S., Roy, A., Rygl, K., Schneider-Bontemps, N., Spinoglio, L., Testi, L., Tothill, N., Ward-Thompson, D., White, G., JCMT, t., & Herschel Gould Belt Survey Teams. 2013, *ApJ*, 767, 126
- Sanhueza, P., Jackson, J. M., Foster, J. B., Garay, G., Silva, A., & Finn, S. C. 2012, *ApJ*, 756, 60

- Sault, R. J., Teuben, P. J., & Wright, M. C. H. 1995, in *Astronomical Society of the Pacific Conference Series*, Vol. 77, *Astronomical Data Analysis Software and Systems IV*, ed. R. A. Shaw, H. E. Payne, & J. J. E. Hayes, 433
- Scalo, J. M. 1987, in *Astrophysics and Space Science Library*, Vol. 134, *Interstellar Processes*, ed. D. J. Hollenbach & H. A. Thronson, Jr., 349–392
- Seo, Y. M., Shirley, Y. L., Goldsmith, P., Ward-Thompson, D., Kirk, J. M., Schmalzl, M., Lee, J.-E., Friesen, R., Langston, G., Masters, J., & Garwood, R. W. 2015, *ArXiv e-prints*
- Shirley, Y. L. 2015, *PASP*, 127, 299
- Shu, F. H., Adams, F. C., & Lizano, S. 1987, *ARA&A*, 25, 23
- Sobolev, V. V. 1957, *Soviet Ast.*, 1, 678
- Solomon, P. M., Rivolo, A. R., Barrett, J., & Yahil, A. 1987, *ApJ*, 319, 730
- Spitzer, L. 1998, *Physical Processes in the Interstellar Medium*
- Storm, S., Mundy, L. G., Fernández-López, M., Lee, K. I., Looney, L. W., Teuben, P., Rosolowsky, E., Arce, H. G., Ostriker, E. C., Segura-Cox, D. M., Pound, M. W., Salter, D. M., Volgenau, N. H., Shirley, Y. L., Chen, C.-Y., Gong, H., Plunkett, A. L., Tobin, J. J., Kwon, W., Isella, A., Kauffmann, J., Tassis, K., Crutcher, R. M., Gammie, C. F., & Testi, L. 2014, *ApJ*, 794, 165
- Swings, P. & Rosenfeld, L. 1937, *ApJ*, 86, 483
- Teuben, P. J., Pound, M. W., Storm, S., Mundy, L. G., Salter, D. M., Lee, K., Kwon, W., Fernandez Lopez, M., & Plunkett, A. 2013, in *American Astronomical Society Meeting Abstracts*, Vol. 221, *American Astronomical Society Meeting Abstracts*, 240.09
- Torres, R. M., Loinard, L., Mioduszewski, A. J., Boden, A. F., Franco-Hernández, R., Vlemmings, W. H. T., & Rodríguez, L. F. 2012, *ApJ*, 747, 18
- van der Tak, F. F. S., Black, J. H., Schöier, F. L., Jansen, D. J., & van Dishoeck,

- E. F. 2007, *A&A*, 468, 627
- van Dishoeck, E. F. & Blake, G. A. 1998, *ARA&A*, 36, 317
- Walawender, J., Bally, J., Reipurth, B., & Aspin, C. 2004, *AJ*, 127, 2809
- Walsh, A. J., Myers, P. C., & Burton, M. G. 2004, *ApJ*, 614, 194
- Walsh, A. J., Myers, P. C., Di Francesco, J., Mohanty, S., Bourke, T. L., Gutermuth, R., & Wilner, D. 2007, *ApJ*, 655, 958
- Ward-Thompson, D., André, P., Crutcher, R., Johnstone, D., Onishi, T., & Wilson, C. 2007, *Protostars and Planets V*, 33
- Weinreb, S., Barrett, A. H., Meeks, M. L., & Henry, J. C. 1963, *Nature*, 200, 829
- Wilking, B. A., Meyer, M. R., Greene, T. P., Mikhail, A., & Carlson, G. 2004, *AJ*, 127, 1131
- Williams, J. P., Blitz, L., & McKee, C. F. 2000, *Protostars and Planets IV*, 97
- Williams, J. P., de Geus, E. J., & Blitz, L. 1994, *ApJ*, 428, 693
- Wilson, R. W., Jefferts, K. B., & Penzias, A. A. 1970, *ApJ*, 161, L43
- Winston, E., Megeath, S. T., Wolk, S. J., Spitzbart, B., Gutermuth, R., Allen, L. E., Hernandez, J., Covey, K., Muzerolle, J., Hora, J. L., Myers, P. C., & Fazio, G. G. 2010, *AJ*, 140, 266
- Young Owl, R. C., Meixner, M. M., Wolfire, M., Tielens, A. G. G. M., & Tauber, J. 2000, *ApJ*, 540, 886
- Zhou, S., Evans, II, N. J., Koempe, C., & Walmsley, C. M. 1993, *ApJ*, 404, 232